Passive and Localised Corrosion Behaviour of a High Magnesium Alloy (Magnox Al80)

A thesis submitted to the University of Manchester for the degree of Doctor of Philosophy in the Faculty of Engineering and Physical Sciences

2013

ROBERT W BURROWS

SCHOOL OF MATERIALS

CONTENTS

Word count: 46,162

LIST OF FIGURES

9

LIST OF TABLES

ABBREVIATIONS

AC	Alternating Current
AFM	Atomic Force Microscopy
CE	Counter Electrode
COSMO	Conductor like Screening Model
CPE	Constant Phase Element
DAP	Diallyl Phthalate
DFT	Density Functional Theory
DN	Double Numerical
DND	Double Numerical plus d-functions
DNP	Double Numerical plus Polarisation
EIS	Electrochemical Impedance Spectroscopy
EN	Electrochemical Noise
ESEM	Environmental Scanning Electron Microscope/Microscopy
FGMSP	First Generation Magnox Storage Pond
FHP	Fuel Handling Plant
GGA	Generalised Gradient Approximation
GULP	General Utility Lattice Program
NII	Nuclear Installation Inspectorate (now ONR)
IAEA	International Atomic Energy Authority
LDA	Linear Density Approximation
MOP	Magnox Operating Plan
NDA	Nuclear Decommissioning Authority
OCP	Open Circuit Potential
ONR	Office for Nuclear Regulation
PBO	Parent Body Organisation
PTFE	Polytetrafluoroethylene
RE	Reference Electrode
SCF	Self Consistent Field
SEM	Scanning Electron Microscope/Microscopy
SRET	Scanning Reference Electrode Technique
SS	Stainless Steel
SVET	Scanning Vibrating Electrode Technique
TEM	Tunnelling Electron Microscope/Microscopy

ABSTRACT

Passive and Localised Corrosion Behaviour of a High Magnesium Alloy (Magnox Al80)

University of Manchester   Robert W Burrows
Doctor of Philosophy   January 2013

The high magnesium alloy Magnox Al80 is used as a clad for nuclear fuel employed in the UK gas-cooled, graphite moderated power station reactors of the same name. Following irradiation, spent fuel elements are stored in aqueous environments. Historical corrosion studies and plant experience have identified suitable chemistry regimes to ensure passivity of the material, by maintaining high pH and very low concentrations of aggressive anions, notably chloride. Despite this large body of work, certain aspects of the corrosion mechanism are not well characterised, notably, the growth kinetics of surfaces with thick passive films, the manner in which chloride initiates film breakdown and the underlying mechanism of localised corrosion in alkaline environments. A variety of corrosion investigation techniques have been applied here to address these knowledge gaps.

Extensive electrochemical work has been supported by characterisation of the corrosion morphology with *in situ* observations including correlated videomicroscopy, quantitative image analysis and micro-tomography. These results have allowed targeting of quantum mechanical atomistic calculations on ionic adsorption and substitution at a simulated passive film lattice interface. Production of magnesium microelectrodes and application for corrosion study have been reported for the first time. Finite element modelling has been used for interpretation and reconciliation of these results, allowing comparison between techniques, previous observations and with plant experience.

The findings of these studies have provided clarity on a number of aspects of Magnox, and magnesium, corrosion behaviour. An extension of the high field film growth model has been proposed, incorporating the effect of an outer hydroxide layer which stabilises the very thin, dense inner oxide at the metal surface. The outcomes of atomistic simulations relating to anions on the passive film lattice interface have been related semi-quantitatively to macroscopic results. Magnesium has been clearly shown to undergo salt film corrosion in conditions not substantially different from those in a fuel storage environment.

Consideration of these findings in the context of previous mechanistic work has led to the proposal of a reaction scheme which reconciles the very different behaviours of these materials with a small number of underlying reactions. These describe corrosion according to reactions across a very thin surface film (whether oxide or salt film) with the rate, evolution and morphology being determined largely by the specific mass transport processes at work.

DECLARATION & COPYRIGHT STATEMENT

No portion of the work referred to in the thesis has been submitted in support of an application for another degree or qualification of this or any other university or other institute of learning

ACKNOWLEDGEMENTS

PREFACE

This project was originally initiated in 2003 following a programme of electrochemical characterisation of Magnox Al80 corrosion behaviour in pond storage chemistries undertaken at the former Berkeley Technology Centre site on the banks of the River Severn in South Gloucestershire. A hiatus ensued following restructuring of the UK civil nuclear industry and associated loss of research funding and facilities. A bursary was awarded by the Nuclear Decommissioning Authority to allow part time completion of the project which then focussed on use of modelling and advanced techniques.

The project has extended across succession of four parent organisations, at least a dozen team structures and seen the end of generation at 11 Magnox reactors. During this period nuclear generation in the UK has avoided emissions in the order of half a billion tonnes of carbon dioxide in production of electricity.

Since the completion of the practical investigations within this project, further programmes of work have been completed on plant-specific aspects of Magnox corrosion performance employing the techniques developed in this research and facilitated by the experience so accrued. On this basis, the investments of the industry in this area were timely and have been shown as demonstrations of foresight and prudence. Ongoing allocation of resources into technical research is evidently imperative to ensure the availability of scientific bases for effective decision making, operational efficiency and robust safety as well as development of capabilities and individuals.

Rob Burrows is an industrial chemist who joined the Plant Chemistry and Corrosion team at Berkeley Centre in 2001 following completion of a degree in Chemical Physics at the University of Bristol. He was involved in undertaking corrosion studies on high temperature waterside steel pitting and behaviour of fuel element materials, as well as plant support on various topics including ion exchange and filtration processes and operational experience review. More latterly, Rob provides interpretation of water reactor primary side chemistry from plant data through application of kinetic transport models, as well as assessment of chemistry aspects of new build reactor design candidates, in addition to continuing practical electrochemistry research in relation to spent fuel storage and management topics.

1   Executive Summary

Significant volumes of spent Magnox nuclear fuel are currently in storage within aqueous environments in the UK. Integrity of the fuel cladding is required to avoid exposure of the metallic irradiated uranium, release of fission product radionuclides and degradation of the fuel. The clad is a high magnesium alloy (Magnox Al80) which is kept passive by maintenance of a high pH and low concentrations of aggressive anions in fuel cooling ponds. Magnox, in common with magnesium, is known to suffer rapid localised corrosion when exposed to chloride and other aggressive anions.

This project has identified three priority areas of direct relevance to Magnox fuel storage to be investigated.

1. What happens during Magnox passivation?
2. Why does localised corrosion initiate?
3. How does surface attack develop into destructive pitting?

A wide variety of corrosion investigation techniques have been applied to address these questions which have been reported through the course of the project (Burrows *et al.,* 2005, Burrows & Harris, 2007 and Burrows *et al.,* 2012).

Highlights have included the first reported production and application of magnesium microelectrodes in corrosion studies. This work showed that even under alkaline bulk chemistry and low chloride concentrations, salt film dissolution occurs on the magnesium surface with rapid dissolution proceeding under a thin layer of magnesium chloride. This is consistent with the results of a variety of morphological characterisations which have been undertaken in parallel, including environmental SEM and *in situ* microtomography. This correlation strongly suggests that the salt film mechanism is the underlying basis of both the filiform-like surface corrosion and destructive bulk pitting which occur on freely corroding surfaces.

Quantum mechanical atomistic modelling has been applied to magnesium oxide lattice structures as an analogue for the Magnox and magnesium passive surface. These calculations have shown that chloride does not strongly interact with the surface at lower surface coverages, but above a particular threshold will substitute into the structure and destabilise the film surface. The chloride level predicted to cause localised corrosion initiation agrees closely with that observed in electrochemical tests for high pH systems. Some simple considerations of migration effects have suggested that ionic movement in the solution near the interface and at geometric features, such as crevices, may account for the trend seen at lower concentrations.

An extended model has been developed to describe the kinetics of oxide growth for Magnox. This is based on an existing expression describing surfaces with very thin surface layers which has been modified to account for the less protective but thicker hydroxide layer which forms on the outer interface. This has reconciled the previous fundamental understanding of Magnox film growth with the behaviour observed over much longer timescales which relate to realistic fuel storage timescales.

On the basis of these outcomes, a consistent mechanistic reaction scheme has been described. A greater understanding of the conditions and processes which influence passivation and pitting of Magnox Al80, and magnesium, has been provided. The techniques which have been developed and applied represent a powerful toolset for subsequent plant specific studies of Magnox behaviour. The outcomes of the work represent an incremental reduction in the risks associated with management of spent Magnox fuel materials in the UK.

2 Introduction

2.1 Project Context

The magnesium alloy Magnox Al80 (0.8%wt Al) is used as a clad material in the UK's first generation gas-cooled, graphite moderated nuclear reactors of the same name. The alloy was selected for its low neutron cross-section, a requirement for the high neutron economy needed for the typically unenriched metallic uranium fuel. The material also showed the necessary performance in high temperature carbon dioxide and, importantly, did not suffer from compatibility problems (interphasing) in the same way as the aluminium cladding which had been used in the early part of the UK nuclear programme (Harris, 1985).

Following discharge from reactor, Magnox fuel (Figure 2-1) is typically stored underwater in cooling ponds to allow heat removal and biological shielding during decay of short lived radioisotopes before reprocessing. As magnesium is a reactive metal, chemical control of the cooling ponds is necessary; typically dosing of sodium hydroxide to maintain a high pH and removal of anions, both adventitious impurities of chloride and sulphate, plus carbonate from absorption of atmospheric carbon dioxide. Under these conditions, Magnox maintains a passive film and very low corrosion rates, although only relatively low levels of aggressive anions are required for localised corrosion to initiate which can lead to rapid clad penetration by pitting (IAEA, 1998). When clad failure occurs, corrosion of the metallic uranium will ensue, allowing release of fission products, notably the highly soluble caesium nuclides.

"The effect of spent fuel being stored much longer in ponds needs to be understood and mitigation put into place."

"Maintaining fuel integrity is a critical activity."

Reference: NDA, 2010 - Magnox Operating Plan (Revision 8)

According to the Nuclear Decommissioning Agency's Magnox Operating Plan (NDA, 2010), which describes the optimised strategy for management of spent Magnox fuel, as of April 2012, a further 3800 tonnes of irradiated fuel (in the region of 300,000 fuel elements) was expected to require reprocessing through Sellafield. The inventory of caesium-137 within this fuel (Macdonald, 1986) can be roughly estimated as of the

order of 10^{18} Bq, which is over an order of magnitude greater than the activity of this nuclide thought to have been released during the Chernobyl disaster. Indeed, during the mid/late-1970s, annual liquid discharges of caesium-137 from the Sellafield site were of the order of 5×10^{15} Bq, much of which was attributable to corrosion of Magnox fuel in storage (Gray *et al.*, 1995).

As well as potential release of radioactivity to the environment, failure of Magnox fuel also poses a variety of additional problems including reduced handleability of the fuel (including ease of transport and reprocessing), production of mobile actinide bearing sludge, evolution of hydrogen (with attendant flammability considerations), potential for formation of pyrophoric uranium hydride, increased local doses to operators from high pond water activity and increased production of secondary wastes. Some of these effects can be self accelerating, for example, the presence of sludge in contact with fuel clad increases corrosion rates (Case and Hilton, 1978) and high pond water activities reduce the range of treatments available to improve chemistry and operator accessibility, so that a situation involving large quantities of degrading fuel may be difficult to recover. Indeed this describes closely the background to the situation of the First Generation Magnox Fuel Storage Pond at Sellafield (see Figure 2-2), where increased storage times following plant outages in the 1970s led to extensive clad corrosion (Richardson & Maher, 2004 and White, 2010). This open-air pond is estimated to still contain many tonnes of fuel (Hansard, 2003), over a thousand cubic metres of corrosion sludge and fourteen thousand cubic metres of contaminated water (NDA, 2012), represents some of the highest hazards on the Sellafield site and is arguably one of the most challenging nuclear clean-up projects in the world (AKtiv Nuclear JV, 2012).

Figure 2-1: Magnox clad fuel elements, (i) following manufacture (left), (ii) showing differing designs (centre) and (iii) with corrosion damage to clad (right) (sources: (i) www.nda.gov.uk and (ii) www.sellafieldsites.com)
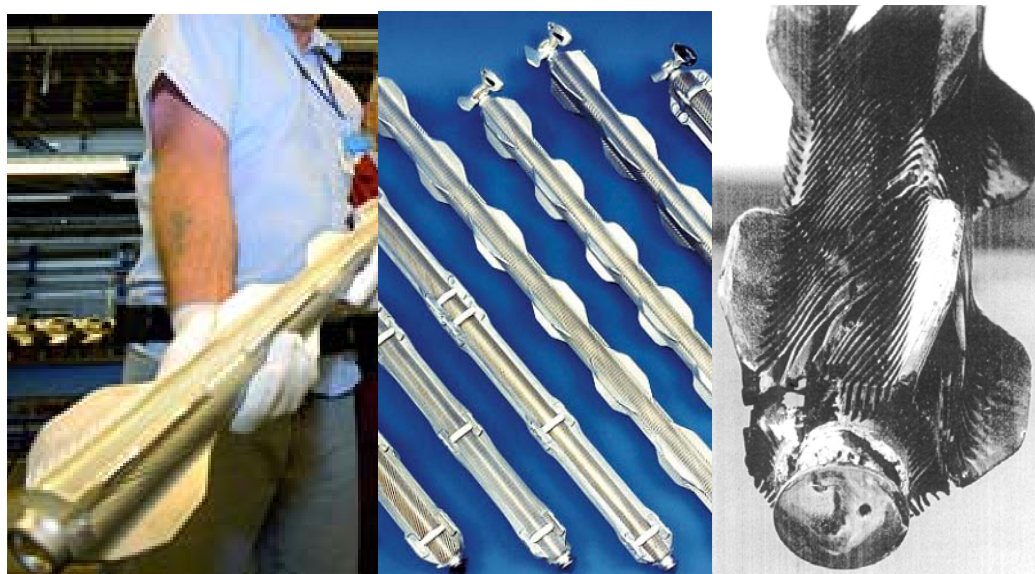
Although more modern waste management and effluent treatment techniques have been able to massively reduce the impact of activity release, there are further examples of problematic Magnox clad corrosion. As well as storage in fuel ponds, Magnox fuel is dry stored, which has the advantage of eliminating the clad-water interaction. However, in an instance where moisture was able to enter a dry store, corrosion occurred on a number of fuel elements (Magnox Ltd, 2011). Recovery of the damaged fuel was complicated by the risk of spreading contamination and was the subject of a number of unsuccessful attempts over some 20 years before being finally removed and consigned for reprocessing. A much more extensive incidence of fuel failures occurred in the Fuel Handling Plant ponds at Sellafield in the late-1990s and early-2000s. Storage times had increased and technical difficulties with the plant meant that the intended very high alkalinity of the fuel storage containers was not being maintained. These problems were compounded by the introduction of a supply of sodium hydroxide used to dose the water which had up to 2%wt chloride rather than 0.01%wt (Manning, 2003 and Richardson & Maher, 2004). These issues together led to an inventory of corroded and difficult to process fuel which caused large increases in the pond water activity and, consequently, heightened environmental discharges coupled with generation of secondary wastes. Although these impacts were of a much lesser order than those experienced from Magnox corrosion in the First Generation Magnox Fuel Storage Pond, the backlog of corroded fuel has been slowly reprocessed over a period of more than a decade (NDA, 2010).

The episodic nature of these corrosion events is a reflection and to some extent a product of the characteristic corrosion behaviour of the material. Under established passivating conditions, corrosion rates are negligible and the performance of the material is so good that it may be stored and managed with apparent ease and without corrosion failures, such that it appears quiescent. In this situation, management of the material may become reactive, with complacency becoming a threat as operational focus moves to other priority areas, or for apparent benefit of economy. Although the material can in some cases tolerate a surprising level of deterioration in conditions, a relatively small change in a particular parameter can equate to a transgression of the line representing passivity, with active corrosion ensuing. The extremely high rates of pitting which may be produced, and the self-accelerating nature of some aspects of the corrosion mechanisms mean that the timescale for widespread failure of fuel can be less than the minimum required for rectification of conditions, particularly in a context of reduced management effectiveness and where other possibly mitigative storage considerations may have already been compromised.

"We recognise that long-term storage will play an increasing role; some technical issues also need to be resolved."
Environment Agency

"The Magnox Operating Plan is a programme of national importance in that its timely delivery ensures that a Magnox spent fuel legacy is not left for future generations to deal with."
Energy Solutions (Magnox Ltd PBO)

"The strategy needs to give greater prominence to the need to review storage capabilities for spent fuels (and nuclear materials) to ensure that they are adequate for future scenarios and contingencies."
HSE Nuclear Directorate NII (now ONR)

"Due consideration of the potential impacts of failed fuel and long term fuel integrity issues."
EDF Energy

Reference: NDA, 2011 - NDA Strategy: Post Consultation Responses on Spent Magnox Fuel

The experience from such events underlines the value of a knowledge of the corrosion behaviour of engineering materials which fulfil key functions. Indeed, extensive work programmes have been undertaken through the history of the UK nuclear industry leading to well defined envelopes for the storage and treatment of Magnox fuel. The benefits of capitalising on the availability of modern corrosion investigation techniques to build on the previous work programmes is clear. As well as reducing risks from enhanced corrosion of Magnox fuel in storage and providing mitigations to any event which could occur, an in depth understanding of the materials performance also provides possibilities to improve operations, particularly in the context of decommissioning the UK's historic nuclear liabilities. One contingency which has been identified for Magnox fuel management is the use of dry storage (Morris *et al.*, 2009). At present, ongoing reduction in fuel inventory by reprocessing is the identified strategy, which involves wet fuel stocks. In the case of a full scale dry storage campaign, the need to dry wetted fuel and underpin the subsequent performance would point to a requirement for knowledge of aqueous corrosion processes. The need for additional understanding of Magnox corrosion behaviour, particularly in relation to longer term storage is evident from NDA strategy documents. An improved confidence in the resilience of the management options serves to underpin the continuing benefit derived from seven decades of electrical generation from Magnox power stations.

Figure 2-2: (i) Fuel skips within FGMSP (upper-left), (ii) corroded fuel in dry store (upper-right), (iii) containers within the fuel handling plant pond (lower) (sources: NDA, 2011, www.nda.gov.uk, Magnox Ltd, 2011, www.magnoxsites.com)
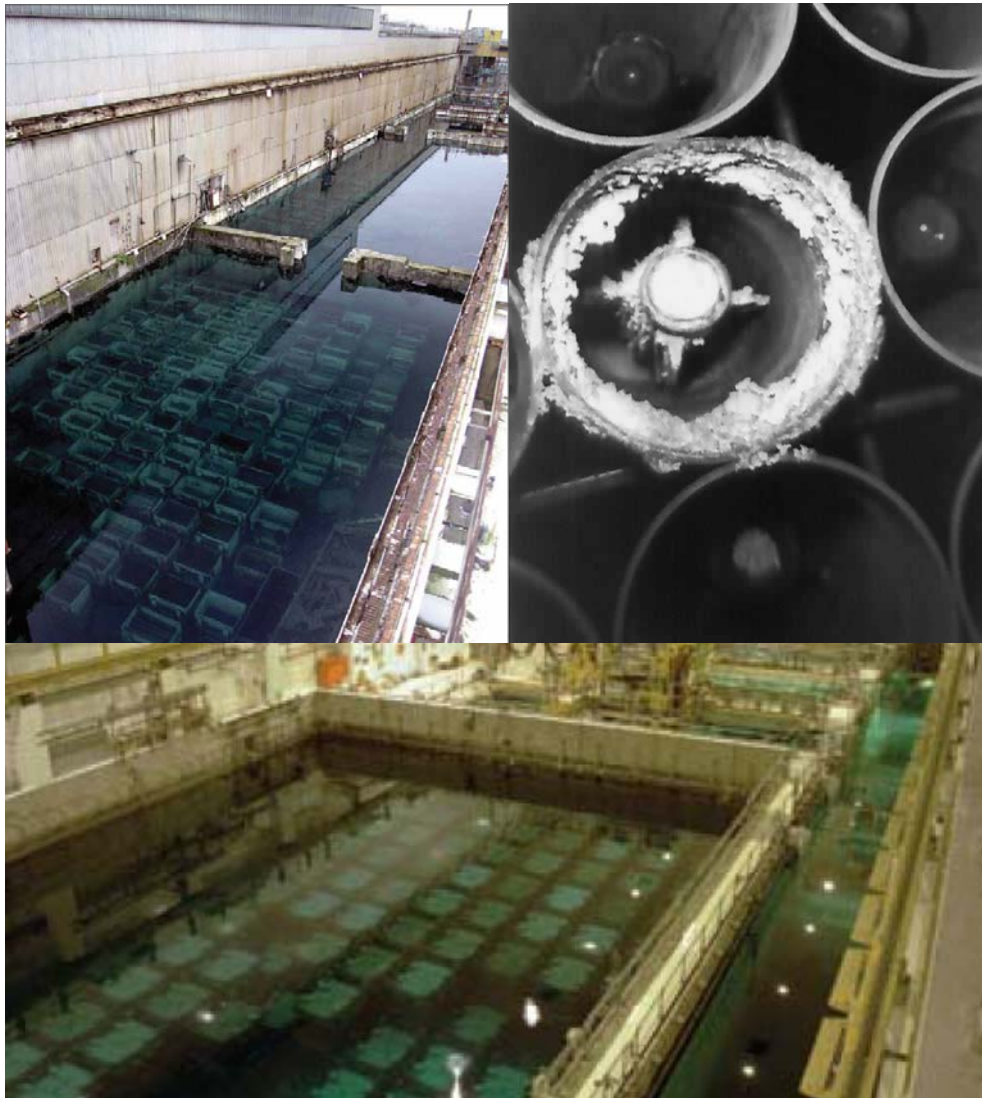
2.2 Magnesium Alloy Clad Nuclear Fuel

The use of a high magnesium alloy as a clad material for metallic uranium nuclear fuel in the UK nuclear industry arose from the need for a low neutron adsorption cross section material imposed by the use of unenriched fuel and the consequent requirement for high neutron economy. Early fuels used aluminium clad, however, the formation of aluminium-uranium interphases led to fuel failures (Harris, 1985). Magnesium, with small additions of alloying elements, showed satisfactory performance in the reactor coolant matrix at operating temperatures up to ~430 ºC and could be readily machined or extruded with heat transfer fins. Although reactive, magnesium could be stored dry or, as has generally been the case, in alkaline cooling ponds which provided additional

advantages in heat removal and biological shielding. In the early history of reactor operations, fuel was stored for relatively short periods of time (~90 days) to allow decay of the short lived isotopes before despatch for reprocessing. Undosed (buffered) open air ponds were the typical storage environment which equated to relatively low pH and high anion concentrations. The typical storage times tended to increase in duration, however, and the specification of pond water chemistry was improved to avoid corrosion problems (Windsor, 1982). A high pH and low anion concentration were maintained by pond water treatment plant, along with heat removal and filtration. Chloride, sulphate and silicate have been identified as causing localised corrosion, although the former is particularly aggressive, causing pitting at levels well below 10 mg kg^{-1} (Masterson & Harrison, 1961). Fluoride was found to be an effective inhibitor, particularly at high temperatures, and although carbonate appeared to reduce the effect of aggressive anions, it appears to do so at the expense of an increase in general corrosion rate (Case & Hilton, 1978).

The early designation of the can alloy was Magnox A12 which was superseded by Magnox Al80, although the specification remained the same, with 0.7 – 0.9%wt aluminium and 0.002 – 0.03 %wt beryllium being the notable alloying elements, added for high temperature oxidation performance (Masterson & Harrison, 1961) and with impurity limits, notably for iron. Henceforth, references to the material Magnox may be assumed to relate to the Al80 alloy unless otherwise noted. Other Magnox alloys are typically used for specific parts of the fuel element, such as "splitters" and end-fittings (Duckworth *et al.*, 1988), however, these do not typically form part of the containment of the uranium bar. Although crevices are likely to be present between the different components, these magnesium alloys are unlikely to be sources of significant polarisation, however, other fittings on fuel elements may credibly produce galvanic coupling. These include steel end-caps, graphite cones, nickel alloy springs and thermocouples (Masterson & Harrison, 1961).

During irradiation, a thick oxide film is formed on the exterior surface of the elements and in some cases this is accompanied by carbonaceous deposits formed from the carbon dioxide reactor coolant (Case & Hilton, 1978). This oxide film is not a barrier to water during subsequent storage, due to microcracking or porosity but undergoes a process of hydration over 50-100 days during which time corrosion at the metal interface also occurs. The susceptibility of a reactor-oxidised surface to pitting attack is also greater (compared to an etched surface). Due to the dimensional changes to the uranium bar which occur during irradiation (Duckworth *et al.*, 1988), it can be expected that there will be deformation of the cladding, which can clearly be seen to lead to crevice formation, for example, where fins come into contact due to waving (see Fig. 2-3). Whilst in storage within cooling ponds, fuel elements are held within painted steel

skips. Although galvanic coupling would normally be precluded due to the skip coating, it has been found that the paint may deteriorate leading to the possibility of electrical contact with the fuel elements. Mechanical handling of the elements is also known to have the potential to freshly expose areas of metal, which introduces a further possible source of polarisation as a film-free surface has a different potential to one bearing a pre-existing film (Kirby, 1987). A further factor identified to have an effect on corrosion is the presence of corrosion product sludges which may accumulate if not removed and have been shown to increase susceptibility to pitting (Case & Hilton, 1978). Where fuel failures have occurred, the precise cause is often difficult to determine in subsequent examinations as the initiation site will often have been extensively disrupted by the point that corrosion is detectable from increases in soluble nuclides. Nonetheless, in certain cases, observation of pitting in the early stages has been able to unambiguously identify this as the clad failure mechanism in post irradiation examination of pond stored fuel elements (Fig. 2-3).

Figure 2-3: Magnox clad fuel element fin deformation due to irradiation (upper) and clad cross section showing transgranular pitting corrosion which occurred during pond storage (lower) (reproduced from Duckworth *et al.*, 1988)
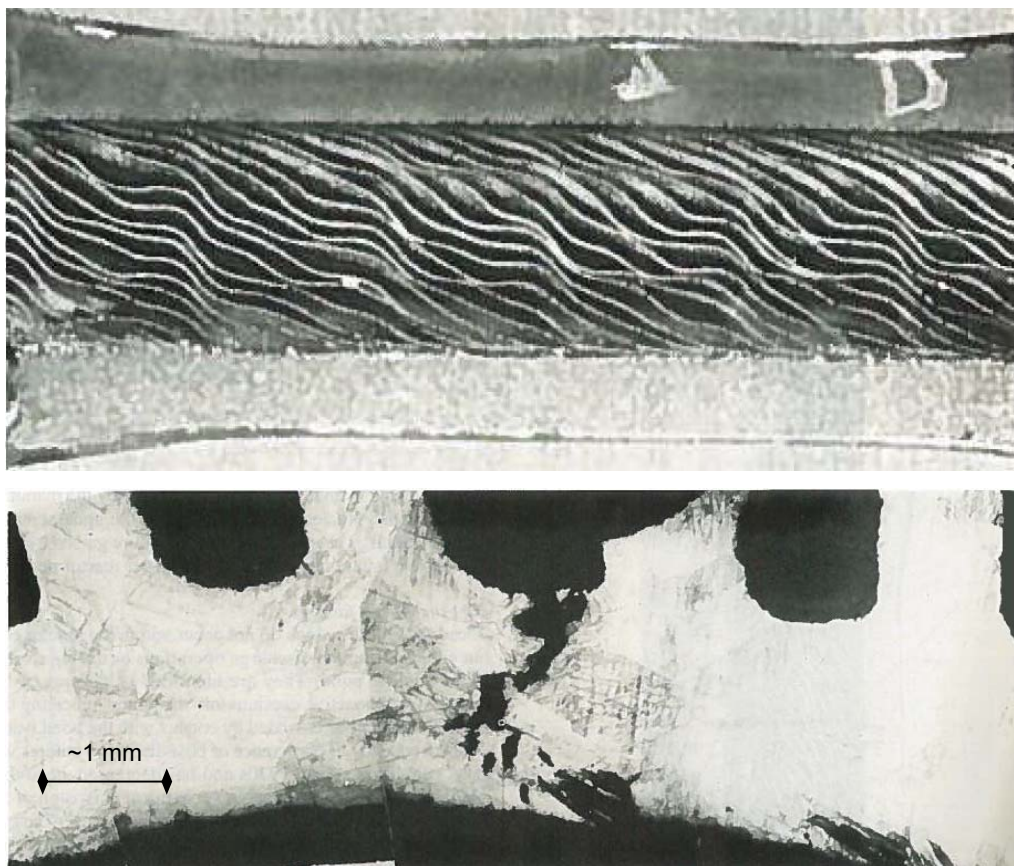
Major work programmes were undertaken to allow successful storage chemistries to be employed (Masterson & Harrison, 1961, Jones & Masterson, 1961, Bradford *et al.,* 1976, Case *et al.*, 1977, Case & Hilton, 1978, Cowan & Harrison, 1979, Friskney, 1981,

Friskney *et al.* 1982, Greef *et al.*, 1986, Kirby, 1987) and these are summarised in Section 2.3. This is in addition to extensive industry literature not in the public domain.

The key consistent output of these studies was the requirement that fuel should be stored in alkaline conditions, with pH >11.5, typically achieved by dosing with sodium hydroxide to 200 mg kg^{-1} (0.005 M) and very low concentrations of aggressive anions by ion exchange treatment. The recommended maximum concentrations of aggressive species were incrementally revised downwards with successive studies from 5 mg kg^{-1} chloride (Masterson & Harrison, 1961) to a target of <0.5 mg kg^{-1} combined chloride and sulphate (Kirby, 1987). Fluoride has been applied as a contingency against acute short term corrosion of Magnox under a fire accident scenario involving an inter-site transport flask by dosing into the flask solution at a concentration of 1000 mg kg^{-1} (fluoride as sodium fluoride). An additional storage matrix which has been used extensively employs containers to allow isolation of the storage solution and consequently much higher alkalinity (pH >13). This is primarily intended to allow inhibition of chloride induced pitting over longer timescales and also to arrest pitting should this have already initiated. The corrosion behaviour of Magnox under differing matrices has implications for other contexts such as reactor fault scenarios (Friskney, 1981) and waste encapsulation (Fairhall & Palmer, 1992), although these mechanisms are somewhat different to the aqueous behaviour. It is noted that magnesium alloys have been used elsewhere in the world for nuclear fuel cladding (Thomas & Weber, 1968, Albright, 1994, IAEA, 1998, Morris *et al.*, 2009).

2.3   Magnesium Aqueous Corrosion

Since the metal was first produced in a tangible form by Bussy (1831), the corrosion behaviour and electrochemistry of magnesium has been a subject of investigation. Beetz (1866) made a number of observations in relation to hydrogen evolution from a magnesium anode during electrolysis. This behaviour was a feature of early publications (Christomanos, 1903, Baborovsky, 1903 and Turrentine, 1908) which accompanied the proposition of a monovalent magnesium ion to explain the increase in hydrogen evolution rate with anodic polarisation despite being a cathodic process. Further studies on the electrochemical behaviour of magnesium under anodic polarisation identified various mechanisms which could explain this effect on the basis of observations from different analyses. Petty *et al.* (1954) undertook oxidation tests and attributed these to the action of the monovalent ion, particularly tests showing reduction of species in solution domains not in contact with the electrode, taken as an inference that a mobile ion was transported away from the reacting surface. Investigations relating to wastage corrosion of battery electrodes (Robinson, 1963) assigned the effects to variation in the

passive film coverage and the relative areas of active sites. Straumanis & Bhatia (1963) undertook microscopic and chemical characterisation of the distinctive black corrosion products and identified the composition as being microscopic particles of metallic magnesium within a magnesium hydroxide matrix, in contrast to early work which had notionally assigned the material as a sub-oxide of magnesium. The action of these minute particulates as the cause of the increase in hydrogen evolution through reactions continuing following detachment from the polarised surface was put forward and the highly reducing nature of detached fine particles noted in relation to the prior observations of reduction *ex situ*.

Consideration of magnesium behaviour in the context of corrosion and protection, rather than electrolysis or cell behaviour, forms part of the discussions by Kolotyrkin (1961), and Hoar (1967) includes considerations of magnesium behaviour in discussion of the passivity of metals in terms of passive film formation and anion induced breakdown.

It was also around this time that study of the corrosion behaviour of Magnox was first reported in the open literature (Masterson & Harrison, 1961 and Jones & Masterson, 1961). The material was found to be highly passive in alkaline storage environments, but this could only be maintained under good chemistry conditions. The importance of understanding the action of anions in causing localised corrosion of the material was also noted due to the potential for release of radioactivity into the storage environments.

Thomas and Weber (1968) also discussed the performance of magnesium alloys as nuclear fuel clad materials and presented similar conclusions on the passivity of the material but also its propensity to localised corrosion at low levels of chloride, particularly as a result of galvanic coupling.

The passive film behaviour of Magnox Al80 was studied by Bradford *et al.* (1976) on the basis of ion beam tests to examine the profile of thick pre-existing hydroxide corrosion films (including reactor coolant formed oxide films) exposed to isotope labelled water and various anions. These showed that the hydroxide corrosion film was porous and formed at the metal interface. There was minimal interaction of labelled water with the pre-existing film, however, fluoride was found to slowly substitute into the film to approach a hydroxyl-fluoride composition which was similar to that grown from a fresh surface in the presence of fluoride. The reactor formed oxide films were found to slowly hydrate to hydroxide, initially from the solution interface, but with reaction of the metal substrate occurring once the hydration had proceeded sufficiently to allow access of water. The presence of the reactor formed oxide films was found to encourage pitting corrosion compared to pre-corroded or fresh surfaces.

The results of tests on Magnox Al80 involving exposure to silicate have also been reported (Case *et al.*, 1977) which suggested that the anion increased corrosion rate, particularly at high temperatures and was incorporated into the corrosion film. Case & Hilton (1978) noted further detail of the pond chemistry employed and the extent of operating experience which had been accumulated. The observation was also made that the general corrosion rates observed would be consistent with indefinite storage times being possible and that indeed, specific instances were known where fuel elements had resided in pond storage over several years without penetration of the clad occurring. Detailed information on the effects of in-reactor exposure, storage chemistry and plant factors was also reported. Friskney *et al.* (1982) reported further information from this programme of work, mainly describing the behaviour at higher temperatures, where a phenomenon known as "breakaway" corrosion was observed.

Cowan & Harrison (1979) also used electrochemical techniques to study the competing effects of chloride and fluoride as aggressive and passivating ions respectively. This followed on directly from the work of Bradford *et al.* (1976) and the results were presented as a basis to allow predictive understanding of behaviour under varying chemistries. The results showed film formation on the magnesium surfaces and included an interpretive equivalent circuit model for EIS data comprising charge transfer resistance and a capacitive element in parallel, with Warburg elements being observed under particular conditions.

Greef *et al.* (1986) used ellipsometry alongside electrochemical testing to study the initial formation of the Magnox passive film and made observations about the effect of differing anions. The work was not successful in identifying a magnesium oxide barrier film beneath the hydroxide layer but did put an upper thickness bound of 5 nm on the basis of the sensitivity of the technique.

Kirby (1987) reported tests using coupons of Magnox Al80, steel and PTFE studying the effects of galvanic interactions and sample geometry on corrosion in pond environments at pH 11.7. This noted that when crevices or galvanic couples were present chloride concentrations of 10 mg kg^{-1} or greater caused extensive pitting and a concentration below 1 mg kg^{-1} was required to avoid attack. Observations were also made of filiform-like surface corrosion prior to bulk pitting and the effects of controlled galvanic coupling of a small number of spent fuel elements within a storage pond to a defectively painted skip. Open circuit potential measurements were also made of spent fuel elements within the storage pond.

In the late 70's and early 80's a number of papers were published concerning electrochemical tests on magnesium consistent with a general aim to make inroads into

the fundamental corrosion behaviour of the material. Tunold *et al.* (1977) used electrochemical techniques to examine the pitting mechanism in relation to the four general mechanisms into which they grouped the explanations on anodic hydrogen evolution from a number of contemporary papers (which are not discussed individually here). This grouping has been referred to by various papers subsequently and can be broadly summarised as; surface disintegration, monovalent magnesium, incomplete film and magnesium hydride. It was observed that corrosion initially proceeded by formation of microscopic pits along the surface of the electrodes followed by development of these into pits and crevices, potentially leading to catastrophic laminar type corrosion. The results were observed to be consistent with potential independent pits with total area being a function of potential. The initiation behaviour was suggested to be related to preferential absorption of aggressive anions in relation to hydroxide or water leading to pore propagation within the film.

A detailed mechanistic study of magnesium salt film corrosion was undertaken (Beck & Chan, 1983) which involved a programme of electrochemical tests and observations on polarised macroscale one-dimensional pit electrodes (5 mm^2 cross section) in molar and supra-molar magnesium chloride solutions. The results definitively demonstrated this aspect of the corrosion mechanism and noted a number of characteristic behaviours as well as mass transport kinetics. At high anodic potential, a continuous salt film was observed to form on the electrode surface leading to a potential independent region once the film was established. In this region, the relative hydrogen generation rate was very low and the cumulative charge was found to be an accurate measurement of the total metal loss assuming a standard ion valence of 2. Hydrogen generation during this phase was attributed to the direct reduction of water and results were consistent with the diffusion of water molecules across the salt film and production of hydrogen at the metal interface. AC investigations showed that the reversible potential corresponded to the theoretical value for the reaction of the metal with chloride and also noted a characteristic capacitive charging and discharging of the salt film at higher frequencies. The conductivity within the artificial pit was measured showing a smooth concentration profile from the base of the pit to the bulk concentration near the mouth. Tests in saturated magnesium chloride solutions showed that the base of the pit could become substantially supersaturated and this was suggested to be as a result of fracturing of the salt film to form very fine particles. Notably, the authors make no comment as to the relevance of the results reported to magnesium pitting corrosion, despite the evident fundamental relevance. It is evident that the conditions studied were substantially different to those relating to Magnox storage in that the chloride is some 5-6 orders of magnitude higher, the pH neutral or mildly acidic and the polarisations required to enable formation of a stable salt film were substantially greater than any likely source within a pond storage environment.

A large number of more recent papers have focussed on the corrosion performance of magnesium and its alloys in the context of structural and particularly automotive applications. Many of these alloys, notably AZ91, are two-phase (cf. single phase microstructure of magnesium and Magnox Al80) and the conditions tend to be neutral or mildly alkaline with high (~molar) levels of chloride. Notably, publications from the University of Queensland (Australia) and collaborators have been prolific (Jia *et al.*, 2007, Song & Atrens, 2007, Winzer *et al.*, 2007, Shi *et al.*, 2010, and Shi & Atrens, 2011). A re-examination of the possible mechanisms accounting for anodic hydrogen evolution given by Tunold *et al.* (1977) using AC techniques in tandem with gas evolution measurements led Song *et al.* (1997) to propose that the corrosion behaviour of Magnox was best explained by a passive film behaviour when in protective conditions, but with an additional mechanism being at work when localised corrosion occurred due to the presence of aggressive anions. The production of monovalent magnesium was identified as a mechanism which could be related to the AC impedance spectra and the observed current efficiency. This reaction has been consistently referred to by these workers despite evidence being "circumstantial" (Song & Atrens, 2007) with little mechanistic support and importantly, no direct observations of the species involved. Papers by other authors have proposed mechanisms which also provide explanations of anodic hydrogen evolution behaviour and are effectively analogous to the proposed monovalent ion mechanism in terms of the macroscale behaviour (Bender *et al.*, 2011), but present the advantage of removing the convolution of an unconfirmed intermediate species of unknown behaviour. A large number of their own studies involving electrochemical methods are reviewed by Song & Atrens (2007), noting that further study of magnesium localised corrosion mechanisms is one area of imperative defensive research.

A critical review of magnesium alloy corrosion by Ghali *et al.* (2004) provides a useful discussion of a large number of references. Of note is an investigation of corrosion morphologies on AZ91 which includes microanalytical study of the filiform-like corrosion observed following initial breakdown in passivity (Lunder *et al.*, 1994) and these features have also been studied by Li (2010) using electrochemical methods. Further environmental factors have been investigated including stress corrosion (Winzer *et al.*, 2007 and Aghion & Lulu, 2010) and the influence of a magnetic field on localised corrosion initiation (Li *et al.*, 2010), again using electrochemical methods. Other papers concerned with typical automotive alloys have included work employing ESEM (environmental scanning electron microscopy) to observe initiation of localised corrosion (Chen *et al.*, 2009) and ellipsometry to measure the thickness of passive films (Hara *et al.*, 2007).

The spatial arrangements of electrochemical processes on a corroding magnesium surface have been studied by SRET (scanning reference electrode technique) and SVET (scanning vibrating electrode technique) which have shown a number of interesting mechanistic features including cathodic activation of corroded surface (Williams & McMurray, 2008 and Williams *et al.* 2010) and this technique has been applied to study inhibition by phosphate and chromate.

Workers at the University of Birmingham (Gonzalez Torreira *et al.*, 2003 and Gonzalez Torreira, 2004) have presented results of electrochemical tests on Magnox Al80 and magnesium of specific relevance to Magnox fuel storage performance, including the effects of varying levels of anions, both aggressive and passivating. The latter reference also comprises an in depth contextual discussion. The structure of the passive film and the filiform-like corrosion features were studied using surface characterisation techniques, which were successful in confirming the presence of an oxide barrier layer as part of a composite oxide-hydroxide passive film. The effect of crystallographic orientation on corrosion behaviour was also examined through micro-electrochemical characterisation of single grains using a glass capillary cell. The short term kinetics of oxide formation studied which showed that these could be explained by the high field model. The tests highlighted the fact that, although subtle differences exist, the corrosion behaviour of magnesium and Magnox Al80 are similar, certainly in relation to a two phase alloy. The following electrochemical half cell reactions are described by Gonzalez Torreira (2004);

$$Mg \rightarrow Mg^{2+} + 2e^- \qquad\qquad \{2\text{-}1\}$$

$$2H_2O + 2e^- \rightarrow H_2 + 2OH^- \qquad\qquad \{2\text{-}2\}$$

Wide-ranging reviews of magnesium corrosion are also included in standard references (Shreir's Corrosion, 2010 - see Section 3.09 and Uhlig's Corrosion Handbook, 2011 - see Section 58) which note the broad behaviour of the material in terms of its propensity to pitting and crevice corrosion in the presence of chloride.

2.4   Project Aims

From the contextual summaries above of UK strategy and the technical background of magnesium corrosion behaviour it is possible to identify focus areas of greatest priority. On this basis, the aim of this work is essentially to reconcile the available information on plant operating experience with the fundamental understanding of electrochemical behaviour.

At present, observations are available from long term storage of material. Electrochemical measurements of the passive film cover only short time periods and although consistency with the high field film growth model has been established, the extent to which this provides an adequate description for much longer timescales and whether this can be related to electrochemical behaviour more generally is not clear. Equally, mechanisms describing differing phases of the localised corrosion of the material in relation to the alkaline storage chemistries are not available.

An accurate representation or simulation of a fuel element for corrosion study is not readily achievable due to the highly heterogeneous and variable nature of the surface and the processes which lead to its formation. Much of the wider literature considers conditions which are not directly relevant to Magnox fuel storage, for example, with very high chloride content or with multi-phase alloys. Nonetheless, the techniques available in the form of electrochemical methods are known to be capable of simulating crevices, the effects of external polarisations and artificial ageing. Also, the information pertaining to other materials and environments may very well be of mechanistic significance to fuel storage as long as the relevant differences may be identified and the implications understood. Accepting that a "real" fuel element is a highly complex object, small scale, inactive work may allow focus on the key mechanisms which could limit the storage lifetime and allow investigation of variations in parameters which would not be possible in plant trials due both to constraints on operation as well as a requirement to avoid risk of fuel failure.

The above summary of academic and industry references relating to Magnox corrosion represents a substantial body of work involving hundreds of man-decades of effort covering a wide variety of differing techniques and investigations. Nonetheless, it is apparent that there are several areas directly related to plant behaviour of clad material which are not fully defined.

Three areas of focus have been identified:

1. The long term passive behaviour of magnesium, specifically the combined effects of the oxide and hydroxide composite films which form over realistic storage timescales.

2. Passive film breakdown and localised corrosion initiation and how this relates to storage chemistry in terms of the presence of aggressive and passivating anions.

3. The mechanism of chloride induced pitting and evolution of surface filament-like corrosion into propagating bulk pits.

These points are proposed to be highly pertinent to Magnox clad fuel performance as they represent the key areas governing the ability of the material to provide a long term barrier to access of water to the metallic uranium fuel and escape of activity. The sequence above is also notable as this represents the importance of the processes in corrosion management. Maintenance of a passive corrosion condition in the absence of any aggressive factors is considered preferable and precludes any corrosion failures. Some non-idealities in condition must be considered possible however, so the envelope which can be tolerated before localised corrosion occurs is relevant. Finally, the observation of localised surface attack may be problematic in itself (e.g., due to evolution of hydrogen), but may not be a threat to clad integrity if the extent is limited and does not result in destruction of the clad containment boundary.

The fact that these points remain unresolved despite the extent of study to date is an indication of the complex underlying behaviour which is typical of many corrosion processes, but not least magnesium.

One particular point to note is that this work has not sought to make a specific examination of the possibility that monovalent magnesium ions may participate in the pitting reaction (Song et al., 1997), except insofar as this may contribute to the understanding of the resulting behaviour. It is noted that although this is an intellectually provocative proposition, the historical work has demonstrated that such a supposition is not required. It has been proposed previously that the observations of anodic hydrogen generation are consistent with potential independent behaviour within pits with the total pit area being a function of potential. The AC impedance behaviour has been explained satisfactorily on the basis of salt film capacitance. Therefore, in the present context an undue focus on arriving at a disproof of this possibility would represent a distraction from the need to understand clad corrosion behaviour.

With reference to the sections which follow, the three focus points described above may be proposed as hypotheses for examination within this thesis:

1. What happens during Magnox passivation?

The short term passivation behaviour of Magnox is dominated by the presence of a thin oxide layer, however, the long term behaviour is also influenced by the thick outer hydroxide layer.

2. Why does localised corrosion initiate?

Initiation of localised corrosion occurs as a result of the interaction of aggressive anions with the passive film interface at the atomic scale.

3. How does surface attack develop into destructive pitting?

Pitting of magnesium occurs due to the presence of a salt film on the metal surface which allows dissolution at very high rates in localised areas even for relatively low bulk levels of aggressive ions.

In order to address these knowledge gaps, work has been undertaken and is described in the following sections involving application of contemporary corrosion investigation techniques to the aqueous behaviour of Magnox Al80, or magnesium, where its use as an analogue is appropriate.

The background and basis for each technique is described in Section 3**.**

Results from conventional electrochemical tests on Magnox, supported by morphological characterisation are described in Section 4.1, with a detailed consideration of the film growth kinetics in Section 4.2

Atomistic simulations using quantum mechanical methods to investigate the magnesium oxide lattice as an analogue for the Magnox passive film are reported in Section 5.

A series of experiments characterising the behaviour of magnesium microelectrodes are reported in Section 6.1 and further detailed mechanistic tests using quantitative image correlation are described in Sections 6.2 and 6.3.

A series of conclusion are drawn in Section 7, along with observations on promising avenues for future investigation and a summary of the project is provided in Section 8.

3   Investigative Techniques

The background and details of the methods used in this work are described in the following sub-sections, including relevant references to preceding work.

3.1   Electrochemical Methods

There is substantial information in the literature describing electrochemical corrosion testing techniques, notably standard texts (Shreir's Corrosion, 2010) and also Gonzalez Torreira (2004), with specific reference to Magnox Al80 and magnesium. This latter reference, in addition to previous studies, underpins the use of these methods for studying corrosion in this application. The conventional techniques extensively employed in the present work are briefly described as follows.

Open circuit potential monitoring simply requires measurement of the voltage of the working electrode against a suitable reference electrode. This is a passive technique which should not affect the working electrode as the measurement is made against a very high resistance so no polarisation should result. Sampling frequencies used here were between 10 Hz and 0.1 Hz depending on the timescale of tests, with higher rates typically being used in the earlier phases of tests when rates of change were higher, or when observations required higher resolution data, e.g., for the study of transients.

Potentiodynamic polarisation involves the potential of the working electrode being controlled (relative to the reference electrode) and swept with a defined rate and range whilst measurement is made of the current which is caused to flow to a counter electrode. These tests will be expected to alter the electrode as the electrochemical surface processes occurring will be affected by the change in potential. Tests here used sweep rates between 0.1 and 20 mV s^{-1}, with the low rates generally being suitable for kinetically stable systems and the high rates being used for more dynamic conditions.

Potentiostatic polarisation involves application of a constant potential (relative to the reference electrode) and measurement of the current at the counter electrode. Galvanostatic polarisations vary the potential to maintain a constant current at the counter electrode.

Electrochemical impedance spectroscopy (EIS), also known as AC impedance, involves application of a sinusoidal potential waveform (typically at OCP) and measurement of the complex current response. By scanning the frequency of the waveform applied,

detailed information about the processes occurring on the working electrode surface can be obtained although interpretation requires mechanistic characterisation of the system. Tests typically involved applying a waveform of 10 mV amplitude over a frequency range from 20 kHz to 0.1 Hz.

Electrochemical noise (EN) involves connection of two similar working electrodes via a zero resistance ammeter to allow measurement of the current passing whilst the potential of the couple is measured simultaneously. This technique is particularly suitable for measuring transients in current and potential which are characteristic of localised corrosion processes.

The electrochemical cell essentially comprised Magnox working electrodes (see Section 3.2) immersed in electrolytes (one litre volume) representative of plant storage chemistries or hypothetical fault conditions. The cells were contained within polypropylene containers to exclude atmospheric carbon dioxide which would cause a drop in pH. Short term tests employed open PTFE containers. Reference electrodes were Ag/AgCl (Thermo Orion), solid state Ag/AgCl (Refex) or in certain cases platinum pseudo-reference electrodes. Platinum mesh electrodes (with high surface area relative the working electrodes) set in chemically resistant epoxy and electrically connected via PTFE insulated wire were employed as counter electrodes. Solartron 1280A electrochemical measurement units, incorporating potentiostat and frequency response analyser were utilised for undertaking experiments with the Scribner Associates suite of measurement and analysis programmes (Corrware, ZPlot, CorrView and ZView, versions up to 3.1).

Reagents were AnalaR grade or equivalent and test solutions were normally prepared from standard laboratory grade demineralised water. The majority of tests employed electrolytes of 200 mg kg^{-1} NaOH (pH$_{25°C}$ 11.7), which corresponds to the pond chemistry specification (see Section 2.2).

Auxiliary measurements of pH and conductivity were undertaken with hand held water testing meters (Fisher Scientific), electrical conductivity with a multimeter (Fluke) and chloride analyses with a chloride ion selective electrode (Thermo Orion).

Electrochemical tests are described throughout Section 4 and 6 with additional details relevant to particular investigations.

3.2 Electrode Production and Specifications

Electrodes and corrosion samples were produced according to a number of designs which were developed over the course the project and, to some extent, reflect the differing requirements of various experimental techniques employed and corresponding timescales.

In the majority of work, Magnox Al80 was used (Magnesium Elektron), with composition given in Table 3-1. Commercial purity 99.9+%wt magnesium (Goodfellow) was also used in some cases.

Table 3-1: Summary of chemical composition of Magnox Al80 (Gonzalez Torreira, 2004)

Element	Abundance (wt%)
Mg	Balance (>99)
Al	0.8
Be	0.005
Ca	0.005
Cu	0.005
Fe	0.003
Mn	0.005
Ni	0.005
Si	0.008
Sn	0.005
Zn	0.005
Pb	0.005

The primary aims of electrode design can be described as follows:

1. Provide a planar surface of known area which may be consistently prepared by polishing or etching.
2. Allow an electrical connection to be made which is insulated from impingement of electrolyte.
3. Present as small as possible a crevice at the electrode-mount interface.
4. Not comprise materials which may release any species that could affect the corrosion behaviour of the electrode.
5. Be robust over the timescales and in the chemical conditions required in the particular experiments being undertaken.

6. Be suitable for employment as part of an electrochemical cell and fulfil other specific requirements according to particular tests (e.g., allow optical observation of the electrode surface).

A summary of the various types of electrodes produced to fulfil these requirements is shown in Table 3-2.

Table 3-2: Summary of electrode design properties

Type	Material	Surface area /cm^2	Mount material	Insulation
A	Magnox	1	SS/PTFE/nitrile	PTFE
B1	Magnox	2	DAP	PTFE
B2	Magnox	2	DAP	Epoxy/PTFE
C	Magnox	2	Epoxy	Epoxy/PTFE
D	Mg	1.23x10^{-4}	Epoxy	Epoxy/PTFE
E1	Mg	~2x10^{-4}	Epoxy	Epoxy/PTFE
E2	Mg	~2x10^{-4}	Transoptic epoxy	PTFE

Type A electrodes comprised a machined Magnox disc held in a stainless steel/PTFE electrode holder with a surface area of 1 cm^2 exposed to the electrolyte by an o-ring seal (Figure 3-1). This type of electrode had the advantage of being rapid to prepare and assemble, but was unsuitable for timescales above a few hours. This was due to the housing being susceptible to leakage which allowed electrolyte to contact stainless steel components, thus creating a galvanic couple, and also areas of the sample other than the intended area. Some propensity for preferential initiation of localised corrosion at the o-ring crevice was also observed.

Type B electrodes were similar Magnox discs (16 mm dia.) mounted in di-allyl phthalate (DAP) thermoplastic compound to give a 2 cm^2 exposed surface area (Figure 3-2). Electrical connection was achieved through conductive epoxy (RS) to PTFE insulated wire with insulation by chemically resistant epoxy (Araldite). These electrodes were suitable for use over extended periods and showed little indication of preferential attack at sample-mount interfaces. The electrode connection insulation was also found to be susceptible to crevicing over very long timescales (several weeks) due to the poor adherence of the insulating epoxy to PTFE. Some staining of the connection wire could be observed in post-exposure examination of electrodes showing that this had occurred

but testing suggested that even in these cases, no significant effect was observed on potential showing that the leak path was of a high resistance and probably labyrinthine nature. The standard Type B1 electrodes had a simple connection wire insulation, while the Type B2 variation used an extended epoxy insulation area so that the connection wire crevice could be positioned above the solution, hence preventing any possibility of leakage at this site.

Type C electrodes were similar to Type Bs, however, chemically resistant epoxy was used for the entire mount (Figure 3-3). As the epoxy is the primary mount, the curing process must be undertaken carefully to ensure a continuous dense substrate with low adherence of bubbles.

Type D electrodes were microelectrodes produced from 125 micron diameter magnesium wire (Goodfellow) with a similar design to Type C electrodes in that the entire mount and insulation was achieved with epoxy to give an exposed surface area of 1.23×10^{-4} cm^2 (Figure 3-4). These electrodes were produced in pairs from a single length of wire connected at both ends which was divided following curing as this allowed the connectivity to be confirmed as testing the face was less consistent due to the very small surface area. The wire connection insulation was extended above the electrolyte surface to prevent leakage which could potentially be significant for these electrodes, again due to the very small surface area.

Type E electrodes were microelectrodes produced from 10 micron thick magnesium foil (Goodfellow) with width typically 2 mm to give exposed surface areas around 2×10^{-4} cm^2 (Figure 3-5). Type E1 electrodes were made of the standard chemically resistant epoxy and required additional consideration in mounting the foil strip during production due to internal stresses in the mount disrupting the foil and leading to loss of conductivity. Type E2 electrodes were mounted in transoptic epoxy to allow *in situ* observation of electrode processes within an artificial pit cavity. The transoptic epoxy was found to have reasonable edge retention and crevicing performance although inferior to the chemically resistant epoxy, however, the tests in which these electrodes were utilised were of short duration so this was not problematic.

Type A electrode surfaces were prepared by a 2 minute etch in 2%wt citric acid at 60 ºC. Type E2 electrodes were cleaved and all other types were polished to 1200 SiC and rinsed with demineralised water.

Figure 3-1: Type A Magnox electrode design
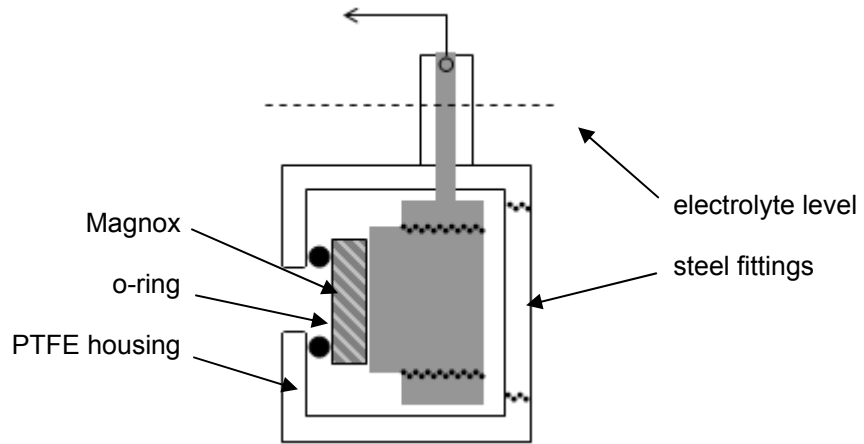
Figure 3-2: Type B1 (left) and B2 (right) Magnox electrode designs
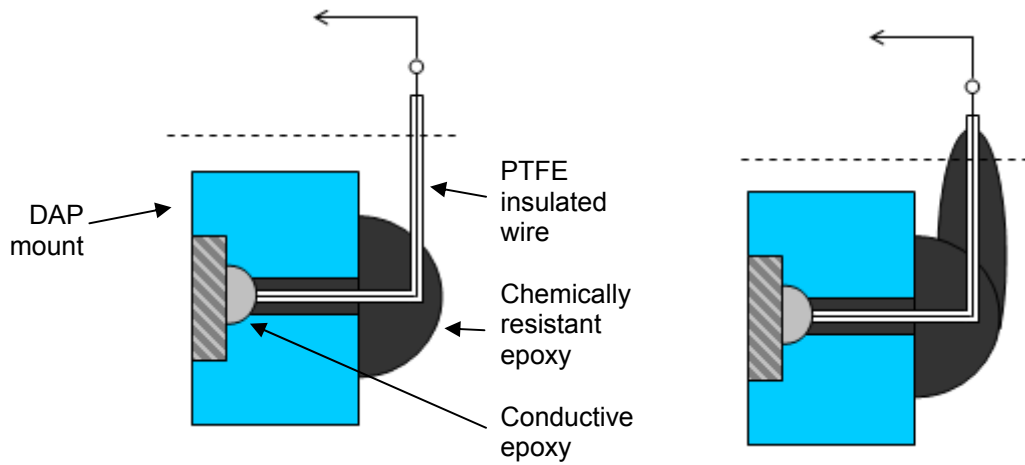
Figure 3-3: Type C Magnox/magnesium electrode design
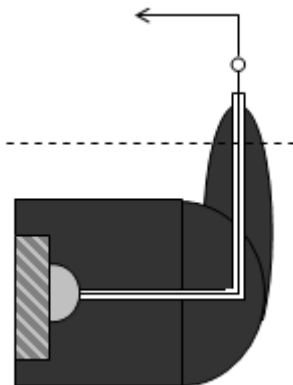
Figure 3-4: Type D magnesium microelectrode design
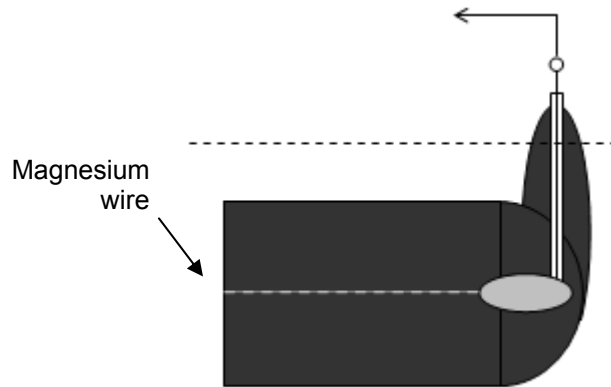
Figure 3-5: Type E1 (left) and E2 (right) magnesium microelectrode designs
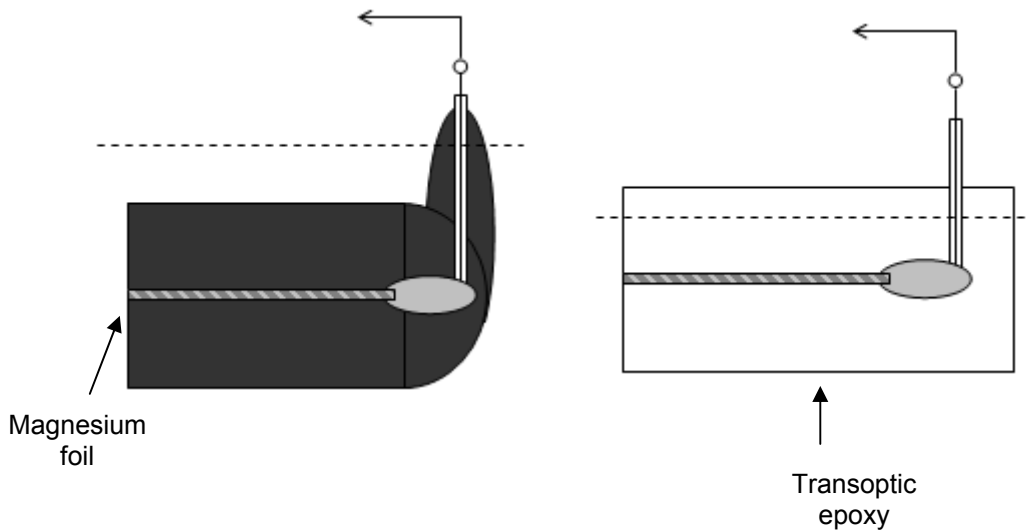
3.3   Microelectrode Corrosion Techniques

Localised corrosion is by its nature heterogeneous, however, there are certain means by which the mechanisms at work may be made more dominant or possibly isolated altogether. In this way, behaviour may be investigated without the parallel effect of a surface undergoing an entirely different reaction. This is very relevant to pitting as this is typified by reactions involving localised chemistries and very high current densities often on extremely small fractions of the surface while the entire remaining surface may be

passive. Therefore the conventional macro-electrode behaviour tends to dilute the responses evident in the localised processes. A number of additional effects can pertain to microelectrodes which may have particular relevance to corrosion processes or offer particular avenues of investigation which would not be available through the use of macro-electrodes. These include observation of mass transport under radial diffusion regimes, modified oxide film behaviour (e.g., due to differences in internal stress), single grain or single crystal surfaces and investigation or manipulation of the chemistry in the micro-channel cavity. Microelectrodes are also widely used for sensing applications due to the possibilities for exploitation of these effects and for situating electrodes in precise locations.

Microelectrodes have been applied extensively in the study of steels (Newman & Ajjawi, 1986, Pistorius & Burstein, 1992, Laycock & Newman, 1997) and also for aluminium (Cook & Newman, 2002) and these studies demonstrated the significance for corrosion behaviour. A discussion of pitting corrosion by Frankel (1998) includes a relevant overview of various microelectrode studies.

Speckert & Burstein (2011) recently used 25 micron diameter aluminium microelectrodes to study very small amplitude pre-initiation transients and this work shows the extent to which signals may be successfully amplified where the magnitude of these would be below the resolution of monitoring hardware against the background noise even on a highly passive macroelectrode.

The use of 250 micron diameter steel microelectrodes for the study of the influence of magnetic fields on corrosion product transport by Tang & Davenport (2007) demonstrated the potential for use of concurrent optical characterisation to interpret electrode behaviour. The behaviour of corrosion products was observed by video-microscopy for an artificial pit dissolving under a salt film.

The behaviour of aluminium microelectrodes is also highly relevant as these have also been shown to behave as one dimensional pits and exhibit mass transport limited behaviour due to dissolution of the electrode under a salt film.

The fact that salt film formation has previously been observed under particular conditions for magnesium macroelectrode artificial pits (Beck & Chan, 1983) and that salt films were also associated with the filiform-like localised corrosion occurring on a magnesium alloy at open circuit potential (Lunder *et al.,* 1994) suggests that the use of microelectrodes to study further aspects of this process is a reasonable proposition. On the basis of the available literature, the fabrication and application of magnesium microelectrodes for study of corrosion behaviour is understood to be novel.

The production of magnesium microelectrodes is described in Section 3.2 and the standard electrochemical tests in Section 3.1. Imaging of the microelectrodes employed apparatus described in Section 3.7. Tests utilising these electrodes are described in Section 6.

3.4   Atomistic Modelling of Passive Oxide Films

The mechanism of initial passive film breakdown in magnesium has not been established. It is apparent that this is related to the action of aggressive ions, with chloride being notable in its action, and that it may be inhibited by hydroxide (i.e., high pH) and fluoride as well as certain other anions. In general, aggressive anions are those which have magnesium salts of high solubility and passivating salts are those which would have a corresponding low solubility. This relationship therefore suggests that the incorporation of these anions into the passive layer may be an important aspect of the mechanism and indeed modification of the film composition in the presence of fluoride to form a mixed hydroxide-fluoride film has been observed (Bradford *et al.,* 1976). One mechanism by which the incorporation of chloride could be expected to lead to breakdown would be via formation and aggregation of small unstable sub-phases within the bulk passive layer structure (Speckert & Burstein, 2011) which would disrupt film formation by being prone to dissolution and consequently leading to increased porosity within the protective oxide film. This could therefore be observed as a mechanism similar to film thinning. However, this would be expected to result in a stepwise increase in corrosion current with increasing chloride concentration and a gradual approach to corrosion initiation which is not observed (see Fig. 5 in Burrows *et al.,* 2005). Instead, a very rapid initiation occurs with the surface depassivating near-instantaneously and localised corrosion ensuing from the initial breakdown sites. This seems more characteristic of some type of cascade film failure mechanism, which has also been proposed (Frankel, 1998), although for very thin passive films, the effect may be the same. In either case, the mechanism may well be related to the passive film behaviour at the atomic lattice scale, particularly with respect to the propensity to accommodate anion groups at locations within the lattice or at surface locations.

The use of atomistic modelling may therefore be proposed as a relevant technique to investigate the behaviour observed. This has been undertaken for other materials, notably, nickel as reported by Bouzoubaa *et al.* (2010). Quantum mechanical methods were used to undertake energy minimised simulations of adsorption and insertion of impurities on a nickel oxide phase representing the nickel passive layer. This appears a

good basis upon which to base atomistic simulation investigations of the magnesium passive film behaviour in the presence of different anions.

The behaviour of magnesium oxide has been the subject of extensive study by atomistic simulation and can be effectively regarded as a technique test subject due to the volume of work in the literature, which is fortuitous in the present instance. Early atomistic studies employed empirically derived expressions for interatomic potentials to calculate the force fields acting within crystal lattices, and these were compared to crystallographic results and other experimental data (Sangster *et al.,* 1970, Sangster, 1973, Catlow *et al.,* 1976, Lewis & Catlow, 1985, Catlow *et al.,* 1985, Lewis & Catlow, 1994, Kumagai *et al.,* 1994, de Leeuw *et al.,* 1995, de Leeuw & Parker, 1998) although these have also been used more recently due to the advantages of being able to undertake calculations for very large numbers of atoms under many spatial permutations (Sakuma *et al.,* 2004 and Allen *et al.,* 2009). As access to high-capacity computational facilities became more widespread, quantum mechanical methods began to be applied to lattice calculations for magnesium oxide involving increasingly non-symmetric geometries (Russo & Noguero, 1992, Kantorovich & Gillan, 1997, de Leeuw, 2001, Wang *et al.,* 2006, Costa *et al.,* 2006, Thyveetil *et al.,* 2007, Labidi *et al.,* 2010). The ability to simulate lattices of many hundreds of atoms along with non-equivalent surface conformations has allowed various bulk and surface properties to be compared in detail with experimental results adding to the precision and confidence in the computational techniques (Ashworth *et al.*, 2003, Carrasco *et al.,* 2010). The dissolution behaviour of MgO has been examined in this manner (Simpson *et al.,* 2002) although this concerned a low pH condition where the rate of dissolution was rapid due to protonation reactions rather than an alkaline system where the surface is comparatively stable and it is the influence of anions which cause breakdown. In this reference, the simulation was found to agree well with TEM observations of evolutions in surface morphology during reaction with water vapour.

As noted above, some applications of *ab initio* simulations in modelling localised corrosion have been undertaken. Calculations of surface energies and energy optimised configurations for passive nickel oxide surfaces relating to adsorption and insertion of chloride are reported by Pineau *et al.* (2003), Bouzoubaa *et al.* (2009) and Bouzoubaa *et al.* (2010). These workers employed density functional theory (DFT) calculations to simulate slab structures comprising several atomic layers of the standard nickel oxide lattice surrounded by vacuum on both sides. The atomic locations of the lower layers were not optimised in the calculation in order to represent the bulk solid, while those at the simulated surface were allowed to adopt a modified conformation according to energy minimisation to show the effect of molecular and dissociative adsorption of water and chloride ions. This showed that the energy of insertion of chloride ions into the first

layer of the lattice decreased with surface chloride coverage, so that although unfavourable at low coverages, once a high proportion of the surface adsorption sites were occupied by chloride, insertion became energetically favourable. This was identified as a basis for the destabilisation of the passive film. The effect of an anodic potential was proposed to be to increase the surface concentration of adsorbed chloride to the point where insertion became favourable. Further calculations including a wider range of halides showed that fluoride ions had a markedly different behaviour and were substituted more favourably even at lower coverages. This was interpreted as an indication that the aggressiveness of fluoride was due to the lack of requirement for an initiation site as it would readily modify a film whereas chloride would only interact with higher energy defect sites.

The corrosion behaviour of nickel contrasts in various mechanistic points although has some similarities, such as the formation of a dense NiO inner layer which is hydrated to form an outer hydroxide layer (Sikora & MacDonald, 2002, Cabrera-Sierra *et al.,* 2006). The results outlined above are particularly interesting in light of the agreement noted with atomic scale characterisations of nickel oxide surfaces undergoing competitive dissolution and passivation (Seyeux *et al.,* 2008).

Atomistic modelling is essentially achieved by comparison of the energies of atomic systems, in this case using DFT, under differing configurations to represent particular structures or reactions occurring within these. This normally involves geometry optimisation allowing short range displacement of atoms to arrive at the lowest energy arrangement within particular spatial constraints.

DFT considers the ground state energy of an atomic system according to the charge density (ρ) within the systems as a sum of the orthonormal molecular orbitals (Φ) (Delley, 1990, DMol^3 Guide, 2001, Materials Studio Guide, 2010) according to:

$$W(\rho) = U(\rho) + T(\rho) + E_c(\rho) \qquad (3\text{-}1)$$

Where the terms are the total (W), kinetic (T), classical electrostatic (U), and exchange-correlation (E_c) energies, respectively.

and (in terms of position under spherical geometry, r)

$$\rho(r) = \sum_k \left| \Phi_k(r) \right|^2 \qquad (3\text{-}2)$$

This allows derivation of the kinetic and classical electrostatic energies.

$$T = \left\langle \sum_{k}^{n} \Phi_{k} \left| \frac{-\nabla^{2}}{2} \right| \Phi_{k} \right\rangle \qquad (3\text{-}3)$$

$$U = \int V_{N}(r)\rho(r)dr + \tfrac{1}{2} \int \frac{\rho(r_{1})\rho(r_{2})}{\left| r_{1} - r_{2} \right|} dr_{1} dr_{2} + V_{NN} \qquad (3\text{-}4)$$

Where V_N is the contribution of the atomic nucleus charge density to electron-nucleus attraction, the second term gives the inter-electron repulsion according to the charge densities at respective positions (r_1 and r_2) and V_{NN} is the repulsion between nuclei.

The exchange-correlation energy requires approximation in order to be practically soluble which is achieved according to linear density approximation (LDA) and more specifically, non-local spin-density approximation, to relate the exchange correlation energy of the system to the local exchange correlation energy in a uniform electron gas (ε_{c}). On this basis, the energy of the system may be calculated from the solutions to the eigenvector equivalent of the stationary Shrödinger equation as derived by Kohn and Sham (1965):

$$\left\{ \frac{-\nabla^{2}}{2} - V_{N} + V_{e} + \mu_{c}(r) \right\} \Phi_{k} = \varepsilon_{k} \Phi_{k} \qquad (3\text{-}5)$$

Where μ_c, ε_{k} and V_e are the exchange-correlation potential (derived from differentiation of the exchange correlation energy), the energy of the kth orbital and the electron-electron repulsion potential, respectively.

This leads to the total energy being expressed as a function of variables which can each be calculated from the charge density:

$$W = \sum_{k} \varepsilon_{k} + \left\langle \rho(r) \left[\varepsilon_{c}(\rho) - \mu_{c}(\rho) - \frac{V_{e}(r)}{2} \right] \right\rangle + V_{NN} \qquad (3\text{-}6)$$

In order to allow practical solution of the expression, molecular orbitals are constructed from the atomic orbitals (ϕ) taken from an appropriate basis set and molecular orbital expansion coefficients (c):

$$\Phi_{k} = \sum_{\sigma} c_{k\sigma} \phi_{\sigma} \qquad (3\text{-}7)$$

Expression 3–5 is then reformulated to account for the non-orthogonality of the atomic orbitals and can be conveniently expressed as a matrix eigenvalue equation:

$$\sum H_{\sigma v} c_{k\sigma} = \varepsilon \sum S_{\sigma v} c_{k\sigma} \tag{3-8}$$

Which involve the Kohn Sham and overlap matrices as follows:

$$H_{\sigma v} = \left\langle \phi_\sigma(r) \left| \frac{-\nabla^2}{2} - V_N + V_e + \mu_c \rho(r) \right| \phi_v(r) \right\rangle \tag{3-9}$$

$$S_{\sigma v} = \left\langle \phi_\sigma(r) \middle| \phi_v(r) \right\rangle \tag{3-10}$$

Evaluation of the total energy is then possible through a typical self consistent field (SCF) method. Briefly, this involves iterative calculation of the molecular orbitals and charge density for a system, from an initial set of molecular orbital expansion coefficients, leading to derivation of potentials and Hamiltonian, which can then be used to produce a new set of molecular orbital expansion coefficients. Convergence is identified when the change in charge density (or another derivative parameter) between iterations falls below a stipulated threshold according to the quality of the calculation required. Geometry optimisation involves fractional movement of atomic locations, subject to symmetry constraints, according to the calculated energy gradient acting on each. Similarly, this proceeds iteratively until convergence criteria are achieved, these typically being the maximum displacements and changes in energy and force for each cycle.

Pineau *et al.* (2003), Bouzoubaa *et al.* (2009) and Bouzoubaa *et al.* (2010) employed VASP (Vienna Ab Initio Simulation Package) to undertake DFT simulations for the NiO surface as a passive film analogue. This was achieved by application of the Perdew and Wang (1992) (PW91) formulations of Generalised Gradient Approximations (GGA) to solve the Kohn-Sham equations. In order to account for the strongly correlated nature of the system, a Hubbard term (LDA+U) was used in the local density calculations. In the atomistic study of MgO, Cho *et al.* (2000) used functionals developed by Perdew *et al.* (1996) (PBE) and Wang *et al.* (2006) used those of Becke (1988) and Lee *et al.* (1988) (B3LYP).

In the present work, the majority of calculations were undertaken using the DMol3 program (Delley, 1990, Weinhert & Davenport, 1992, Delley, 2000, Delley, 2010). This employs numerical atomic basis sets which are stored as cubic spline coefficients and spatially confined by a cutoff value (r_c). Different qualities of computational solution may

be achieved by variation of the latter parameter and also the size and resolution of the basis set numerical integrals. Pseudopotentials may be used to replace non-valence orbitals for the benefit of computational efficiency. A further parameter which may be adjusted to provide a desired level of computational quality is the molecular grid which is used for interpolation of the atomic orbitals. In the majority of this work, the exchange correlation energy was based on local functionals derived by Perdew & Wang (1992) with some further comparative tests using GGA functionals according to Perdew et al. (1996) (PBE) and Boese & Handy (2001) (HCTH). Most calculations employed the "double numerical plus d-functions" (DND) basis set with a smaller number using the more accurate, but computationally expensive "double numerical plus polarisation" (DNP) basis set.

A continuum solvation model, COSMO (conductor-like screening model), may be used within DMol3 to approximate the influence of a polarisable solvent (Delley, 2002). This is an alternative means of allowing the screening effects of a solvent to be considered without including layers of realistic solvent molecules, as optimisation of the conformations of these can be practically challenging. Screening charges are calculated on a "solvent accessible surface" around a cavity, constructed geometrically on the basis of the summed Van der Waals radii of the individual atoms in a structure, within a dielectric continuum representing the solvent. This charge is included in the Kohn-Sham Hamiltonian and therefore incorporated in the SCF iteration. In this work, the COSMO approximation has been employed to consider the effect of an aqeous medium at the passive film-solution interface.

Some additional calculations were undertaken using a diverse DFT code, CASTEP (Clark et al., 2005), for the purposes of comparison and support of DMol[3] calculations. This code uses plane wave pseudopotentials and hence requires periodic structures, although this was consistent with the approach applied throughout. The CASTEP basis sets are well suited to simulation of bulk lattice structures, whereas the DMol[3] numerical basis sets are appropriate for achieving computational efficiency for surfaces. The calculations here utilised the GGA-PBE functionals (Perdew et al., 1996).

Simulations with DMol[3] and CASTEP were both undertaken using the Materials Studio interface (Accelrys Systems Inc.). This facilitates construction of periodic structures, script set up, job submission and visualisation of results. Some manual editing of script files was undertaken in particular instances.

Section 5 describes quantum mechanical atomistic simulations undertaken in relation to the initiation of localised corrosion on Magnox and magnesium.

3.5   Oxide Growth Kinetic Models

Due to the uniformity of many passive films grown on metals, their behaviour may be reasonably described through one-dimensional expressions of the reactions occurring. Standard references (Shreir's Corrosion, 2010) describe various forms of oxide growth kinetics including simple diffusional, point defect model and high field. It is this latter which has been shown to be an appropriate descriptor of the initial stages of magnesium and Magnox Al80 passive film formation (Gonzalez Torreira *et al.,* 2003). The high field model is based on the transport of ions or defects through an energy barrier into (or out of) an oxide lattice potential well under an electric field.

The morphology of magnesium oxide films have been studied by surface characterisation techniques. Nordlien *et al.* (1995) used TEM measurements on sectioned pre-exposed foils to show that in demineralised water, magnesium formed a dense magnesium oxide layer with a deposited outer layer at the solution interface. A heterogeneous, partly hydrated layer was observed although the formation of this appeared to be affected by the electron beam during the analysis so probably represented an *ex situ* artefact. Do *et al.* (1997) noted that the formation in water vapour was consistent with the oxide transport theories of Cabrera & Mott (1949) once the extent of adsorption was sufficient for a continuous layer to have formed.

Case & Hilton (1978) and Greef *et al.* (1986) both convincingly showed that the composition of the Magnox passive film on long stored surfaces is essentially porous magnesium hydroxide although were unable to positively identify a dense oxide barrier layer, noting that one was kinetically inferred. Bradford *et al.* (1976) showed that the film grew close to the metal surface, suggesting that the film grows through epitaxial hydration rather than re-precipitation in higher pH matrices where a substantial cation gradient in the solution close to the surface will not exist. These were relatively thick films and typical of Magnox surfaces in real fuel storage environments. The influence of the reactor formed oxide is not considered here on the basis that this was shown to be largely non-protective against contact of water with the metal and that corrosion proceeded beneath this layer from a short a short time following exposure to water, e.g., whilst the reactor oxide hydration reaction was still at an early stage. Gonzalez Torreira *et al.* (2003) successfully identified and characterised the thin, dense oxide film which grew on a freshly exposed metal surface (of a thickness consistent with the maximum proposed by Greef *et al.,* 1986), which hydrated at the solution interface, although only the initial stages were studied. The kinetic considerations based on these measurements implicitly considered the film to be homogeneous and excluded loss of the film at the solution interface by using a very high electrolyte pH to preclude

dissolution, but did not consider hydration. The kinetic model so far available has therefore only been examined for relatively small film thicknesses and also has not been considered in terms of the effect of hydration of the film at the oxide/solution interface. These observation sets need to be reconciled to explain the evolution of a thin freshly formed layer mainly comprising magnesium oxide with only surface hydration to become a thick highly hydrated layer mainly formed of magnesium hydroxide with a similar, thin underlying oxide barrier layer. The ultimate aim is to provide a means of describing the overall behaviour. The passive layer structures for Magnox under alkaline conditions according to different workers are illustrated in Figure 3-6 which highlights this aim.

The modification of oxide kinetic models to incorporate passive film heterogeneity on the basis of electrochemical data has led to propositions of developments in standard models by Kinnunnen (2002) and, notably, Cabrera-Sierra *et al.* (2006), concerning the role of a porous and less-protective, but nonetheless contributory, hydroxide outer layer in nickel and titanium kinetics based on the point defect model.

Further consideration of the oxide growth kinetics pertaining to the passive behaviour of Magnox is described in Section 4.2.

Figure 3-6: Illustration of Magnox passive layer structures formed under typical high alkalinity, low anion conditions (pH 11.7, 5 mM NaOH, 0 mg kg^{-1} chloride) according to different workers
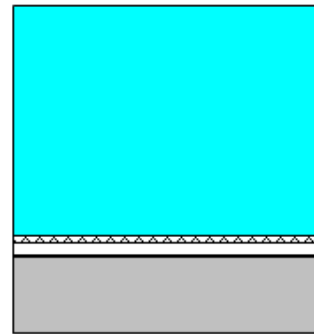
freshly formed surface with thin oxide with minimal hydration as studied by Gonzalez Torreira *et al.*, 2003
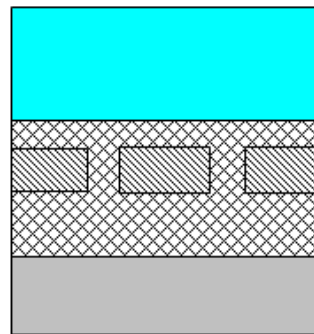
thick, porous hydroxide film with residual, unhydrated, non-protective reactor formed oxide according to Case and Hilton, 1978

← ???
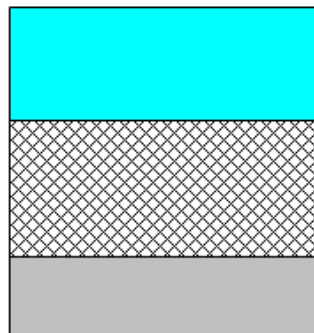
thick, porous hydroxide film according to Greef *et al.*, 1986

← ???
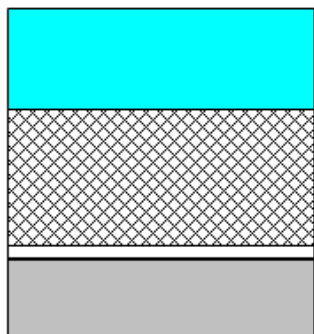
representative surface for behaviour of clad surface under fuel storage conditions proposed for investigation

KEY:

Magnox substrate

electrolyte (eg, pond water)

dense oxide passive layer

porous hydroxide layer

un-hydrated reactor oxide
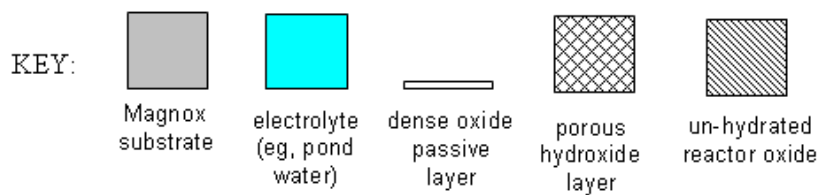
3.6   Finite Element Modelling Techniques

In order to assist in interpreting electrochemical data, a finite element multiphysics package has been used to provide numerical solutions for standard transport relationships under defined geometries. The advantage to this technique in the present work is that quantitative results may be readily produced for an equation system representing a multi-component electrolyte in an electrochemical environment for a non-trivial geometry. This supports the aim of producing a realistic representation of the observed behaviour on the basis of the mechanism being modelled.

The FEMLAB package (V3.0a) by COMSOL (now superceded by COMSOL Multiphysics) has been employed for this purpose. The finite element method is a standard approach for solution of partial differential equation systems, and is a widely employed technique for evaluating stresses in materials as well as an increasing variety of physical systems in recent decades. Typically, a geometry describing the system of interest is converted by a meshing algorithm into a node model which allows definition of a matrix equation system on the basis of one or more partial differential relationships (which may be coupled) representing the processes of interest. Definition of appropriate boundary conditions and starting values allows numerical solution through a suitable mathematical method. Much of this process is automated by the software package and, for relatively simple systems, the computational advantage of an algebraically reduced geometry may be sacrificed in favour of ease of model definition and interpretation of results.

The FEMLAB package includes a pre-defined electrochemical mass transport model based on solution of diffusion and migration under a condition of electroneutrality (FEMLAB user guide, 2004, FEMLAB Chemical Engineering Module user guide, 2004).

The concentration of a reacting species is defined (assuming zero convection), according to the Nernst-Planck equation:

$$\frac{\partial c}{\partial t} + \nabla \cdot (-\underline{D}\nabla c - zuFc\nabla V) = R_c \qquad (3\text{-}11)$$

Where c (mol m^{-3}) is the concentration, t (s) is time, D (m^2 s^{-1}) is the diffusion coefficient, z (mol mol^{-1}) is charge, u (m^2 mol s^{-1} C^{-1} V^{-1}) is mobility, F (C mol^{-1}) is Faraday constant, V (V) is potential and R_c (mol m^{-3} s^{-1}) is reaction rate.

With the mobilities given by:

$$u = \frac{D}{RT}$$

(3-12)

Where R (C V mol^{-1} K^{-1}) is the ideal gas constant and T (K) is the temperature.

The electroneutrality condition is satisfied by maintaining:

$$\sum_{i=1}^{n} z_i c_i = 0$$

(3-13)

which allows elimination of one species from the equation system.

In the present model, three boundary conditions are employed. The bulk solution region interface is represented by a boundary with a defined concentration for each species and potential according to:

$$c_i = c_{i,0}$$

(3-14)

$$V = V_0$$

(3-15)

This is also used to represent an electrode surface in some cases where an assumption of constant concentration is required.

Under most assumptions, an interface with defined flux is used to represent an electrode surface according to:

$$-n \cdot (-\underline{D}_i \nabla c_i - z_i u_i F c_i \nabla V) = N_i$$

(3-16)

The final boundary condition which allows continuity in models without the need for explicit definition of symmetry is conservative insulation according to:

$$n \cdot (-\underline{D}_i \nabla c_i - z_i u_i F c_i \nabla V) = 0$$

(3-17)

In addition to the transport relationships defined above, the following expressions are used to represent the behaviour of water as a background electrolyte without this being explicitly present.

$$Kw = 10^{-6} c_{OH} c_H \tag{3-18}$$

$$Rw = k(10^{-14} - Kw) \tag{3-19}$$

with k being a suitably large number in comparison to the minimum time step used in solution, in the present case $\sim 10^9$. The reaction rates for c_{OH} and c_H are consequently Rw, while all others are zero. The stability of the model, particularly with respect to imposed flux at boundaries may be ascertained by confirmation that Kw does not deviate substantially from the equilibrium value of 10^{-14}.

The results of the model are presented as functions of species concentrations, as defined above, and total flux according to:

$$J_i = \left| -\underline{D}_i \nabla c_i - z_i u_i F c_i \nabla V \right| \tag{3-20}$$

Also, some specific functions are defined:

$$pH = 14 + Log(10^{-3} c_{OH}) \tag{3-21}$$

We can therefore undertake some simple calculations relating to linear diffusion to test a trivial model against an analytical solution of Fick's Second Law for the one dimensional case (Shreir, 2010):

$$c_{x,t} = c_{0,t} erfc\left(\frac{x}{2\sqrt{Dt}}\right) \tag{3-22}$$

With the flux at x being given by:

$$J_{x,t} = D\frac{dc}{dx} = \frac{Dc_{0,t}}{\sqrt{\pi Dt}} \exp\left(-\frac{x^2}{4Dt}\right) \tag{3-23}$$

We will assume that the concentration of Mg^{2+} at the electrode surface in 5 mM NaOH is at the solubility limit (7×10^{-5} mol m^{-3}) for that matrix based on the standard K_{sp} (7×10^{-12} mol^3 dm^{-9}, Shreir, 2010). This value is assigned to $c_{Mg,0,t}$ which also forms one fixed concentration boundary condition, with the other concentrations being given in Table 3-3. The opposing side of a regular sub-domain is also a fixed concentration condition and the other two sides being symmetry boundary conditions (see Figure 3-7). A time

dependent solution is then generated employing the standard values in Table 3-3 and sample results are plotted in Figure 3-8 along with those calculated according to Fickian diffusion. It can be seen that the two solutions are closely comparable.

Table 3-3: Parameters used in electrode migration finite element multiphysics model

Parameter	Unit	Value
$c_{OH,0,t}$	mol m^{-3}	$5 + 10^3.10^{-11.699} + 1.4 \times 10^{-4}$
$c_{Na,0,t}$	mol m^{-3}	5
$c_{Mg,0,t}$	mol m^{-3}	7×10^{-5}
$V_{0,t}$, $V_{x,0}$	V	0
D_{OH}	m^2 s^{-1}	5.3×10^{-9}
D_{Na}	m^2 s^{-1}	1.3×10^{-9}
D_{Mg}	m^2 s^{-1}	1.4×10^{-9}
D_H	m^2 s^{-1}	9.3×10^{-9}
D_{Cl}	m^2 s^{-1}	2.0×10^{-9}
$c_{OH,x,0}$, $c_{OH,d,t}$	mol m^{-3}	$5 + 10^3.10^{-11.699}$
$c_{Na,x,0}$, $c_{Na,d,t}$	mol m^{-3}	5
$c_{Mg,x,0}$	mol m^{-3}	0
d	m	10^{-3}

Figure 3-7: Geometry used in two-dimensional electrode migration (defined concentration) finite element multiphysics model

fixed concentration = $c_{i,d,t}$
(bulk electrolyte interface)

sub-domain initial
concentration = $c_{i,x,0}$

insulation/
symmetry

insulation/
symmetry

fixed concentration = $c_{i,0,t}$
(electrode surface)

sub-domain (regular) side length = d
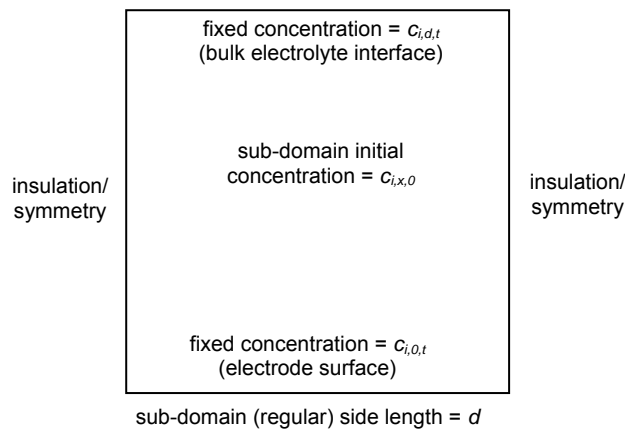
Figure 3-8: Comparison of results from electrode migration finite element multiphysics model and fickian diffusion expression

Legend:
—— 1-D Fickian diffusion
◇ Finite element model

y-axis: J /mol m^2 s^{-1}

x-axis: time /s
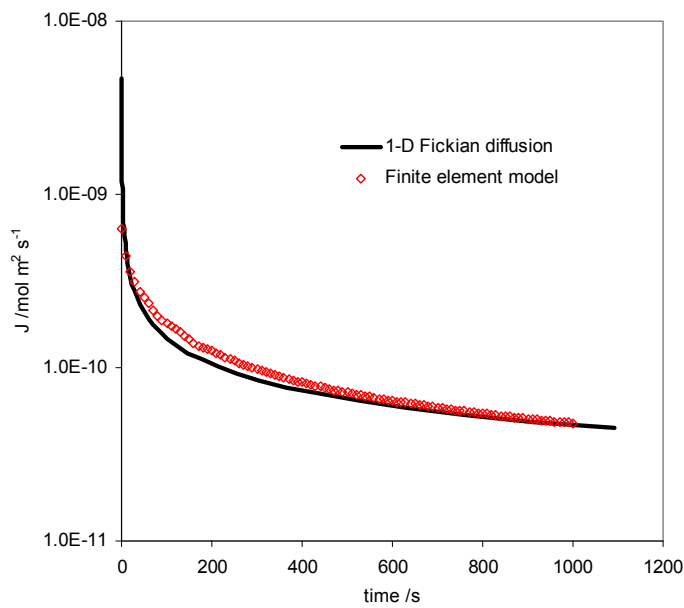
Figure 3-9: Geometry used in two-dimensional electrode migration (defined flux) finite element multiphysics model

fixed concentration = $c_{i,d,t}$
(bulk electrolyte interface)

insulation/
symmetry

sub-domain initial
concentration = $c_{i,x,0}$

insulation/
symmetry

defined flux = $J_{i,0,t}$
(electrode surface)

sub-domain (regular) side length = d
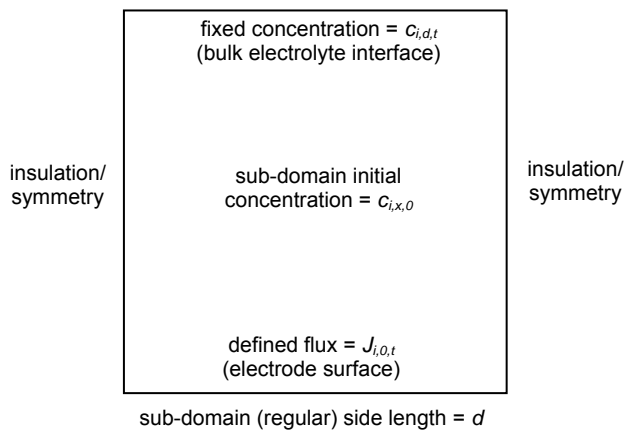
A more versatile variation of this model uses the same basic geometry with a defined flux boundary condition for the electrode surface (see Figure 3-9). A further model geometry is used to consider mass transport for microelectrode surfaces. So as to realistically model hemispherical diffusion, this uses a 3-dimensional geometry comprising a cubic sub-domain with a circular boundary at the centre of one cube face to represent the electrode surface set in an inert mount (see Figure 3-10). This model is analogous to the 2-dimensional one and uses a defined flux condition for the circular electrode surface, fixed concentration for the bulk solution electrolyte at the opposing square surface and the four square surfaces orthogonal to the electrode and insulation/symmetry for the remainder of the square surface containing the electrode. This model considers only diffusive transport for a single species, by omission of the migration term so that u_i is effectively set to zero, as well as D_i for all but one species and all values of z.

The results of solutions produced for these models are discussed in the sections to which they pertain, with two dimensional migration calculations being presented in Section 4.2 and 5 and radial migration calculations in Section 6.1.

Figure 3-10: Geometry used in three-dimensional electrode migration finite element multiphysics model

fixed concentration = $c_{i,d,t}$
(bulk electrolyte interface)

sub-domain initial
concentration = $c_{i,x,0}$

fixed concentration = $c_{i,d,t}$
(bulk electrolyte interface)

defined flux = $J_{i,0,t}$
(circular electrode surface)

insulation/
symmetry

sub-domain (regular) side length = d
electrode surface radius = r
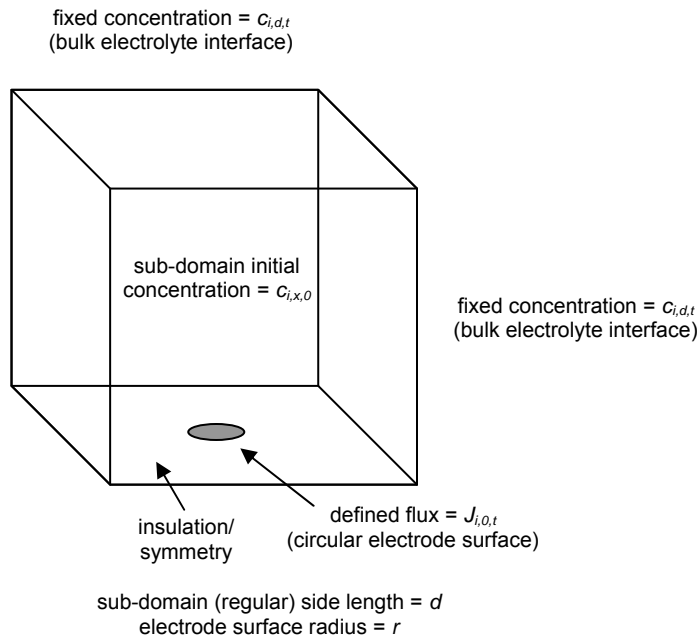
3.6 Corrosion Morphology Imaging Techniques

Electron microscopy is a standard technique for characterisation of corrosion morphology on electrode or coupon surfaces which has been employed extensively in investigations of magnesium and Magnox (Lunder *et al.,* 1994, Gonzalez Torreira, 2004, Li, 2010). Chen *et al.* (2009) used ESEM to study the transport of chloride on an automotive alloy and the initiation of localised corrosion in relation to the two-phase microsctructure.

In this work, a Zeiss EVO60 ESEM was used to study pre-corroded Magnox samples. These samples had been polarised in a standard matrix to initiate localised corrosion immediately prior to examination and were then stored wet for the short period of transfer to the electron microscopy facility to avoid disruption of the surface. They were briefly rinsed with demineralised water immediately prior to placement in the electron cavity so as to avoid the formation of deposits of sodium hydroxide on the surface which would obscure imaging. The relative humidity of the cavity was controlled to avoid dehydration of the surface. The results from these characterisations are shown in Section 4.1.

Numerous electrode examinations were made both before, during and after aqueous exposure. A Nikon 16-80x binocular optical microscope was employed, with standard commercial digital image capture equipment being used for recording micrographs or video footage.

For the substrate dissolution measurements described in Section 6.2, the optical equipment used was a LaVision Imager ProX 4M digital image correlation apparatus which operated at the maximum capture rate of 1 Hz. The DaVis software suite was used for image processing and export

The quantitative image processing and correlation described in Sections 6.2 and 6.3 was performed manually using standard software (GNU Image Manipulation Program, Fraps and Microsoft media suite).

Microtomography has been employed for study of magnesium alloys by Davenport *et al.* (2007). The technique involves recording of numerous x-ray images of a sample under varying angular geometries which are then computationally reconstructed to allow generation of three dimensional representations of internal structures. In the present work, *in situ* measurements were undertaken by x-ray microtomography using a Nikon Metris XTH225 with 225 kV emission energy with analysis (reconstruction and thresholding) and visualisation using VGStudio (Volume Graphics GmbH). Corrosion coupons were exposed to a high pH, high chloride matrix until localised corrosion had initiated and propagated into bulk pitting (Figure 3-11). Use of an x-ray transparent vial allowed the coupons to be imaged (capture time of ~ 30-60 minutes) whilst remaining immersed in a small volume of electrolyte before being returned to an enclosed container. This allowed the progression of the internal structure to be determined over time without affecting the process through removal and drying of the samples or undue carbonation of the electrolyte. The outcomes of these investigations are presented in Section 4.1.

Figure 3-11: Geometry used in three-dimensional electrode migration finite element multiphysics model
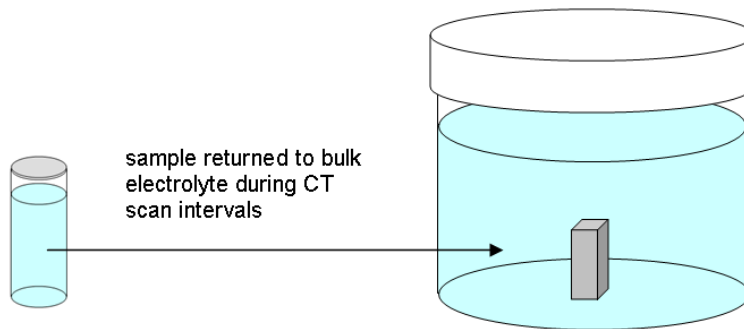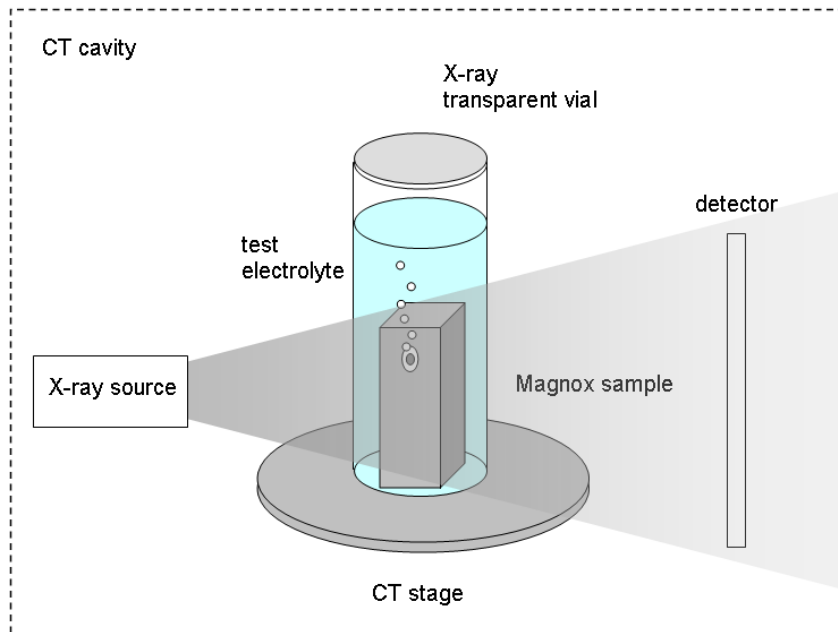
4 Magnox Corrosion Electrochemistry

4.1 Characteristics of Macroelectrode Electrochemistry

Prior to focussing on specific aspects of the Magnox corrosion mechanism, a general understanding of the conventional behaviour, as well as the standard techniques employed must be derived to contextualise the detailed investigations presented subsequently. This section describes electrochemical behaviour of Magnox electrodes supported by various observations of corrosion morphology. Aspects of the work which have been reported previously (Burrows *et al.,* 2005, Burrows & Harris 2007) are summarised here with additional detail.

4.1.1 Passive corrosion

Potentiodynamic polarisations undertaken with electrolyte pHs of 11.7 and above show strongly limited anodic current densities consistent with surface passivation (Figure 4-1 and Figure 4-2), whilst the cathodic arm shows that the hydrogen evolution process occurs readily. At lower pHs, the anodic current densities are somewhat higher although they also show passivation, particularly at pH 11. Corrosion rates derived from Tafel analyses are subject to quite large uncertainties; in the earlier stages of passivation this is due to the rapid changes in the corrosion current which cannot be easily distinguished from the Tafel behaviour as evident in the non-log linear current response in the region close to OCP. Later in the passivation, the current will have dropped to a substantially lower level so that noise in the corrosion signal, and from external interference, complicate the fitting. Consequently, Tafel approximations have not been employed in this work. Galvanostatic tests show an approximately linear rise in potential during early film formation (Figure 4-3) which has previously been shown to be consistent with film formation according to the high field model (Gonzalez Torreira *et al.,* 2003 and Gonzalez Torreira, 2004). Oxygen evolution is apparent at over-potentials above ~+3 V vs OCP which particularly affects the extent to which galvanostatic tests can be employed to accelerate film growth.

Figure 4-1: Typical anodic polarisation results for Magnox Al80 electrodes in electrolytes of pH 10.0, 11.0, 11.7 and 12.0 (0.1, 1, 5 and 10 mM NaOH, respectively) (reproduced from Burrows *et al.*, 2005)
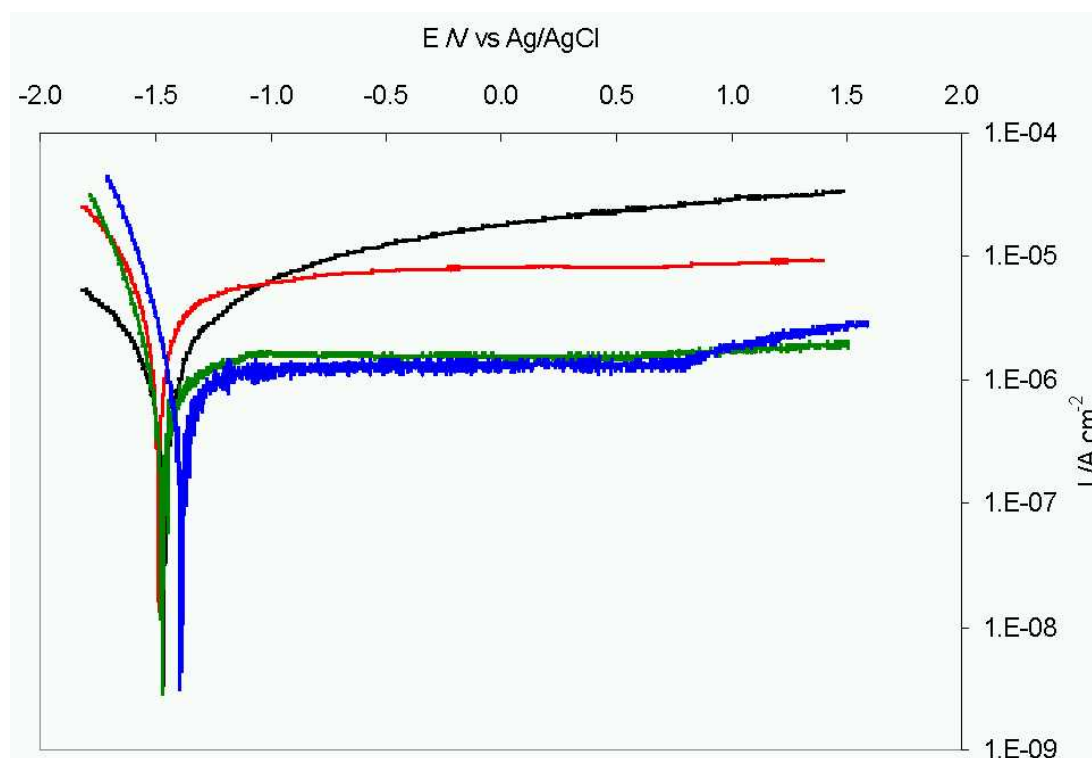
Figure 4-2: Typical potentiostatic polarisation results (E= -0.5V vs Ag/AgCl) for Magnox Al80 electrode in pH 11.7 electrolyte.
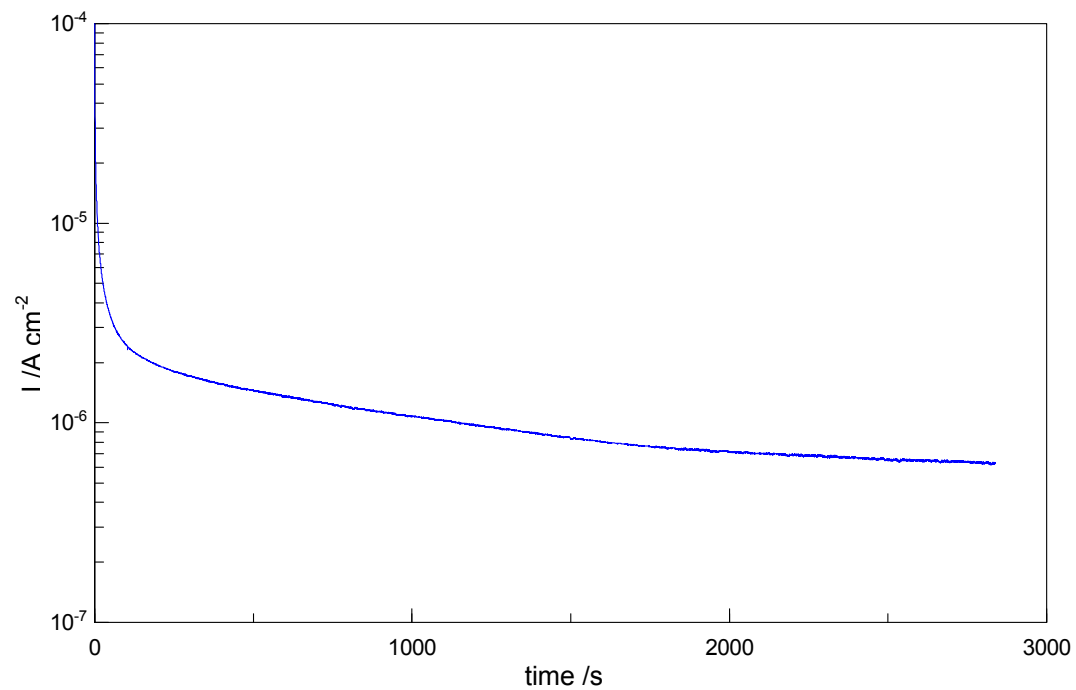
Figure 4-3: Typical galvanostatic polarisation (I = 10 μA cm^{-2}) for Magnox Al80 electrode in pH 11.7 electrolyte
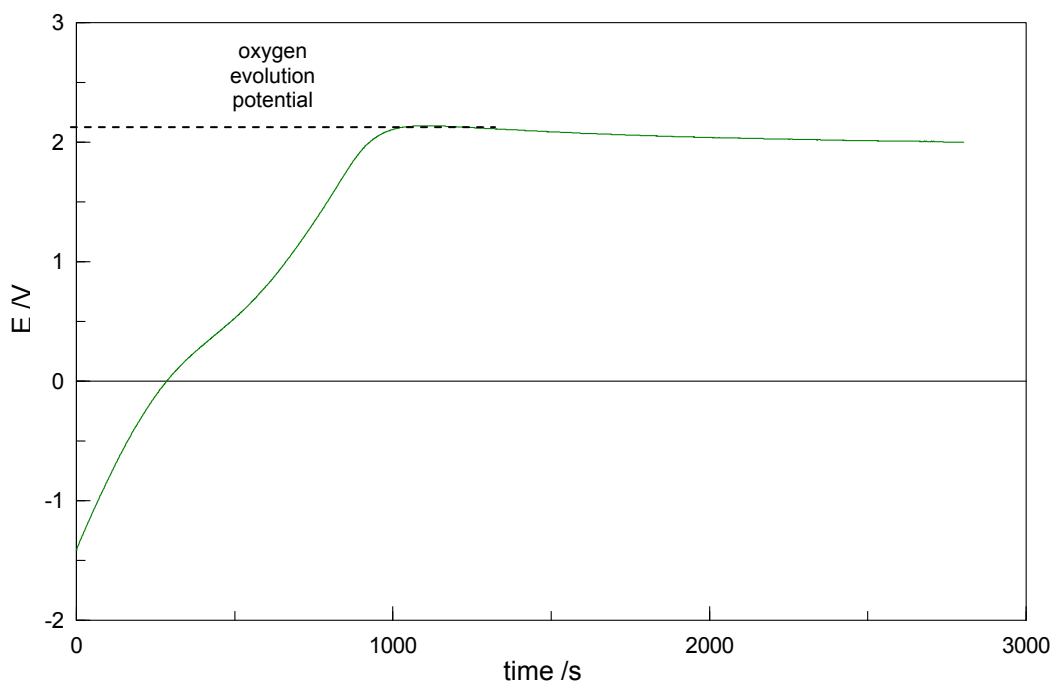
The behaviour of freely corroding Magnox in the absence of external polarisation may be investigated with the use of EIS (Figure 4-4). For the moderate corrosion rates observed at very short timescales, and for relatively low pHs, a clear double time constant is observed in the spectrum and this can be effectively modelled by the equivalent circuit shown in Figure 4-5, as can be seen in Figure 4-6. The mid-low frequency time constant can be clearly associated with the passive film formation. Indeed, as soon as a moderate level of passivation has been achieved, the spectrum is dominated by the low frequency time constant (Figure 4-7), although the contribution from a Warburg or constant phase element (CPE) type process remains clear. For these passivating conditions, a simpler CPE equivalent circuit is appropriate as shown in Figure 4-8 with the fitting result in Figure 4-9. Longer timescale EIS tests show continuing increase in the size of the time constant, equivalent to increase in the surface resistance (Figure 4-10). The spectrum may become noisy at the low frequency limit, despite practical steps to limit interference and occasionally experimental artefacts can be observed in this region, as per the small discontinuity in this data. For purposes of deriving corrosion rates, the EIS fitting range excludes this part of the spectrum which can otherwise complicate the fitting. It is noted that application of either equivalent circuit results in comparable fittings for EIS corrosion rate results even under differing surface conditions.

The EIS results therefore show a similar behaviour to the passivation under electrochemical polarisation with a rapid initial decrease in corrosion rate and the lowest rates corresponding to the highest pH (Figure 4-11).

Figure 4-4: Impedance Spectra of Magnox in 40, 200 & 400 mg kg^{-1} NaOH (pH 11, 11.7 and 12, respectively) after 1 (×), 5 (°) & 10 (•) hours (reproduced from Burrows & Harris, 2007)
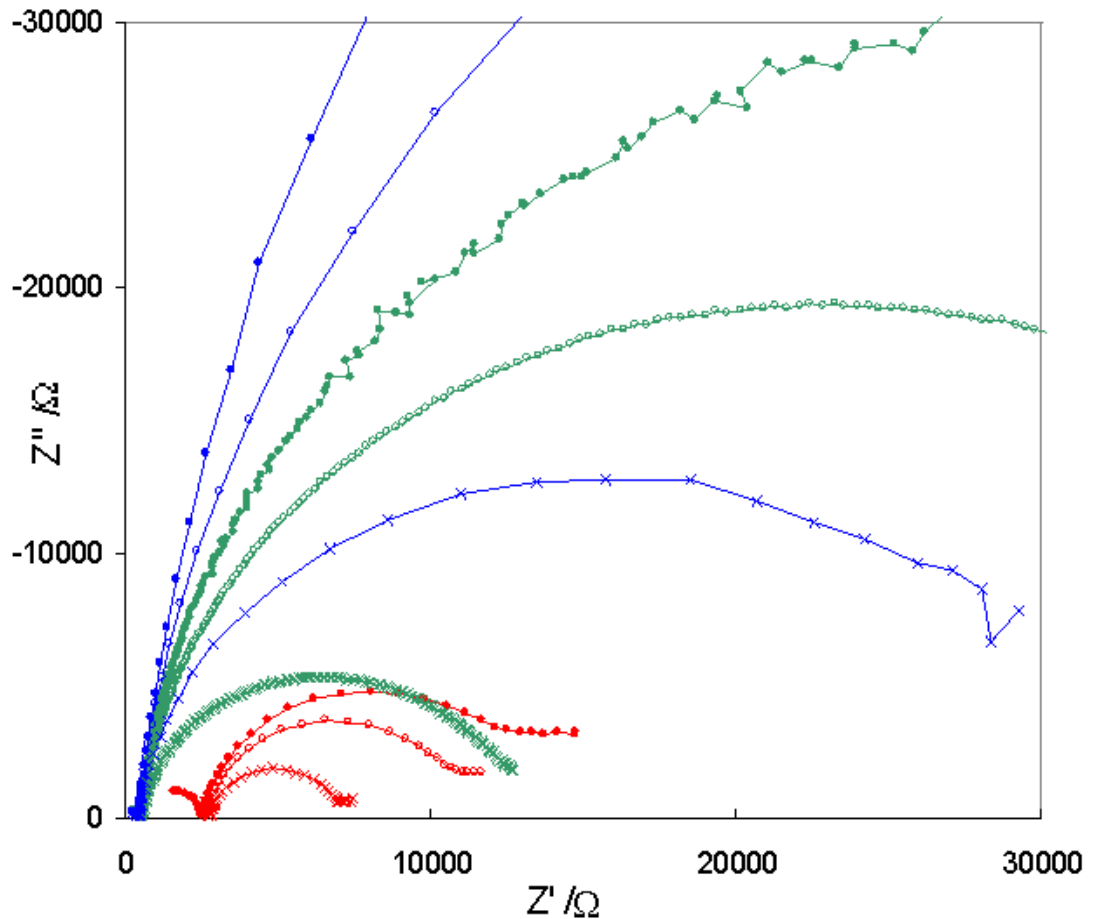
Figure 4-5: Equivalent circuit for EIS results for Magnox in early stages of passivation.

Key
R_s – Solution resistance
R_{ct} – Charge transfer resistance
C – Capacitive element
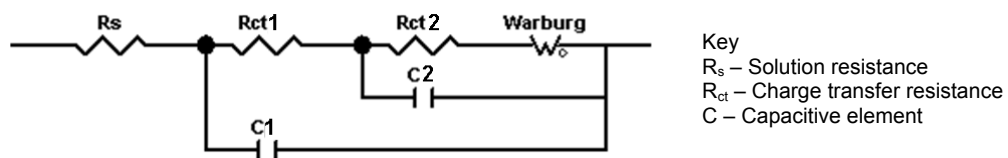
Figure 4-6: Nyquist plot showing typical EIS spectra for Magnox in pH 11.0 electrolyte with fit result according to equivalent circuit shown in Figure 4-5
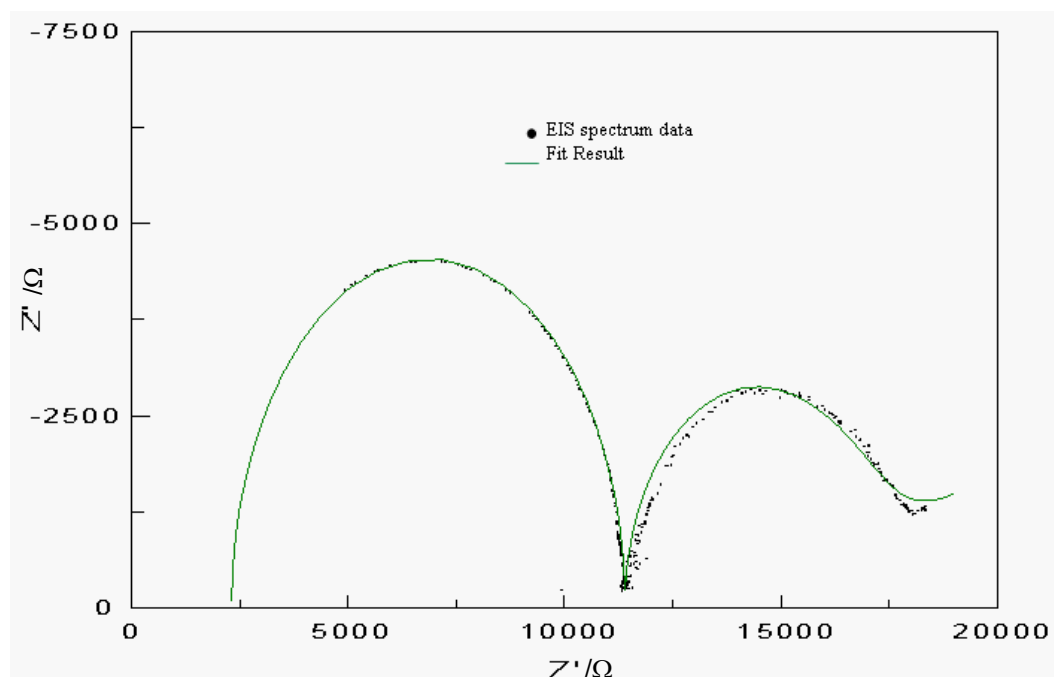
Figure 4-7: Nyquist plot showing typical EIS spectra for Magnox in pH 11.7 electrolyte over 1 - 6, 7 - 12, 13 - 18 and 19 - 22 hours
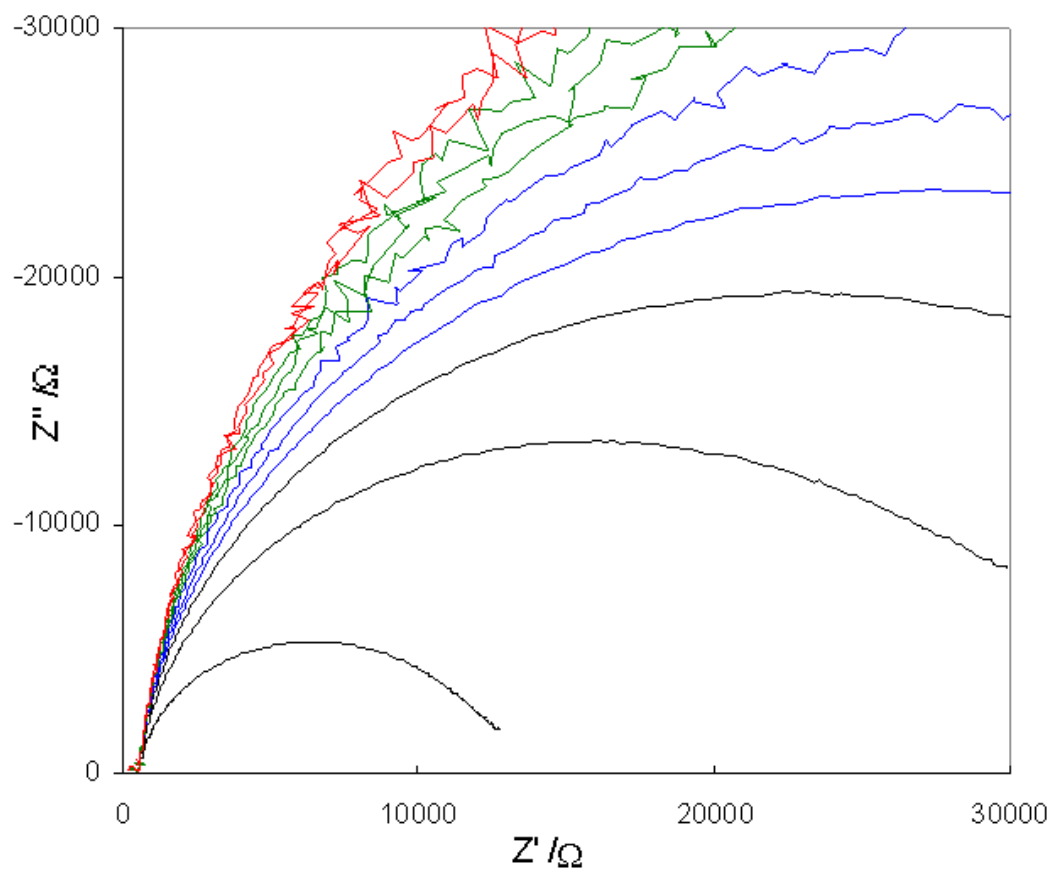
Figure 4-8: Equivalent circuit for EIS results for passivated Magnox
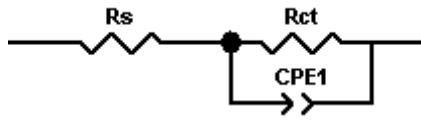
Figure 4-9: Nyquist plot showing typical EIS spectra for Magnox in pH 11.7 electrolyte with fit result according to equivalent circuit shown in Figure 4-8.
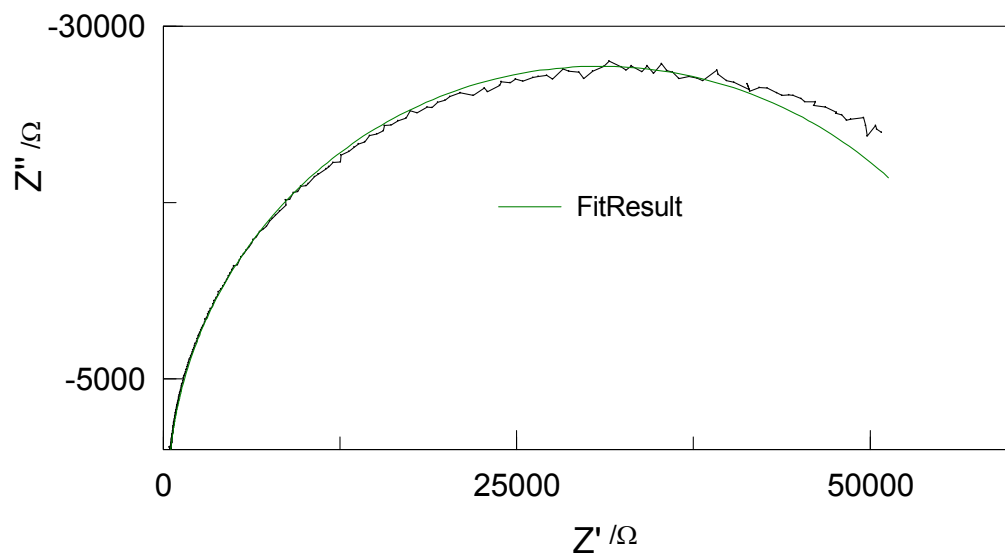
Figure 4-10: Nyquist plot showing wider region of sequential EIS scans measured over the initial ~18 hours of passivation of Magnox electrode in pH 11.7 (short and long scans shown)
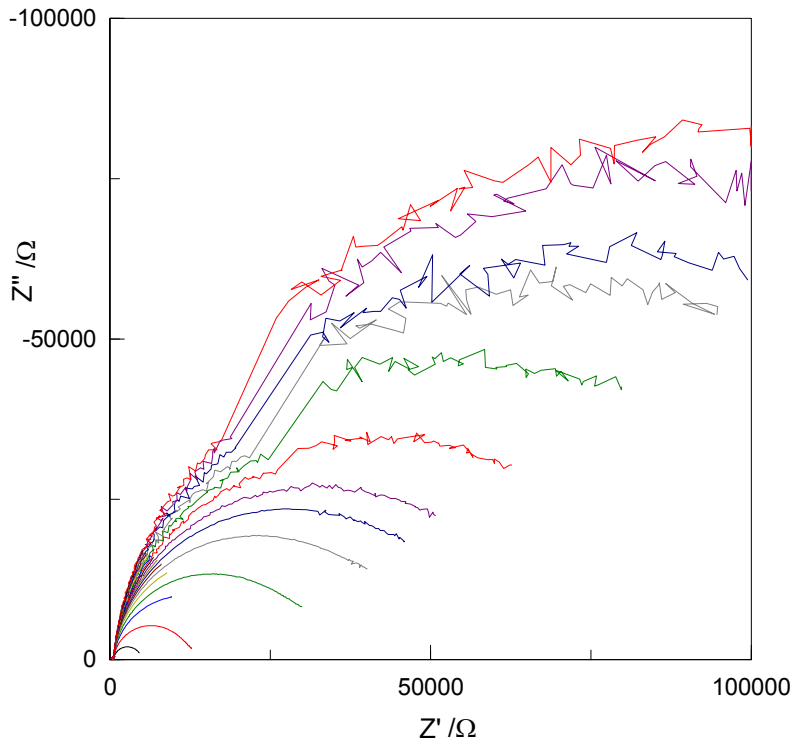
Figure 4-11: Calculated corrosion current densities derived from fitting of EIS spectra for Magnox in pH 11.0, 11.7 and 12.0 electrolytes
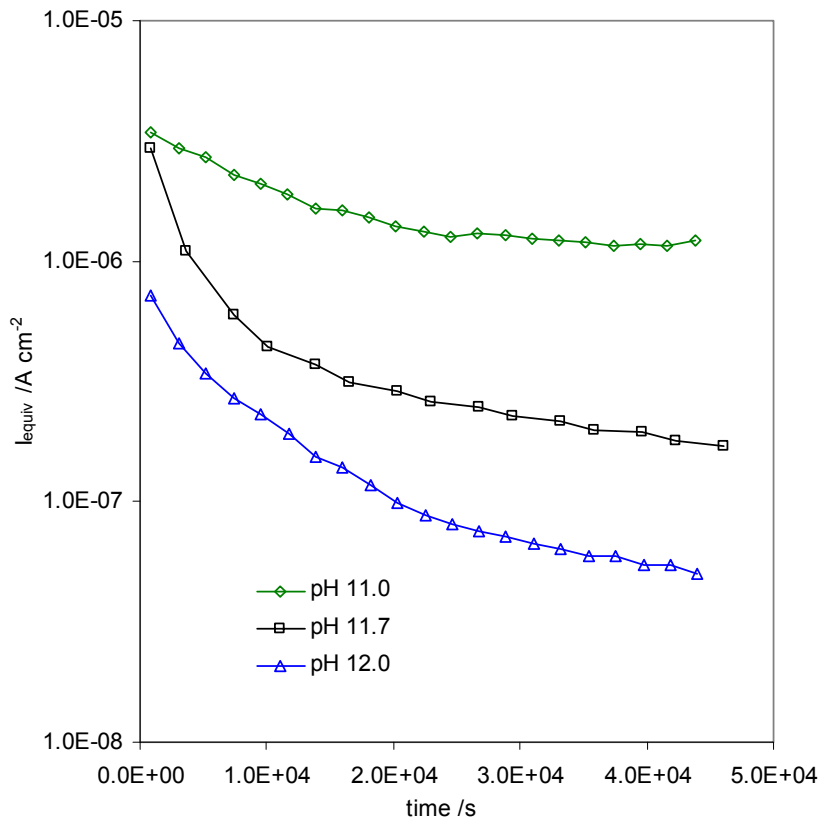
Figure 4-12 shows a set of three polarisation tests each repeating three sweeps from initial exposure of a new electrode surface to a passivating solution (pH 11.7 without chloride), with limiting current densities (from the anodic arm of the sweep) in Figure 4-13. Different solutions were used in these tests; one was a fresh solution, while the other two had been used in previous tests, one having been exposed to atmosphere for some 4 hours, and the other around 6 hours. It is evident that although there is some variation in the limiting current densities, the passivation observed is similar for the surfaces in all three solutions showing that the passivation behaviour is not strongly affected by either (i) initial stages of pH depression from carbon dioxide absorption, (ii) low levels of carbonate anions or (iii) pre-exposure of the solution to a surface (e.g., the concentration of magnesium ions).

Figure 4-12: Polarisation tests for fresh Magnox surfaces exposed to 10 mM NaOH solutions (pH 12) of varying age; fresh (black), 4 hours aged (red) and 6 hours (blue)
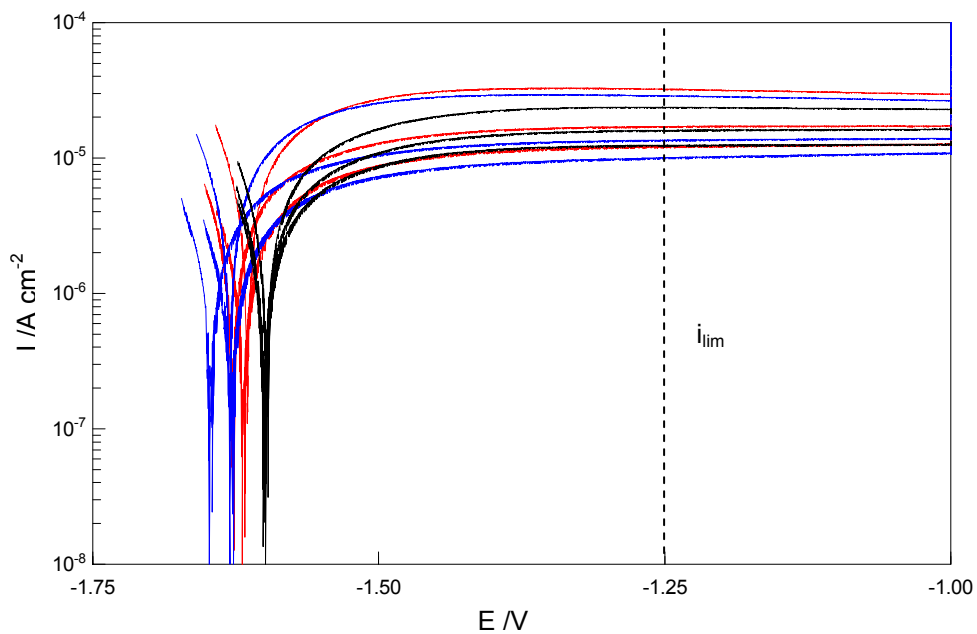
Figure 4-13: Limiting current densities (at E = -1.25V) for fresh Magnox surfaces following initial immersion in 10 mM solutions (pH 12); fresh (black), 4 hours aged (red) and 6 hours (blue)
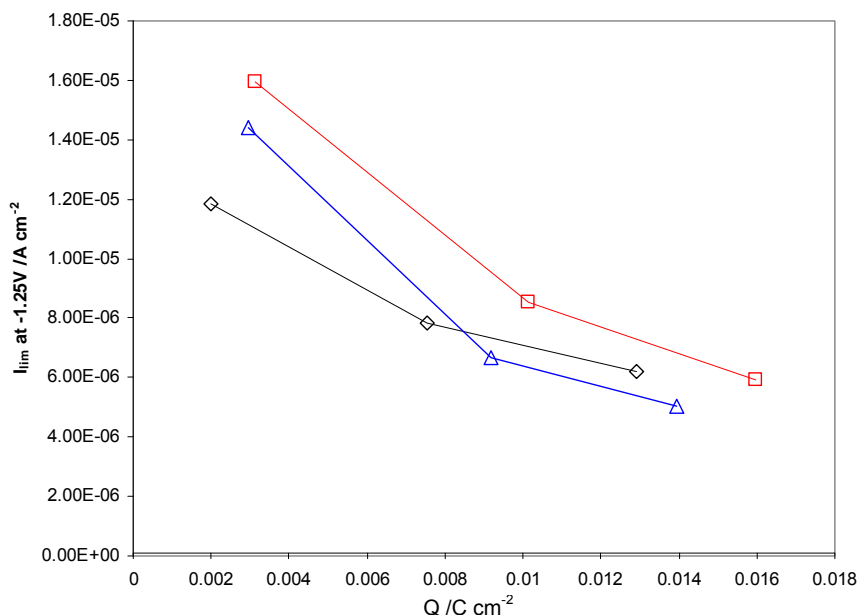
4.1.2   Surface Localised Corrosion

The presence of even low levels of chloride causes rapid onset of localised corrosion which is observed as a near-instantaneous rise in corrosion current density for potential control polarisation or a drop in applied potential for galvanostatic tests (Figure 4-14, Figure 4-15 and Figure 4-16). Initially this takes the form of propagating tracks of corrosion which progress across the electrode surface with rapid hydrogen evolution at the growing filament head (Figure 4-17). It is clear that the area of active corrosion is very small and must therefore involve an extremely high current density. This mode of corrosion has been compared to filiform corrosion, although clearly occurs in the absence of an applied surface coating which would normally be involved in this mechanism. Also, the mechanism is not understood to involve differential aeration (Ruggeri & Beck, 1983) and consequently, this mechanism is referred to here as filiform-like corrosion. These features appear to constitute a dense line of coalesced microscopic pits (Gonzalez Torreira, 2004) which are over-filled with dense corrosion product. ESEM has been used previously, and in the current work, to show that the corrosion product is highly hydrated as the morphology changes substantially when subjected to air drying. These aspects may all be seen clearly in a single ESEM image (Figure 4-18) which captured a partly dehydrated corrosion filament showing (i) a hydrated portion of corrosion product strand (as-formed), (ii) a dehydrated segment which has pulled away from the surface due to shrinkage stress revealing (iii) the series of micro-pits in the substrate metal.

Figure 4-14: Typical anodic polarisation curve for a Magnox electrode in a pH 11.7 electrolyte (5 mM NaOH) with and without 10 mg kg^{-1} (3x10^{-4} M) chloride (reproduced from Burrows *et al.*, 2005)
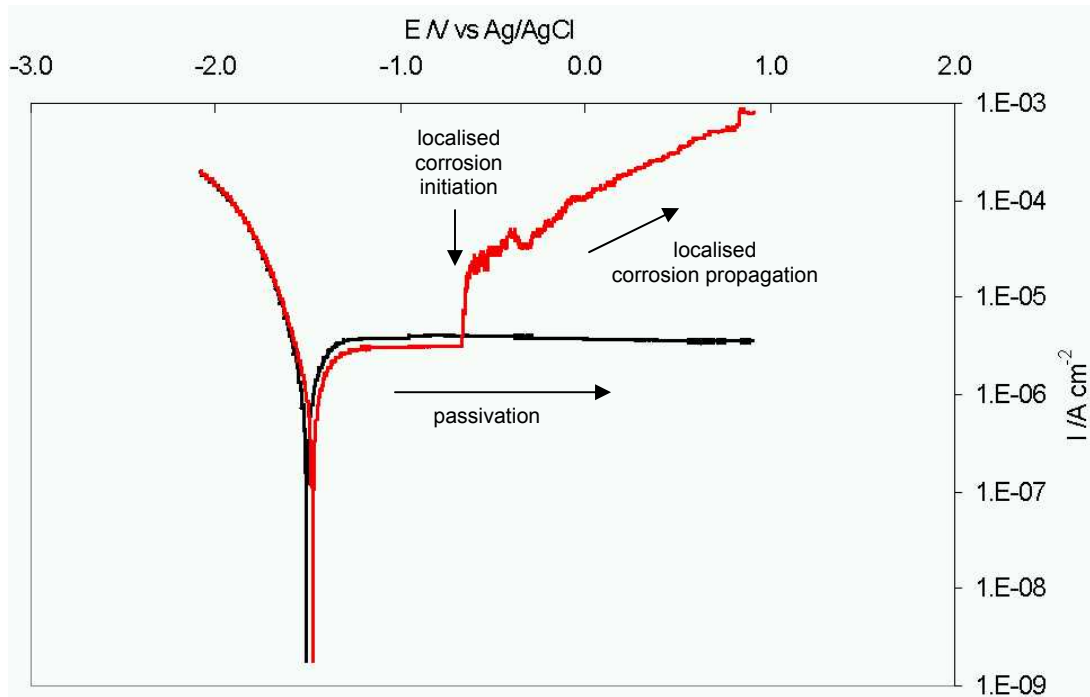
Figure 4-15: Typical potentiostatic polarisation curve (E = -0.5V vs Ref.) for a Magnox electrode in a pH 11.7 (5 mM NaOH) electrolyte with 15 mg kg^{-1} (4x10^{-4} M) chloride
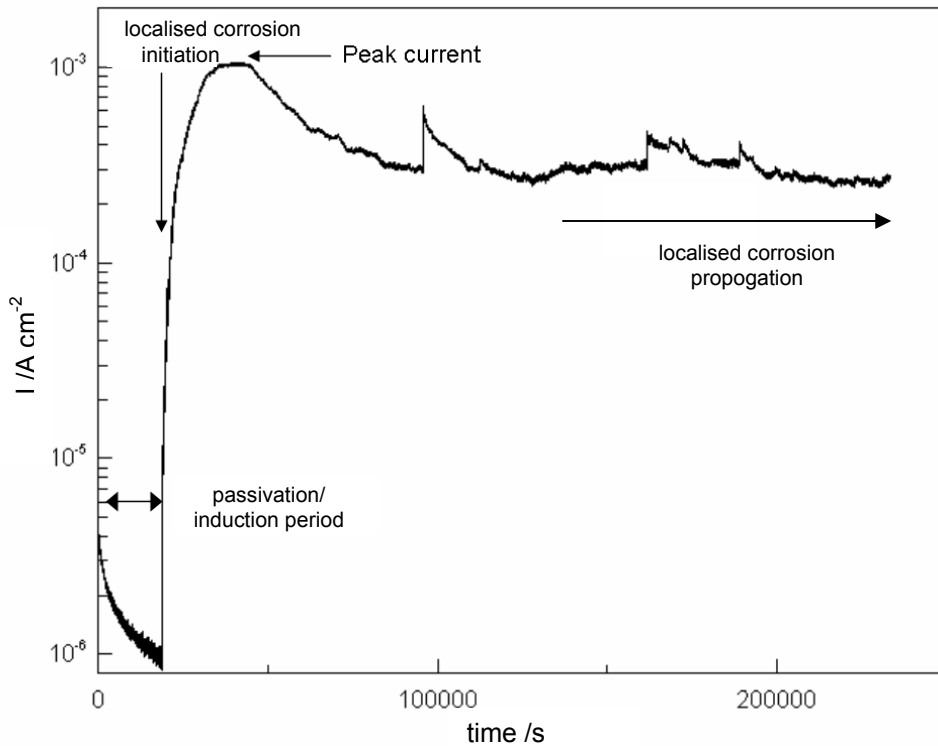
Figure 4-16: Typical galvanostatic polarisation curve (I = 5 μA cm^{-2}) for a Magnox electrode in a pH 11.7 (5 mM NaOH) electrolyte with 10 mg kg^{-1} (3x10^{-4} M) chloride
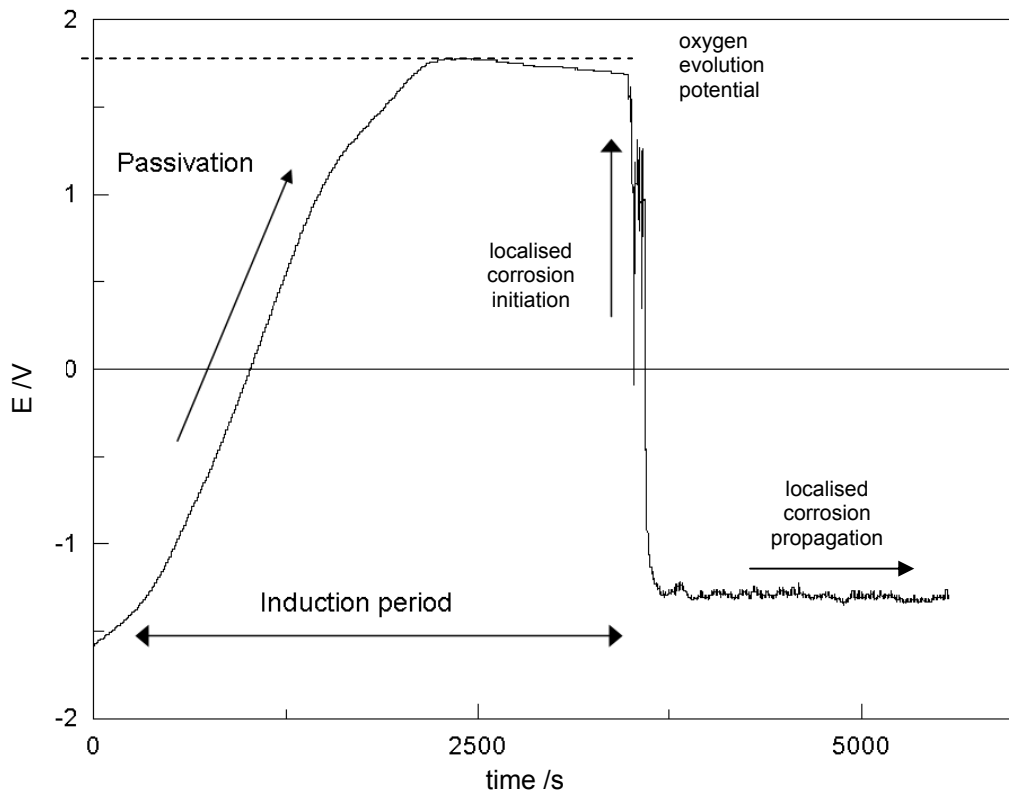
Figure 4-17: Optical micrographs of filiform-like corrosion occurring *in situ* on polarised Magnox electrodes in pH 11.7 (5 mM NaOH) electrolyte with ~20 mg kg^{-1} (6x10^{-4} M) chloride

(video still)
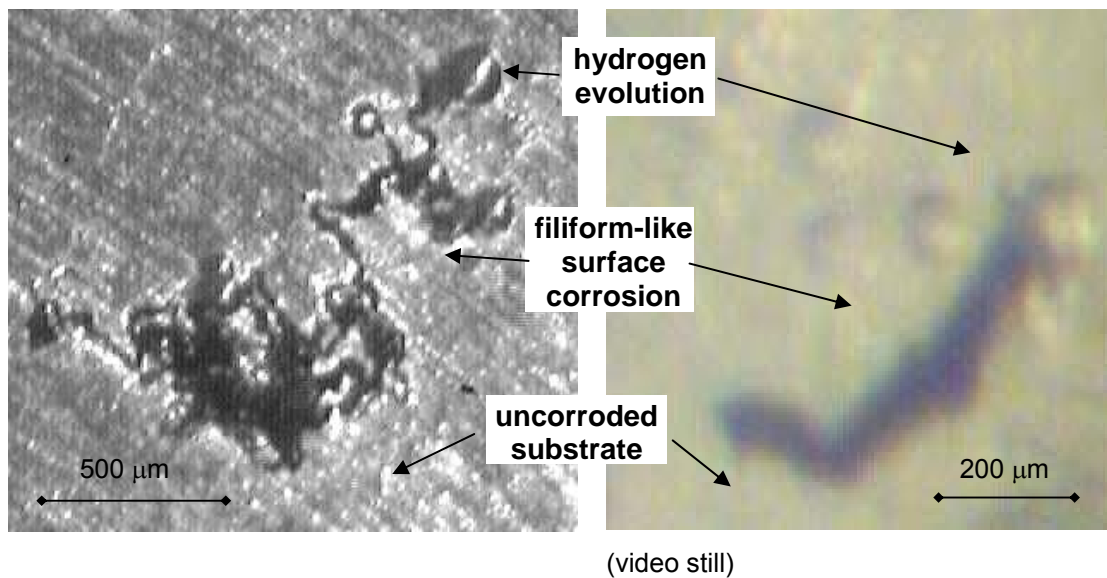
Figure 4-18: Environmental SEM micrograph of corrosion filament on a Magnox electrode in pH 11.7 (5 mM NaOH) electrolyte with ~20 mg kg^{-1} (6x10^{-4} M) chloride
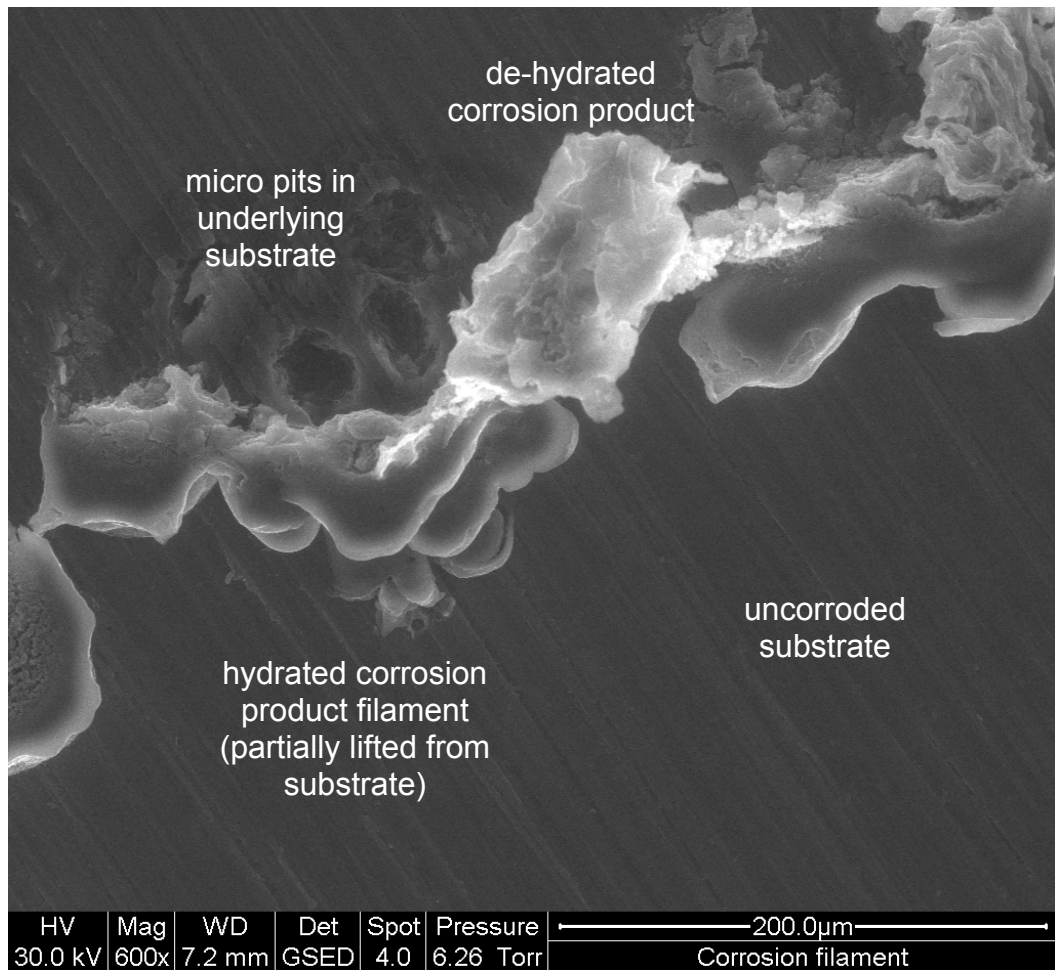
Following initiation, the current density typically increases rapidly, reaching a peak when the surface corrosion growth begins to be limited by availability of undamaged surface, usually as a result of reaching the edges of the electrode, or convergence with other areas as can be seen on Figure 4-15. In the return sweep of potentiodynamic tests, it is apparent that although the corrosion current falls, the localised attack does not readily repassivate and the current density remains well over an order of magnitude above the passive rate.

The overpotential at which breakdown is observed decreases with increasing chloride concentration (Figure 4-19), as is typical of anion induced attack. Figure 4-20 shows a series of potentiostatic tests undertaken at different pHs in which the chloride concentration was incrementally increased until initiation of localised corrosion was observed. The concentrations of chloride required are shown in Figure 4-21. As expected, high pH is protective and increases the chloride concentration required for film breakdown at the particular potential. Furthermore, the peak current density (see

Figure 4-15) may be observed to be a function of chloride concentration, with the highest chloride test showing the highest peak corrosion value despite the very high pH (Figure 4-22). Figure 4-21 also shows the pitting-passivity boundary for the chloride concentration required for breakdown under polarisation compared to the specification for pond storage of spent fuel.

Figure 4-19: Anodic polarisation of Magnox in pH 11.7 (5 mM NaOH) electrolyte with 20 and 200 mg kg^{-1} chloride (6x10^{-3} and 6x10^{-4} M, respectively) showing outward and return sweeps
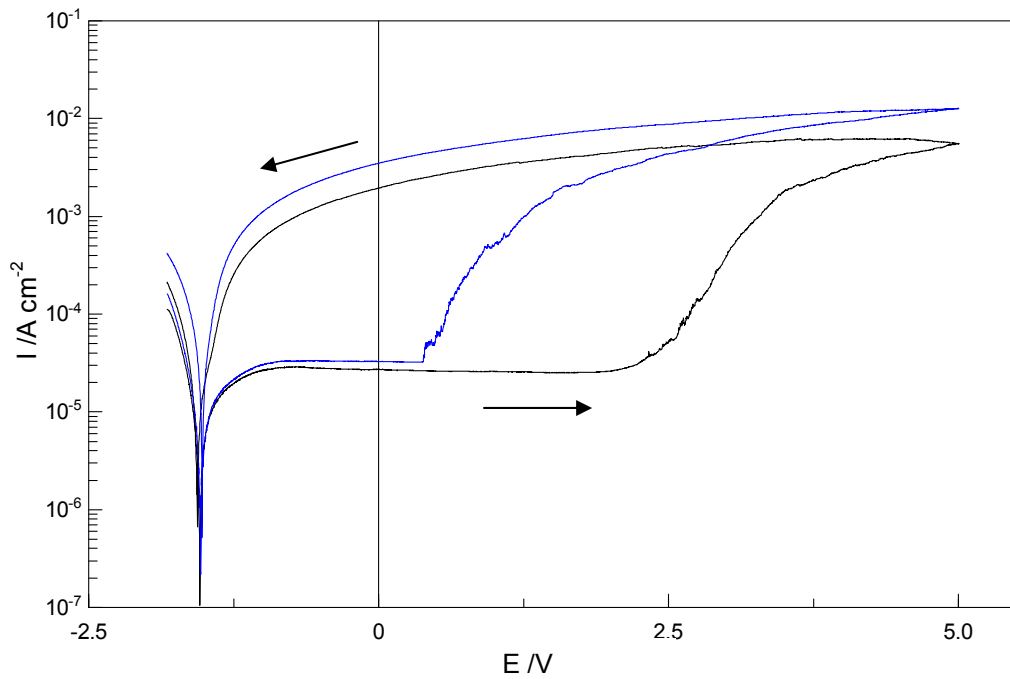
Figure 4-20: Corrosion current for potentiostatic polarisation experiments (E = -0.5V vs Ref.) for Magnox samples in solutions of 200, 400, 1200 and 4000 mg kg⁻¹ NaOH and incrementally increasing chloride concentration (shown in Figure 4-21)
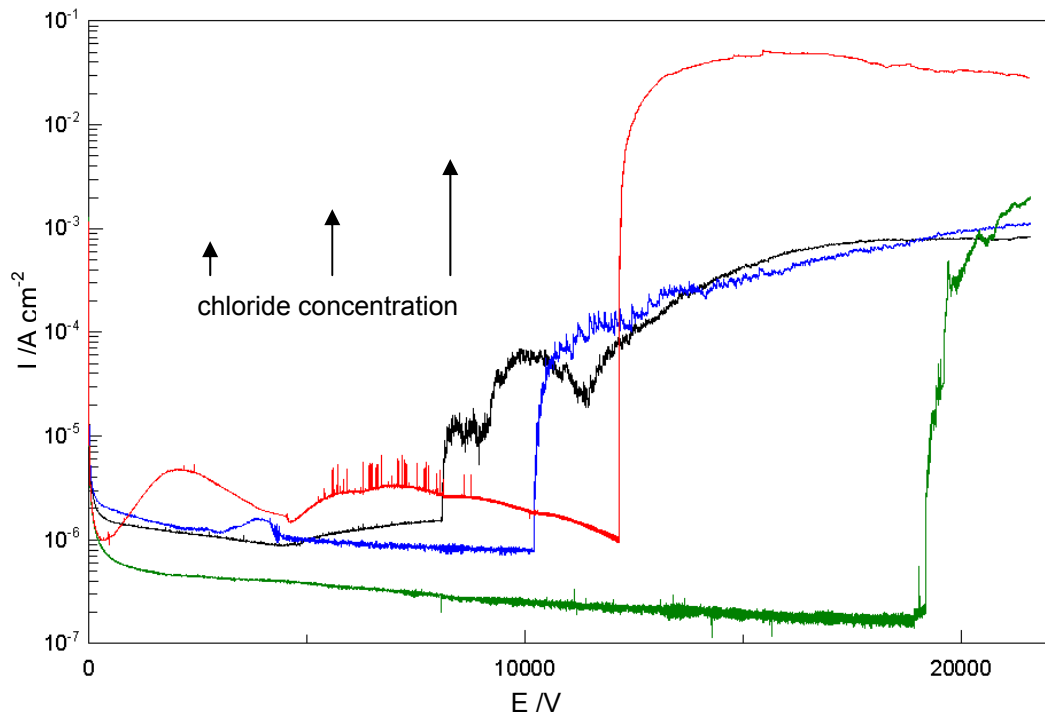
Figure 4-21: Indicative pH-chloride stability boundary for potentiostatically polarised (E = -0.5V vs Ref.) Magnox samples
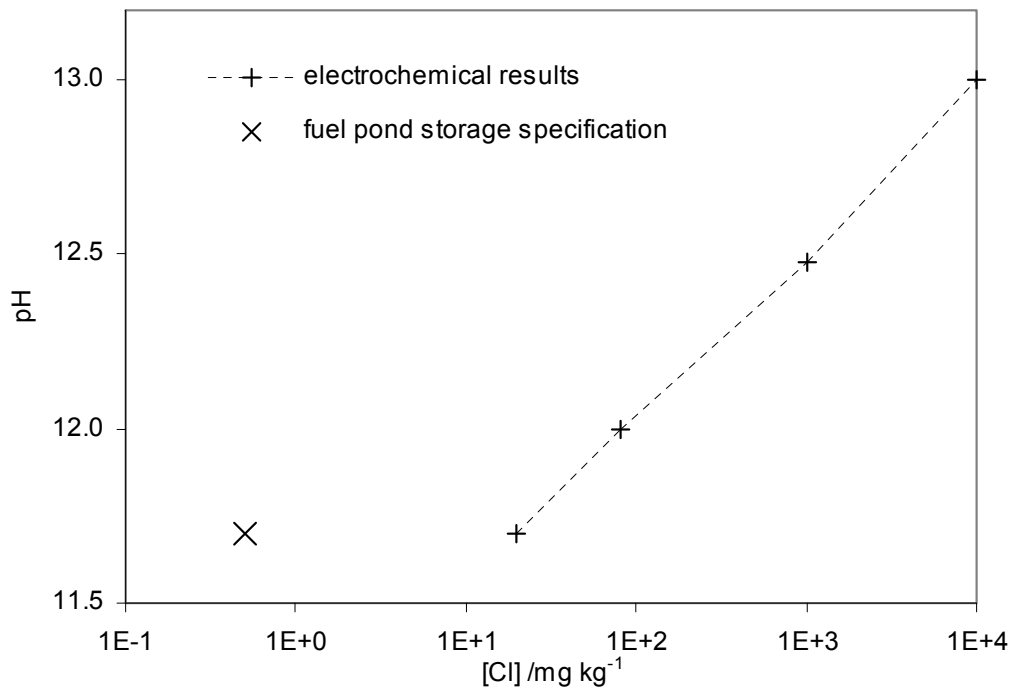
Figure 4-22: Relationship between chloride concentration required to initiate pitting and peak corrosion current
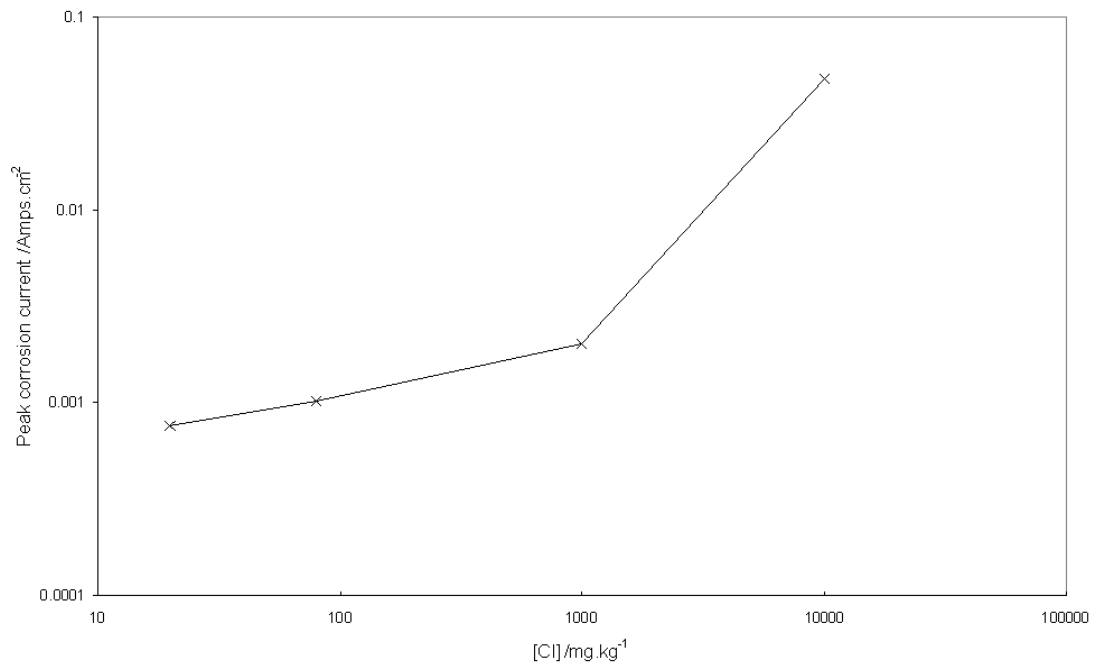
Figure 4-23: Anodic polarisation of Magnox in pH 12.3 electrolyte with 20 mg kg^{-1} chloride
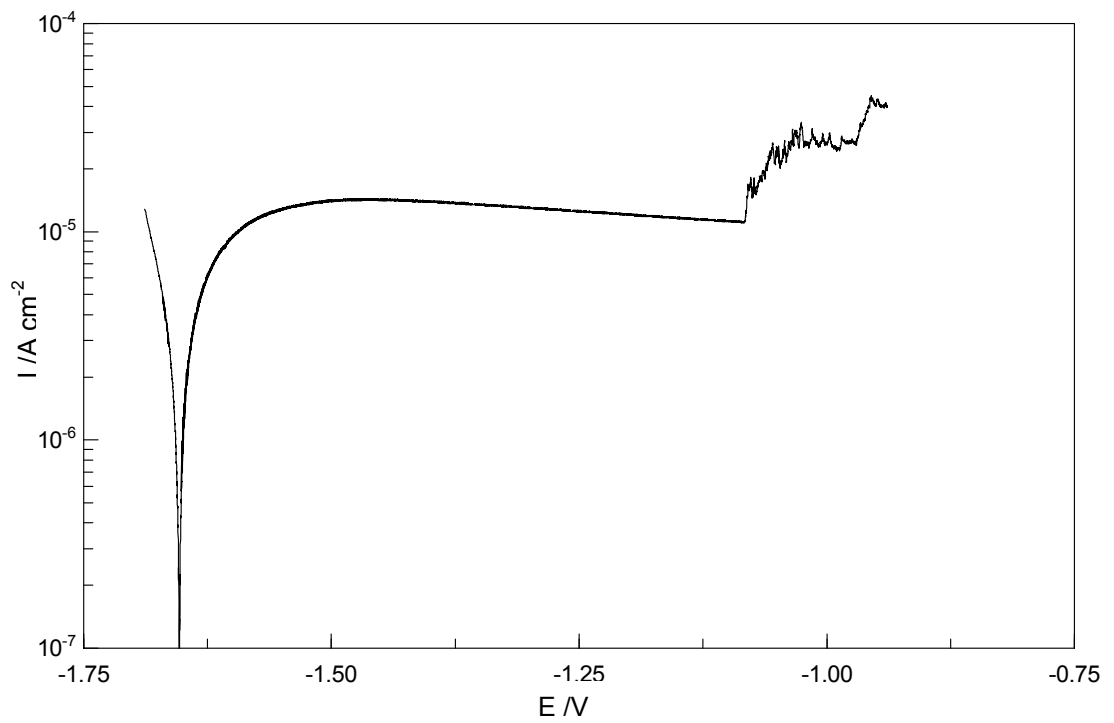
Figure 4-24: Potentiostatic polarisation of Magnox in pH 12.3 electrolyte with 20 mg kg^{-1} chloride at -1.10 V (red), -1.20 V (yellow), -1.25 V (green), -1.30 V (blue), -1.35 V (black)
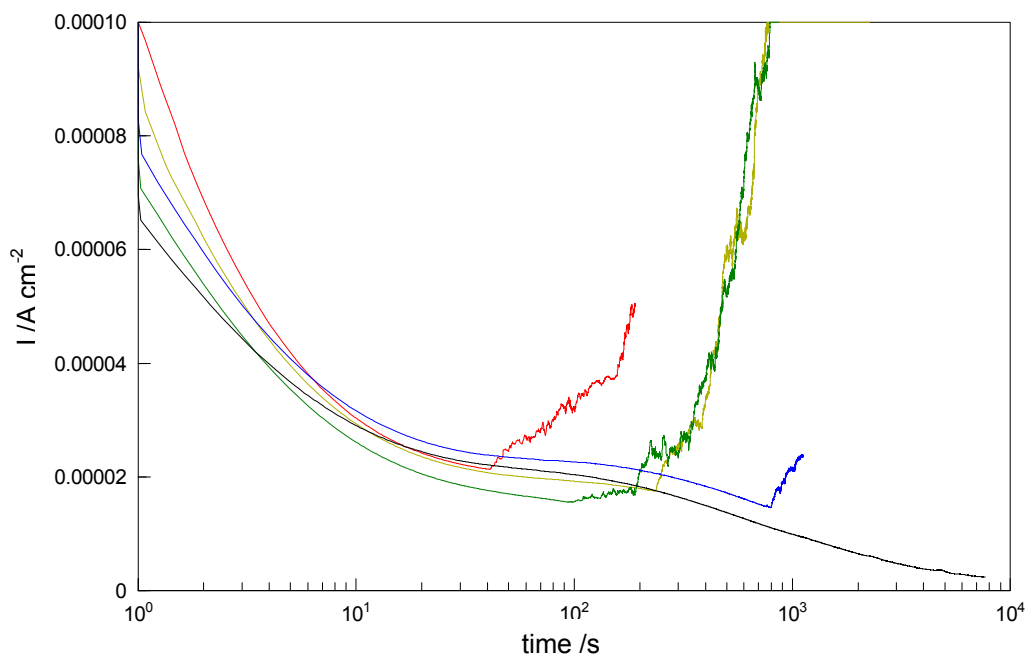
Figure 4-25: Time to initiation of localised corrosion for potentiostatic polarisation of Magnox in pH 12.3 with 20 mg kg^{-1} chloride
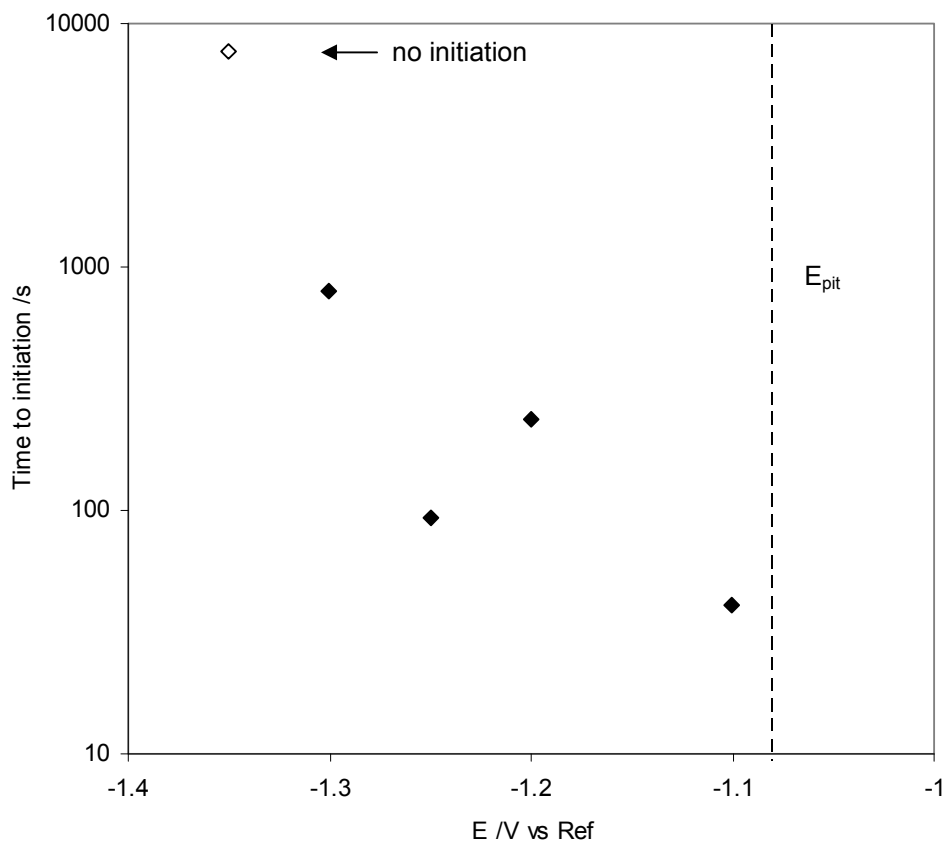
The rapidity of localised corrosion onset for a particular pH and chloride concentration is affected by the polarisation at values close to E_{pit}. This effect was investigated through potentiostatic tests undertaken at a relatively high alkalinity (pH 12.3) to reduce the effect of carbonate absorption over longer timescales.

Figure 4-26 shows electrochemical noise results for a pair of Magnox working electrodes in pH 11.7 electrolyte with 20 mg kg^{-1} Cl. This clearly shows both transient attack and propagating filiform-like corrosion initiation. The potential rises rapidly over the first ~5 hours of the test from the initial value near -1.5 V to approaching -1.0 V, correlating to passivation of the surfaces. Then a series of half a dozen transients are observed with a drop and recovery in potential coinciding with a current spike, the polarities of which show that these transients are occurring on both working electrodes in approximate alternation. Although the transient frequency is not highly regular, there is a clear periodicity. This appears to be due to the potential gradually rising until close to the pitting potential, when localised corrosion initiates on one electrode, causing the mixed potential to drop and allowing the initiating pit to repassivate. At around 25 hours, there is a period of propagation of around 3 hours before repassivation and following this localised corrosion activity ceases until around 42 hours when the potential has risen to nearly -0.7 V. At this point, one further transient occurs followed by a sustained propagation with a clearly increasing current density. These results show clearly the interaction between ennoblement of the passivating surface and onset of localised corrosion from low levels of chloride.

Figure 4-26: Electrochemical potential and current noise results for Magnox in pH 11.7 electrolyte with 20 mg kg^{-1} chloride (Reproduced from Burrows *et al.*, 2005)
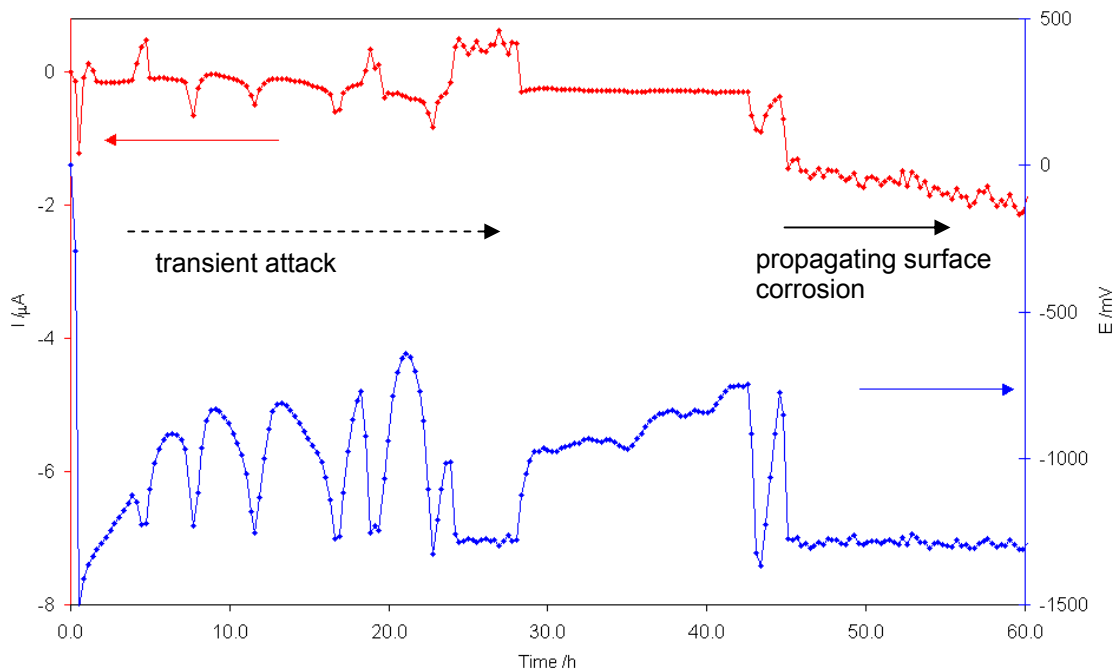
4.1.3 Bulk Pitting

At the macroscale, a widening coverage of filiform-like corrosion appears as an essentially continuous area of surface corrosion. As the attack progresses, the areas which have been affected may then suffer bulk pitting which is normally only visible on the surface from the voluminous and gelatinous highly hydrated corrosion product which is expelled by the pits (Figure 4-27). The size of the pits can be considerable and often, a large number of smaller pits are observed to coalesce into large propagating pits (Figure 4-28 and Figure 4-29), with smaller etch pit-type structures also in evidence, which were associated with salt film corrosion by Lunder *et al.* (1994). In these cases, there is often extensive voidage in evidence apparently relating to channels from hydrogen evolution. It is notable that this behaviour occurs for both electrochemically polarised and freely corroding samples, although it is the case that polarised samples tend to experience a larger number of smaller corrosion sites, whereas un-polarised (or lower polarised) corrosion tends to take place in a more limited number of locations but may be more concentrated (Figure 4-30). This is notwithstanding the fact that anodic polarisation substantially accelerates the onset and propagation of localised corrosion as would be expected. A further interesting characteristic is the fact that, even following extensive localised corrosion of the surface, large areas of the electrode will be apparently unaffected (Figure 4-17 and Figure 4-27) and the filament corrosion will not have spread continuously but instead appears to cease expansion and be replaced by bulk pitting. This gives the corrosion products of the three mechanisms of corrosion notably contrasting appearances;

- the thin passive surface film is essentially transparent although affects the colour of the surface as it grows thick,
- the dense filiform-like corrosion products and pit bases are matt black and,
- the hydrated bulk pit corrosion product is a white, gelatinous or crystalline reprecipitate.

The colour of the filaments changes to white once these areas are removed from solution. This is consistent with the observations of Straumanis & Bhatia (1963) in representing a phase of magnesium micro-particles within a magnesium hydroxide matrix.

Figure 4-27: Images of Magnox electrodes showing areas of uncorroded substrate and surface filiform-like corrosion (left) and additionally bulk pitting corrosion product (right) (following polarisation test) immediately following removal from electrolyte
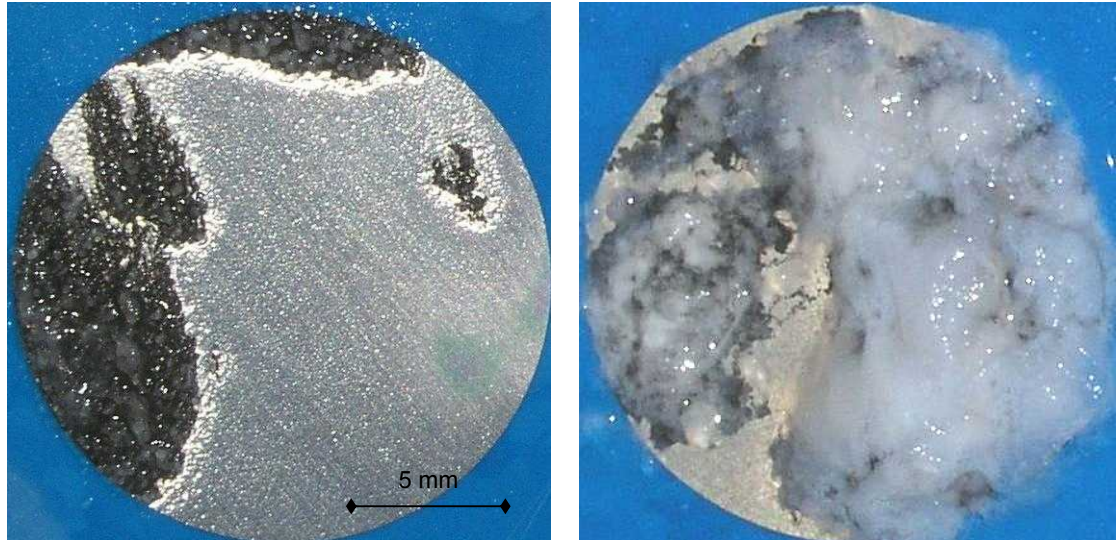
Figure 4-28: Optical micrograph of a sectioned Magnox electrode showing extensive surface pitting, propagation of bulk pit, corrosion product and channels within pit
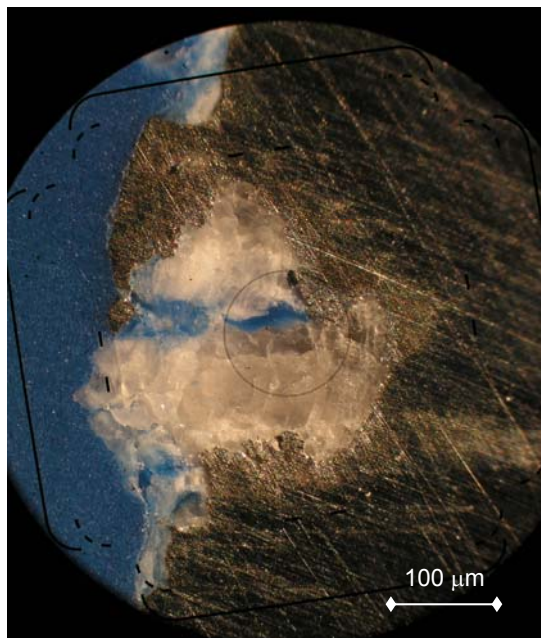
The electrochemistry of a polarised electrode undergoing bulk pitting does not show a fundamentally divergent behaviour from one experiencing surface filiform-like corrosion. This suggests that the two modes of corrosion may result from the same underlying mechanism. This is supported by the fortuitous observation of an unusual type of

atmospheric corrosion in a test sample following sectioning for examination. Figure 4-301 shows that an aggressive phase present in the base of a bulk pit has become mobile and formed a "dry" filament on the sectioned surface. This is believed to have been due to ambient moisture being absorbed by the hygroscopic chloride deposit and has resulted in the filament propagating across the surface in a manner closely reminiscent of the filiform-like corrosion which occurs under aqueous conditions. It also appears that chloride is conserved, as transport along the length of the filament from the sectioned pit does not seem credible, implying a moving concentrated phase at the filament head. In this case, the characteristic filament tail of disrupted magnesium metal in a corrosion product matrix has not formed. This may relate to the fact that availability of water was likely to have been the limiting factor in the rate of propagation, so the reaction rate at the substrate interface was much lower and less disruptive.

A typical polarisation at high pH and high chloride, where transition into bulk pitting follows rapidly from surface filiform-like corrosion, is shown in Figure 4-32. Following initiation of localised corrosion, the corrosion current increases with the perimeter of corroding area until this is constrained by either the electrode edge or coalescence with another corroding area. Following this, the corrosion current from filiform-like corrosion is expected to decrease but may be replaced by bulk pitting, which typically results in a corrosion current somewhat lower than the peak surface corrosion value but of a similar order of magnitude.

Figure 4-29: Optical micrographs of sectioned Magnox rod samples showing bulk pitting from unpolarised corrosion
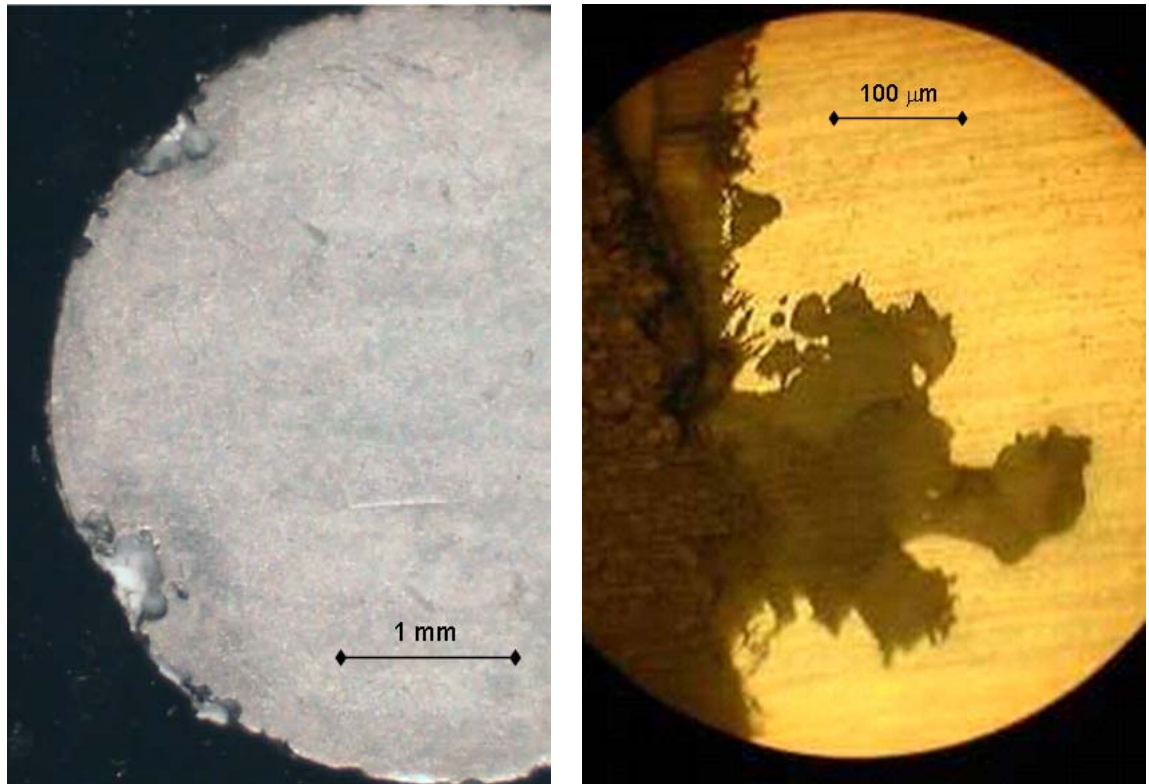
Figure 4-30: Magnox electrode surfaces showing localised corrosion initiated under polarisation (left) potentiostatic (E = -0.5V vs Ref) and (right) potentiodynamic (E_{max} = 3V vs Ref)
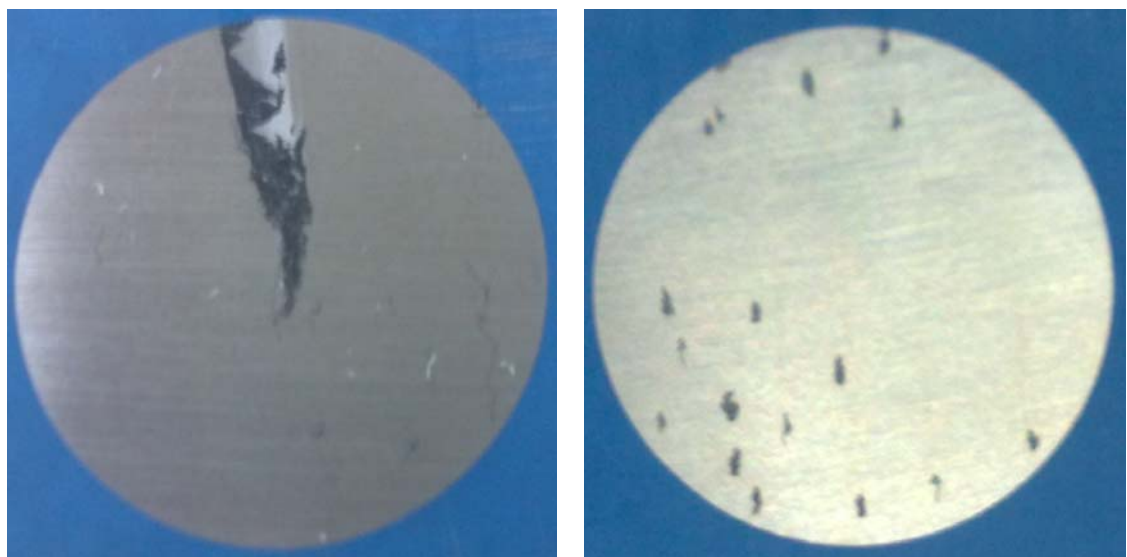
Figure 4-31: Optical micrograph of sectioned Magnox sample showing "dry" surface corrosion filament initiated from sectioned bulk pit
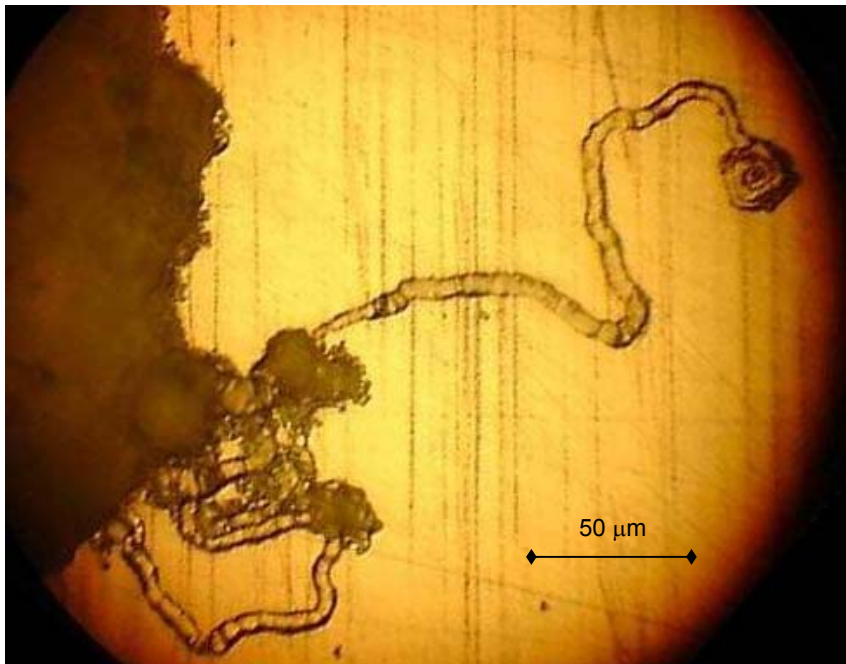
Figure 4-32: Potentiostatic polarisation (E = -0.5V vs Ref.) of Magnox in pH 13 electrolyte with 0.4%wt (0.1 M) chloride showing transition to bulk pitting
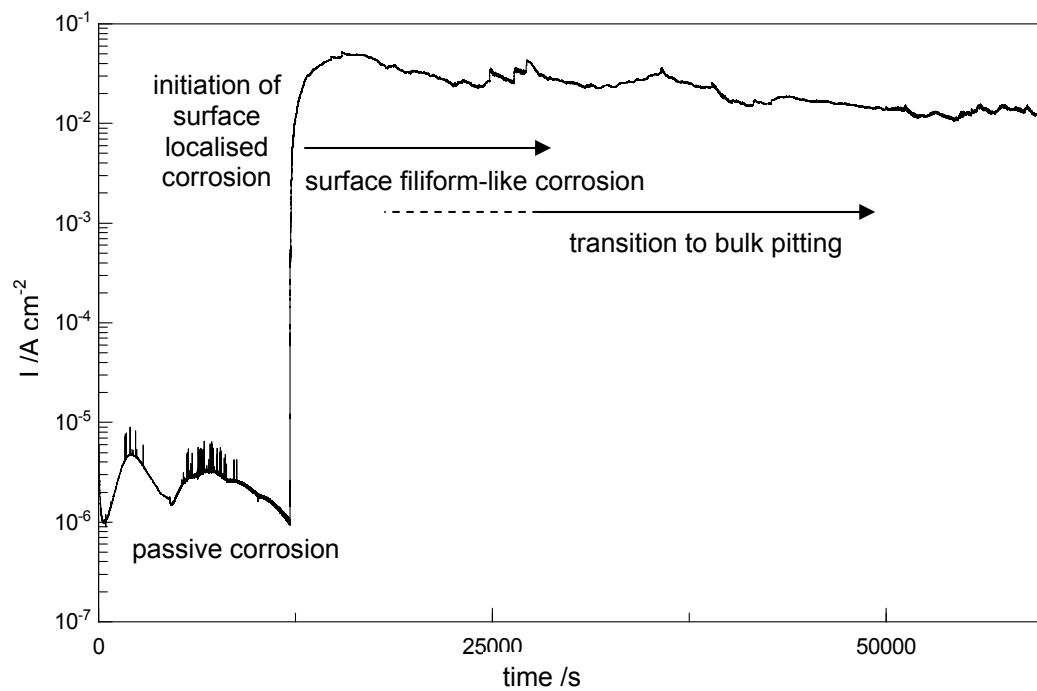
Figure 4-33: Image of extensively corroded magnesium rod specimen from unpolarised corrosion in pH 13 electrolyte with 1%wt (0.3M) chloride immediately following removal from solution

hydroxide jacking

uncorroded surface

bulk pitting

surface filiform-like corrosion

spalled corrosion product

2 mm
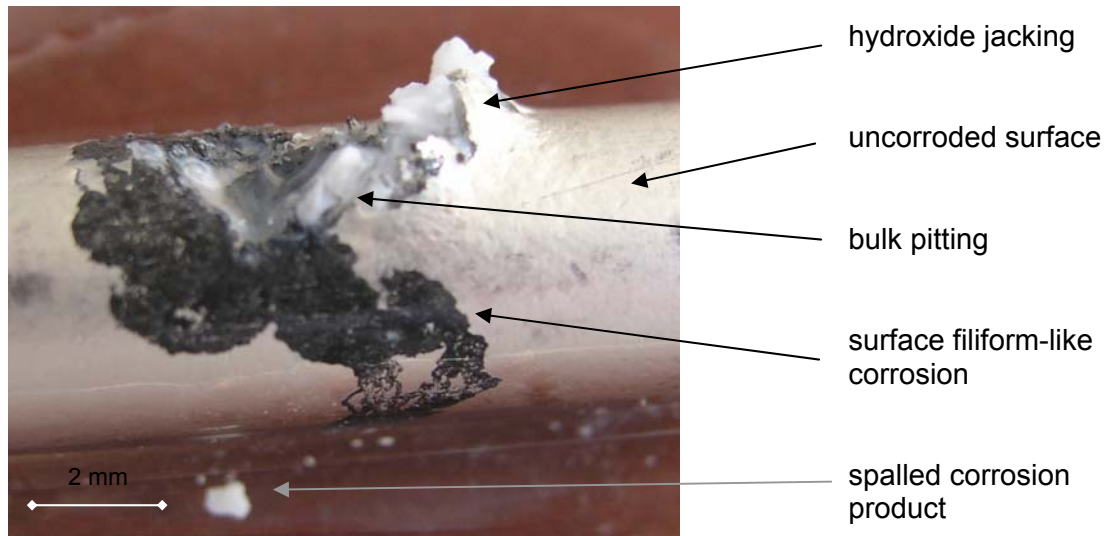
Figure 4-34: Micrograph of Magnox coupon cross-section showing crevice-like pitting around micro-drill inclusion (approximate extent of original feature shown in blue dashed line)

100 μm
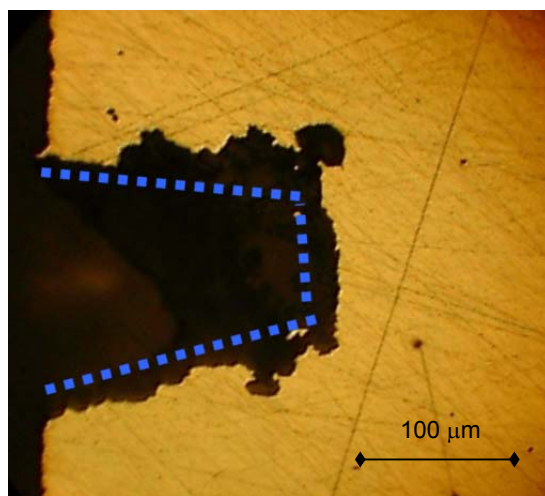
In cases of severe attack, the extent of penetration into the bulk material, coupled with the expansive nature of the hydroxide corrosion product leads to mechanical disruption of the material as can be clearly seen in Figure 4-33, which again shows the three distinctive corrosion products concurrently. The effect of crevice-like features with restricted geometry is also apparent and these tend to provide sites for preferential initiation of pitting, although the mechanism appears to be similar on the basis of pit geometry (Figure 4-34). It should be noted that one method for producing such crevices

involved use of a microdrill which may be expected to leave traces of iron on the surface which are also likely to promote localised corrosion.

Some further investigations were undertaken using x-ray microtomography (see Section 3.7). This involved square section coupons of Magnox Al80 (approx 5mm x 5mm x 20 mm) which were placed in high pH, high chloride (pH 13, 1%wt Cl) electrolyte until corrosion had initiated and progressed into bulk pitting under freely corroding conditions. One coupon was then placed into an x-ray transparent plastic vial with sufficient electrolyte to remain immersed. *In situ* characterisation of the sample was then undertaken and the coupon unloaded from the x-ray cavity and replaced in the bulk electrolyte. In this manner, it was possible to undertake successive scans without affecting the propagation of pitting during the time period by drying or substantial alteration of the chemical conditions. Reconstructed images from these investigations are shown in Figure 4-35 and Figure 4-36, showing three dimensional representations of the substrate metal with corrosion product and electrolyte removed, pit interior with substrate removed, and pit cross section, respectively. These notably show very similar features to those apparent in the sectioned samples: hemispherical bulk pit geometries filled with corrosion product, hydrogen channels and mechanical disruption of the bulk metal. The progress of the bulk pitting in expansion of the pitted area within the sample and the mechanical damage to substrate metal at the pit mouth are evident.

Figure 4-35: Micro-tomographic three dimensional reconstructions of Magnox Al80 coupon undergoing bulk pitting over period of 20 hours between left (time=T) and right (time=T+20h)

time = T   **time = T + 20h**

(i) corner projection with corrosion product and electrolyte phases removed
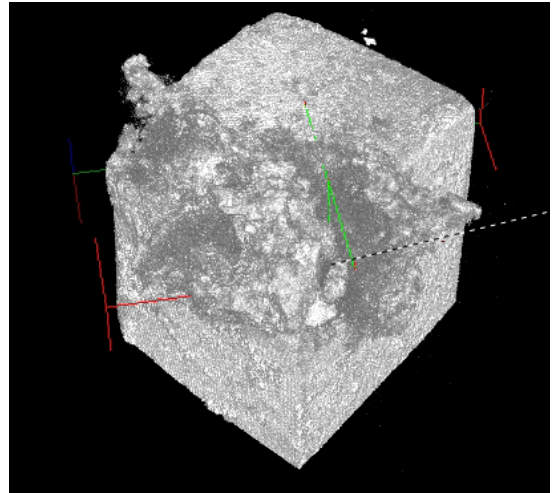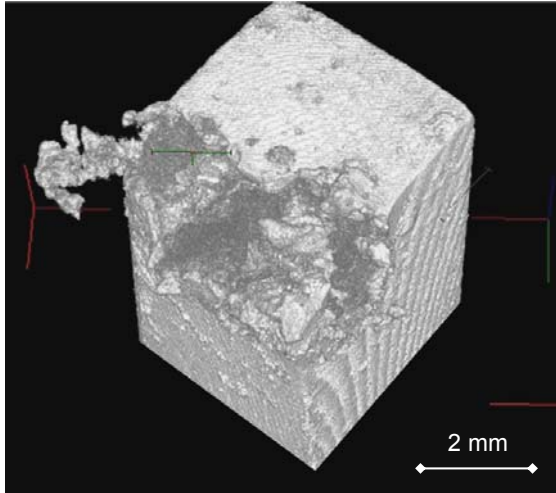
(ii) end projection with corrosion product and electrolyte phases removed
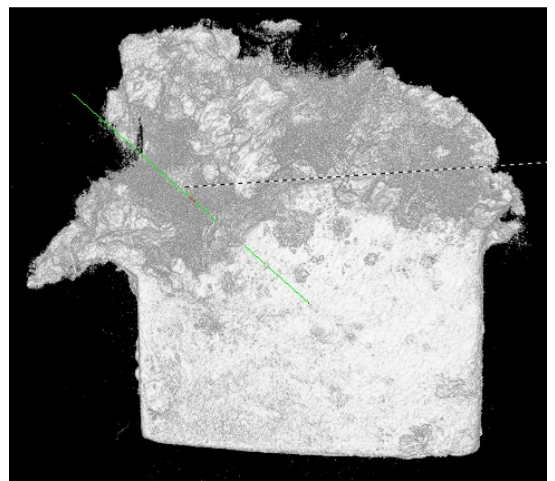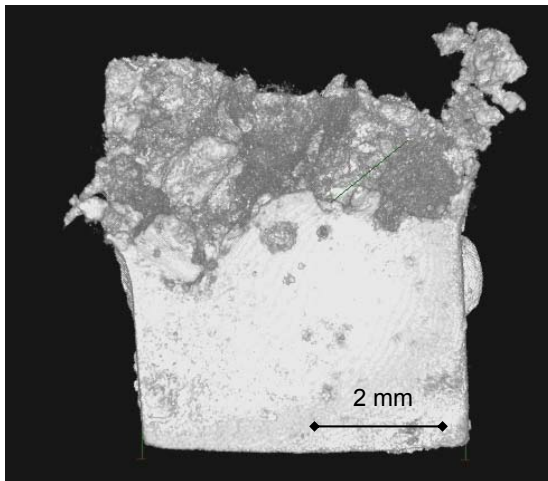
(iii) inside corner projection with substrate metal removed showing internal pit geometry
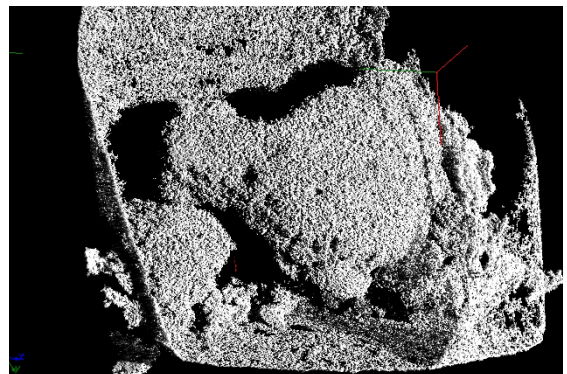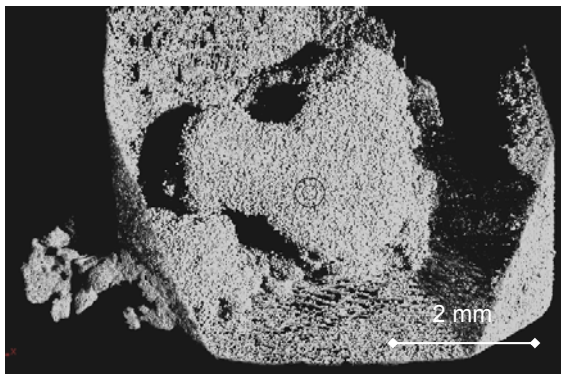
Figure 4-36: Micro-tomographic section reconstruction of Magnox Al80 coupon undergoing bulk pitting
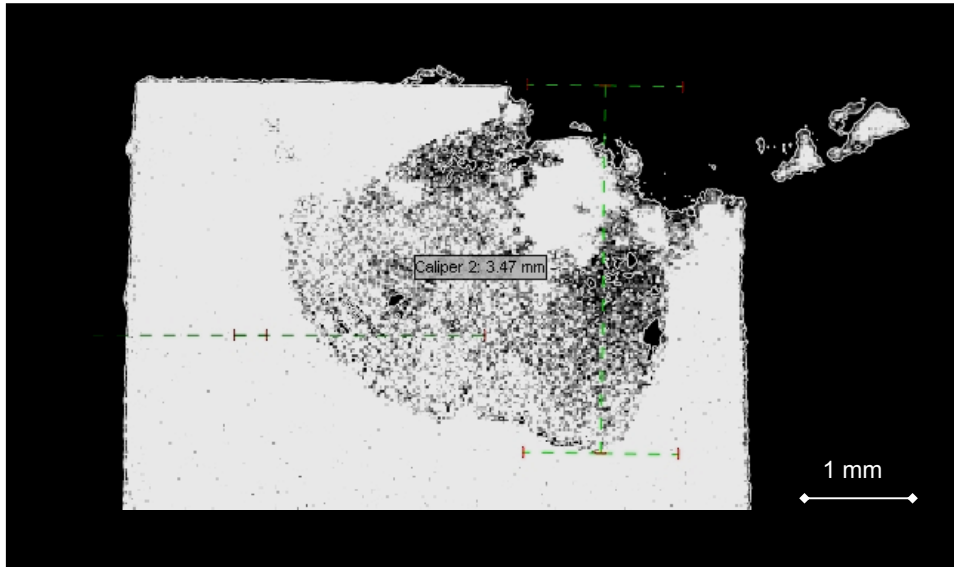
4.1.4   Fluoride Inhibition

As discussed in Section 2.3, fluoride is well known as an inhibitor of chloride induced attack on Magnox and this effect can be observed clearly in polarised tests where localised corrosion is prevented over a timescale substantially greater than that required for initiation with sodium hydroxide alone (Figure 4-37). A fundamentally different behaviour is observed during initial film formation, where the film initially grows at a faster rate but then passivates more robustly (Figure 4-38 and Figure 4-39). This is consistent with the mechanisms proposed historically in which the passive film incorporates a high proportion of fluoride (which has an insoluble magnesium salt) which subsequently forms a denser and more protective film.

Figure 4-37: Galvanostatic polarisation (I = 2 μA cm^{-2}) of Magnox samples in pH 11.7 electrolyte with 20 mg kg^{-1} chloride and with and without 1000 mg kg^{-1} fluoride
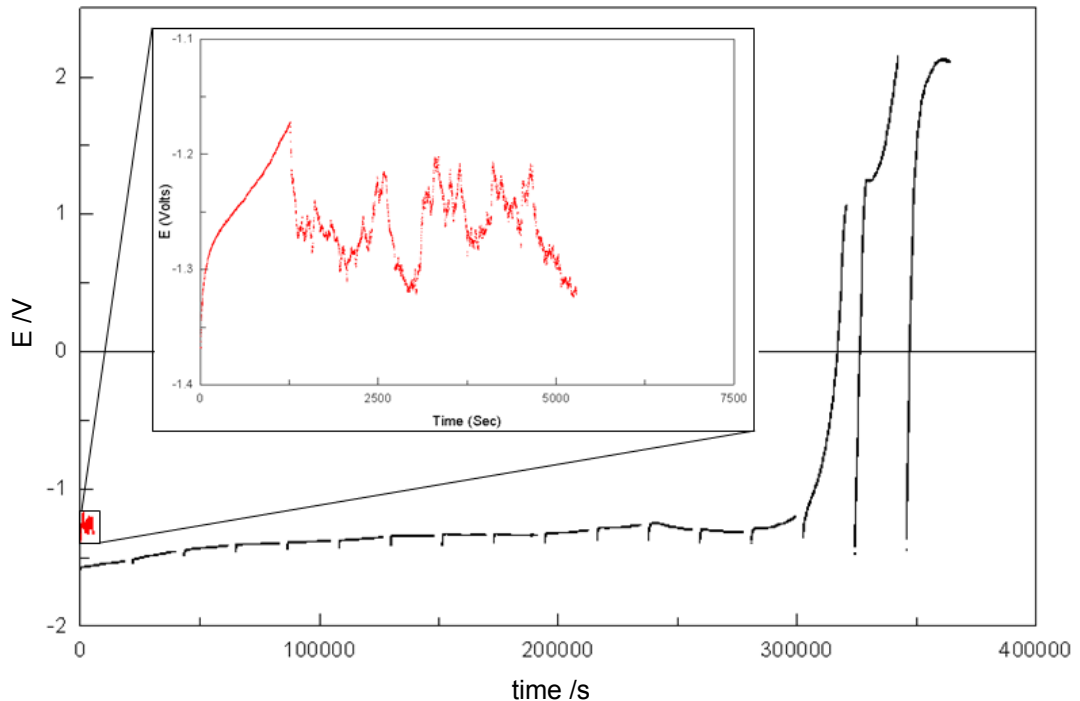
Figure 4-38: Anodic polarisation of Magnox samples in pH 11.7 electrolyte with and without 1000 mg kg⁻¹ fluoride
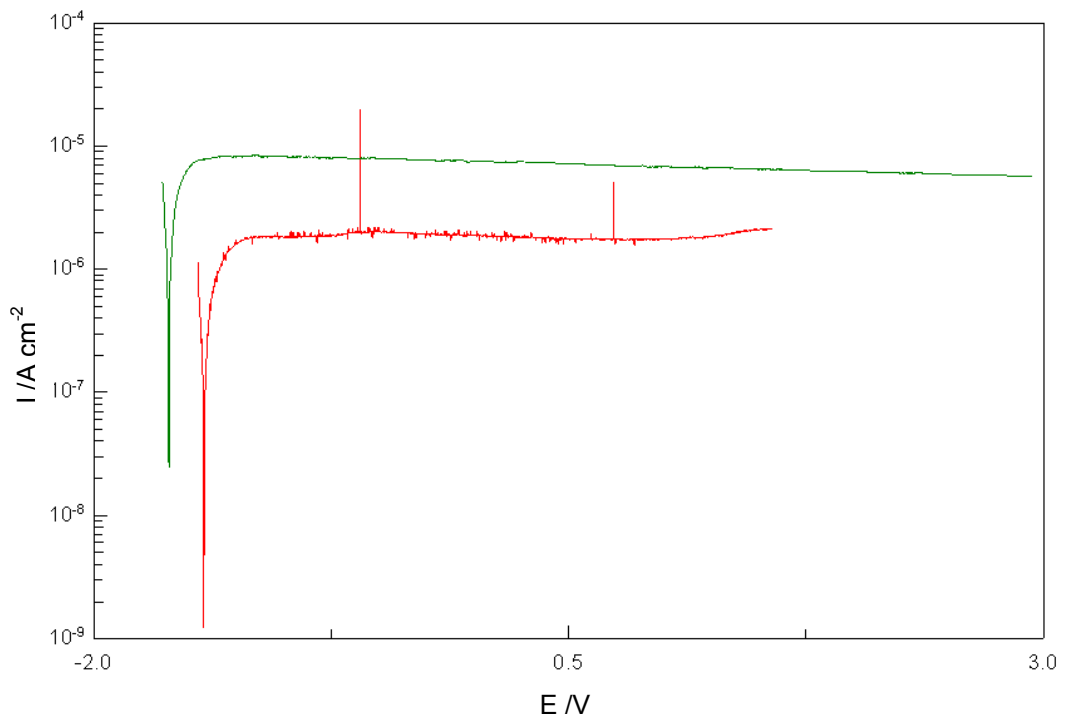
Figure 4-39: Calculated EIS corrosion rate for Magnox samples in pH 11.7 electrolyte with and without 1000 mg kg⁻¹ fluoride
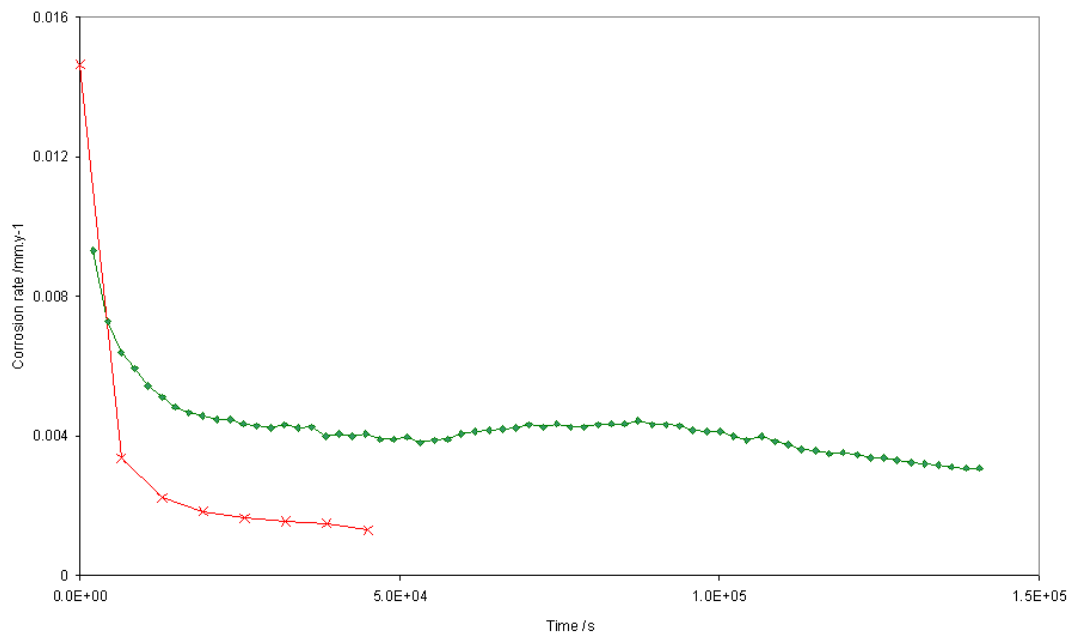
4.1.5   Summary of conventional electrochemical corrosion characterisations

From the results discussed above it is clear that the electrochemical behaviour of Magnox corrosion observed for conventional macroelectrode systems under standard techniques (potential control, galvanostatic, EN and EIS) can be interpreted consistently and with confidence.

Although the practical considerations relating to study of this material are numerous, the behaviour is repeatable and is not unduly affected by moderate variations in practical parameters which cannot be readily controlled through standard experimental measures.

There remain some more detailed aspects of electrochemical behaviour relating to the longer term passive film behaviour which have not yet been explained completely. These will be considered further in Section 4.2.

In alkaline environments, Magnox surfaces passivate readily due to formation of a protective film and corrosion rates rapidly fall to low levels.

The open circuit potential of a passivating electrode can be seen to rise from initial potentials typically more active than -1.5 V to -1.0 V and higher which has been observed to be a means of self-initiation of localised corrosion.

The presence of low levels of chloride causes the onset of localised corrosion, with the pitting potential approaching the open circuit potential as chloride concentration increases.

The presence of fluoride has the parallel influence of causing a thicker passive film to form on Magnox as well as inhibiting against chloride attack.

In most conditions, Magnox surfaces are initially affected by filiform-like corrosion, this comprising characteristic trails of coalesced microscopic pits similar to the filiform strands seen on coated surfaces. Bulk pitting may be seen to ensue with extensive formation of corrosion product which may mechanically disrupt the material.

As well as being an initiator of localised corrosion, anodic polarisation is clearly observed to increase the rate of both passive and propagating localised corrosion (surface or bulk).

The morphology of chloride induced localised corrosion has been observed over a wide length scale range with *in situ* optical microscopy, ESEM, conventional sectioning and *in situ* micro-tomography, and shows particular characteristics of salt film corrosion, such as etch pits.

4.2   Passive Film Growth Kinetics

The results of polarisation experiments show notable characteristic features, particularly during passivation. This behaviour is important to understand as it represents the passive corrosion behaviour of the material. It is also key in reconciling observation made on freely corroding material with tests employing electrochemical methods.

Some simple tests were undertaken involving repetitive polarisation of Magnox electrode surfaces.

Figure 4-40 shows a series of consecutive polarisation curves undertaken at 1.5 mV s^{-1} on a Type B Magnox electrode (Section 3.2), with Figure 4-41 showing the limiting anodic current density (at -1.25V) against cumulative charge passed. The cumulative charge shown for each sweep is the integrated charge up to the beginning of that polarisation with the exception of the initial value which is the charge passed up to -1.25V. During this series of polarisations, particular interventions were made at certain points. After the 6th sweep, the electrode was briefly removed from the solution and replaced (subsequent polarisations shown in blue on Figure 4-40), then after a further three sweeps, the solution was replaced with a freshly prepared solution of identical composition (subsequent sweeps shown in red), which was then thoroughly stirred after a further three sweeps (subsequent sweeps shown in green). The limiting current densities can clearly be seen to reduce through successive sweeps with a near-exponential reduction. This is not strongly affected by disturbance of the electrode, stirring or replacement of the solution. Some variation is in evidence at the lower limiting current densities.

Figure 4-40: Polarisation tests undertaken on Magnox in pH 12 (10 mM NaOH) following initial immersion of a ground surface (black), temporary removal of electrode from solution (blue), replacement of solution (red) and stirring of solution (green)
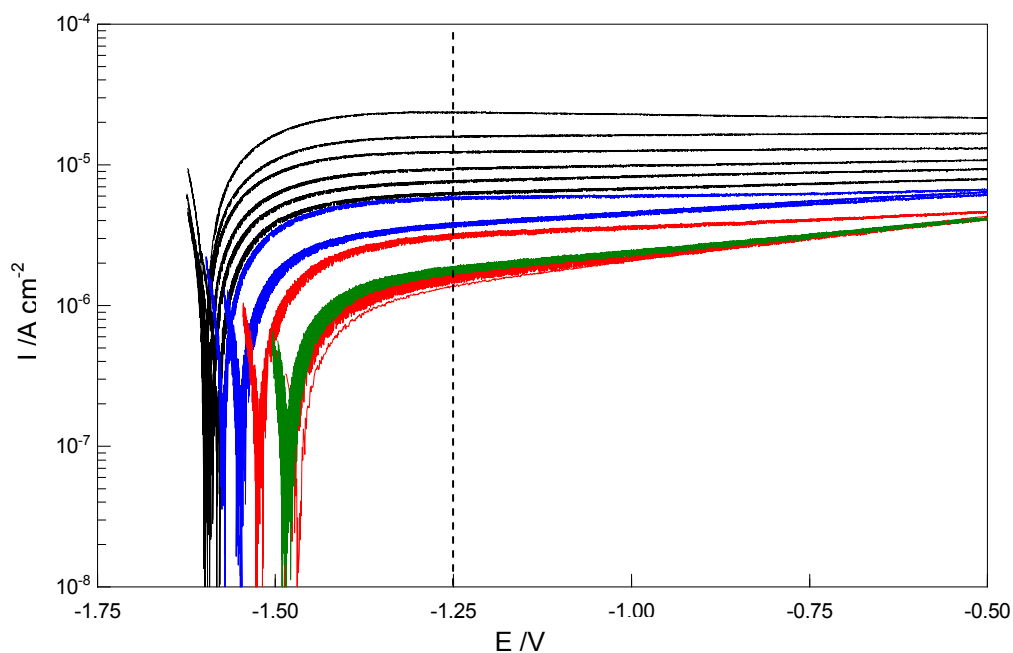
Figure 4-41: Limiting current densities at -1.25V (vs Ag/AgCl) against cumulative charge passed from polarisation tests on Magnox in pH 12 (shown in Figure 4-40)
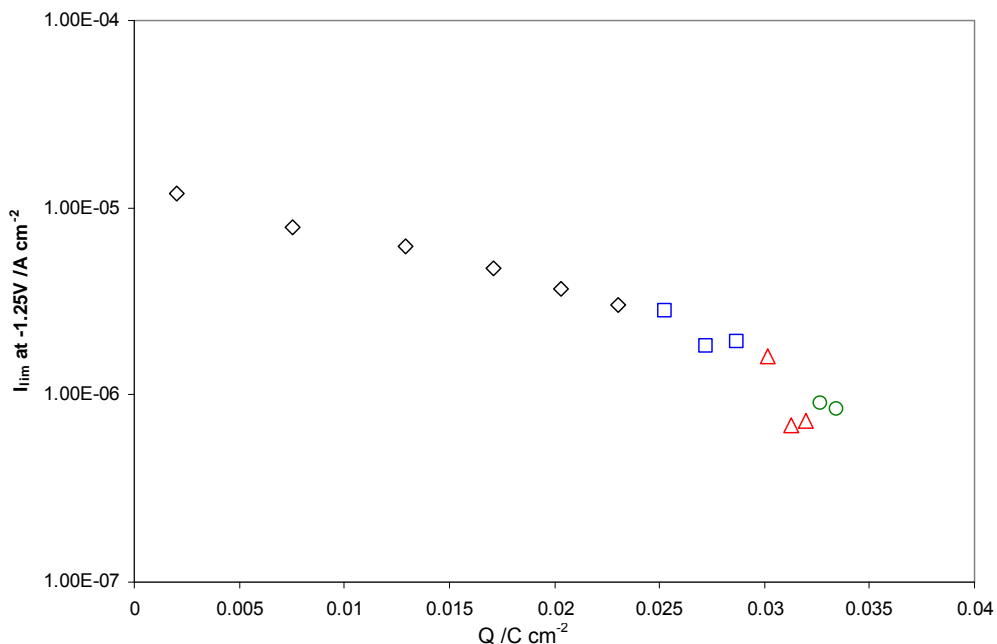
NB: Tests following initial immersion of ground surface (black diamond), temporary removal from solution (blue square), replacement of fresh solution (red diamond) and stirring of solution (green circle).

In the initial polarisation sweep, it is evident that the rate of passivation is sufficiently fast that the rate of change in current with respect to potential (di/dV) is negative. According to the film growth model, for this to occur the proportional change in the film thickness over the time period has to be larger than the proportional change in potential, that is d(E/Q)/dt must be negative (assuming for the moment that film thickness is proportional to charge). In subsequent sweeps, di/dV is positive as would be expected when the rate of change in potential is sufficiently large compared to that in charge such that it is dominant in controlling the current density.

The standard high field film growth expression has been re-written in terms of cumulative charge density as used by Gonzalez Torreira (2004):

$$i_f = A \exp\left[\frac{B\eta}{Q}\right] \qquad\qquad (4\text{-}1)$$

Where: i (A cm^{-2}) is the film growth current density, η (V) is the overpotential, Q (C cm^{-2}) is the cumulative charge denisty and A (A cm^{-2}) and B (C V^{-1} cm^{-2}) are kinetic coefficients.

These expressions are derived from the standard high field expression (Shreir, 2010) based on the assumption that the film thickness (x) may be calculated faradaically from the cumulative charge passed (Q). The assumption was justified by Gonzalez Torreira (2004) on the basis that the matrix used in the work was of sufficiently high alkalinity that film dissolution was not expected. As the polarisation results presented here cover much larger timescale and cumulative charge ranges than that in Gonzalez Torreira (2004), it must be considered that the mathematical equality which leads to the high field expression from the general field film formation expression (Shreir, 2010) may not be valid, so it is prudent to employ the full form of the model. This can be similarly written in terms of the same coefficients which brings the practical benefit of working in experimental parameters as well as reducing the number of assumptions which must be made with regard to the passive film properties.

$$i_f = 2A \sinh\left[\frac{B\eta}{Q}\right] \qquad\qquad (4\text{-}2)$$

We can also write the low-field expression which is helpful for comparison at limits of large cumulative charge:

$$i_f = 2A\frac{B\eta}{Q} \qquad\qquad (4\text{-}3)$$

By numerically evaluating the appropriate film growth expression as a function of time it is therefore possible to predict the measured current density (i_{meas}) on the basis of an applied polarisation (η =f(t) which need not be a well-behaved function) and the simple relationship for charge:

$$\frac{dQ}{dt} = i \qquad\qquad (4\text{-}4)$$

Where t (s) is the time from beginning of the polarisation.

As i_f is very large for small film thicknesses, a value of Q(0), the charge at t=0, of around 1×10^{-4} C cm^{-2} is used, the exact value being selected to be large enough to avoid asymptotic behaviour at the initial potential, but small enough so as not to be determinant of the long-term behaviour of the corrosion current.

Figure 4-42 shows i_f, the current density predicted by the film growth expression, evaluated according to the potential in the standard polarisation test shown in Figure 4-40 and with the results of the first sweep shown for comparison. The potential region considered in the evaluation is that above 100 mV positive of OCP. The numerical evaluation has employed two means of calculating the cumulative charge; the more correct coupled form uses i_f as the rate of increase, whilst the other uses the measured current density (i_{meas}) which makes this more forgiving of errors in the evaluation as the expression is not a true partial differential. In this instance, the initial behaviour of i_f (calculated on either basis) is fairly strongly dependent on Q(0) due to the relatively high rate of change in potential. What is evident, however, is that both expressions substantially underpredict the current. This is particularly true for the expression using the measured cumulative charge (as this is based on the much higher value of i_{meas}) which is more than an order of magnitude less than would be predicted by the measured current. It would be possible to vary the kinetic parameters in the film growth expression, however, this would be at odds with the outcomes of previous work. Considering that dQ/dt =i_f and dη/dt = c (where η(0) and the constant c are positive),

it can also be shown analytically (despite the problematic integration of hyperbolic sine functions) that the rate of change observed in current density across the overpotential range is not consistent with a positive value of B in the film growth expression. The drop in i_f is only slightly less from n=0.6 to 0.9 V than it is from n=0.3 to 0.6 V, which over a

period of 200 s with a sweep rate of 0.0015 V s^{-1} is not consistent with any value of A or Q(0) with a positive exponent term (and hence a positive value of B) unless $i_f \ll i_{meas}$.

Figure 4-42: Predicted corrosion current from high field model compared to results from potentiodynamic polarisation of Magnox
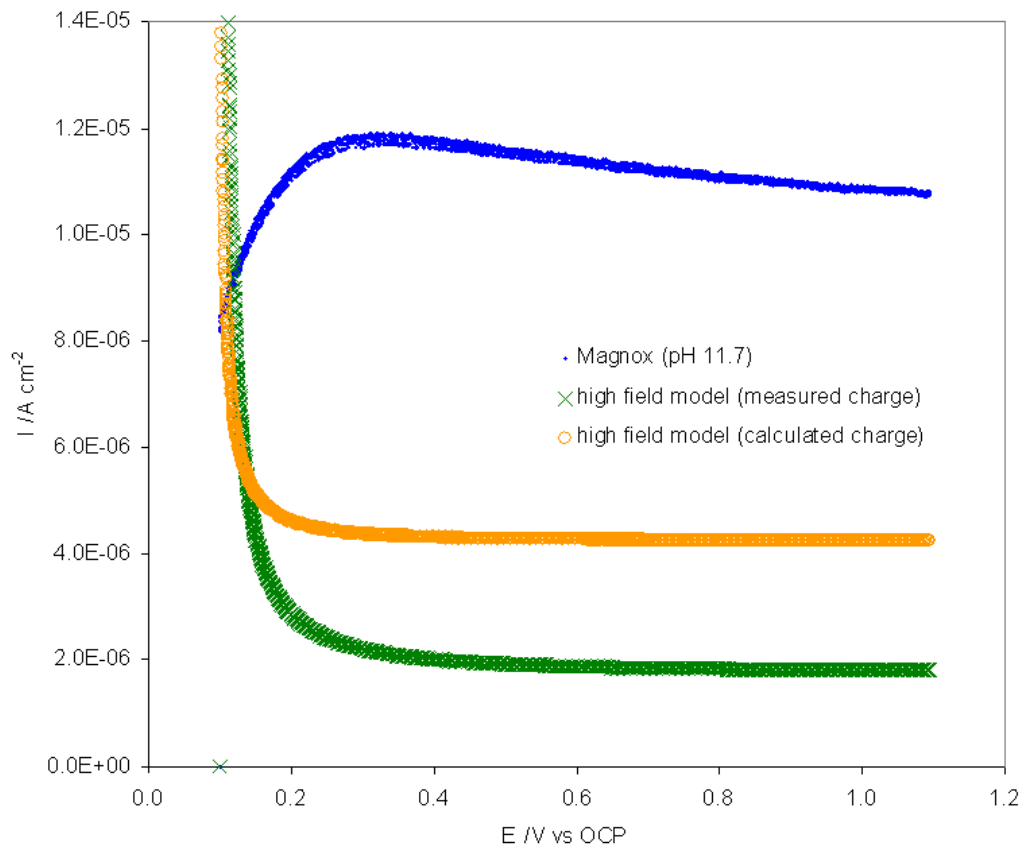
Figure 4-43: Anodic polarisation of Magnox in pH 11.7 (black, 5mM NaOH) and 13 (blue, 100 mM) electrolytes
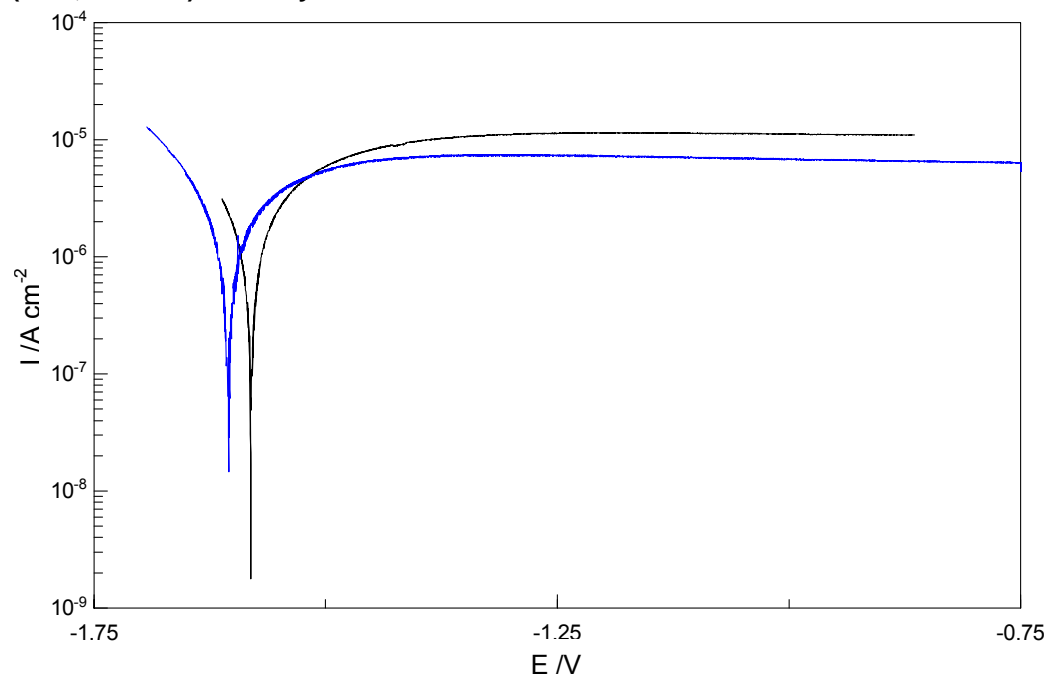
The possibility that the current density is elevated due to dissolution of the passive film and mass transport away from the surface is discussed further below, however, an identical sweep using a matrix of 100 mM NaOH (pH 13) is also shown in Figure 4-43 which shows that this effect is not sufficient to account for the large difference. Therefore, the most reasonable explanation which can reconcile the electrochemical behaviour is that the passive film is substantially thinner and increases in thickness at a much lower rate than would be expected from the measured current density.

It is evident that by the final four sweeps (Figure 4-40), the behaviour of current with respect to potential is becoming close to reversible, i.e., the electrochemical characteristics are not changing substantially between successive sweeps. It is clear that at this point di/dV has become positive and the two variables are related by a near exponential expression.

Figure 4-44 shows one of these latter sweeps with the current density predicted on the basis of general film growth expressions fitted to the curve from potentials above 150 mV positive of OCP. It is clear that the exponential form of the expression at the high field limit is a very close fit to the current behaviour whereas the linear low field limit does not represent the behaviour well. It is notable that although the total charge passed at the start of this test was greater than 0.03 C cm^{-2}, the value for Q derived from the high field fitting, (using values from Gonzalez Torreira, 2004 of 1x10^{-6} A cm^{-2} and 4x10^{-3} C V^{-1} cm^{-2} for A and B respectively), is 1.3 x 10^{-3} C cm^{-2}, in other words the effective film thickness is less than 10% of that predicted from the integrated current.

Figure 4-44: Polarisation of Magnox in pH 12 electrolyte with fitted general film growth expression
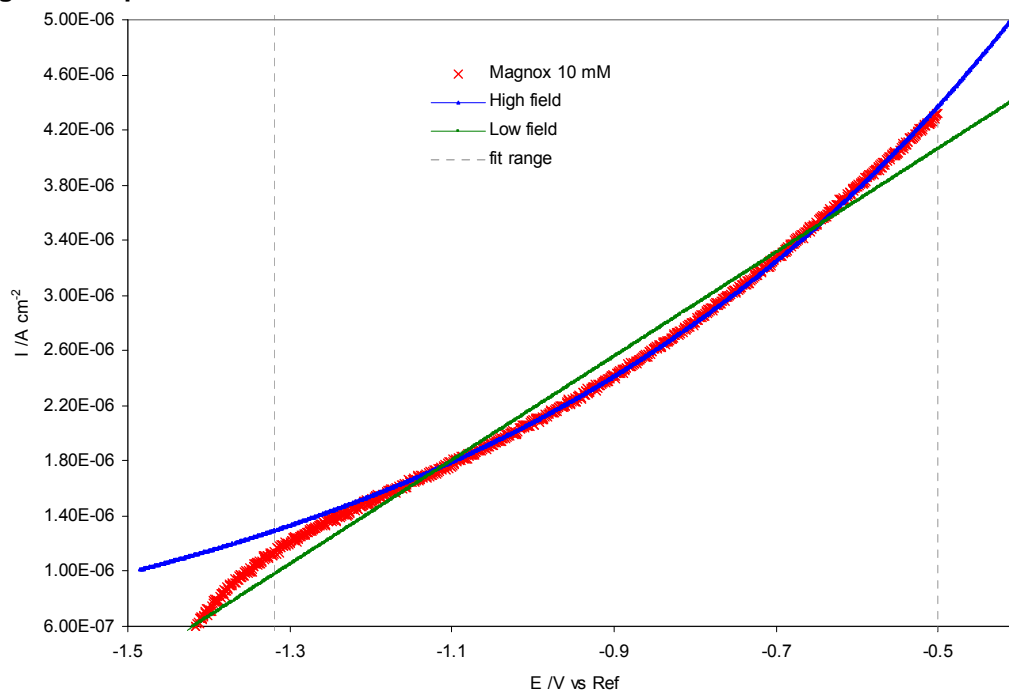
The gradient of the fitted low field approximation also suggests a similar value for Q of 1.3×10^{-3} C cm^{-2}. It is also noted that the general form of the low field model used here also describes migrative flux where x is invariant. Two straightforward explanations for the very low apparent film thickness could be that (i) extensive film dissolution has taken place with the majority of the oxide/hydroxide layer having been transported away from the electrode surface or (ii) the inner barrier film thickness is limited due to hydration at the solution interface leading to formation of a thick outer film, whilst the polarised film growth behaviour is still governed by the thin inner film under high field conditions.

The second of these two possibilities is consistent with previous observations and investigations which showed that the main surface film is thick hydroxide, with an inner "barrier" oxide controlling film growth rate. Gonzalez Torreira (2004) measured total film thicknesses (inner plus outer) of 4 nm for an etched surface (e.g., air-formed film alone) growing to around 10 nm after ~15 s polarisation although it was proposed that this was likely to be overestimated due to surface roughness. As discussed in Section 3.5, previous workers have characterised the outer layer as a porous magnesium hydroxide film of micron-scale thickness and pointed to the likely presence of a thin inner oxide barrier layer although lacked analytical resolution to confirm this or make direct thickness measurements. Investigations employing ion beam analysis and ellipsometry asserted that the maximum thickness of a barrier layer was 100 nm (Bradford et al., 1976) and 5 nm (Greef et al., 1986), respectively. From the parameters derived by Gonzalez Torreira (2004) and the fitted high field expression in Figure 4-44, the limiting inner oxide film thickness calculated here is around 2.5 nm.

There are a number of further bases for proposing that the dissolution and transport of the majority of corrosion product away from the electrode surface has not occurred.

A simple calculation of magnesium ion solubility at pH 12 on the basis of solubility product for magnesium hydroxide (7×10^{-12} mol^3 dm^{-9}) suggests that the saturation concentration should be around 7×10^{-8} mol dm^{-3}. This is around an order of magnitude below the soluble concentration which would have arisen if it were assumed that the difference in apparent film thickness at the end of the set of polarisations was due to dissolution and mixing in the bulk solution (one litre volume). The local solubility of magnesium could be elevated if a significant OH$^-$ concentration gradient existed at the surface. A simple diffusion/migration calculation was carried out (see Section 3.4) to estimate the extent of this effect for domains of 1×10^{-3} m dimension. This used typical ionic flux calculated from the measured corrosion current (Figure 4-45) and nominal bulk solution concentrations. The calculated hydroxide profile close to the electrode surface is shown in Figure 4-46 and suggests that for the rates of reaction observed, the

process is not limited by aqueous diffusion and a significant concentration gradient does not exist, which in turn suggests that the magnesium saturation concentration is not substantially elevated. On the basis of a magnesium solubility an order of magnitude above the value indicated by solubility product calculations, a further calculation was undertaken to estimate the likely flux rate arising from aqueous diffusion due to a constant concentration at the electrode surface. This conservative calculation indicated that the Mg^{2+} diffusive flux was of the order of $2x10^{-9}$ mol m^{-2} s^{-1} for timescales and diffusion lengths likely to be relevant (see Figure 4-47) which is around 2 orders of magnitude below the average rate required to reduce the film thickness by this mechanism. The calculations outlined above are relatively crude but provide an indication that these processes do not account for the large discrepancy seen in film thickness.

Figure 4-45: Equivalent corrosion rate interfacial Mg^{2+} flux used in finite element multiphysics simulation of pH at electrode surface
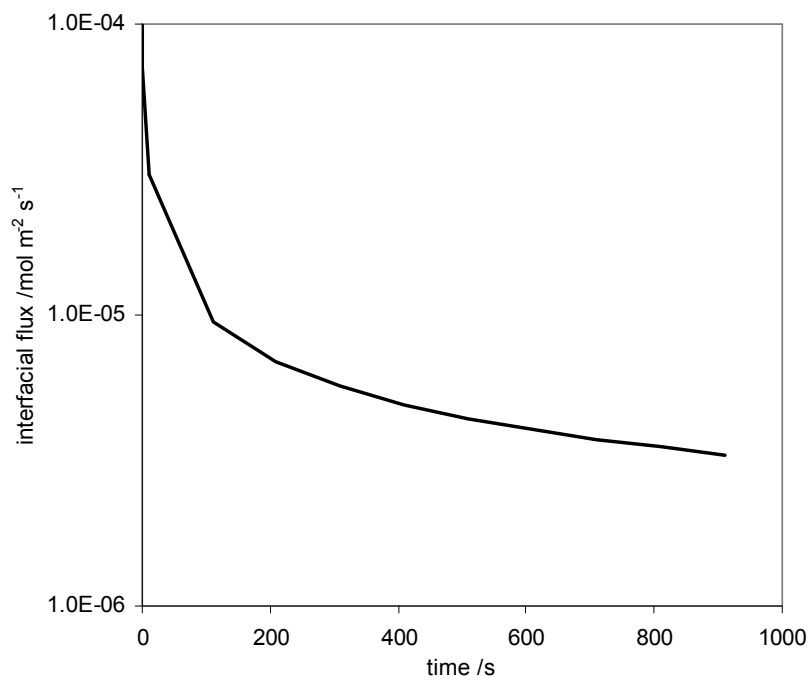
Figure 4-46: Results from finite element multiphysics simulation of pH at electrode surface
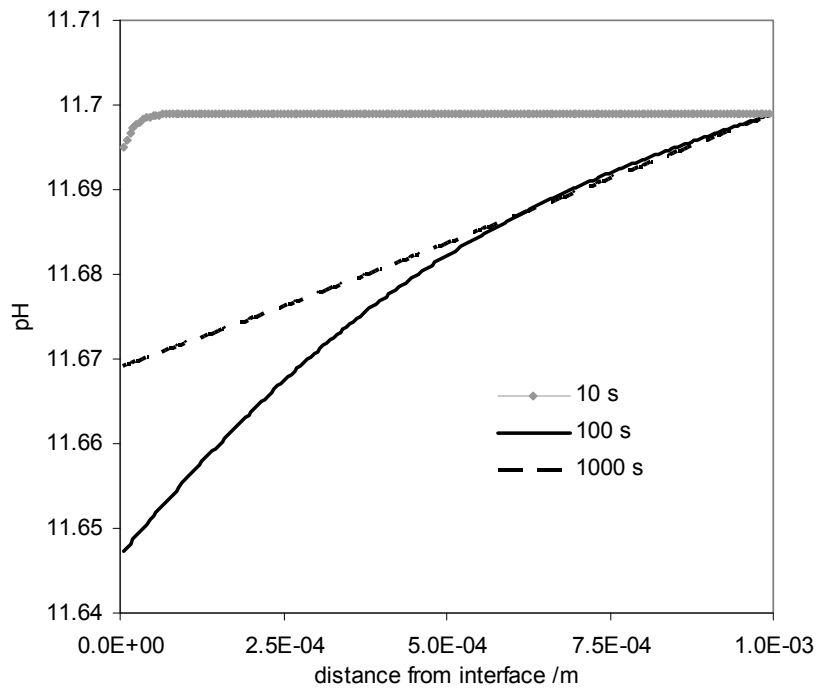
Figure 4-47: Results from finite element multiphysics simulation of magnesium diffusion at electrode surface
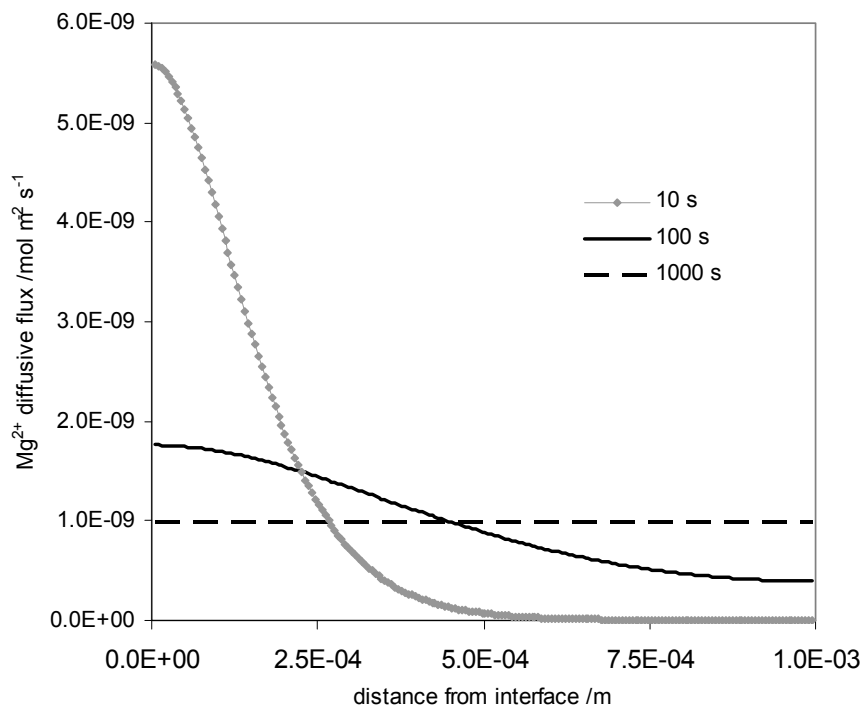
The rate of magnesium ion transport could be enhanced above those notionally expected by migration, and also by heterogeneous transport following precipitation in local areas of supersaturation. Nonetheless, if a substantial rate of transport were being

supported away from the surface then larger variations in current might be expected. Large changes could also be expected when the solution began to reach saturation. In actuality, what is observed is near-linear behaviour close to OCP and very close to high field behaviour with overpotentials above ~150 mV. For the corrosion current to be as steady as observed over relatively long periods of time, the dissolution rate would need to be closely related to the film growth rate which is unlikely in a mass transport mechanism, but much more likely in a system involving coupled inner/outer layer growth.

The most definitive evidence against a very high rate of mass transport of magnesium ions away from the electrode surface is from comparison of solution stirring effects at much higher pH, where the solubility will be minimal. Figure 4-43 shows anodic polarisations (at a higher rate of 2 mV s^{-1}) for Magnox electrodes in 5 mM and 100 mM NaOH. At this higher alkalinity, the solubility of magnesium is negligible and any transport rates will similarly be lower. Gonzalez Torreira (2004) showed that mass transport has effectively no influence on Magnox corrosion at this pH and the results in Figure 4-43 also indicate that although the corrosion current is lower for the high pH solution, and that the dI/dV becomes negative more quickly, the difference is not large and the characteristic behaviour is the same. If the film formation were strongly influenced by film dissolution and transport of magnesium ions under the low-convection conditions of these tests, then much larger differences in behaviour would be in evidence. It is noted that in conditions where mass transport rates were enhanced, for example due to stirring, thermally induced convection or non-linear diffusion, then the behaviour might diverge more substantially (see Section 6.1).

Figure 4-48 shows data from four potentiostatic polarisations which were originally undertaken as part of pit initiation investigation studies but have been cropped to show only the pre-initiation part of the data. The experimental set up is slightly different in these tests, including use of a different electrode type, as discussed in Section 3.2. Although low levels of chloride were present in the electrolytes, the current density does not show any apparent influence as a result in this part of the polarisation. From these data, the effective charge has been calculated as a function of time according to the film growth expression.

$$Q_{eff} = \frac{\eta B}{\operatorname{arcsinh}\left[\dfrac{i_f}{2A}\right]} \qquad (4\text{-}5)$$

In other words, the parameter Q_{eff} is the equivalent film thickness which would give the current density for the polarisation at that time accepting all the assumptions of this model.

Some interesting behaviour can be observed in Q_{eff} and this is plotted relative to Q_{meas}, the cumulative measured charge (derived from i_{meas}), in Figure 4-49. Also, the ratio of Q_{eff}/Q_{meas} is shown in Figure 4-50. This suggests two points; at the start of the polarisations, there is a film of tangible thickness already present on the electrode surface and the inner film thickness is lower than would be predicted from the cumulative measured charge. This is a similar observation to that based on the potentiodynamic test above, despite differences in the magnitude of the ratio which are clearly dynamic and will be affected by differences in the point from which the cumulative charge integration is started.

Figure 4-48: Corrosion current in potentiostatic polarisation of Magnox in pH 11.7 electrolyte
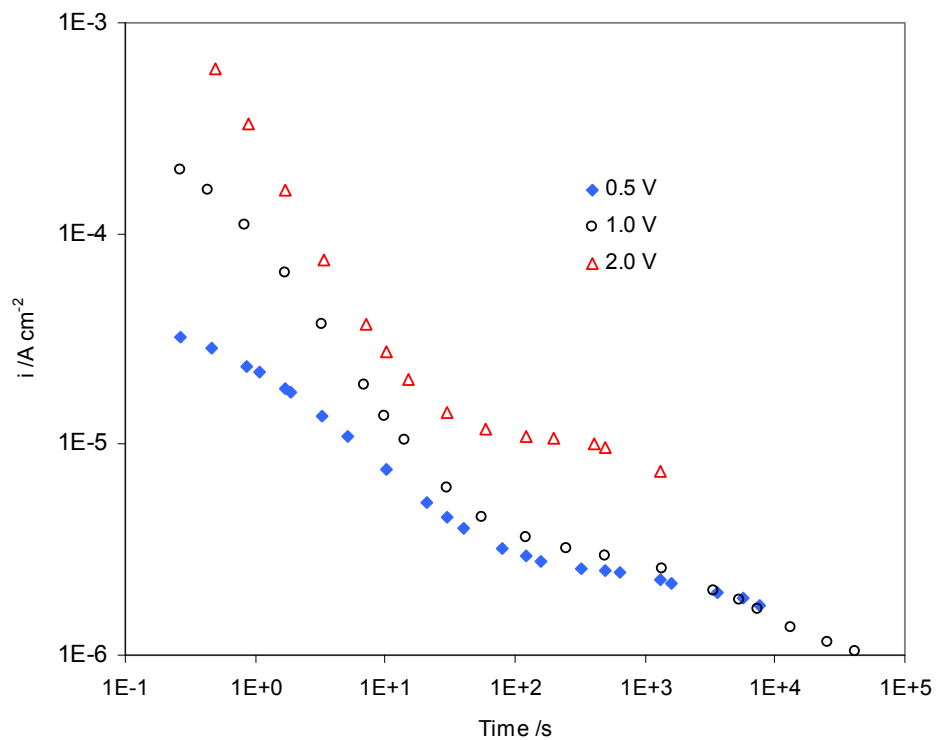
Figure 4-49: Calculated effective cumulative charge against cumulative measured charge for potentionstatic polarisations of Magnox
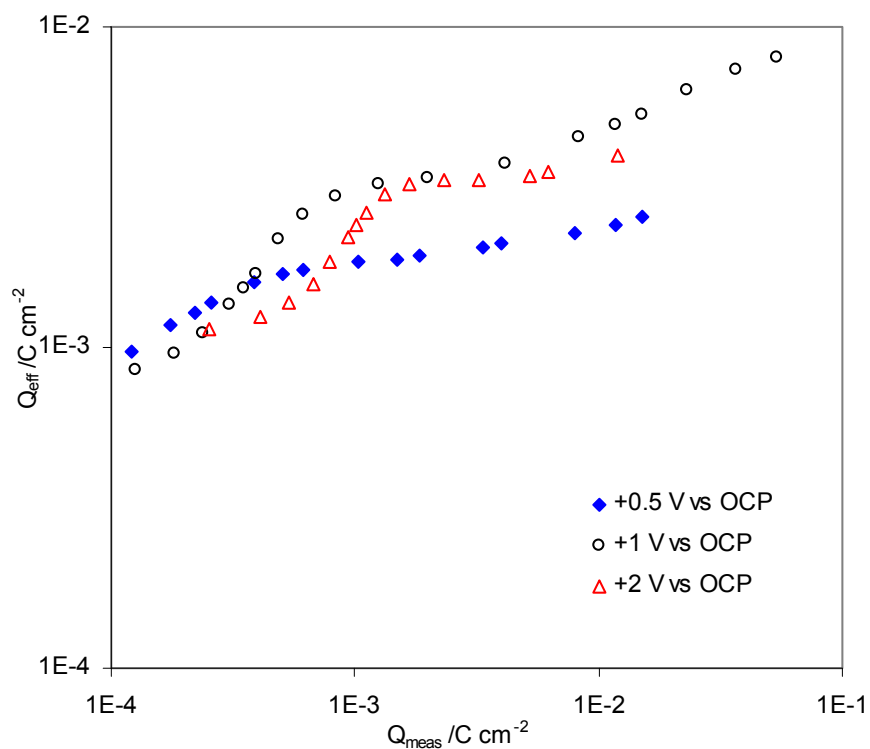
Figure 4-50: Ratio of calculated effective charge to measured charge against measured charge for potentiostatic polarisations of Magnox
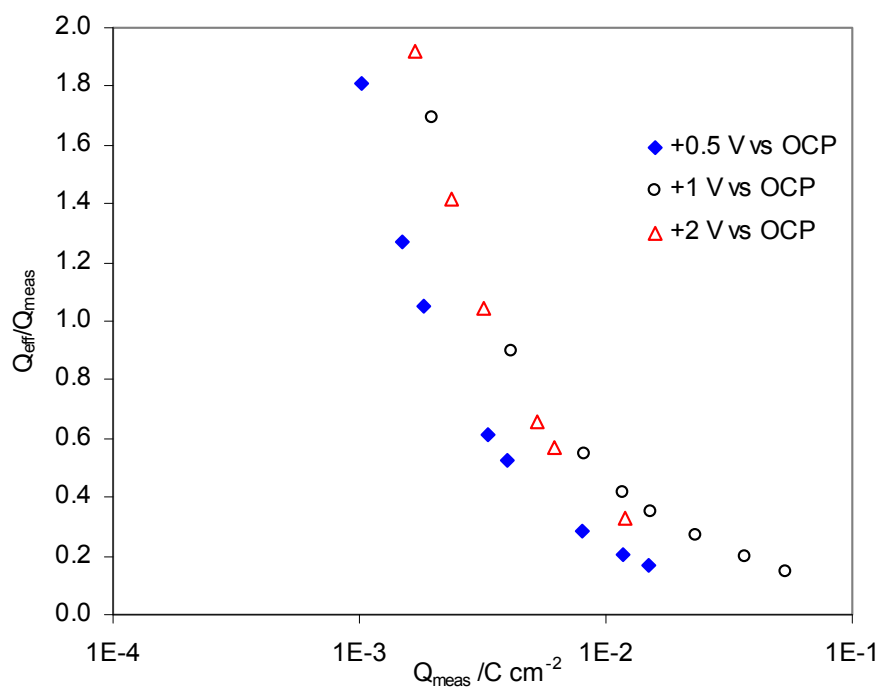
Figure 4-51: Comparison of measured current density and calculated effective current density (from full field model) for potentiostatic polarisation of Magnox
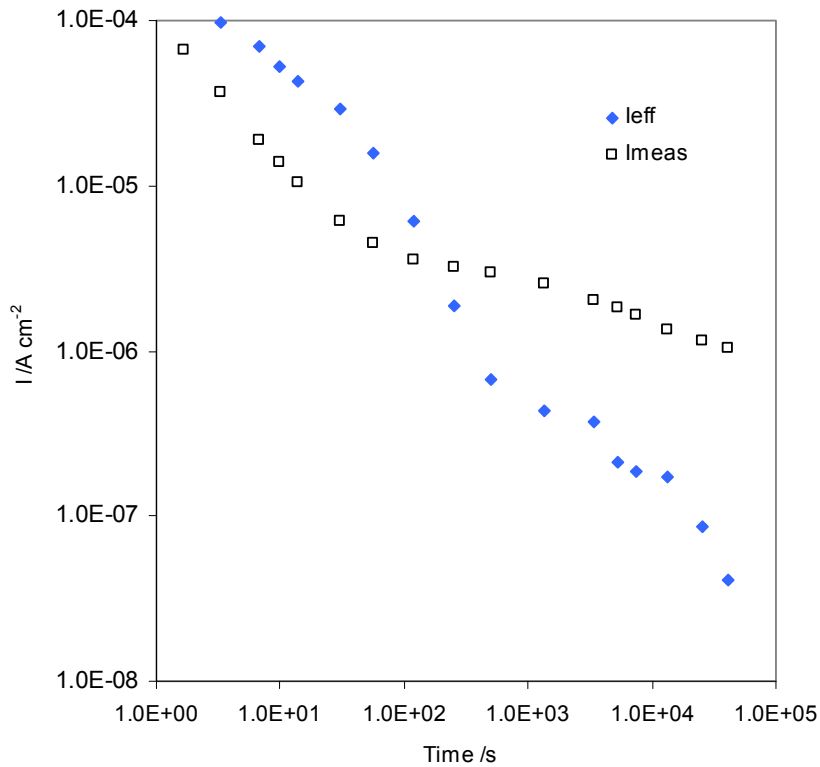
What is conspicuous is a clear trend in the ratio of effective film thickness to measured film thickness is apparent. This is an important observation as it shows that in the initial phase of a polarisation (following first immersion), the assumption that the film thickness parameter in the full field film growth expression is proportional to the cumulative charge density is valid, as illustrated with effective and measured current densities in Figure 4-51. This also supports the use of values for the kinetic parameters A and B close to those reported by Gonzalez Torreira (2004). The initial above-unity value of the charge ratio is proposed to relate to the presence of a pre-existing film on the electrode surface which was accounted for carefully by Gonzalez Torreira (2004) but has not been controlled here. The exponential decrease in the charge ratio requires some further investigation. It is notable that at high Q_{meas}, the value of Q_{eff} tends to a similar upper value and the behaviour in the Q_{eff}/Q_{meas} ratio is similar across the potentiodynamic polarisations.

In considering the uncertainties in these calculations, it is apparent that the error arising from variability in measurement is likely to be small, whereas the variability between two equivalent tests is likely to be larger. The broad magnitude of this variability has considered in Section 4.1.1 and shown to be modest, although the impact of this on derivation of kinetic parameters is more difficult to ascertain. The consideration of

several sets of data from differing experimental set-ups not only provides an indication of the test-to-test variability but also minimises the impact of a specific technique-related error. The reliability of the data with respect to fitting of the results is considered further later in this section.

The results of a dynamic polarisation in pH 13 electrolyte (100mM NaOH) are shown in Figure 4-52 with calculated effective cumulative charge. The form and limiting value of this parameter is similar to those above and reinforce the postulation that the film loss rate is not simply a product of solution mass transport as the solubility of magnesium ions in this matrix is negligible as shown by Gonzalez Torreira (2004) (Figure 4-53).

Figure 4-52: Corrosion current, cumulative measured charge and calculated effective charge for potentiodynamic polarisation of Magnox in pH 13 electrolyte
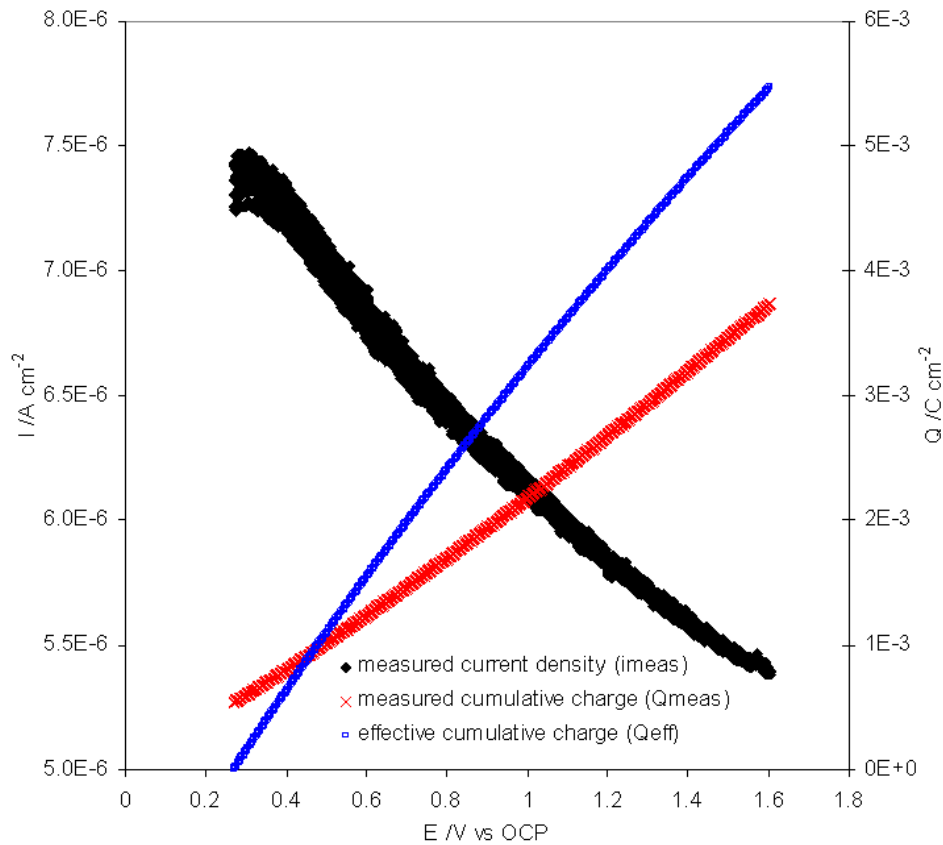
Figure 4-53: Effect of mass transport on corrosion current of potentiostatically polarised pure magnesium at pH 12 and pH 13 (reproduced from Gonzalez Torreira, 2004)
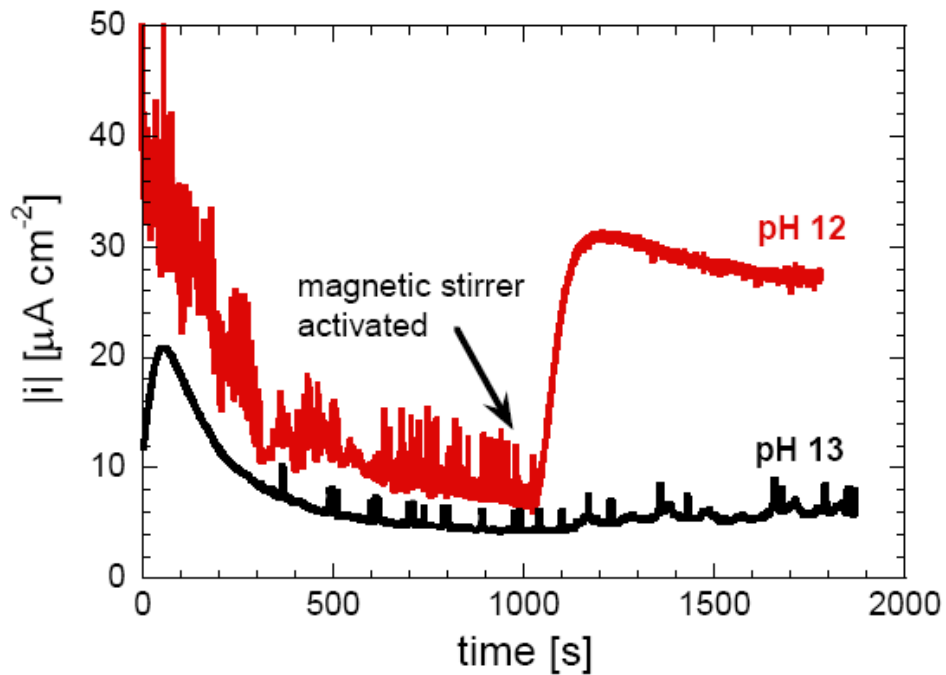
A similar fitting can be performed using the results of galvanostatic tests. The measured potential against time for a series of tests at 5×10^{-6} A cm^{-2} is shown in Figure 4-54, covering the initial section of increasing potential. After this initial increase the potential levels off, signifying the oxygen evolution potential and from this point, this reaction will account for a large proportion of the measured current density so the assumption of film growth being proportional to current density is not valid. On this basis, the calculated effective cumulative charge is shown against cumulative charge (below oxygen generation potential) in Figure 4-55.

This shows an interesting feature, that in between periods of polarisation, the effective film thickness falls back to a much lower value, but that with each successive test, the film grows to the higher value at a slightly faster rate.

The full set of data from the potentiodynamic polarisations in Figure 4-40 covering the anodic regions more positive than 150 mV from OCP is shown in Figure 4-56 as a function of total time (including intervening periods of OCP monitoring). This shows clearly the same longer-term trend evident in Figure 4-41 of a steady decrease in current density, but at the same time shows the increase in current density within each sweep as a result of increasing polarisation (with the exception of the initial sweep). The change of sign and subsequent incremental increase in di/dV is also evident.

Figure 4-54: Applied potential for galvanostatic polarisations (I = 5 μA cm^{-2}) of Magnox (successive scans) in pH 11.7 electrolyte
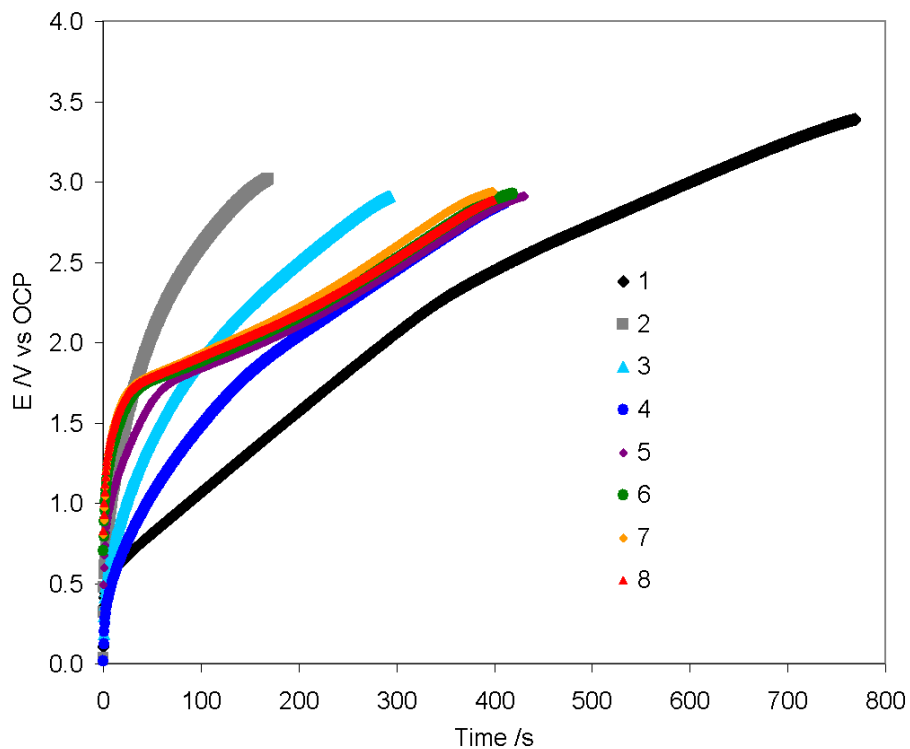
Figure 4-55: Calculated effective cumulative charge against cumulative measured charge for successive galvanostatic polarisations (I = 5 μA cm^{-2}) of Magnox
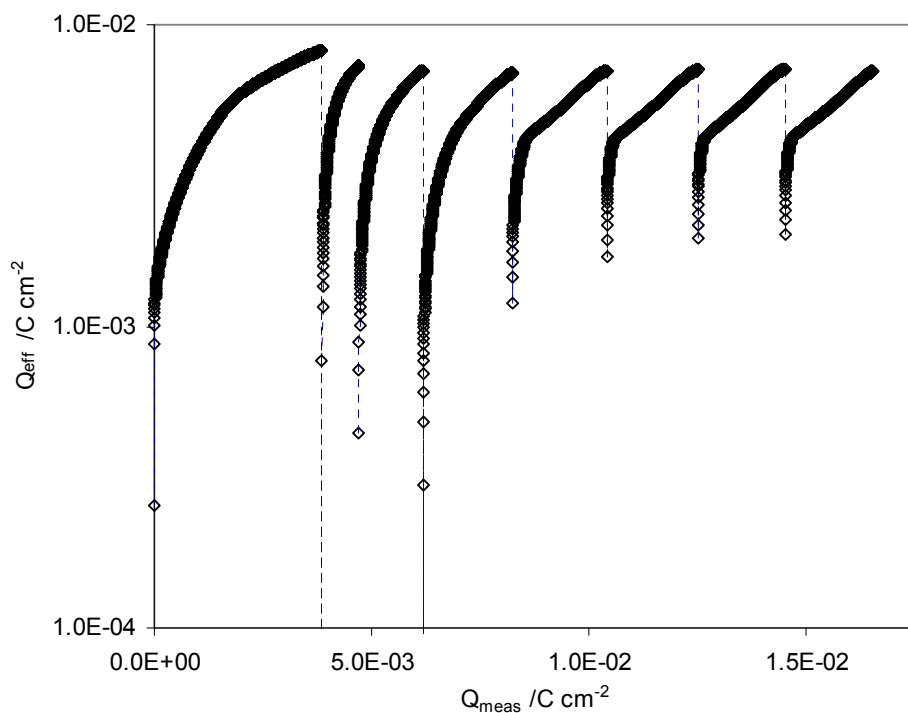
Figure 4-56: Corrosion current for repetitive potentiodynamic polarisations of Magnox in pH 12 electrolyte
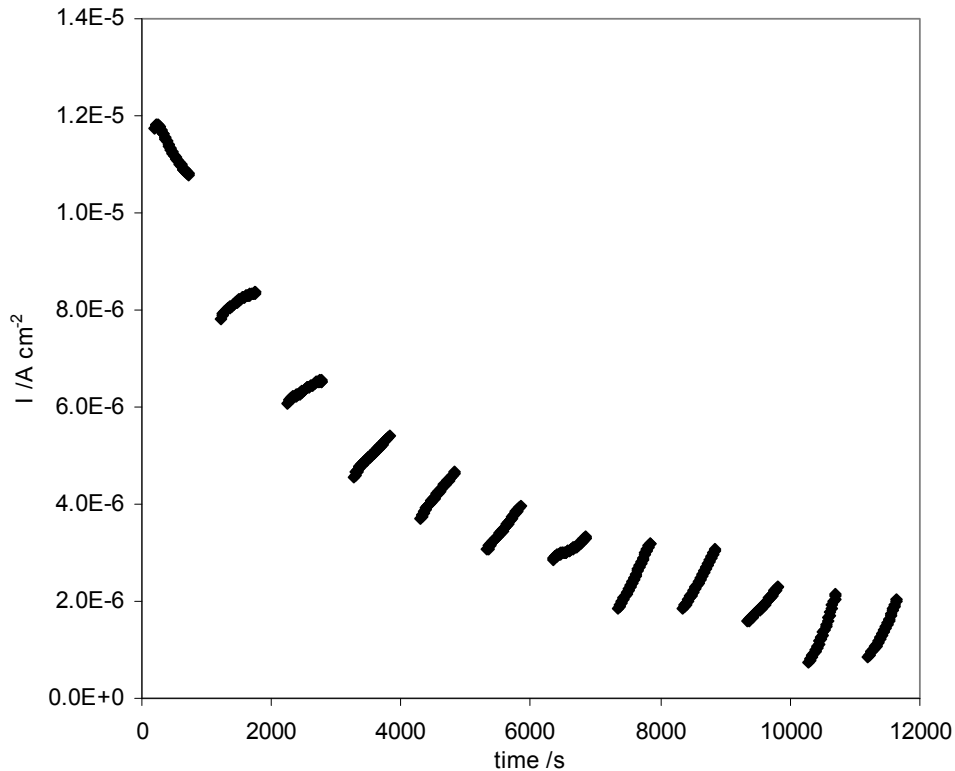
The value of the effective cumulative charge (which is proportional to film thickness) corresponding to the electrochemical parameters in each test according to the film growth expression (full field form), along with the measured cumulative charge, is shown in Figure 4-57. This behaviour is shown in terms of equivalent film thickness in Figure 4-58.

These graphs represents an interpretation of the current data density on the basis of a relatively simple mechanism, however, the form of the results generated in this way is remarkable. Two parallel and complementary passivation mechanisms are clearly inferred. In the short timescale individual polarisation tests, there appears to be a rapid increase in the passive film thickness and this is broadly consistent with the trend seen in the potentiostatic tests (Figure 4-48). However, between the end of each test and the start of the next, the thickness rapidly drops back to near, but consistently slightly above, the previous initial value (with only a single exception) in the same manner as the galvanostatic tests (Figure 4-55). Whilst the large changes in film thickness and extent of overlap of these ranges are conspicuous in comparison to the change in anodic current density seen in Figure 4-56, this can be seen as a reflection of the strength of the film thickness variable in the film growth rate expression at these small thicknesses, when the current assumption that the electric field effectively only has a gradient over the thin inner layer. It is noted that the calculated effective charge density

according to the high field expression becomes asymptotic in certain regions (Figure 4-59) which supports use of the full field form of the expression as this is well-behaved for larger values of Q. The significance of this is that at the larger film thicknesses observed in the latter polarisations within this series of tests, the film is of a dimension which exceeds the assumptions of the high field model. The ratio of effective to measured charge density for this series of potentiodynamic tests is shown for comparison in Figure 4-60.

Figure 4-57: Calculated effective cumulative charge and cumulative measured charge for repetitive potentiodynamic polarisations of Magnox
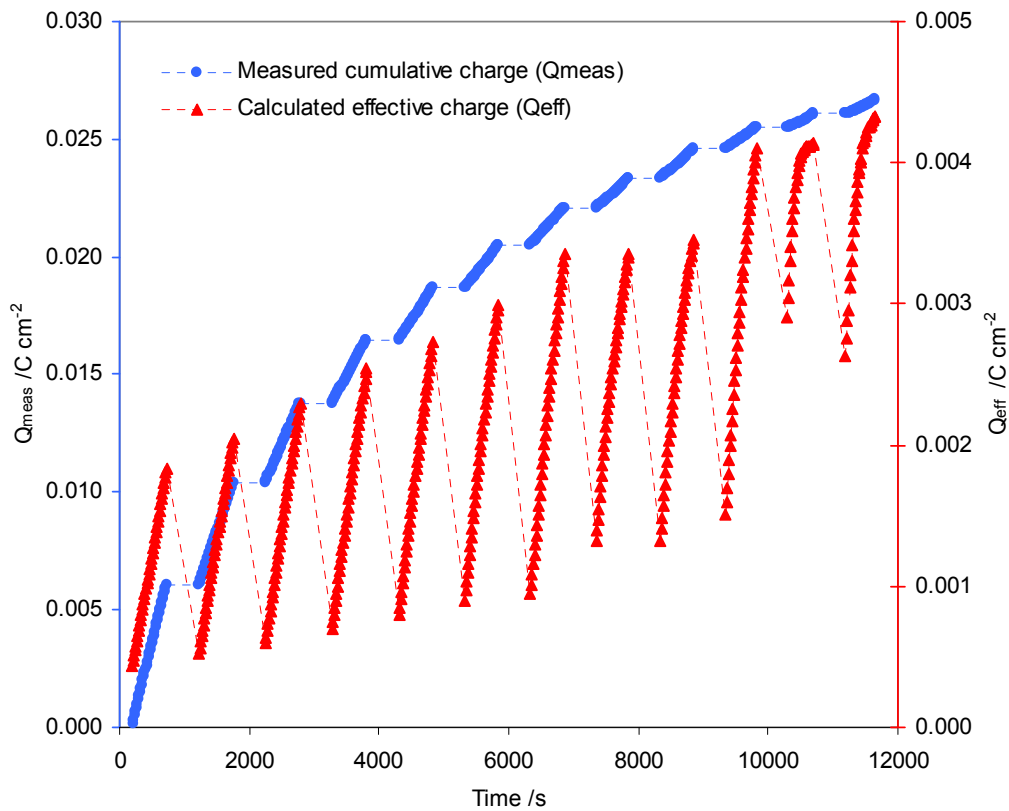
Figure 4-58: Equivalent film thickness for repetitive potentiodynamic polarisations of Magnox
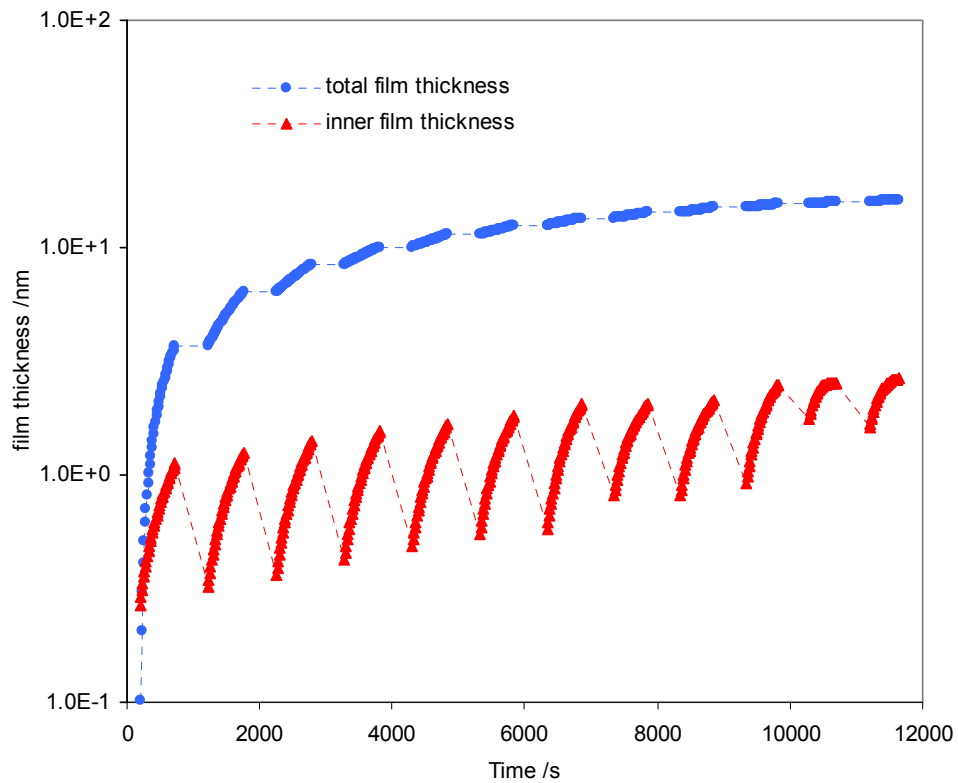
Figure 4-59: Calculated effective cumulative charge against cumulative measured charge for repetitive potentiodynamic polarisations of Magnox
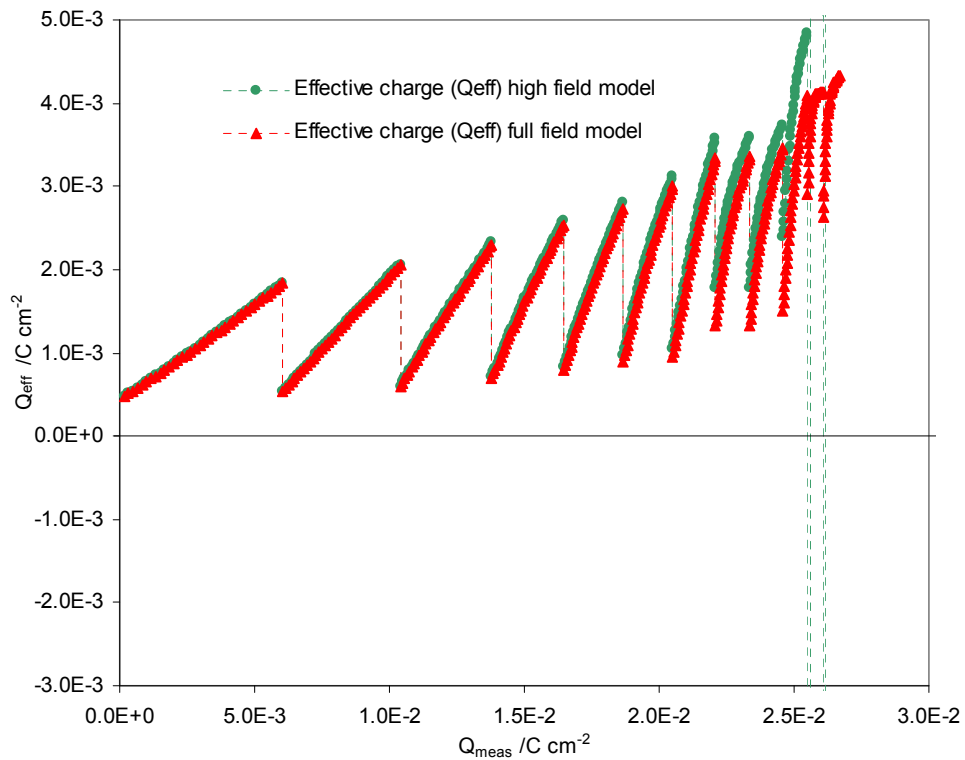
Figure 4-60: Ratio of calculated effective charge to measured charge against measured charge for potentiostatic polarisations of Magnox
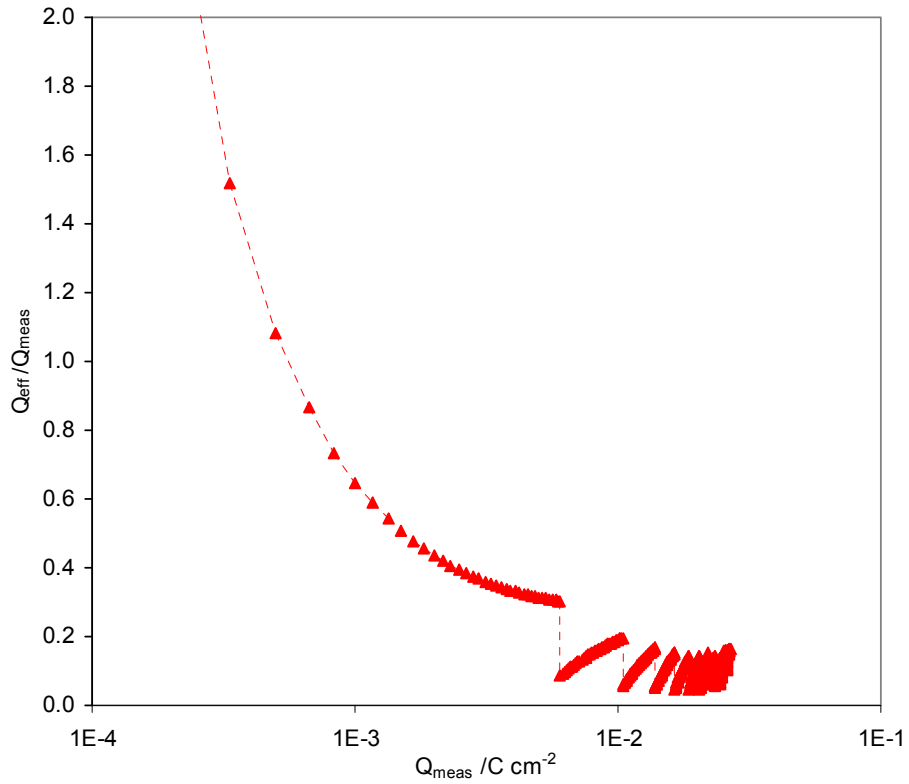
Figure 4-61: Measured and equivalent current densities for repetitive potentiodynamic polarisations of Magnox
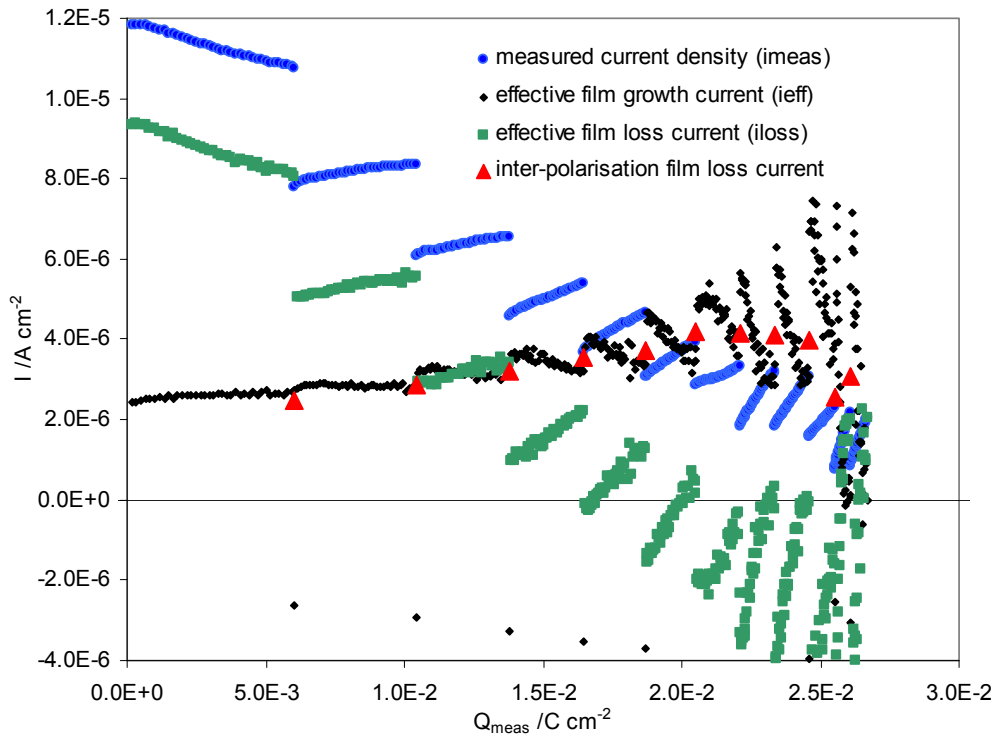
From the discrepancy between the measured current density and the rate of change in calculated effective charge, it is possible to derive a parameter for the rate of film loss (as an equivalent current density):

$$\frac{dQ_{eff}}{dt} = i_{eff} = i_{meas} - i_{loss} \qquad\qquad (4\text{-}6)$$

These parameters are shown in Figure 4-61 as a function of $Q_{meas.}$, thereby outling the development of the effective film growth current density (proposed to be dictated by the effective film thickness) and the effective film loss current density (according to the difference between measured and effective film thicknesses), as functions of the total measured effective film thickness. The calculated rate of film loss (as an equivalent current density) in the period between polarisation tests is also shown which can be seen to be very close to the value of i_{eff}. This point is largely coincidental as in these tests, the duration of the polarisations was equal to the period open circuit monitoring between each one, so this value simply reflects the fact that almost complete loss of the film occurs between each polarisation. The fact that the rates of film formation and film destruction are so closely related suggests that, either both rates are affected similarly by a high-field type mechanism, or more likely, that i_{loss} is a function of the inner film thickness. A proposition which would reconcile these observations is that the rate of film loss is a function of the effective cumulative charge and the measured (total) cumulative charge as in:

$$i_{loss} = f(Q_{eff}, Q_{meas}) \qquad\qquad (4\text{-}7)$$

The physical significance of this would be that the film growth is primarily controlled by a barrier layer which has a limiting thickness, probably due to hydration assisted by micro-fracturing or fissuring as a result of internal stresses. The rate of movement of ions through this film dictates the rate of reaction at the film/metal interface (e.g., the corrosion rate) which may be described by the field film growth model, so is dependent on the overpotential and the inner film thickness. The reaction of the film at the outer surface (fissuring and hydration) controls the maximum thickness which can be attained but the rate at which this occurs is affected by the thickness of the hydrated (outer) film. Therefore, for a particular polarisation and outer film thickness, a particular steady state thickness will be achieved by the inner film. The rate of film hydration is not proposed to be directly affected by polarisation, but is dictated by the inner film thickness (with a growth rate governed by overpotential), so the rates of growth and loss will both increase when the overpotential increases.

On the basis of the form of the calculated film hydration equivalent current density (i_{loss}) in Figure 4-61, it can be proposed that this variable may be related to Q_{meas} and Q_{eff} by a function of the form:

$$i_{loss} = C_1 \exp(C_2 Q_{meas} - C_3 Q_{eff})$$
(4-8)

where C_1, C_2 and C_3 are kinetic parameters.

Both these values are shown as a function of measured cumulative charge in Figure 4-61.

From this figure, it can be seen that in the final few sweeps, the calculated rates of film growth and hydration begin to overlap. At this point, negative values for film loss begin to be observed, the direct interpretation of which would be that the film is growing at both interfaces. Although there are some related physically meaningful processes which this could represent, such as capacitive effects or presence of a further barrier film or reaction intermediates, any such further convolutions to the proposed mechanism are likely to represent speculation without more detailed kinetic data and this observation may be more credibly attributed to scatter within the data set which becomes significant within the interpretive calculations at these small current densities

Using the relationships outlined above, it is possible to undertake some notional fitting of the data sets discussed here to a notional generalised film growth expression. For clarity, the equations employed are as follows for potential controlled tests:

$$i_f = 2A \sinh\left[\frac{B\eta(t)}{Q_{eff}}\right]$$
(4-9)

$$i_{loss} = C_1 \exp(C_2 Q_{meas} - C_3 Q_{eff})$$
(4-10)

$$\frac{dQ_{eff}}{dt} = i_f - i_{loss}$$
(4-11)

$$\frac{dQ_{meas}}{dt} = i_f$$
(4-12)

For galvanostatic tests, the potential may be predicted by rearranging the full field film growth expression to give the following equation:

$$\eta = \frac{Q_{eff} \, \text{arcsinh}\left[\dfrac{i}{2A}\right]}{B}$$

(4-13)

Although the expression for i_f reaches zero when the potential is zero, the expression for i_{loss} does not tend to zero for low value of Q_{eff}, which could result in an unphysical behaviour during periods between polarisations. The data at present give little information on the value of i_{loss} in the absence of polarisation, (e.g., the rate at which the inner film returns to lower values), except that this happens relatively quickly. This inconsistency has been dealt with by resetting the value of Q_{eff} to a notional minimum close to the starting value between successive polarisations, to represent re-attainment of the non-polarised steady state value. The quality of the fittings was improved substantially if a value for the B kinetic parameter at the lower end of the uncertainty range quoted in Gonzalez Torreira (2004) is employed of 2×10^{-3} C V^{-1} cm^{-2}.

A notional fitting of the C_x kinetic parameters in the i_{loss} expression above has been undertaken for the set of polarisations shown in Figure 4-40, and the resulting prediction of measured current density and di/dt are shown in Figure 4-62.

Figure 4-62: Comparison between measured current density and semi-quantitative film growth model results for repetitive potentiodynamic polarisations of Magnox
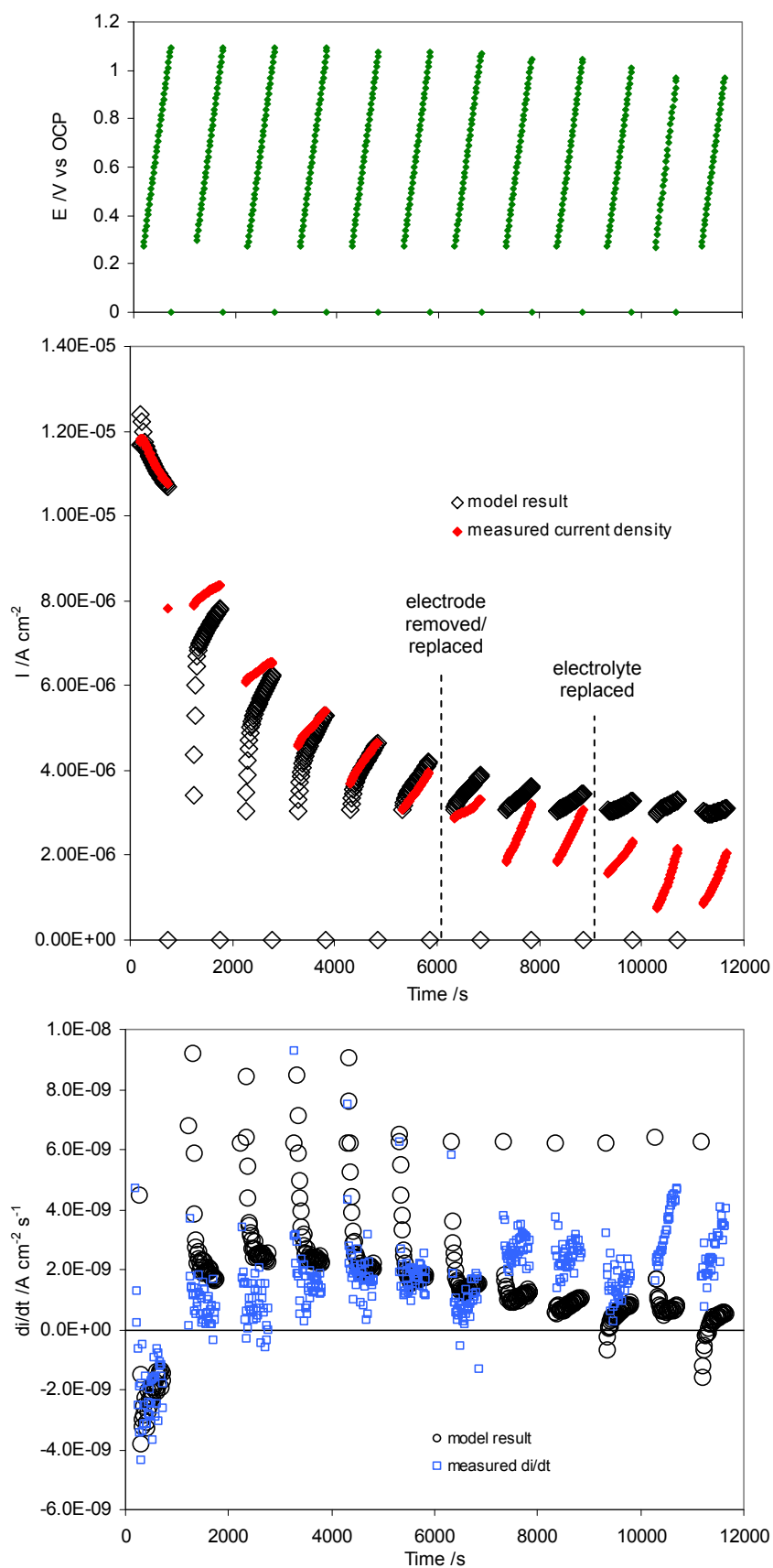
This shows a good semi-quantitative agreement in the initial sweeps, with characteristics in the second derivative being reproduced qualitatively. The behaviour diverges noticeably from the point at which the electrode is disturbed and subsequently, more so when the electrolyte is replaced. These events would be expected to be associated with changes in long-range mass transport processes (e.g., solution convection) and it is interesting that the model diverges following these points (with the current fitting) despite the fact that this was not particularly evident in the data without this interpretation. As the model does not consider corrosion product transport beyond the outer film, it appears reasonable that divergence of the model prediction coincides with events which would significantly influence processes which might affect this, such as an increase in convective transport following stirring of the electrolyte.

A separate fitting has been undertaken to derive a second set of C_x parameters for a further set of potentiostatic polarisations. The results of this prediction are shown in Figure 4-63. Note that this is a separate fitting to that discussed above, but is common to all three polarisations. A third fitting has been undertaken for data from a galvanostatic test undertaken at 5×10^{-5} A cm^{-2} and these results are shown in Figure 4-64. Fittings attempted for data from tests with lower polarisations gave qualitative agreement but was less successful, probably partly as the expression system does not attempt to account for behaviour nearer the OCP and also, as observed above, does not satisfactorily replicate film hydration behaviour at these lower potentials.

Figure 4-63: Comparison between measured current density (solid points) and semi-quantitative film growth model results (open points) for potentiostatic polarisations of Magnox
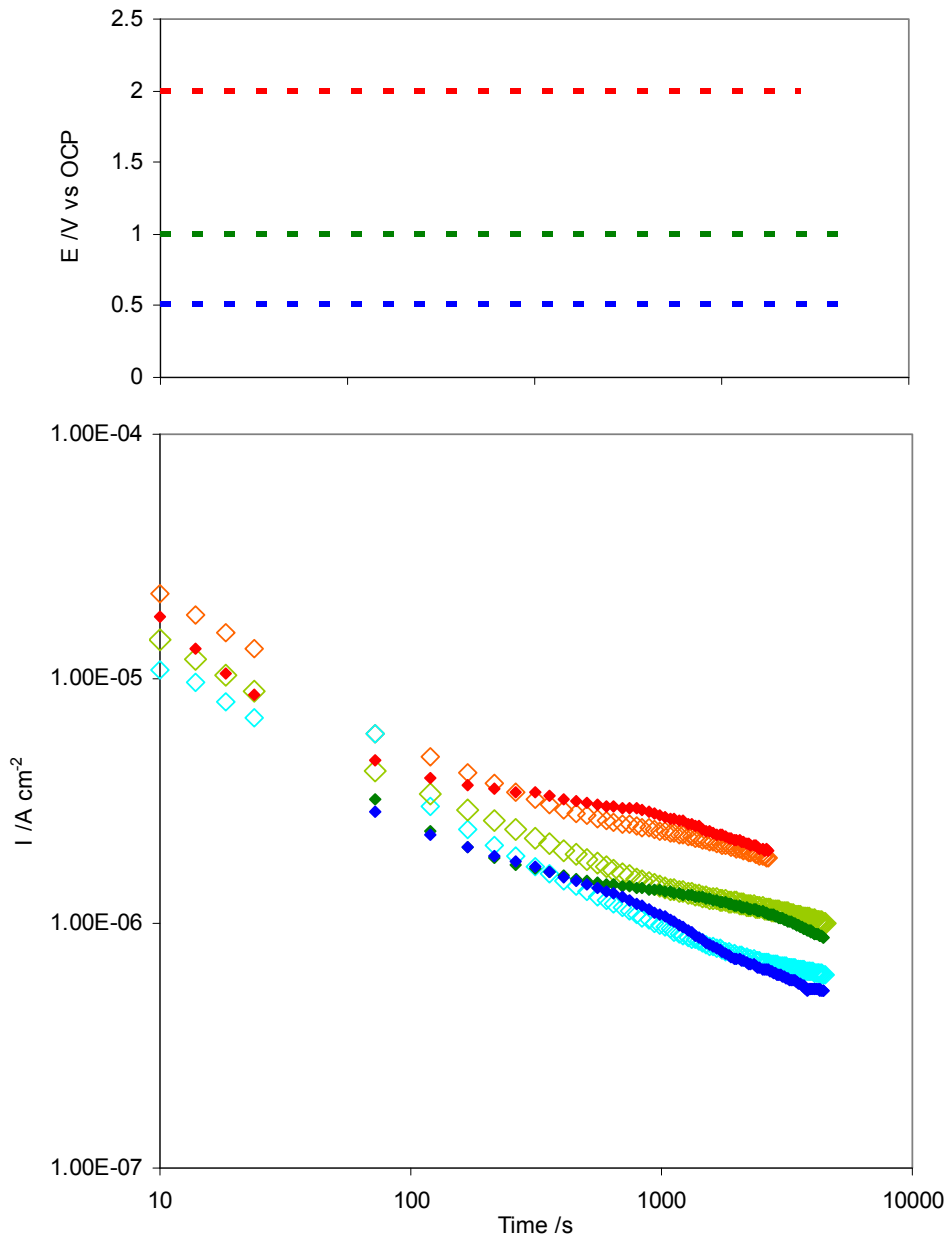
These results show successful quantitative modelling for different types of electrochemical experiment over moderate timescales on the basis of a general expression, although fitting of some kinetic parameters is required. The values of the C_x coefficients for each of the three fittings is shown in Table 4-1. It is notable that these differences mainly appear to relate to small variations in the values of i_{loss} in different ranges of Q_{meas} and Q_{eff}. As can be seen in Figure 4-65, the electrochemical tests shown lie within characteristic ranges of these values. Relatively speaking, the repetitive potentiodynamic polarisations are at low Q_{eff}/high Q_{meas} (with a thick outer film being produced by repeated fast growth of thin inner films), whilst the long-term potentiostatic polarisations are high Q_{eff}/mid Q_{meas} (with a thick inner film being grown in one test) and

the galvanostatic tests being low Q_{eff}/low Q_{meas} (with both films remaining at relatively small thicknesses). It may be that a general fitting of all three datasets to a different form expression for i_{loss} may reconcile the behaviour across the ranges of inner and outer film thicknesses.

Figure 4-64: Comparison between measured current density and semi-quantitative film growth model results for repetitive potentiodynamic polarisations of Magnox
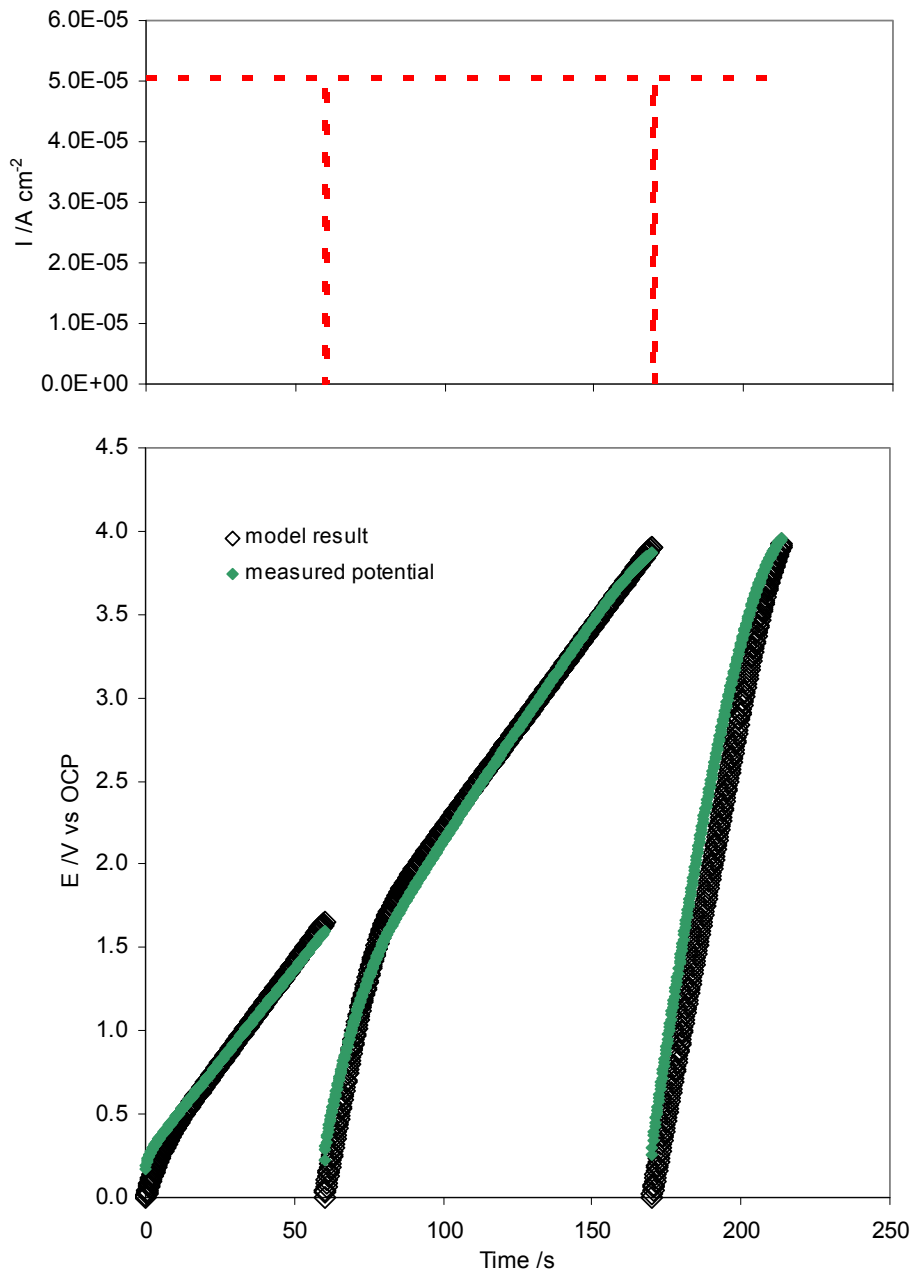
Table 4-1: Empirically fitted parameters from extended passive film growth model for different types of electrochemical test on Magnox

Coefficient	C_1	C_2	C_3
	/A cm^{-2}	/C^{-1} cm^2	/C^{-1} cm^2
Repetitive potentiodynamic	1.00E-05	1.40E+02	1.00E+03
Single potentiostatic	1.00E-09	8.00E+02	3.00E+03
High-i galvanostatic	1.90E-05	1.70E+03	5.20E+03

Based on kinetic parameters A = 1 x 10^{-6} A cm^{-2}, B = 2 x 10^{-3} C V^{-1} cm^{-2} (from Gonzalez Torreira, 2004, with B value taken at the lower error bound)

Figure 4-65: Indication of coverage extent for current data on electrochemical tests for Magnox
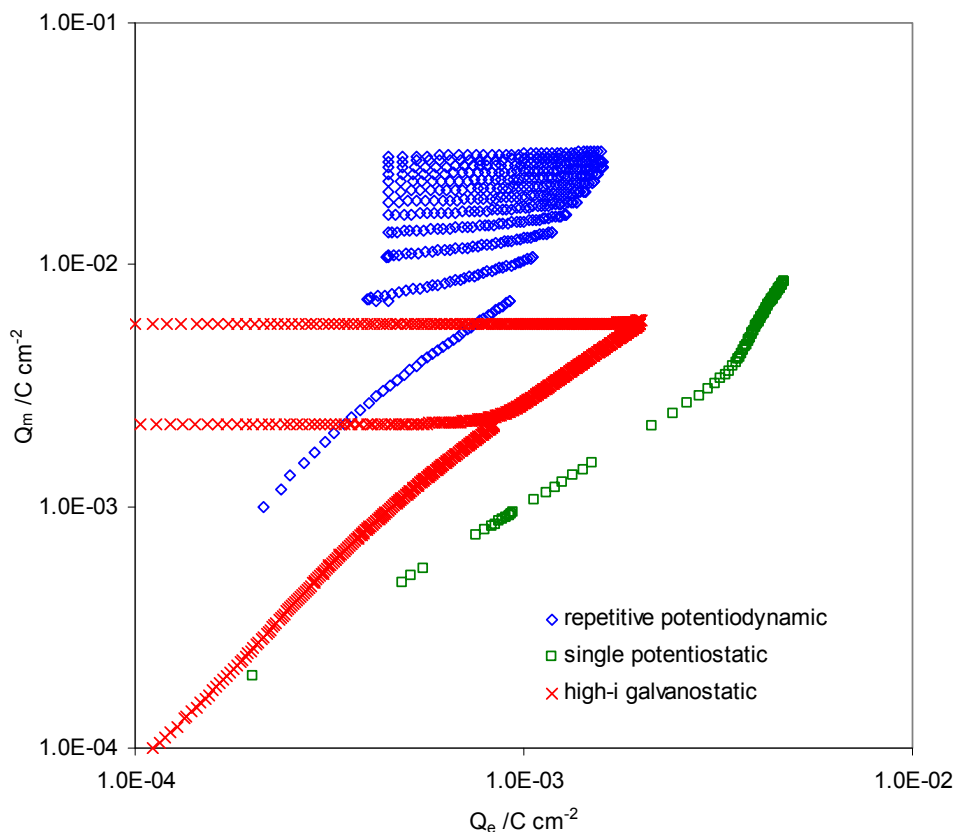
This consideration is instructive in terms of the passive corrosion mechanism of Magnox and magnesium, however, it is noted that the evident underlying complexities could be interpreted according to other mechanisms. The model proposed here gives a level of understanding which is helpful in interpreting these polarisation experiments and has also allowed a semi-quantitative model to be formulated on the basis of the standard film growth model. Further interpretation is not attempted at this point as this is regarded to require focussed tests to derive data which would differentiate some of the mechanisms which may be indistinguishable or equivalent according to the current data.

The main aim of the current work is to increase understanding of Magnox clad failure mechanisms over nominal storage timescales which, as discussed previously (see Section 2.2), would normally be expected to be dictated by pitting corrosion. The current level of understanding is deemed to be a development from that afforded previously and certainly sufficient to credibly support subsequent interpretation of electrochemical data and characterisation of transition from general to localised forms of corrosion to be underpinned. Importantly, it is clear from the kinetic information derived that the corrosion rate is affected by both the dense inner oxide but also the porous outer hydroxide, albeit more weakly.

4.2.1   Summary of passive film growth kinetics findings

The results presented in this section clearly show that the passivation of Magnox is primarily governed by the formation of an adherent film.

The initial stages of a polarisation test undertaken at the first immersion of an electrode appear to be well described by the high field, or full field film growth expression using the kinetic parameters reported by previous workers.

Following this initial period, the behaviour diverges both quantitatively and qualitatively from that which would be expected from the simple form of this expression:

- The limiting current density during initial film formation is substantially above that which would be expected.

- The negative rate of change in current density during this phase in tests with scanning potential persists across a much larger potential region than would be expected for a surface which is forming a film at a rate proportional to the measured current density.

- Where polarisation tests are punctuated by periods without polarisation (e.g., open circuit monitoring), the current density at the beginning of each polarisation is much higher than would be expected from that at the end of the preceding one.

- The current densities gradually reduce with increasing total polarisation whether this is from a single polarisation or numerous successive ones.

- Even at large total cumulative charges, the current density behaviour with changing potential implies that the thickness of the passive film is sufficiently small that the behaviour is close to high field behaviour.

Film dissolution and solution mass transport processes could account for some aspects of the quantitative differences but do not reconcile the observations, importantly, in terms of qualitative behaviour, although they may be more dominant in situations where these rates are enhanced.

Interpretation of the measured current density with the full field film growth expression to derive the effective film thickness suggests that the passive film thickness exhibits a complex but consistent behaviour:

- During the initial phase of the first polarisation, the effective film thickness is slightly larger than that predicted from cumulative charge.

- For the initial $\sim 10^2$ seconds within a polarisation, the effective film thickness grows at a rate close to the measured current density.

- Following this period, the rate of growth gradually drops with the calculated film thickness tending to a value of around 1 nm, although this limiting value continues to increase slowly with total cumulative charge.

- Where polarisation is non-continuous, the film thickness appears to rapidly decrease and return to a lower value when the polarisation is removed, although the rate at which the previous steady state thickness is attained increases with total cumulative charge.

Overall these observations are consistent with a passivation process which is primarily controlled by a thin inner oxide film which grows according to a mechanism described reasonably by the full field film growth expression but becomes increasingly unstable with increasing thickness and hydrates at the outer interface to form a partially protective and adherent outer film which contributes to stabilising the inner film.

The corresponding reactions are:

at the metal-oxide film interface
$$Mg + O^{2-} \rightarrow MgO + 2e^- \qquad \{4\text{-}1\}$$
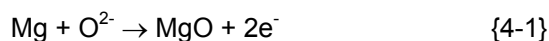
at the oxide-hydroxide interface

120

$$MgO + 2OH^- \rightarrow Mg(OH)_2 + O^{2-} \qquad \{4\text{-}2\}$$

cathodic reaction

$$2H_2O + 2e^- \rightarrow H_2 + 2OH^- \qquad \{4\text{-}3\}$$

at the hydroxide-solution interface

$$Mg(OH)_2 \longleftrightarrow Mg^{2+} + 2OH^- \qquad \{4\text{-}4\}$$
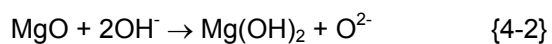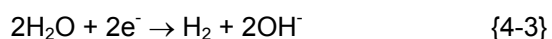
An expression has been proposed which describes the rate of hydration of the inner film as a function of the thicknesses of the inner and outer films. Fitting of the kinetic parameters within this expression to particular experimental conditions allows successful semi-quantitative modelling of data from sets of both galvanostatic, potentiostatic and potentiodynamic polarisation over moderate timescales. This is an extension of the previous model for oxide growth kinetics for thin films to incorporate thick films relevant to fuel storage timescales.

This behaviour may be mechanistically related to the effect of internal stresses in the inner oxide. The difference in molar volume between bulk metal and oxide, along with topotactic mismatches between lattice structures will mean that the oxide is increasingly prone to micro-fissuring as the thickness increases, which provides a greatly increased surface area for hydration to occur. The presence of the porous hydroxide outer film provides some element of stress relief to the inner film, thus stabilising the surface and reducing the extent of fracture and hence the rate of hydration.

These findings are consistent with previous surface characterisation studies which showed an inner layer of MgO which grows at the metal interface with a porous outer layer of $Mg(OH)_2$ and reconcile these with the short term kinetic studies of the initial stages of film growth.

5   Atomistic Modelling of the Passive Film Interface

It has been shown that passivation of Magnox and magnesium occurs primarily due to the presence of a very thin, dense oxide film (Section 4.2) and that depassivation can occur near-instantaneously due to the presence of very low concentrations of chloride ions (Section 4.1). These observations focus the attention of considerations relating to the film breakdown mechanism on the passive layer interface and the influence of anions at this location. As the typical passive layer thicknesses are of the order of many layers of an atomic lattice, atomistic simulation is an appropriate method to investigate this structure. This section presents the results of a program of quantum mechanical calculation undertaken using the magnesium oxide surface as an analogue for the passive film interface.

5.1   Modelling Approach

As described in Section 4.1, the initiation of localised corrosion on a polarised magnesium electrode is typically seen as a very rapid increase in corrosion current (Figure 4-14). It is notable that depassivation can occur at very low chloride concentrations and without significant divergence of the electrochemical characteristics prior to initiation. Particularly, the limiting current density is not seen to increase, although in extended polarisation below the pitting potential, meta-stable pitting transients can be observed (see Section 6.1.2). These observations would be consistent with an initiation mechanism which primarily affected the solution-passive layer interface without extensive film thinning. Modifications occurring at the metal-passive layer interface might be expected to be more disruptive and show more prolonged electrochemical responses.

The most likely pre-cursor mechanism which could lead to local accumulation of chloride to a level which could cause film breakdown would be migration within sites of restricted geometry, such as crevices. The solution-MgO interface is likely to be a complex structure of topotactically grown porous $Mg(OH)_2$, which will influence migration of chloride. Similarly, fuel element surfaces have a pre-grown oxide layer comprising micro-cracks which will also present crevice sites (Section 2.2) and this is in agreement with the consistent observation that pre-oxidised samples are substantially more susceptible to pitting corrosion during initial hydration (Section 2.3).

Given this potential for accumulation of chloride near the passive layer interface, various processes which could lead to film breakdown are possible. Speckert and Burstein (2010) have postulated that pre-initiation transients in aluminium were caused by

formation and rupture of microscopic blisters of chloride phases on the passive layer surface and some related mechanism involving incorporation and phase transition in the magnesium passive film would be consistent with this. An important aspect of any mechanism of this nature is likely to be the propensity of chloride to adsorb and substitute hydroxide (and other anion) positions at the interface.

Recent work by Pineau *et al.* (2006), Bouzoubaa *et al.* (2009) and Bouzoubaa *et al.* (2010) employed atomistic modelling of lattice structures to explore the localised corrosion behaviour of the passivated nickel surface and showed a notable behaviour of chloride on nickel oxide lattice surfaces (Figure 5-1). At low fractional coverages, chloride ions had a favourable (negative) energy for adsorption onto surface sites, but a strongly unfavourable energy for insertion into the lattice. As the coverage increased, the adsorption energy became less strongly negative and the insertion energy followed an overall decreasing trend until it became favourable (and more negative than the adsorption energy) at near 100% coverage. This suggests that the oxide becomes spontaneously unstable at a high chloride coverage due to an inability for a stable surface oxide to form with preferential modification to a chloride phase.

As chloride structures are likely to hydrate very readily, the observations of Bouzoubaa *et al.* (2010) would imply a possible depassivation mechanism involving self-propagating cascade failure of the passive layer as chloride rapidly follows the newly created fissuring surface, initially adsorbing and then substituting. This ultimately could be expected to result in a near instantaneous localised depassivation of an initially intact and near perfect MgO lattice passive layer with only surface adsorbed chloride groups, due to a change from topotactic and partially protective hydration (see Section 4.2) to depassivating chloride induced breakdown. This is an important postulation as this matches closely with the observed behaviour in the electrochemical work (Section 4.1).

Figure 5-1: Variation of the energies of adsorption and insertion per Cl on NiO with Cl coverage (reproduced from Bouzoubaa *et al.*, 2009)
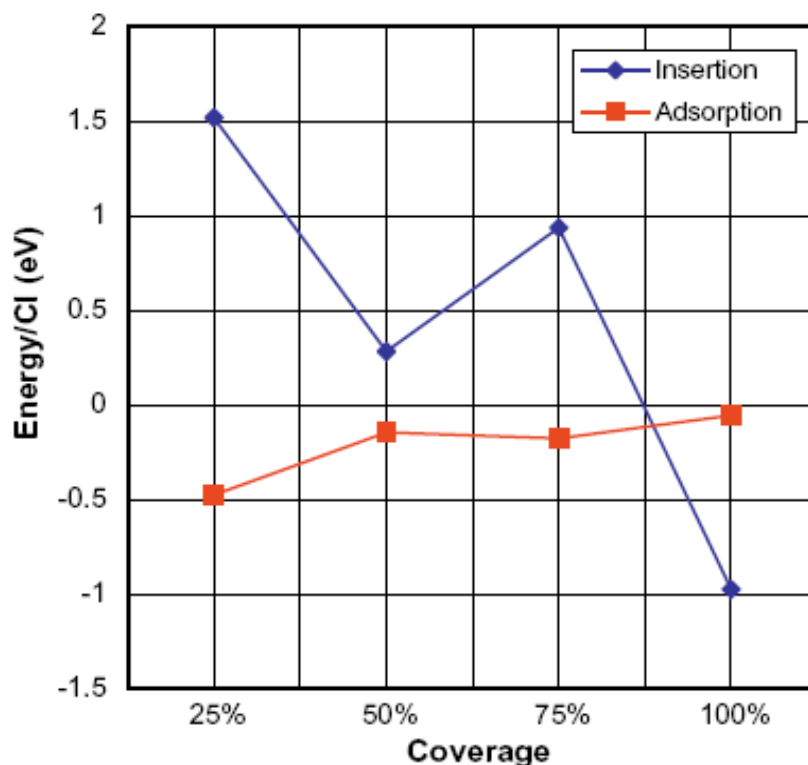
Consequently, the properties of the magnesium oxide surface and the effect of chloride adsorption and substitution on its stability are of interest. This section describes a series of quantum mechanical atomistic calculations aimed at gaining information on these processes and the extent to which these could support a proposed depassivation mechanism of the type outlined above.

The background and bases to the techniques employed are described in Section 3.4.

Initially, a number of scoping trials employing classical simulation "force-field" methods were undertaken which offer advantages in being significantly less processor intensive than quantum mechanical calculations. These employed the General Utility Lattice Program (GULP) by iVEC (Gale and Rohl, 2003), however, a significant initial obstacle was the availability of standard interatomic potentials corresponding to the various atomic pairs within the simulation. Whilst the standard magnesium oxide structure has been studied extensively (see Section 3.4) and calculations involving halides and hydration groups have been reported, these have not been undertaken in the same structures. One possibility was to generate the required parameters by performing a limited number of high quality quantum mechanical simulations and then using

simultaneous parameter fitting to derive new expressions for the interatomic potentials which were not available from the literature. This process proved problematic however, as although it was possible to derive fitted equations, these tended to be very specific to the behaviour of atoms in particular configurations The number of potential expression parameters required to reasonably allow lattice minimisation would therefore be large. This would also increase the risk that the reconfiguration of the atoms in a structure may become artificial leading to favouring a conformation other than that with the lowest energy. It was also apparent that the behaviour of atoms was most significantly different at surfaces, which was the feature of most interest. Consequently, classical simulation was abandoned on the basis that in the current context it had the potential to produce erroneous results due to the constraints introduced by the force fields used. Quantum mechanical methods were therefore progressed as a more reliable means of producing representative simulations of lattice behaviour.

As described in Section 3.4, calculations were undertaken with the use of the SCF code DMol^3 (Delley, 1990 and Delley, 2000). In common with all quantum mechanical calculation codes, DMol^3 is reliant on approximations, however, the current work employs analogues which are very well-characterised systems (magnesium oxide lattice structure, halides and dissociated water) which were the basis of much of the development of the code. In order to increase the reliability of the results, a small number of comparative calculations have been undertaken for the purposes of calculational diversity using the CASTEP code (Clark *et al.*, 2005), which uses DFT but employs alternative approaches in a number of details (see Section 3.4) so provides an element of independence in the calculations. In both cases, the Materials Studio package (by Accelrys Systems Inc.) was primarily used for definition and visualisation of structures, with aspects of manual editing in certain cases. Calculations were undertaken either using a dual processor (Intel x86 1860 MHz) desktop computer or the National Nuclear Laboratory high performance computing cluster ("Gemstone") with a maximum of 32 processors (Intel Woodcrest and AMD Opteron).

In this work, the fundamental approach has been to model the magnesium passive layer as an MgO lattice, with the solution interface being simulated by a partially hydrated cleaved plane.

A unit MgO cell was geometrically optimised (including cell parameters) as the basis for subsequent calculations. The imposition of FM3M group symmetry substantially reduced the computational time but did not change the simulation output. The "binding energy" parameter calculated by DMol^3 was -11.489 eV (per unit MgO primitive cell). On the basis of the ionisation and electron affinity energies given in Table 5-1, a lattice energy of -41.21 eV is produced which is in good agreement with literature values of -

41.07 and 41.35 eV (Huggins & Sakamoto, 1957, de Leeuw *et al.*, 1995, respectively), recognising that these are indicative comparisons.

Table 5-1: Ionisation and electron affinity energies for Mg and O

Atom	Energy	/eV	Ref.
Mg	First ionisation	7.646	CRC, 2001
	Second ionisation	15.035	CRC, 2001
O	First electron affinity	-1.461	CRC, 2001
	Second electron affinity	8.491	Huggins & Sakamoto, 1957

This lattice structure was then cleaved in the required direction. DMol^3 requires a 3-d periodic structure so this surface was converted into a "vacuum slab" with sufficient vacuum that interactions across the planes would be negligible. Symmetry was not used as this would not be consistent with the introduction of surface groups or lattice substitutions.

A further geometry optimisation (without variation of cell parameters) was undertaken to relax the surface. Subsequent calculations involved geometry optimisations without variation of the cell parameters, as this is the most representative means of simulating the relaxation of a surface interface which is the termination of an infinitely deep bulk lattice.

Previous works (de Leeuw *et al.*, 1995) have identified that the 310 surface of MgO is a closer representation of a real surface than the perfect 100 plane but is likely to be more abundant than the very high energy unmodified 110 and 111 surfaces, due to the stepped edge which, despite being regular, comprises sites with varying co-ordination. This means it has more characteristics in common with typical of defects, micro-cracks and grain boundaries on a real surface. The hydration behaviour of the MgO surfaces would also suggest that the 310 surface is of primary interest as the 100 surface has a positive energy of hydration for most surface coverage fractions, suggesting that it may be relatively inert in terms of the hydroxide layer growth (see Figure 5-2 showing data from de Leeuw, 1995). The 310 surface, however, was reported to have consistently negative hydration energy for all surface coverage fraction. Use of the 310 surface as a passive interface analogue is also practically favourable as this surface is non-polar, which simplifies the simulation and reduces the assumptions required.

Consequently surface simulations have been focussed on the behaviour of the MgO 310 surface. This is also considered a reasonable compromise between a cell that is small, highly symmetric and calculationally reducible, but unrealistic, and a very large, complex, low co-ordination defect which may represent a more chemically active site. It is noted that the percentage hydration figure for the "310 edge" given in Figure 5-2 relates only to this particular site on the surface, i.e., only 1 in 4 of the 4-co-ordinated surface sites.

Figure 5-2: MgO surface energy as a function of surface hydration for 100, 110, 111 and 310 surfaces (data from de Leeuw, 1995)
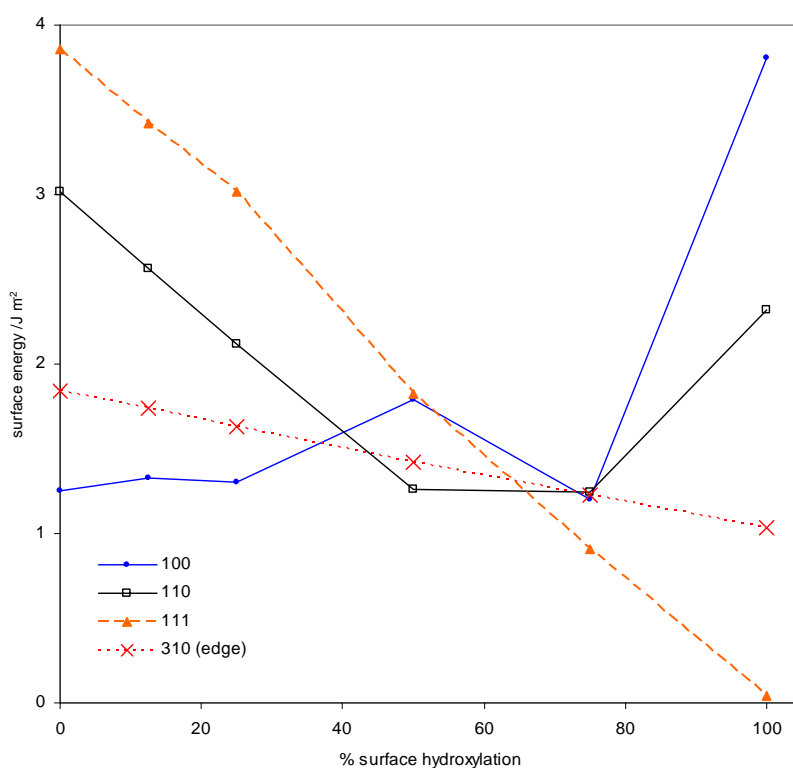
Although some previous investigations have derived surface energies to allow comparison of the favourability for formation of a particular modification of surfaces, because the groups being substituted in this work comprise different atoms and consequently relate to differing reaction energies, it is possible the uncertainties in the literature values, and the complexity of applying corrections for aqueous behaviour to gas-phase experimental parameters may be sufficient to obscure the relatively modest changes in surface energy which are of interest. This is illustrated in Table 5-1 which shows the basis for calculation of a correction parameter derived by de Leeuw *et al.* (1995) and from a set of thermodynamic parameters from a different reference (CRC, 2001). The difference is clearly significant and underlines the advantage of direct use of

energy difference (dE) for interpretation of these calculations. A further consideration is that this type of energy correction should only strictly be made when the assumption that the modifying species are fully dissociatively adsorbed is valid as in cases where the adsorption is weaker, there may be an over-correction for interactions which are not in fact being predicted.

Consequently, the most robust method available for comparison of simulated periodic structures has been primarily employed which is to directly compare the energies of two structures possessing identical numbers of each atom and are distinguished in configuration alone. As well as having the benefit that results can be interpreted unambiguously without reliance on experimentally determined enthalpy values, this approach is recognised as being preferable due fortuitous cancellation of calculational errors from two equivalent simulations. In some cases, surface energies are reported as indicative parameters, and these have been corrected against simulations undertaken to calculate binding energies for isolated molecules of the modifying type and with corrections for surface interactions based on enthalpies of formation. For consistency, the corrections in Table 5-2 presented by de Leeuw *et al.* (1995) (factor "A") and the modified factor "D" have been used for the hydroxylation and the chloride substitution steps respectively so as to allow consistency with the values reported by de Leeuw (1995).

The surface reactions simulated are therefore:

$$MgO + H_2O \rightarrow Mg(OH)_2 \qquad\qquad \{5\text{-}1\}$$

$$MgO + HCl \rightarrow \tfrac{1}{2}Mg(OH)_2 + \tfrac{1}{2}MgCl_2 \qquad\qquad \{5\text{-}2\}$$

$$Mg(OH)_2 + 2HCl \rightarrow MgCl_2 + 2H_2O \qquad\qquad \{5\text{-}3\}$$
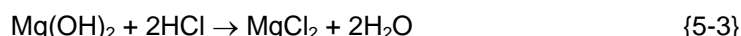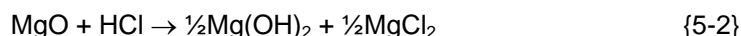
These reactions have the advantages of conserving numbers of atoms and allowing simulation of a non-polar surface which avoids the requirement to account for interaction of adjacent surfaces within the simulated periodic structure.

The reactions above neglect vacancy transport within the MgO lattice. With an assumption that the oxide layer thickness is conserved, as part of the overall reaction scheme, these are equivalent to:

$$MgO + 2OH^- \rightarrow Mg(OH)_2 + O^{2-} \qquad\qquad \{5\text{-}4\}$$

$$MgO + OH^- + Cl^- \rightarrow \tfrac{1}{2}Mg(OH)_2 + \tfrac{1}{2}MgCl_2 + O^{2-} \qquad\qquad \{5\text{-}5\}$$
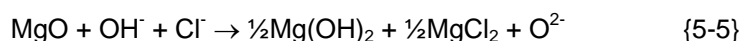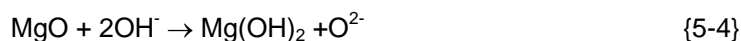
Table 5-2: Basis for derivation of indicative correction factors for hydration and chloride substitution of MgO surface (all values in KJ mol^{-1})

		MgO+H$_2$O→Mg(OH)$_2$		Mg(OH)$_2$+2HCl→MgCl$_2$+2H$_2$O	
		de Leeuw "A"	CRC "B"	CRC "C"	Modified "D"
Enthalpy of formation	MgO	-601.7	-601.6		
	H2O	-285.8	-285.8	-285.8	-285.8
	Mg(OH)2	-924.5	-924.5	-924.5	-924.5
	HCl			-92.3	-92.3
	MgCl2			-641.3	-641.3
Lattice energy	MgO	-3984.8	-3795.0		
	Mg(OH)2	-3378.3	-2870.0	-2870.0	-3378.3
	MgCl2			-2477.0	-2477.0
Correction factor for anion adsorption/ substitution		-643.5	-962.1	-496.8	-1005.1

For a relaxed but unmodified 310 surface of a 40MgO unit cell with a surface area of 54.899 A^2 (Figure 5-3), the binding energy calculated by DMol3 was -11.176 eV (per unit). This corresponds to a surface energy of 1.83 J m^{-2}, which is in close agreement with the value reported by de Leeuw *et al.* (1995) of 1.84 J m^{-2}. This cell was the primary basis for subsequent calculations.

It is notable that the thickness of the oxide layer in the periodic structure was of the same order as the passive film thickness calculated in Section 4.2 and measured by Gonzalez Torreira *et al.* (2003).

Further calculations investigated the varying coverage of the 310 surface with OH$^-$/H$^+$ groups and Cl$^-$/H$^+$ groups.

The DMol3 calculational parameters corresponding to either "medium" or "fine" were used, as shown in Table 5-3, although in some cases, the coarse settings were used either for indicative calculations, or for preliminary optimisation of structures prior to optimisation at higher calculational precision. Similarly, some preliminary calculations were undertaken using smaller representative cells of 10MgO or 20MgO. Calculations were undertaken both without further compensation for solvation effects, which is essentially a simulation of gas-phase behaviour, and also using the COSMO solvation approximation (see Section 3.5). For indication, the solution time (involving geometry optimisation but not adjustment of the cell parameters) for a single calculation using 24 processors under medium or fine quality (pre-optimised) based on the 40MgO system was typically in the region of 1 to 4 hours, although the more convoluted surface configurations in many cases required substantially longer times in the region 6 – 15 hours due to much larger numbers of geometry optimisation iterations.

Figure 5-3: Geometrically optimised, unmodified 310 MgO surface for standard optimisation cell employed (40MgO, 55 A^2 surface area)

top view

side view
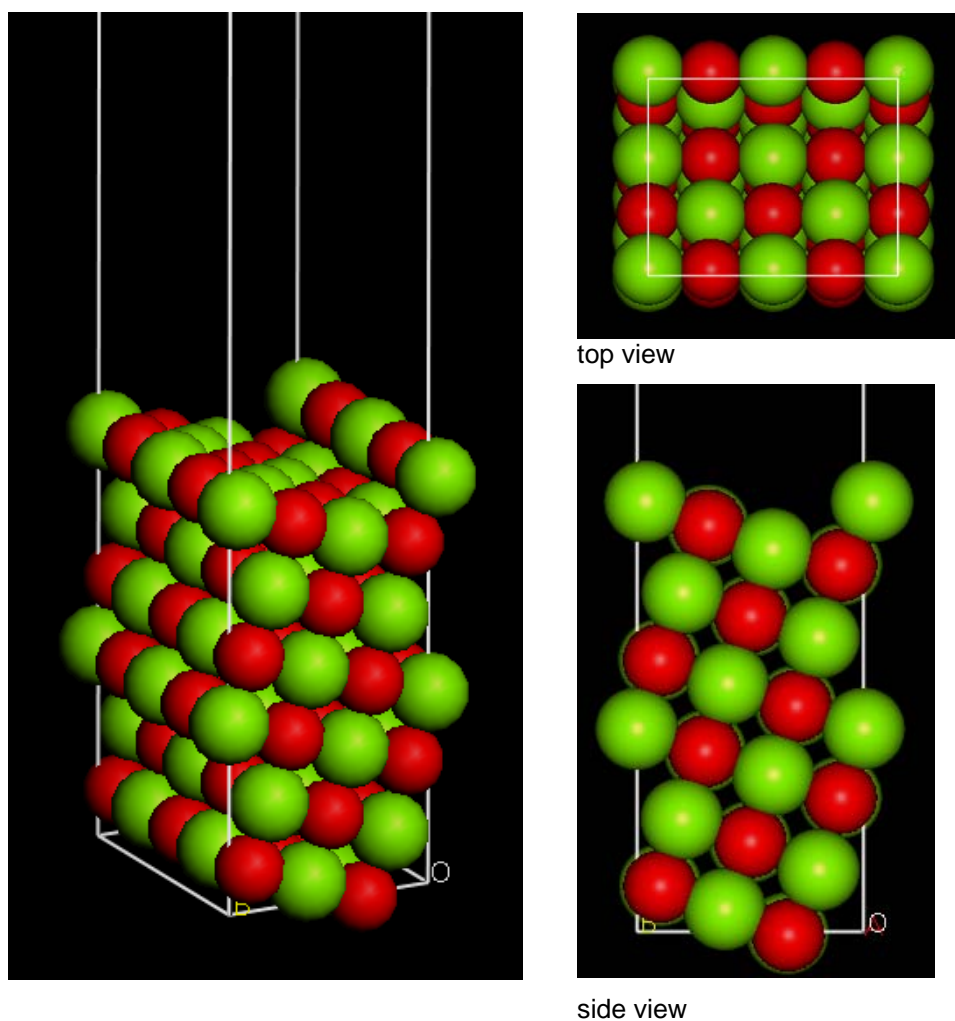
Table 5-3: Calculation quality settings within DMol3 (see Section 3.5)

Quality setting			Coarse	Medium	Fine
SCF tolerance			1E-4	1E-5	1E-6
Basis set			DN	DND	DNP
Cutoff		/A	3.7	4.3	4.9
Geometry convergence tolerance	Energy	/Ha	1E-4	2E-5	1E-5
	Force	/Ha A^{-1}	2E-2	4E-3	2E-3
	Disp.	/A	5E-2	5E-3	5E-3

5.2   Simulation Results

Hydration of the surface to around 33% coverage was energetically favourable as shown in Figure 5-4, which corresponds with de Leeuw *et al.* (1995) noting that the coverage fractions in this work correspond to all the 5 co-ordinated surface groups rather than just the edge sites as quoted for the 310 surface by de Leeuw (1995), with 33% corresponding to full hydration of the edge sites. Higher fraction surface hydration was unfavourable compared to the unmodified surface. This tends to support use of the 310 surface as a passive film analogue on the basis that the defect sites are more highly reactive.

A series of optimisations were undertaken for increasing degree of adsorption of Cl^- and H^+ on the 310 surface (see Figure 5-4, Figure 5-5 and Figure 5-6). Surface adsorption of chloride was unfavourable for surface coverages below 50%, but favourable above this, with surface energy then increasing with surface coverage to become unfavourable by 83%.

Substitution of surface adsorbed hydroxide groups for chloride was unfavourable at low and moderate chloride coverage, but still produced a surface with a negative energy compared to a free surface. At high coverage of adsorbed chloride ion (above 67%), the energy of exchange for an adsorbed chloride with a surface lattice hydroxide group decreases and becomes negative. At very high coverages, the calculations were often found to become non-convergent, with surface subunits associated with chloride atoms detaching and leading to divergent geometry. Although this notionally represents a preferential dissolution of the lattice, the actual behaviour at an aqueous interface will be more complex with strong dependency on the local activity of water and pH.

Figure 5-4: Calculated indicative MgO 310 surface energies (DMol^3) for variable hydration, chloride adsorption and substitution
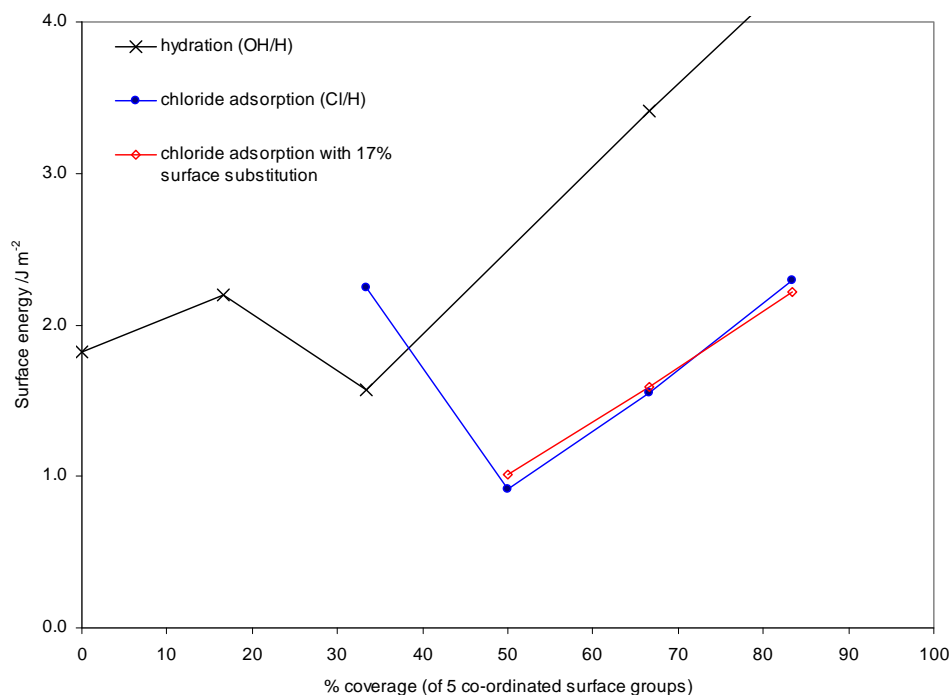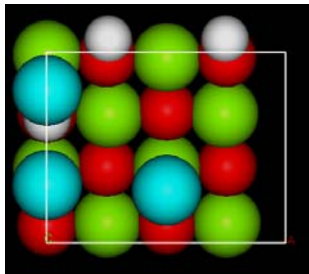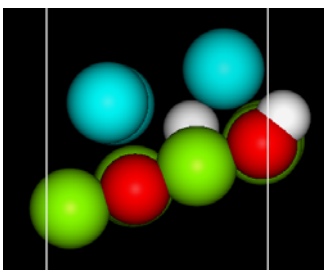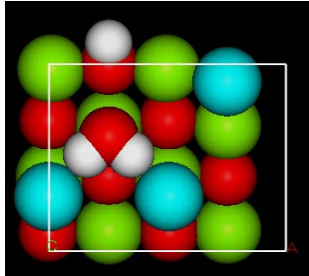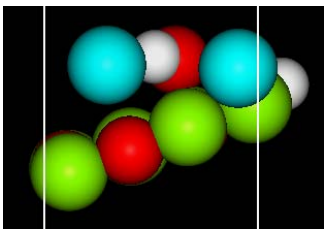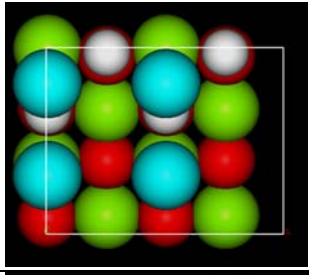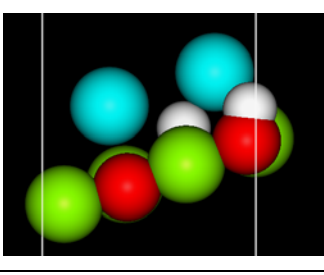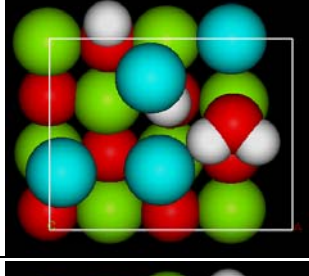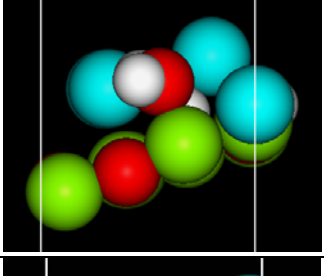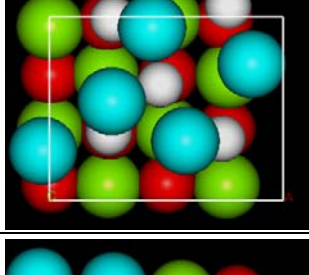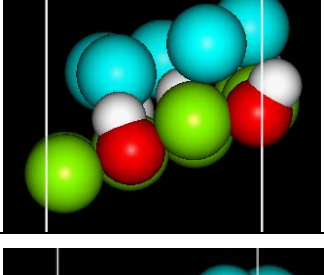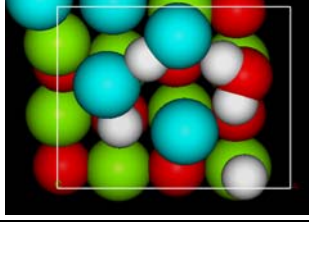
A number of conformational possibilities exist in certain cases. Although these were not examined exhaustively, a number of investigations were undertaken which showed that the differences between optimised energies of near-equivalent surfaces were small (for example, an adsorbed hydroxide group being either opposite or adjacent to a chloride group), or that the calculation would spontaneously optimise to the same low energy configuration from two or more differing starting geometries.

Geometries including simulation of a solvating layer by inclusion of a layer of water molecules above the surface were also optimised. These were more dominated by conformational rearrangements of the water molecules and produced larger energies, although reproduced the same overall trend. These were non-convergent at near 100% chloride adsorption and showed a trend suggesting that this point also corresponded to the point of zero substitution energy.

Figure 5-5: Calculated MgO 310 surface optimised configurations (DMol^3) for varying chloride adsorption and 0 or 17% chloride surface substitution

NOTE: only surface layer atoms shown (oxygen - red, magnesium - green, chloride - blue, hydrogen – white)

%cov.	%ins.	Top view	Side view	dE /eV
50	0			0.629
50	17			
67	0			0.291
67	17			
83	0			-0.532
83	17			

Figure 5-6: Calculated energy differences for MgO 310 surface (DMol³) with adsorption-only and 17% chloride surface substitution for varying chloride coverage

% coverage (of 5 co-ordinate surface groups)
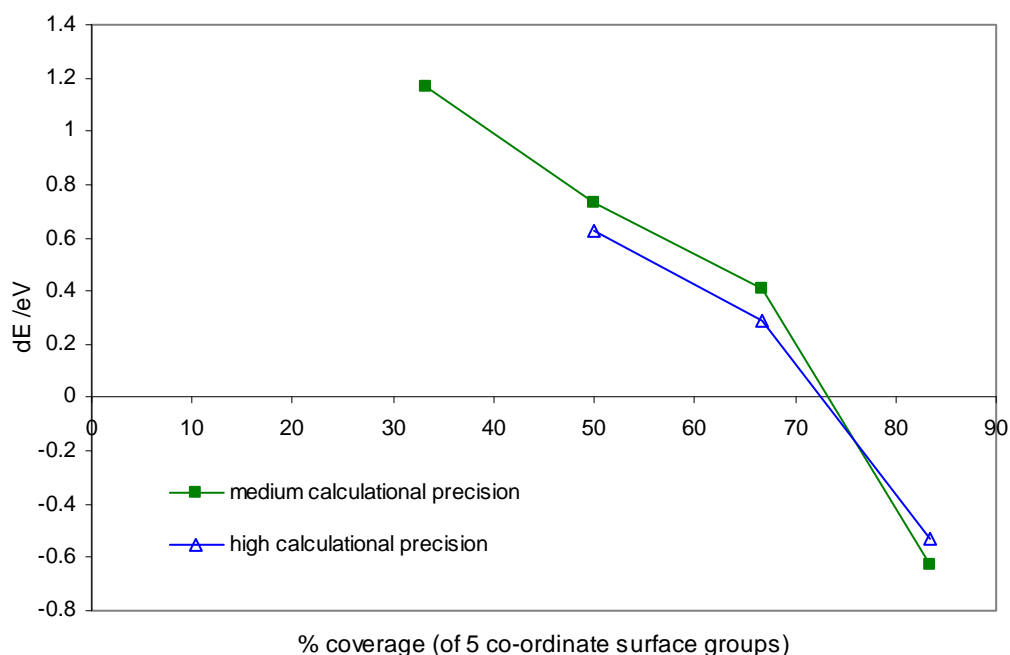
Figure 5-7: Sensitivity of calculation to different functionals and diverse DFT code

% coverage (of 5 co-ordinate surface groups)
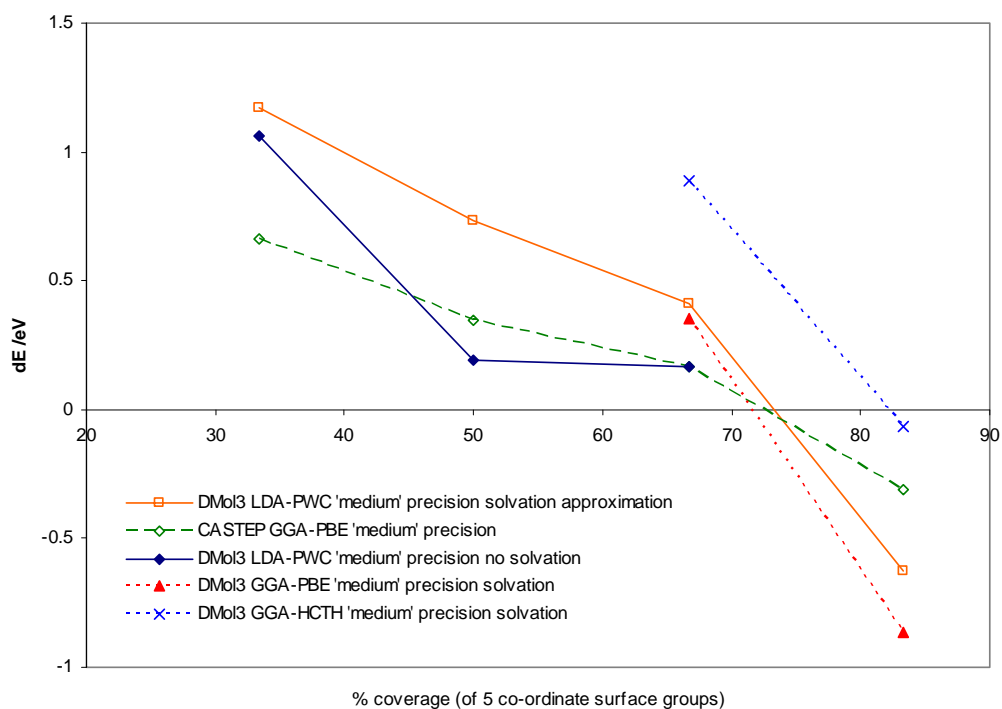
The energy differences (dE) presented here are based on direct comparison of structures with equivalent numbers of atoms but differing configuration. As such, these can be considered to be substantially more robust than the indicative surface energies (Figure 5-5) using energy corrections, as noted above. For this reason, the energy

differences (dE) shown in Figure 5-6 are considered the most robust outputs of this work. These results are then suitable for comparison to similar work on hydration and halide adsorption by Bouzoubaa *et al.* (2010) on the simulated nickel passive layer. This is supported by the result in Figure 5-7 showing that although the point of zero substitution energy varies slightly, there is not a substantial sensitivity to (i) the basis set, (ii) a diverse DFT code or (iii) solvation approximations.

This supports an important observation as the trends in energy difference (dE) demonstrate a credible mechanism for chloride induced depassivation. When a sufficiently high ratio of chloride to hydroxide ions is present at the solution-MgO interface, then the chloride will be substituted into surface lattice positions. This will be expected to result in significant lattice distortion, causing internal stresses and increasing potential for mechanical disruption.

These results may be related to electrochemical results for this system. Figure 5-8 shows the molar fraction of chloride (relative to total chloride and hydroxide) for pitting of samples under polarisation (Section 4.1 and Burrows *et al.*, 2005). It is apparent that the fraction at the high concentration limit (0.738) agrees well with those calculated from interpolation of the surface coverages (considering only surface groups) at the point of zero substitution energy (0.733 and 0.726 for medium and fine quality calculations respectively). Considering the basis of the calculations, the closeness of the agreement is probably incidental at least to some extent, although the trend towards this value is certainly striking. This could be interpreted according to an adsorption mechanism, where the surface coverage molar fraction required for film breakdown is constant whilst the partitioning of ions between bulk and surface is a function of bulk concentration. Accordingly, the ratio of surface to bulk chloride molar fraction is shown as a function of chloride concentration in Figure 5-9. This can be fitted to an expression of the form:

$$\frac{x_{surf}}{x_{bulk}} = ac^{-n}$$

(5-1)

Where x is the chloride molar fraction and c is the chloride bulk concentration. The constants a and n have values of 0.18 and $^2/_3$, respectively, for the fitting shown in Figure 5-9. A number of interpretations may be possible, however, the influence of migration seems a likely mechanism which could relate to a variation of fractional concentration of chloride at an interface under an ionic flux as a function of the bulk concentration of the active species. A simple finite element model has been used to illustrate this. A fixed flux two dimensional migration model was employed as described in Section 3.6 (without water dissociation reactions). The geometry was modified slightly to include a partially occluded region representing a crevice (see Figure 5-10). The

simulated electrode boundary (including the crevice) was attributed a fixed flux of 5×10^{-5} mol m^2 s^{-1}, which is representative of that discussed in Section 4.2. Values for the bulk hydroxide, sodium and chloride concentrations were according to those in Figure 5-8. The model outputs were the ratios of chloride molar fraction between bulk and surface, both at the planar region and within the crevice. These are shown in Figure 5-9.

Figure 5-8: Comparison of chloride molar fractions for film breakdown between atomistic model and electrochemical results
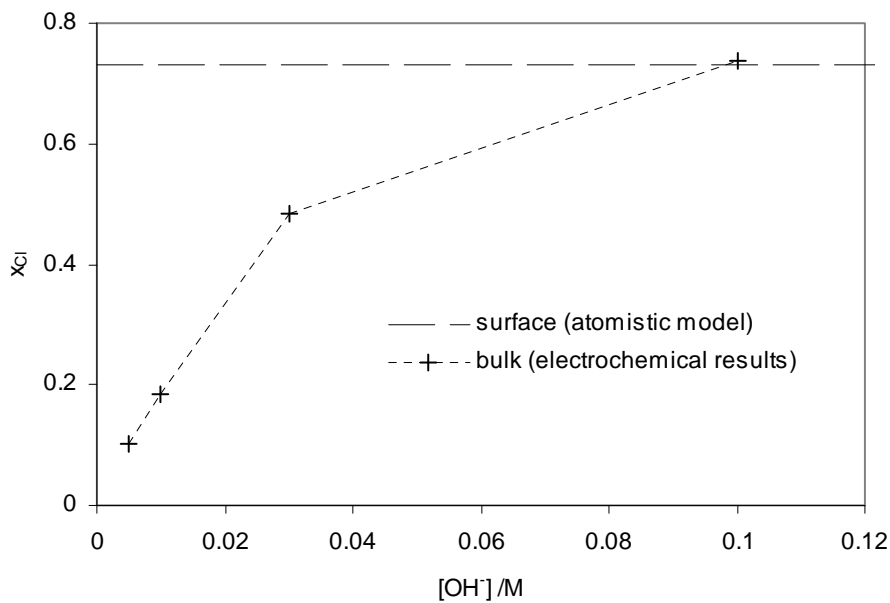
Figure 5-9: Ratio of chloride molar fraction as a function of hydroxide concentration from atomistic modelling and electrochemical results compared to migration calculations
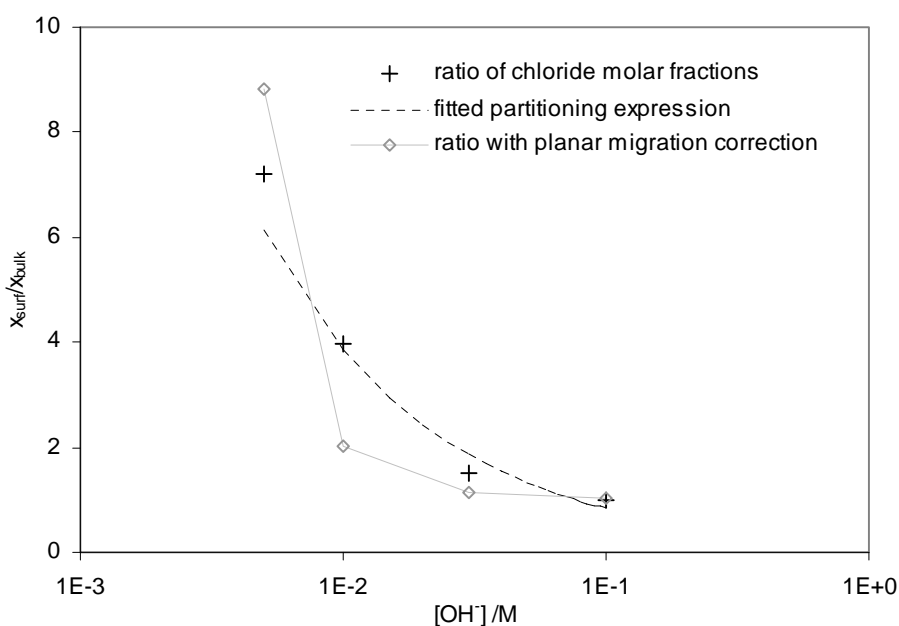
Figure 5-10: Illustrative output of simple fixed flux chloride migration finite element model showing spatial variation of chloride molar fraction for a 0.01 M NaOH, 0.0023 M NaCl electrolyte
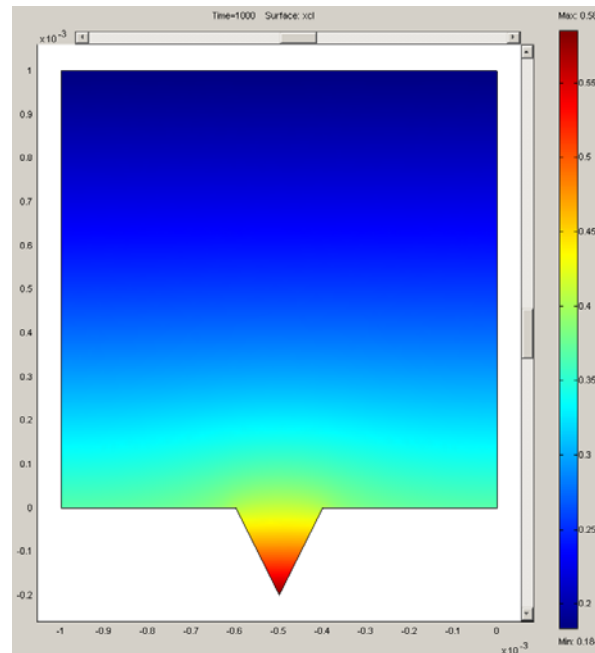
It is also interesting to apply the atomistic modelling results in predicting the pH-chloride passivity and pitting boundaries. The calculated pH required to prevent chloride induced breakdown on the basis of the atomistic model is shown in Figure 5-11 along with the electrochemical results described above and the fuel pond storage specification. In addition this figure shows the atomistic model results corrected by the chloride molar fraction ratios arising from the migration calculations. This shows that the atomistic model results can be semi-quantitatively reconciled against experiment on the basis of simple allowances for migration effects. The boundary for crevice geometries is also an important outcome as this is consistent with operating experience that real fuel elements may be vulnerable to pitting at chloride concentrations <10 mg kg^{-1} and that crevice specimens are more susceptible to attack (Section 2.3). Although these results are presented as indicative and further validation would be required prior to predictive applications, a good correlation is noted between the different data sets and the specification for fuel storage chemistry. It may be that specific geometric parameters (such as crevice dimensions), will relate to a characteristic initiation behaviour in terms of the passivity-pitting boundary.

Figure 5-11: Illustrative pH-chloride boundaries for passivity and pitting on the basis of atomistic model, migration calculations and electrochemical results
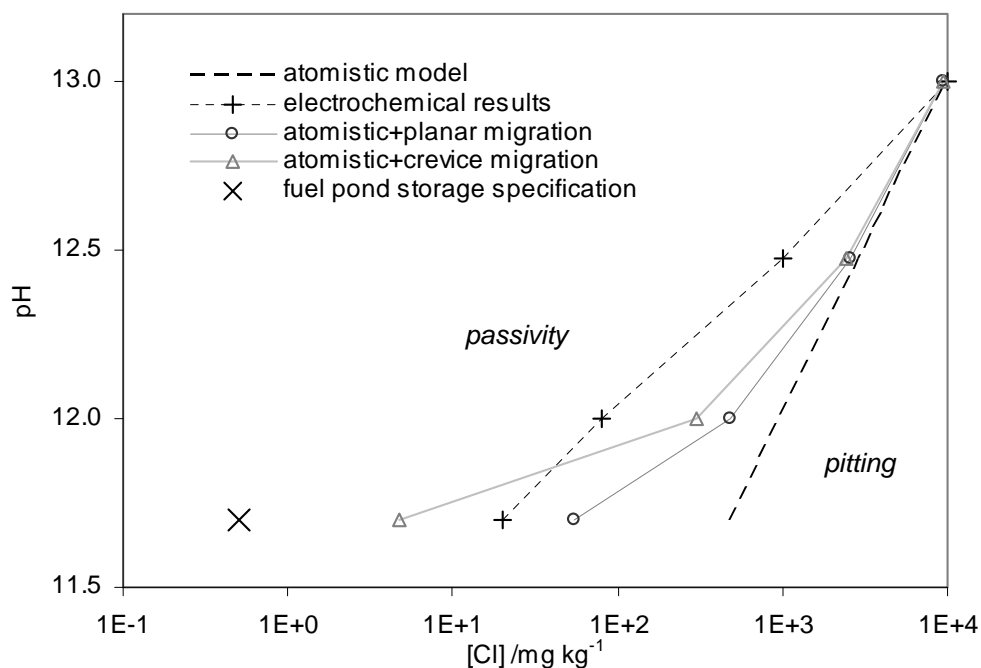
Further calculations were undertaken for adsorption and substitution of fluoride ions on the MgO surface. These were undertaken in a similar manner to that described above with replacement of the halide atoms at surface positions. This produced a similar trend in results but notably showed negative substitution energies at substantially lower surface coverages than chloride (see Figure 5-12). This is again an important result as it is consistent with the inhibiting effect of fluoride on chloride induced breakdown being due in part to ion competition for surface adsorption. As magnesium fluoride is a stable insoluble phase, modification of the bulk lattice is expected to stabilise rather than depassivate the film.

The point of zero substitution energy has been calculated and used to predict the passivation – fluoride inhibition boundary (Figure 5-13), which can be seen to be consistent with the fuel transport chemistry specification.

Figure 5-12: Calculated energy differences (dE) for MgO 310 surface (DMol^3) with adsorption-only and 17% fluoride surface substitution for varying fluoride coverage

% coverage (of 5 co-ordinated surface groups)
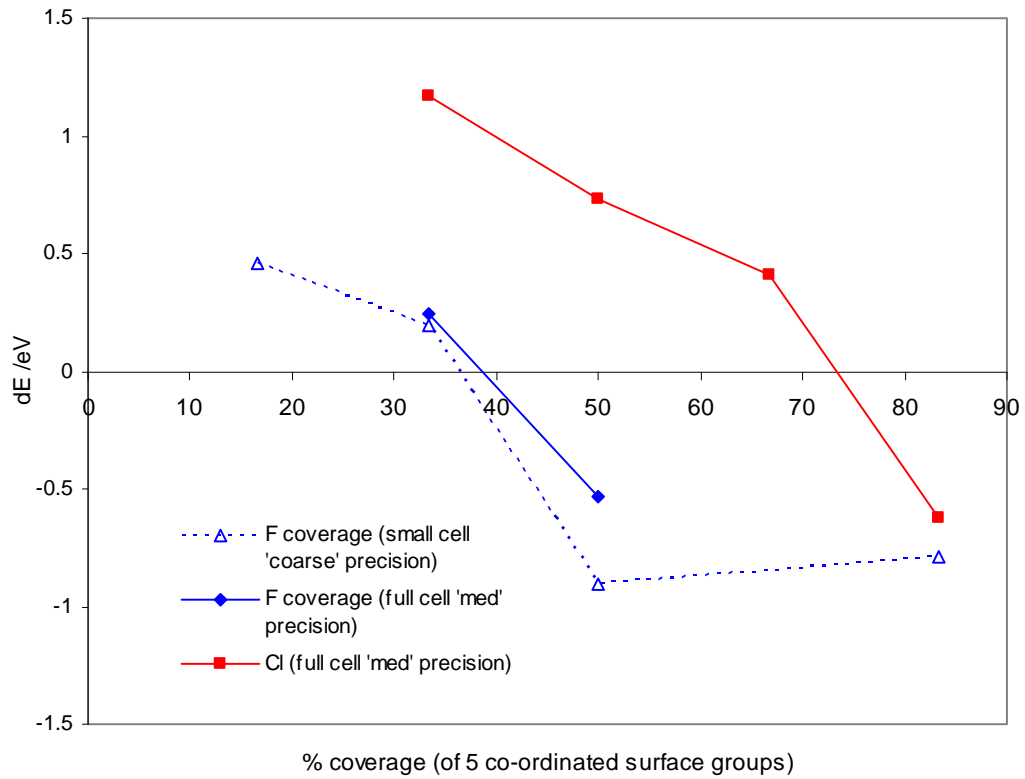
Figure 5-13: Indicative boundary between passivity and fluoride inhibition on the basis of atomistic model
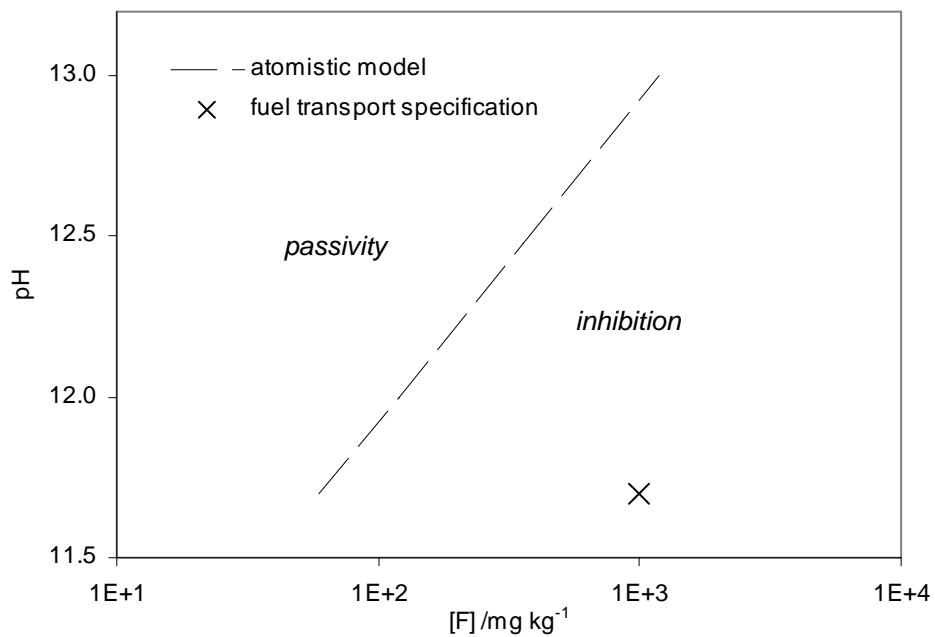
5.3   Outcomes of Atomistic Passive Film Modelling

The application of quantum mechanical lattice simulation methods to the MgO-water-halide system as an analogue for the magnesium passive surface has been undertaken and described here.

The simulations have investigated a magnesium oxide surface with varying coverage of hydroxide and chloride groups which were geometrically optimised and energies calculated by DFT methods.

As fractional coverage (adsorption) of chloride on the magnesium oxide surface increases, the energy difference of surface lattice substitution reduces and becomes negative for coverages above ~75%.

For the higher chloride adsorption fractions, the calculated lattice geometry became non-convergent in a number of cases depending on the specifics of the geometry and calculation. In these cases, detachments of lattice sub-units was observed. This may indicate preferential dissolution of the lattice, although the behaviour under solvated conditions at a real interface will be more complex, and a more robust interpretation is that the lattice surface has ceased to be stable.

Calculations have been undertaken to understand the sensitivity of the results to (i) different atomic orbital basis sets, (ii) diverse DFT codes and (iii) approximations to account for solvation effects. Whilst these different conditions lead to small differences in the values of the chloride fraction which corresponds to zero substitution energy, they are consistent is predicting that at high chloride concentrations, chloride admission into surface positions of the MgO lattice becomes energetically favourable.

At lower concentrations, chloride does not appear to strongly interact with the passive film. The transition from stability to instability appears to occur over a relatively small range of chloride coverage which is consistent with the rapid depassivation observed in electrochemical tests. This supports a rapid cascade failure mechanism in which chloride would follow the propagating surface and would also result in the defect arriving at the metal substrate with an occluded concentrated phase of chloride which would be consistent with formation of a salt film.

Further scoping calculations have been undertaken relating to the effect of fluoride which are also consistent with experiment in predicting the inhibiting effect of this anion.

The calculated coverage corresponding to the point of zero substitution energy agrees closely with the bulk concentration of chloride required to cause film breakdown at high pH in electrochemical tests. Simple calculations of the effect of migration at an interface on chloride molar fraction shows that the atomistic results may be reconciled with the electrochemical results and fuel storage regimes.

Ab initio atomistic modelling of the magnesium oxide lattice surface structure, supported by some simple migration calculations, has provided a credible mechanism for depassivation in magnesium which has been shown to be semi-quantitatively consistent with observed electrochemical behaviour and plant operating experience.

6   Magnesium Microelectrode Corrosion Investigations

This section discusses corrosion investigations employing magnesium microelectrodes aimed at clarifying the pitting mechanism of Magnox and magnesium. The general characteristics are discussed in Section 6.1 with comparison to the behaviour of Magnox macroelectrodes. This shows that electrodes of small dimensions undergo salt film corrosion, in both potential dependent (ohmic) and potential independent (mass transport limited) regimes. Section 6.2 presents further results focussing on the ohmic behaviour of two dimensional electrodes, which corresponds to the behaviour of magnesium under low potential polarisation. Tests relating to the behaviour of microelectrodes in the mass transport limited salt film regime are reported in Section 6.3.

The fabrication and application of magnesium microelectrodes (Sections 3.2 and 3.3) for study of corrosion behaviour is understood to be novel, this not having been previously reported in the available literature.

6.1   Characteristics of Microelectrode Electrochemistry

6.1.1   Passive behaviour

The results of anodic polarisation tests under passivating conditions for a magnesium microelectrode (Type D) and a Magnox Al-80 macroelectrode are shown in Figure 6-1. Whilst showing broadly similar characteristics in terms of the shape of the Tafel region and limited anodic current behaviour, it is striking that the microelectrode current density is over an order of magnitude greater than the macroelectrode. Although some moderate uncertainties could be attributed to the electrode area measurements due to effects such as surface roughness, or non-circularity of the cross-section (which could expected to be larger for a microelectrode), it can be ascertained through visual inspection that these errors are of small magnitudes.

In order to attempt to reconcile this discrepancy, a series of simple finite element models were used to calculate the impact that electrode size might be expected to have on diffusive flux of species near the surface.

Figure 6-1: Typical anodic polarisation results for magnesium microelectrode (red) and Magnox macroelectrode (black) in pH 11.7 electrolyte
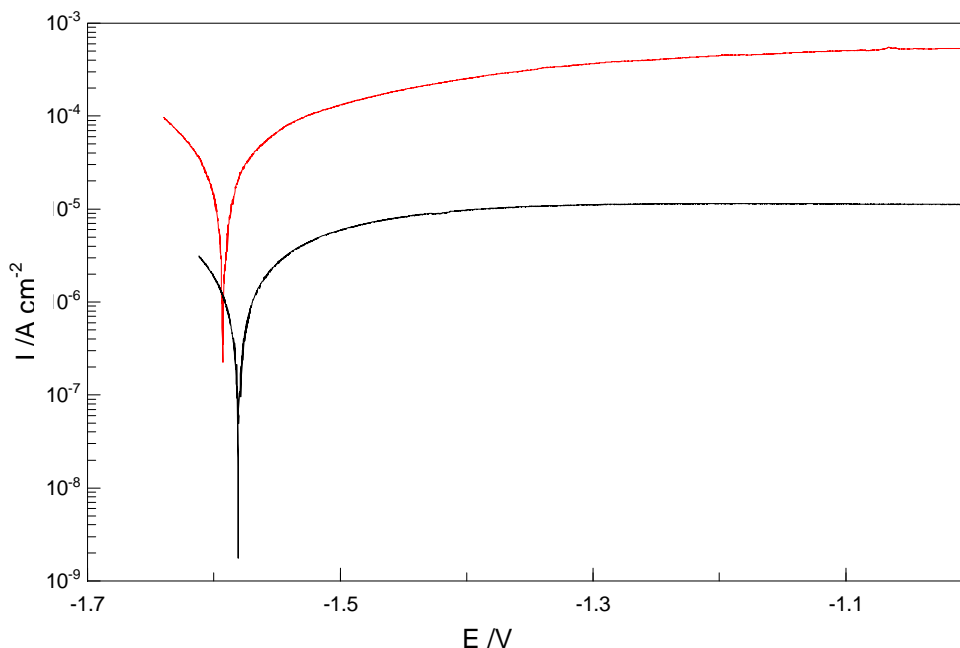
These employed a 3-dimensional model (as described in Section 3.6) comprising a cubic subdomain of which five faces represent bulk solution interfaces and one face represents an inert mount with a circular electrode surface in the centre. Transport is based solely on diffusion of a single species. The model is based on the assumption that magnesium ions will be present at the electrode surface at the solubility limit ($7x10^{-5}$ mol m^{-3}). The microelectrode scale model has d = 10^{-3} m, with the circular electrode surface radius, r = $6.25x10^{-5}$ m. This was then scaled up in the same size ratio with d = 10^{-2} and 10^{-1} m. The dimensions of the electrode at the larger of these sizes is comparable to the standard macroelectrode size used in the electrochemical tests.

Some initial solutions at the larger size (where the ratio of standard mesh size to concentration gradient will be largest) showed that the behaviour at short time scales is sensitive to the mesh size (Figure 6-2), so a minimum mesh size constraint at the electrode surface of 3 x 10^{-4} m is applied which appears satisfactory in producing reasonable convergence for timescales greater than a few seconds. The concentration profile at t = 1000 s and the change in J_{diff} over time at a position 10^{-6} m from the electrode surface at the centre point are shown in Figure 6-3 and Figure 6-4 respectively.

Figure 6-2: Sensitivity of calculated Mg²⁺ diffusional flux at electrode surface to finite element model mesh size constraint
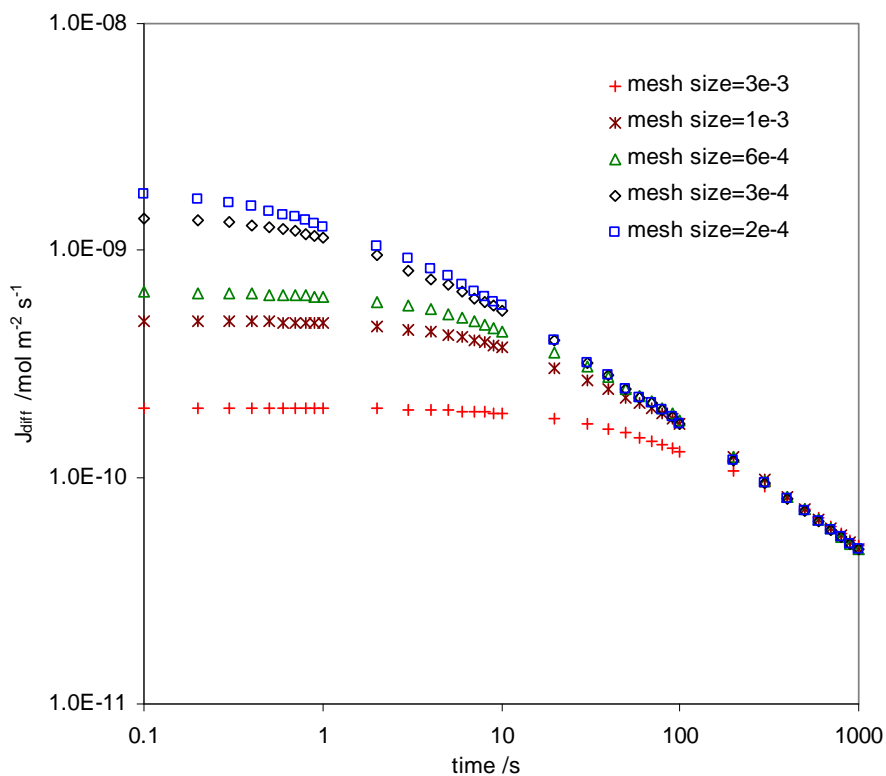
From these results, it may be expected that a microelectrode of the dimensions used may experience a substantially enhanced rate of mass transport at the surface due to radial diffusion.

The discussion of film growth in Section 4.2 does not quantitatively consider the effects of solution mass transport, as this is proposed to have a lower order, although nonetheless potentially influential, effect. Consequently, it is not possible to apply the predicted kinetic information to the specific film formation mechanism and thereby mechanistically reconcile the difference in current density on the basis of mass transport.

Figure 6-3: Calculated Mg^{2+} diffusional flux at electrode surface for circular electrode domains of varying size
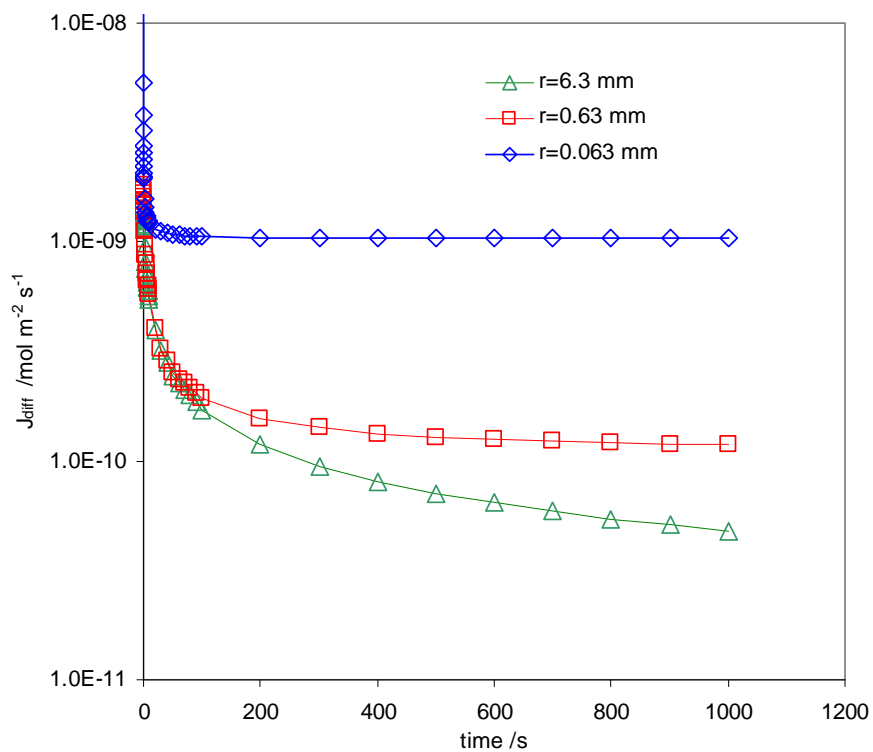
Figure 6-4: Calculated Mg^{2+} concentration at electrode surface for circular electrode domains of varying size
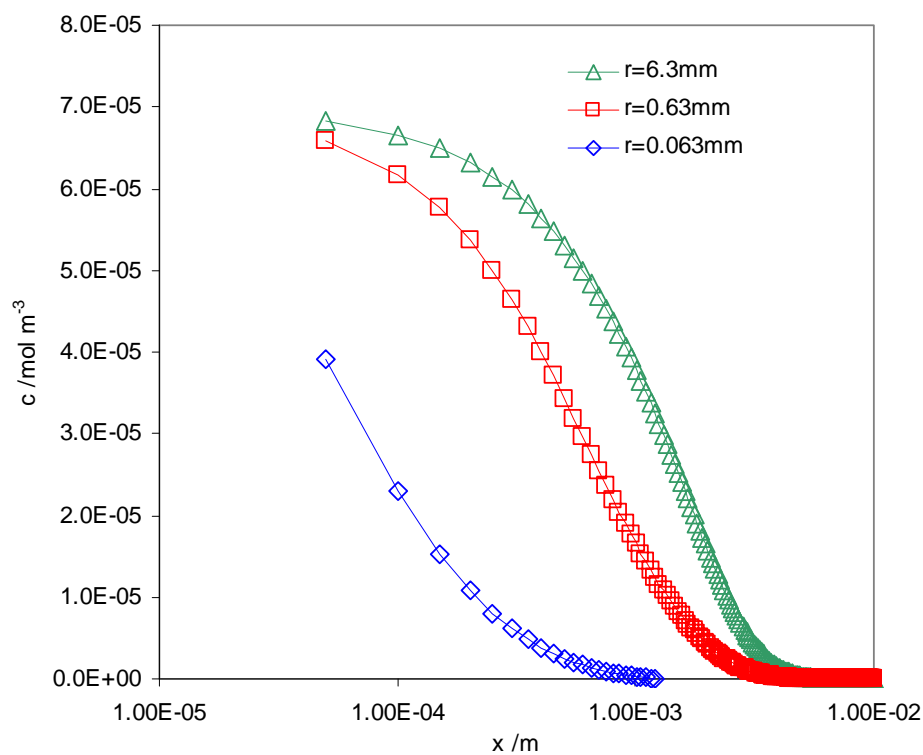
A series of further simple tests comparing the behaviour of micro and macro-electrodes in varying pH (Figure 6-5) clearly shows that the microelectrodes are more strongly affected than the macro-electrodes which supports this postulation. The results produced by Gonzalez Torreira (2004) also show the somewhat higher corrosion rate of magnesium compared to Magnox Al80, which could also be a contributor to the discrepancy here. It may therefore be considered that whilst the difference seen in current density in microelectrodes has not been fully reconciled, it does not appear at odds with the understanding of processes taking place or reduce confidence in the interpretation of results.

Figure 6-5: Anodic polarisation results for magnesium microelectrodes (red, green, yellow) and Magnox macroelectrodes (black, blue, purple) in pH 11.7, 12.6 and 13 electrolytes respectively
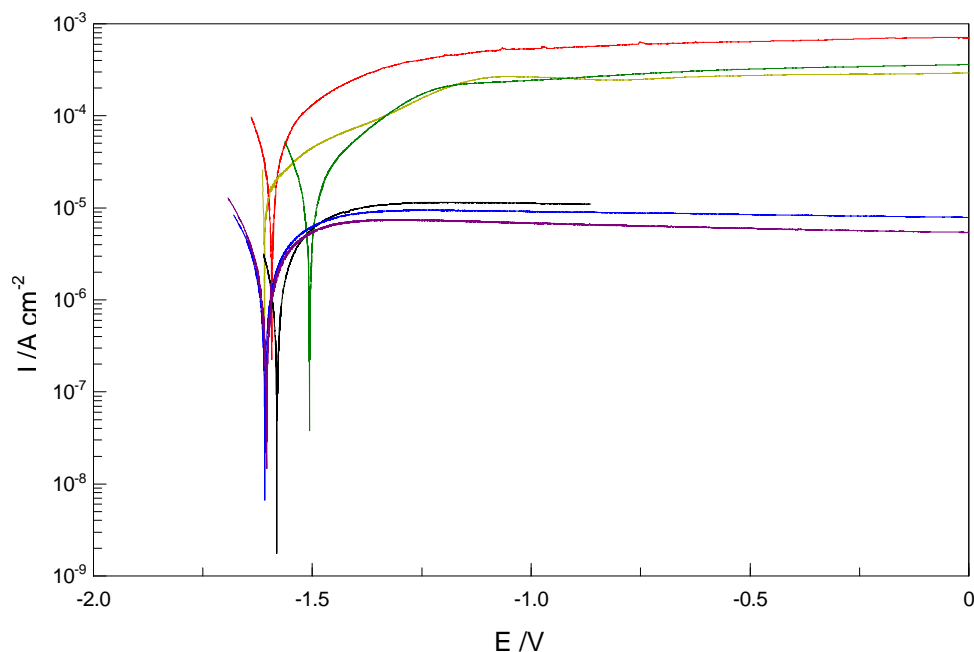
6.1.2 Localised corrosion

Anodic polarisation tests in the presence of chloride produced a breakdown in passivity at around +2 V vs Ag/AgCl (for 6×10^{-3} M chloride), somewhat more anodic than that observed in macroelectrodes and further notable differences were in evidence (Figure 6-6). A peak current density was observed shortly following pitting initiation and was confirmed by visual correlation to correspond to surface corrosion of the microelectrode surface with extensive hydrogen evolution. Once the entire surface was corroded, the current reduced and became less noisy. This was followed by an extended period of electrode dissolution with a characteristic periodic current transient observed to correspond to hydrogen bubble emission from the pit cavity. The current densities

observed agree closely with reported by Beck & Chan (1983), a further confirmation that salt film corrosion is occurring. The fact that the current density under conditions of one-dimensional diffusion (within the pit cavity) is consistent with previous work is also an additional indication that the enhancement of the microelectrode limiting current density under the passive regime (prior to formation of a cavity) is largely related to transport by radial diffusion.

Figure 6-6: Anodic polarisation of magnesium microelectrode (black dashed line) and Magnox macroelectrode (grey solid line) showing initiation of localised corrosion
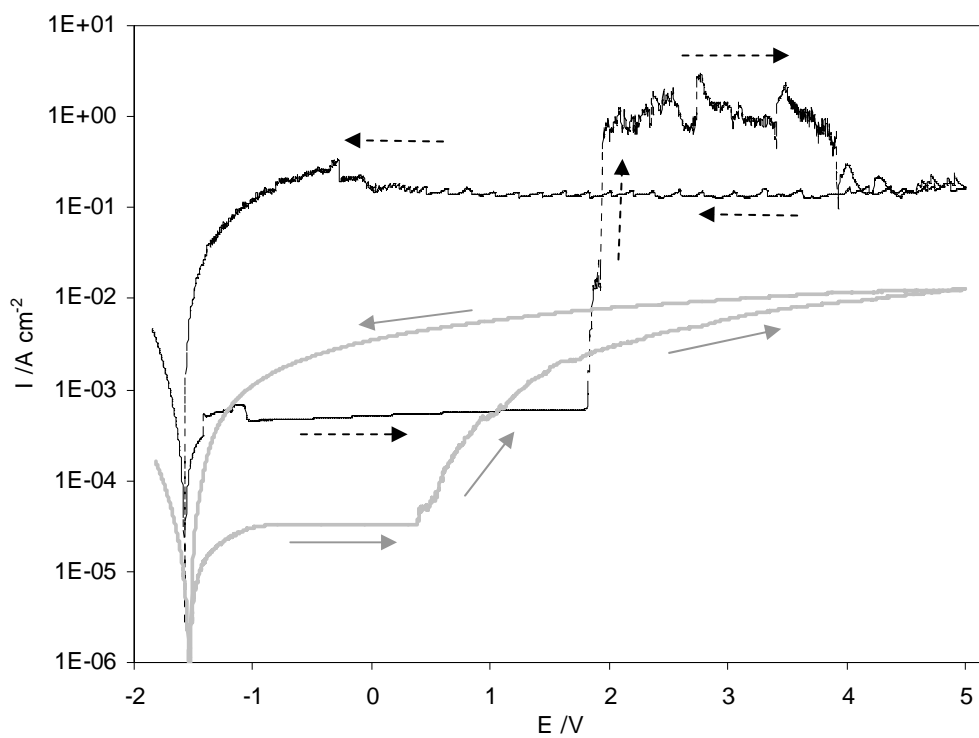
Figure 6-7: Electrochemical current (upper) and applied potential (lower) during potentiodynamic polarisation of magnesium microelectrode in pH 11.7 electrolyte with 200 mg kg^{-1} chloride
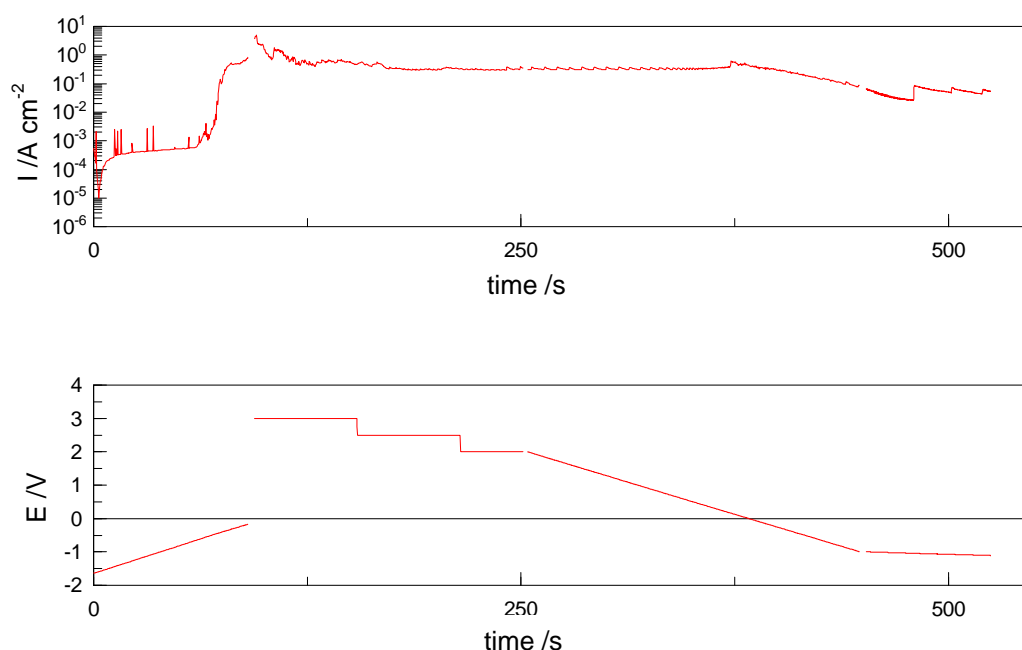
The current response in this phase of behaviour was found to be potential independent, falling gradually in notional correspondence to transport in a cavity of increasing depth (Figure 6-7). This also corresponds closely to the results of Beck & Chan (1983) using a macroelectrode in concentrated chloride electrolytes and also those produced for steel and aluminium microelectrodes in artificial pit studies (Moayed & Newman, 2005, Soltis *et al.*, 2007) and is a clear indication that the magnesium surface is undergoing salt film dissolution. The behaviour is in notable contrast to magnesium macroelectrode behaviour under similar chemical conditions, where the current clearly remains under ohmic control at all potentials (Figure 6-6). In some cases, the current was observed to drop to low levels, consistent with re-passivation of the pit, which is suggested to be a result of blockage of the cavity by hydrogen bubbles or precipitated corrosion product. It was found that a continuous polarisation was required to maintain dissolution as interruptions led to repassivation. Also, periodic variation of potential was found to be advantageous in avoiding spontaneous passivation, which corresponds to previous experience of one-dimensional electrode dissolution (Cook & Newman, 2002). Although sustained dissolution did occur in electrolytes of 6×10^{-4} M chloride (20 mg kg^{-1}), this behaviour was much more variable and prone to apparent re-passivation. Nonetheless, this is a significant observation as this concentration is within the range that could credibly be considered in a storage pond fault scenario.

A transition from potential independence to ohmic behaviour was observed on reduction of potential. This is seen as an increase in the rate of hydrogen evolution as the transition potential is approached, followed by an increase in current with voluminous hydrogen production which stabilised but nonetheless remained at a relatively high rate with the current subsequently behaving ohmically. The potential at which this transition occurred showed a certain amount of variability between tests, although the range covered potentials which could be considered credible within a fuel storage pond environment (Figure 6-6).

A correlation of videomicroscope recordings and electrochemical results has been undertaken to allow identification of the corresponding processes occurring on the electrode surface (Figure 6-8 and Figure 6-9). During the potential independent phase of dissolution, a characteristic variation in current density is evident (Figure 6-9) and this may be unambiguously identified as coinciding with evolution of single hydrogen bubbles from the microelectrode pit cavity. It can therefore be proposed that these transients represent increases in convective transport within the cavity due to laminar flow around the moving bubbles. The influence of convective transport from hydrogen bubbles has been discussed further in Burrows *et al.* (2012).

Figure 6-8: Electrochemical current for potentiodynamic polarisation of magnesium microelectrode with correlated videomicroscope images showing initiation of localised corrosion and establishment of stable dissolution/pitting
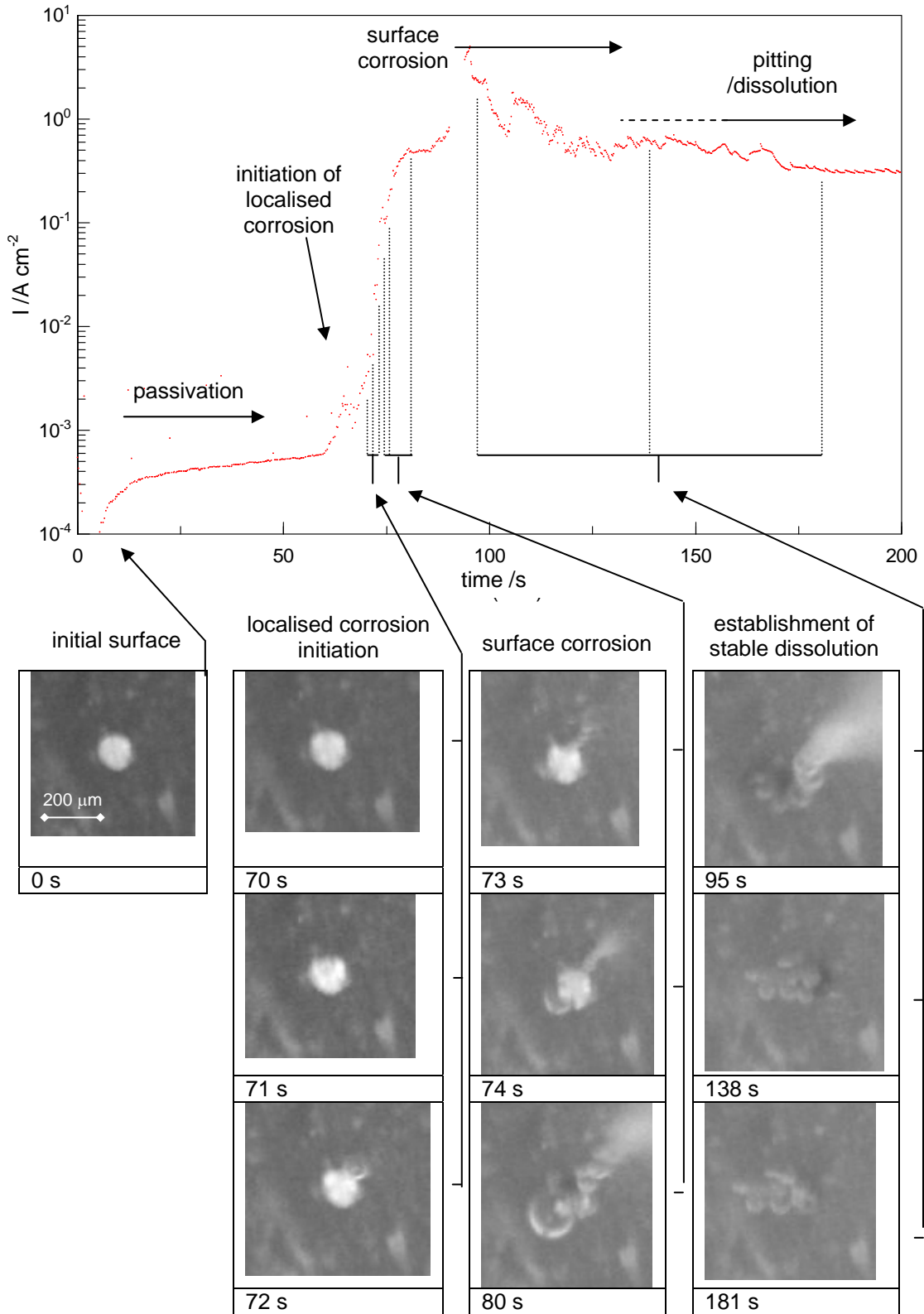
Note: Applied potential shown in Figure 6-7

Figure 6-9: Electrochemical current for potentiodynamic polarisation of magnesium microelectrode with correlated videomicroscope images showing potential independent dissolution/pitting and transition to ohmic control
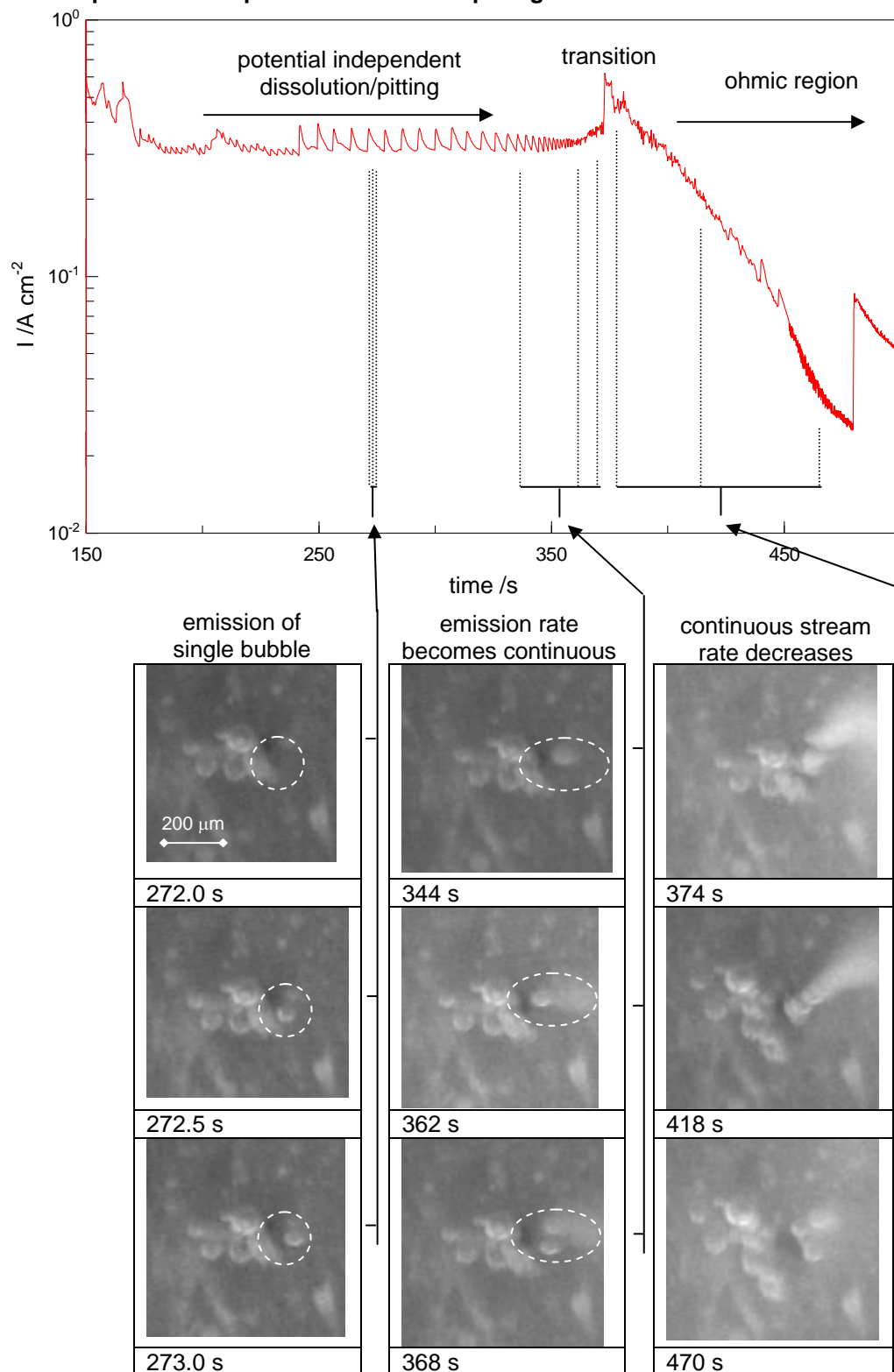
Note: Applied potential shown in Figure 6-7

Figure 6-10 shows the potential independent section of several artificial pit tests, with the noisy initial sections removed. This is compared to the predicted current density for metal dissolution under a salt film limited by one-dimensional diffusion (e.g., in an artificial pit) of corrosion product species away from the saturated interface (Moayed & Newman, 2005).

$$i = \frac{nFDC_{sat}}{h}$$
(6-1)

Where n is the number of electrons involved, F is the faraday constant, D is the diffusion coefficient, C_{sat} is the saturated concentration of the salt and h is the pit depth.

The standard value of 5.9 mol dm^{-3} (CRC, 2001) is used for the saturated concentration of magnesium chloride (C_{sat}) and a range of Mg^{2+} diffusion coefficients slightly below the standard value of 1.4 x 10^{-9} (CRC, 2001) are shown on the basis that diffusion rates may be depressed in the concentrated phase. It is assumed that the pit depth may be related faradaically to cumulative charge, with a current efficiency of 2 being used for the initial periods of each test before the salt film is established and the hydrogen generation rate is high, although the initial depths are nonetheless thought to be underestimated to some extent due to difficulties with treatment of the initial data. The magnitude of the current density and rate of decrease with pit depth show reasonable correspondences to those expected for one-dimensional salt film dissolution, although the values appear somewhat low and attenuation may be less rapidly than would be expected. It is clear that transport was increased by convection from plug flow of electrolyte resulting due to periodic movement of these hydrogen bubbles. This is also consistent with some of the large variations in current observed, as bubble movement will be less consistent than a homogeneous process. It is also notable that the current density peak at the transition point on return to ohmic control is substantially above the limit predicted for one-dimensional diffusion, which is a clear indication of the effect of convection from hydrogen bubbles on corrosion product transport and corrosion rate. Corrosion product transport within the artificial pit cavity has been discussed further in Burrows *et al.* (2012).

Figure 6-10: Potential independent regions from a series of scoping polarisations of magnesium microelectrodes in pH 11.7 electrolyte with 6×10^{-3} or 6×10^{-4} M chloride
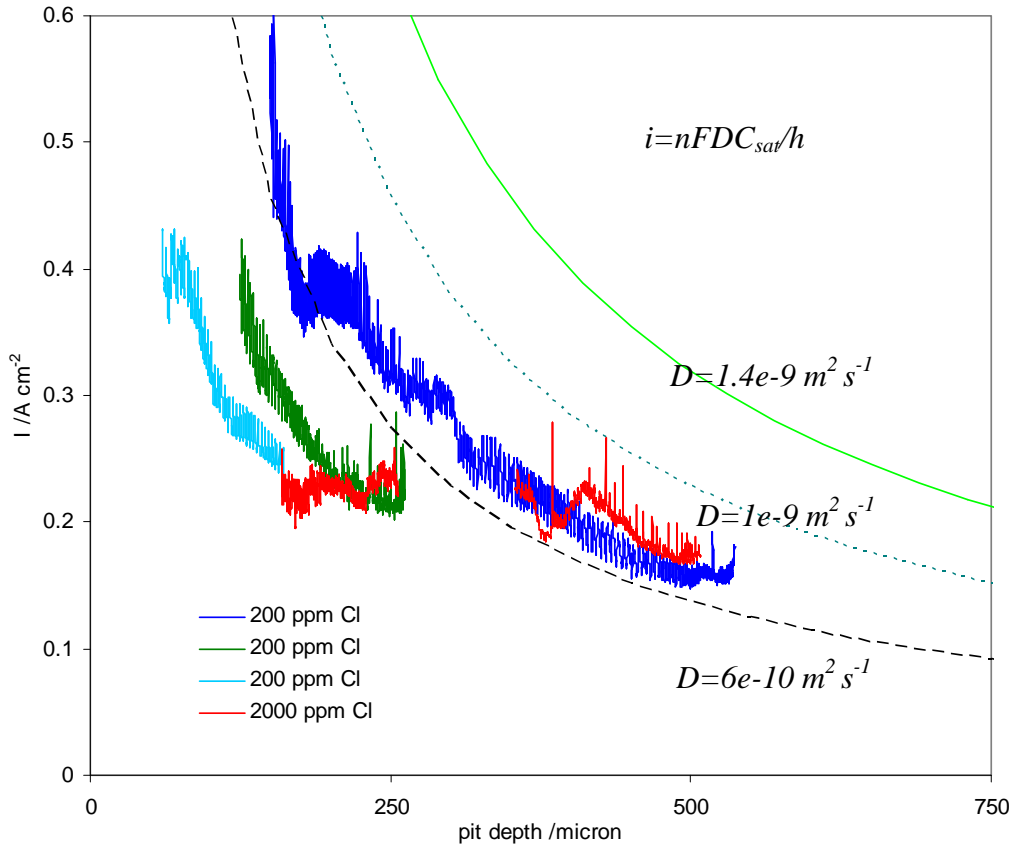
Collection of EIS measurements was undertaken for a microelectrode corroding in the salt film region (Figure 6-11). A low frequency range AC excitation was superimposed at a potential of +2V to maintain the salt film coverage, which was confirmed through short periods of potentiostatic measurement between each test. For frequencies between ~2 and 100 Hz, the spectra were near linear and appeared consistent with a mass transport limited regime, as well as being quite consistent. At frequencies below this, the response became noisier and more variable. Immediately following removal of polarisation, the OCPs measured for microelectrodes were around -1.75 V and rapid ennoblement was observed. The OCPs reached -1.6V within a few hundred seconds and further rose to eventually stabilise around -1.2V. Further EIS measurements were undertaken at OCP during this period and are shown in Figure 6-12. These are consistent with re-passivation of the surface and formation of a stable oxide layer, as observed for a freshly formed surface (Section 4.1.1).

Figure 6-11: Results of polarised EIS measurements for magnesium microelectrode undergoing salt film corrosion (successive tests at ~400 s intervals)
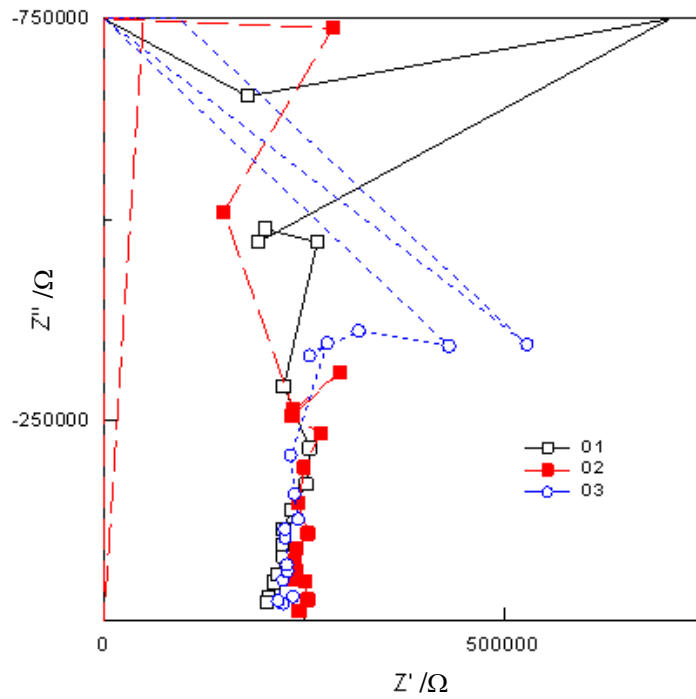
Figure 6-12: Results of open circuit EIS measurements for repassivating magnesium microelectrode following salt film corrosion (successive tests at ~400 s intervals)
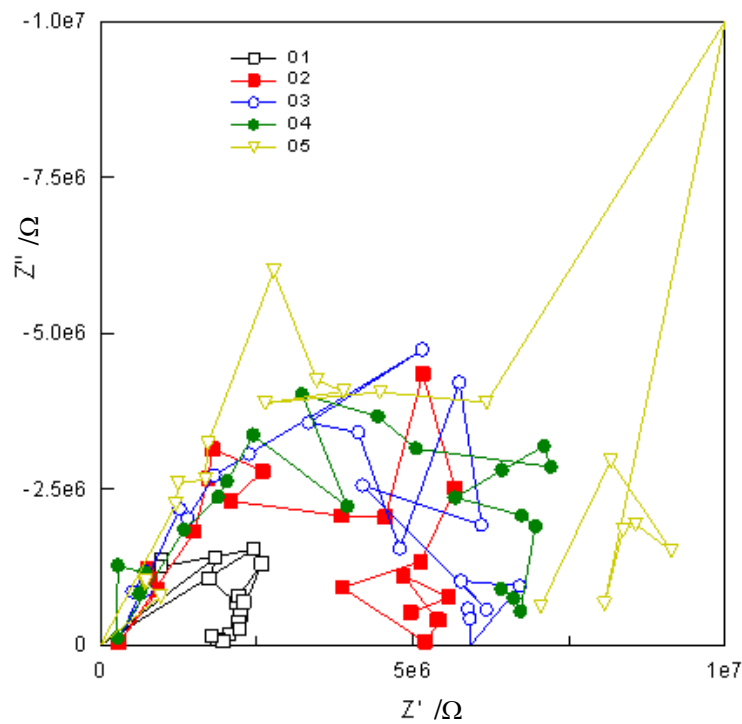
Figure 6-13 shows the transition to ohmic control observed for artificial pits under potentiodynamic control once the potential was reduced below the value required to maintain a salt film over the entire surface. This shows comparable behaviour between tests, with the transition potential and the slope of dI/dV being similar, although large variations in current density are in evidence which can be attributed to hydrogen bubble behaviour around the cavity entrance. The slope is weakly affected by a change in scan rate, suggesting that the predominance of processes on the electrode surface is changing fairly rapidly, in this case, probably passivation of locally corroding sites. The transition potential does not appear to be highly sensitive to cumulative charge, suggesting that the *iR* drop within the cavity is not a dominant factor.

Figure 6-13: Transition from potential independent region to ohmic control for several polarisations of magnesium microelectrodes in pH 11.7 electrolyte
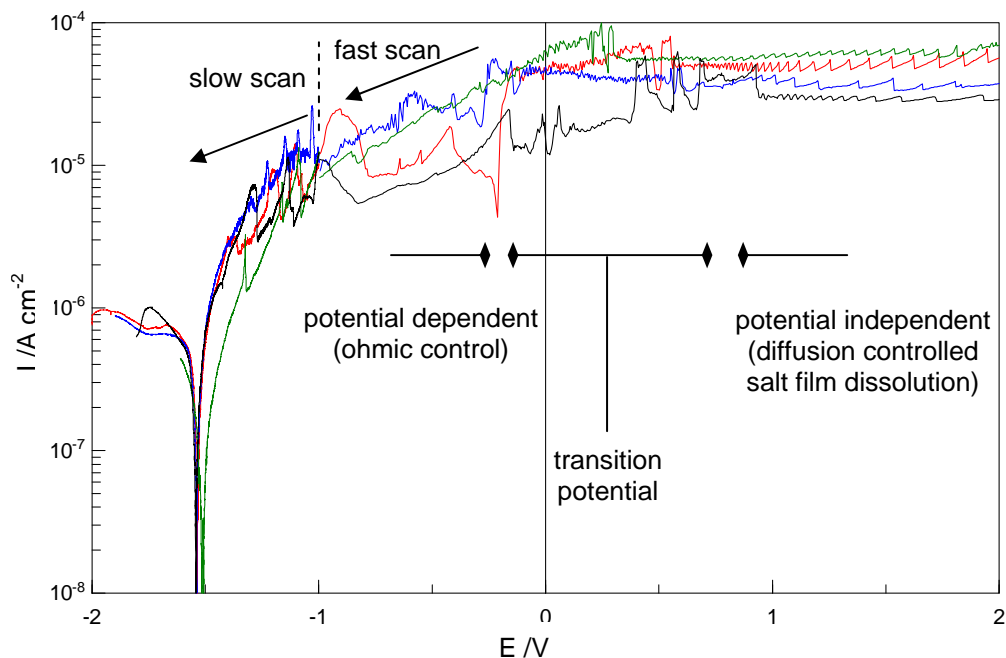
The effect of variation in bulk electrolyte chloride concentration on pitting potential can be seen in Figure 6-14 and Figure 6-15 which also show that a higher scan rate may have the effect of shifting the breakdown potential to a slightly more anodic value. The effect of polarisations close to the pitting potential on pitting induction time has been discussed in Section 4.1.

A further opportunity presented by microelectrodes is the observation of current transients against a much lower noise background. A single corrosion event on a microelectrode represents a very large proportional change in the current density for

that electrode in comparison to a macroelectrode. Therefore pre-initiation events may be much more readily identified.

Figure 6-14: Polarisation of magnesium microelectrode at fast scan rate of 20 mV s^{-1} in pH 11.7 electrolyte with 6x10^{-4}, 6x10^{-3} and 6x10^{-2} M (20, 200 and 2000 mg kg^{-1}, respectively) chloride
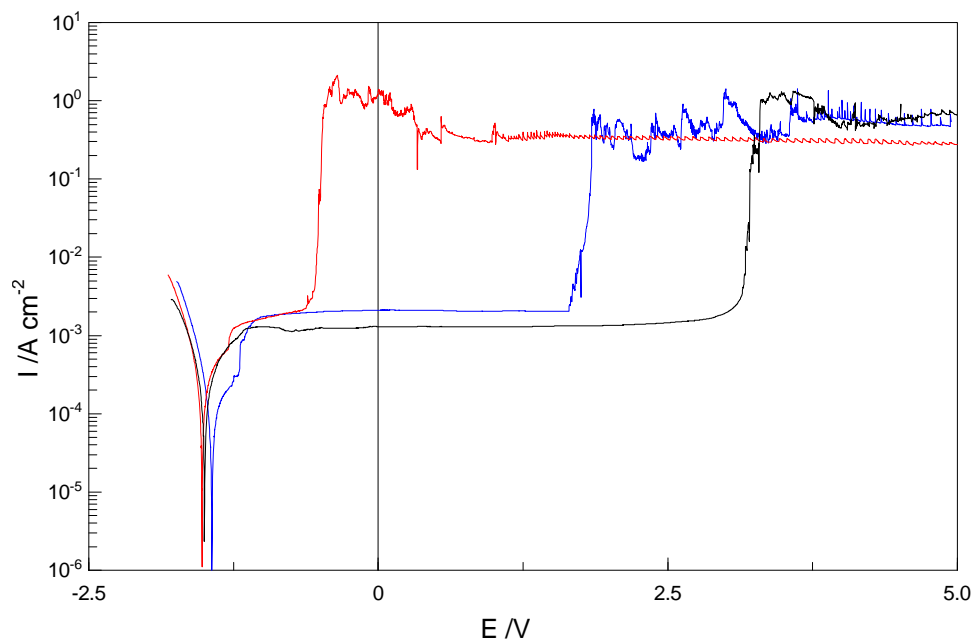
Figure 6-15: Polarisation of magnesium microelectrode at slow scan rate of 2 mV s^{-1} in pH 11.7 electrolyte with 6x10^{-5}, 6x10^{-4} and 6x10^{-3} M chloride
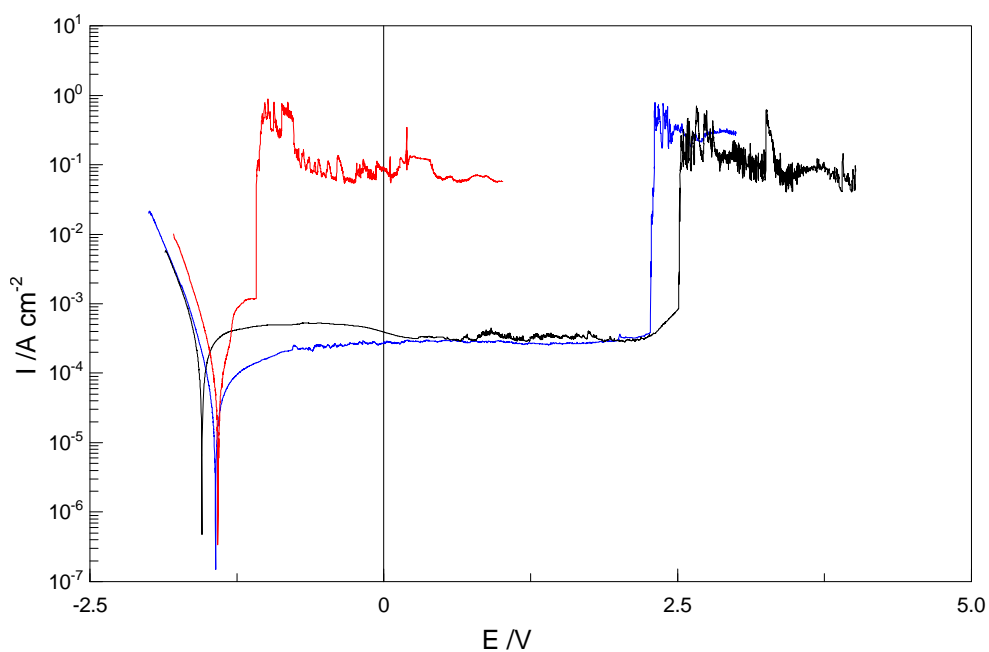
Potentiostatic tests at potentials cathodic of the pitting potential were undertaken using microelectrodes to allow increased resolution of current transients against a much lower background of surface activity (see Section 3.3). A higher alkalinity electrolyte was used to minimise effects of carbonate absorption over the duration of the test which would have been expected to have an increased effect on chloride breakdown characteristics. Although a sustained onset of pitting does not occur in any of these three tests, a large number of transients are in evidence with the number and size of these increasing as the potential becomes increasingly anodic. It is also evident that the transients reduce in frequency and magnitude with increasing elapsed time. An exception to this is the lower potential test, where, the transients, although remaining small, seem to increase in frequency towards the end of the test. This could be explained qualitatively through a mechanism in which there are a finite number of initiation sites on the electrode surface which at high overpotential are subject to transient attack quite rapidly, but are then rendered inactive, whereas at lower overpotential these are initially inactive but activate following an induction period (as observed in Section 4.1), leading to a different distribution of transients over time. These trends can also be clearly observed in the standard deviation of the current density (Figure 6-17)

Further studies on the corrosion behaviour of magnesium microelectrodes are described in Sections 6.2 and 6.3.

Figure 6-16: Corrosion current from potentiostatic polarisations (at +1V, +0V and -1V vs. Ref.) of magnesium microelectrodes in pH 12.3 electrolyte with $6x10^{-4}$ M chloride
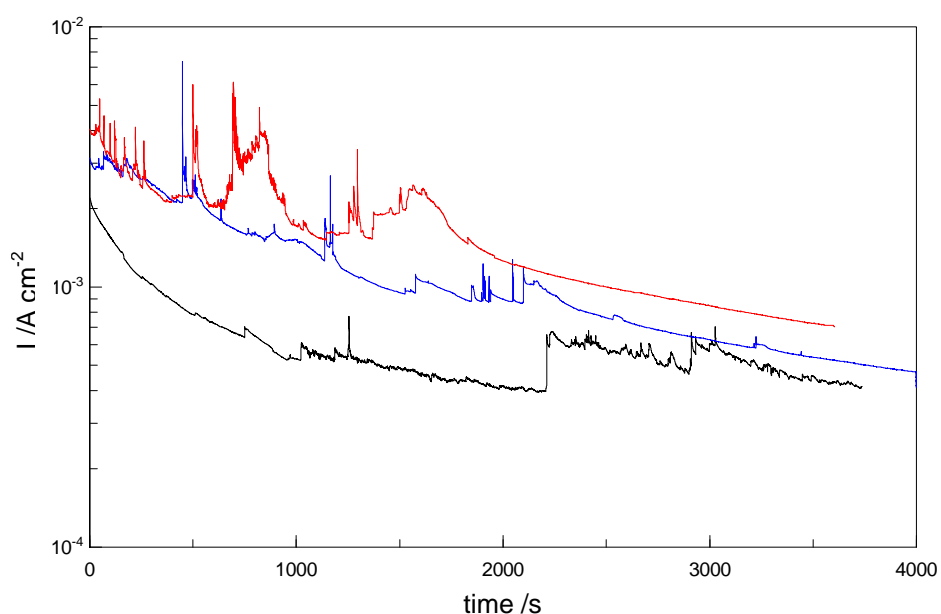
Figure 6-17: Standard deviation of electrochemical current for potentiostatic polarisations (at +1V, +0V and -1V vs. Ref.) of magnesium microelectrodes in pH 12.3 electrolyte with 6x10^{-4} M chloride
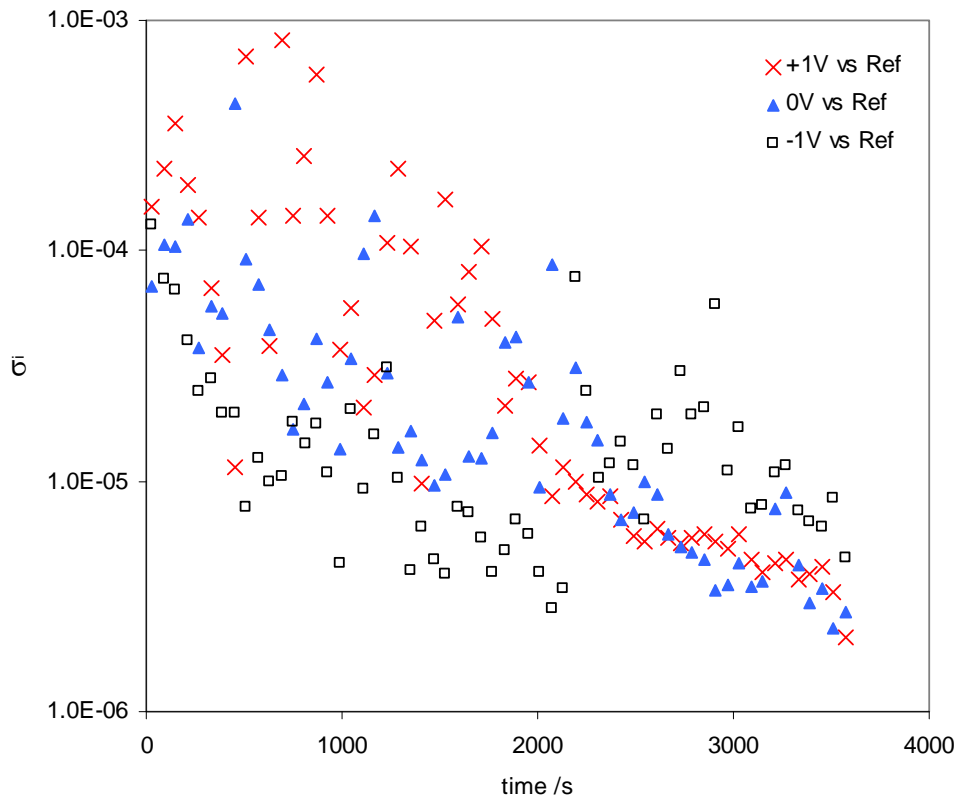
6.1.3   Summary of microelectrode characterisation tests

Magnesium microelectrodes show clear characteristics of salt film dissolution with an extended potential independent region in alkaline electrolytes with chloride concentrations ranging down to those consistent with a fuel storage pond fault scenario.

These results correspond closely to previous observations of salt film corrosion in other materials and notably, the detailed work of Beck & Chan (1983).

The limiting current density of microelectrodes under passive behaviour is somewhat higher than that observed for macroelectrodes which appears to be due to a predominance of radial diffusion.

Pre-initiation transients may be clearly observed on polarised microelectrodes, with highly polarised electrodes showing frequent, large transients, the frequency of which decreases from an initially high value, whilst electrodes at a lower overpotential exhibit

an increasing frequency and size of transients. In either case, the behaviour seems broadly consistent with activity at a similar number of activation sites which deactivate after producing a transient.

The electrochemical behaviour associated with initiation of localised corrosion on a magnesium microelectrode has been correlated with the physical processes occurring on the surface with videomicroscopy. This has shown that localised corrosion initiates near-spontaneously, which is consistent with previous observations and the passive film breakdown model described in Section 5. Following a brief period of surface corrosion, the microelectrode enters into a salt film dissolution regime with a low rate of hydrogen evolution.

The magnitude of the current density under salt film conditions agrees well with previous work on this mechanism and the rate of change with equivalent pit depth is comparable to that expected for one-dimensional diffusion from a saturated surface although the influence of convection arising from laminar flow around hydrogen bubbles is apparent.

When the electrode potential drops below a certain value, a return to ohmic control is observed. The point at which this transition occurs shows some variability but the range covers potentials consistent with credible galvanic polarisation sources in the pond storage environment.

6.2   Two Dimensional Artificial Pit Studies

This section describes tests employing transoptic microelectrodes behaving as two dimensional artificial pits. Correlated quantitative image analysis is used alongside electrochemical measurement to allow the determination of current efficiency. The practical importance of current efficiency is apparent in allowing accurate derivation of corrosion rates from electrochemical data. It is also of mechanistic importance alongside additional observations on the corrosion behaviour under these specific conditions.

6.2.1   Transoptic microelectrode test methodology

A standard electrochemical cell was used to undertake potentiostatic tests on optically mounted magnesium microelectrodes (Type E) with simultaneous microscope image capture.

The microelectrodes used in these tests were produced from commercial high purity magnesium foil of 10 micron thickness (as described in Section 3.2) and were of 2 mm width. A standard electrochemical set up was employed as described in Section 3.1. Electrodes were subject to a short period of open circuit monitoring before potentiostatic tests were initiated with potential held at values between -1.2 and 4 V. Note that all potentials presented in this section are relative to Pt pseudo-reference electrode.

The arrangement of the microelectrode in the electrolyte and orientation of image capture is shown in Figure 6-18. Due to the low hardness of the electrode mount, polishing was not possible and instead it was necessary to cleave the material to produce a straight clean electrode edge. For the same reason, the original mount surface had to be preserved to maintain good optical properties. In order to allow a good image of the electrode edge, this was cut at around 10 degrees from the normal so that the damaged, non-optical, cut edge did not produce reflections or refractions that would interfere with the image. Similarly, the effect of hydrogen bubbles at, or in close proximity to the electrode edge was minimised by inclining the electrode angle at an angle of approximately 10 degrees to the horizontal. A corresponding correction to the image area is applied based on this simple geometry. The small depth of focus of the optical apparatus meant that the entire electrode surface was not in focus during the tests, and the well resolved region was limited to an area near the electrode surface.

Although tests were typically undertaken for periods of several minutes, it is mainly the initial 30 seconds of each test which has been subject to analysis. This is the part of the test in which the fastest rate of dissolution occurs, so is of most interest. Restricting the

time period also reduces the potential effect of electrode crevicing. This occurs when electrolyte is able to penetrate along the interface between the electrode and mount. It is highly undesirable as it can change the mechanism of corrosion by providing a crevice of restricted geometry in addition to that intended and for microelectrodes will substantially change the electrode surface area. Crevicing is mainly prevented by use of a mount material with good edge retention, although for transoptic electrodes, this property is generally compromised at least to some extent. Due to its very high propensity for crevicing, magnesium is particularly prone to these problems. The selection of mount material has been made largely with this issue in mind, as discussed in Section 3.2, however, it is nonetheless evident that these electrodes may be susceptible to crevicing in any case. Crevicing was only observed in these tests at low potentials and once the artificial pit has become well established (i.e., not in the early stages of the test). Consequently, the impact of this effect on the results has been minimised by using the first section of each test.

Interpretation of the electrode images was achieved using semi-automated integration of the pit boundary. For each image, a boundary was defined according to the electrode surface, which was then used as the basis for definition of the boundary for subsequent image. A common boundary was defined for the initial electrode surface to allow the lateral cross sectional area of the pit to be determined by pixel counting. This method substantially reduced the subjectivity of the boundary assignment whilst ensuring consistency between images and greatly improving the sensitivity over that which could be achieved by fully automated edge detection and integration or threshold definition. Boundaries were defined in this manner for a selection of images from each test, mainly using all images from the early stages of the test (1 Hz) with the frequency reducing to around 0.2 Hz by the end of the analysis period. In cases where individual frames were more difficult to process (e.g., due to temporary obscuration of an important area by hydrogen bubbles), or where little change in pit dimension occurred, further frames were omitted to avoid arbitrary boundary definition which would increase uncertainty in the measurement.

The integrated pit areas have been converted into standard units by comparison with the image electrode width which was known from conventional measurements. As noted above, a factor is applied to account for the inclination of the electrode plane, in addition to small corrections to cover pixel counting errors in certain images. The amount of metal dissolved in a particular time period is then available based on a set of assumptions primarily covering the behaviour of the electrode as 2-dimensional, including the absence of under-cutting or crevicing.

The current efficiency has then been calculated as the apparent corrosion rate (from electrochemical current) as a fraction of the total corrosion rate (according to optical measurement of metal dissolution).

Figure 6-18: Diagram of two-dimensional transoptic microelectrode configuration
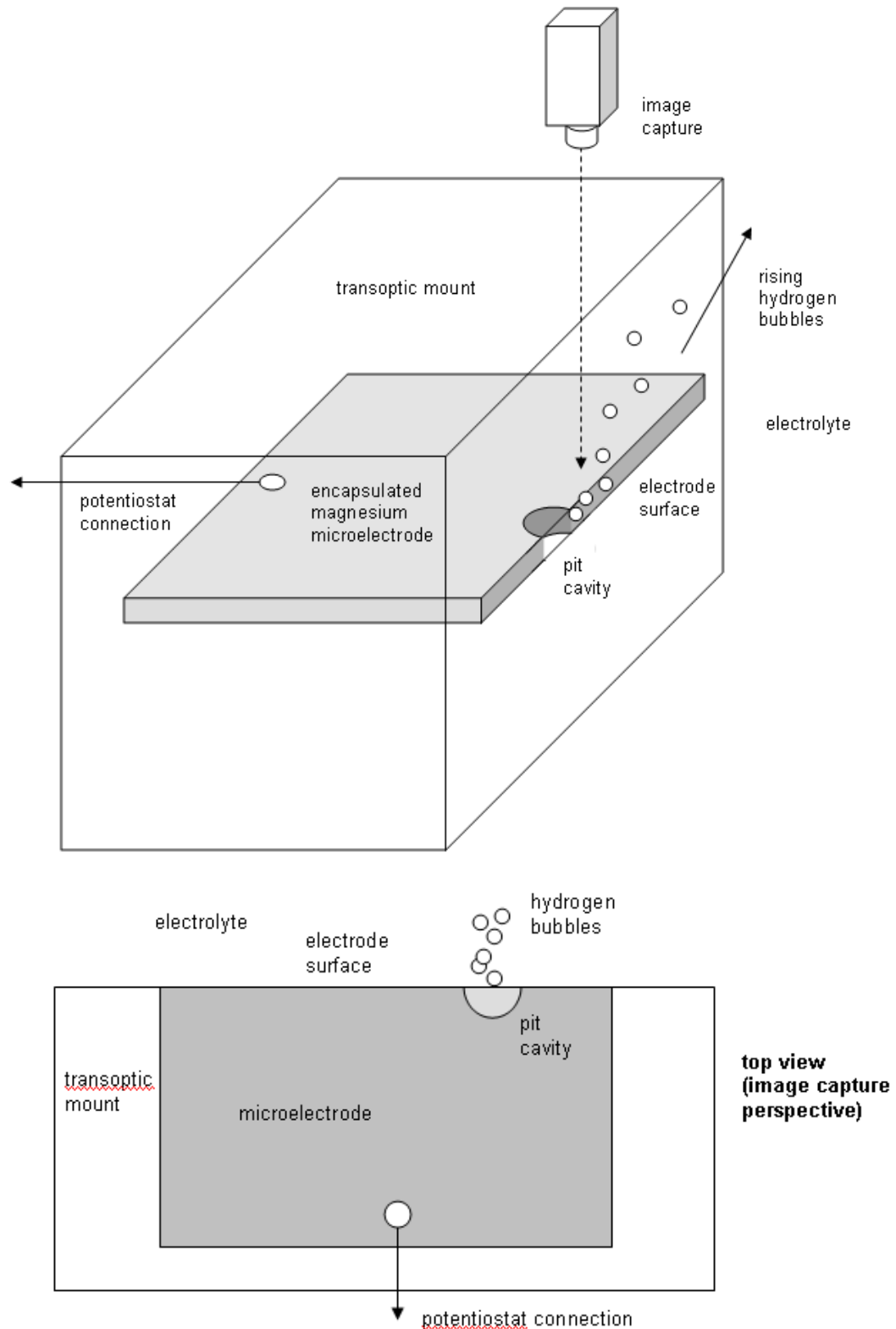
Figure 6-19: Images of transoptically mounted magnesium electrode undergoing 2-dimensional artificial pit dissolution at 4V polarisation (images at 6 and 14 second intervals)
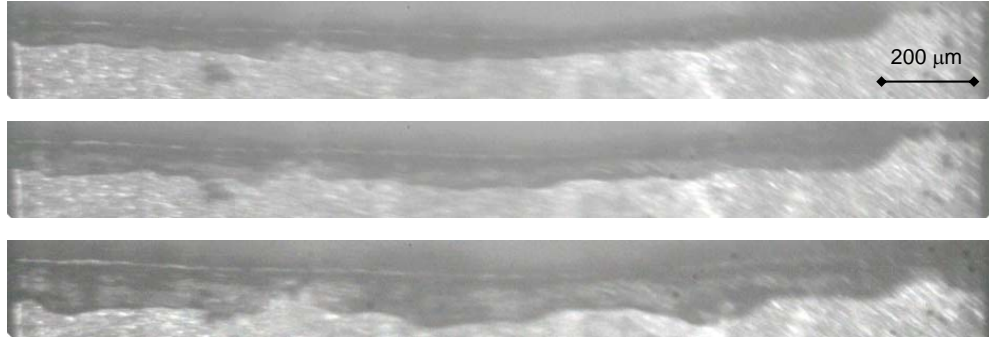
Figure 6-20: Images of transoptically mounted magnesium electrode undergoing 2-dimensional artificial pit dissolution with pit boundary assignment shown
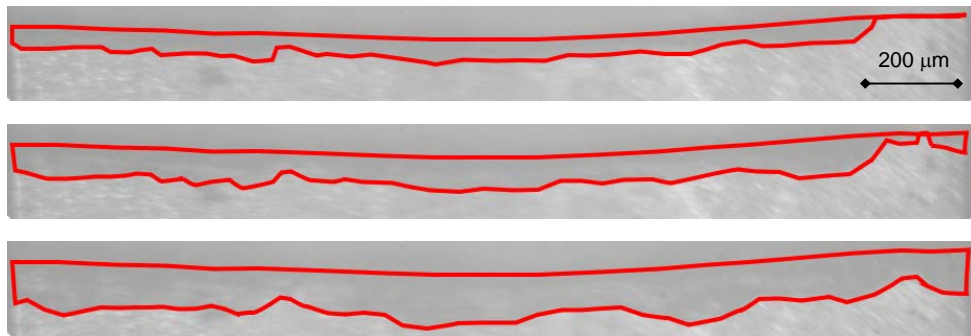
Figure 6-21: Electrochemical current response for transoptically mounted magnesium electrodes undergoing potentiostatic 2-dimensional artificial pit dissolution
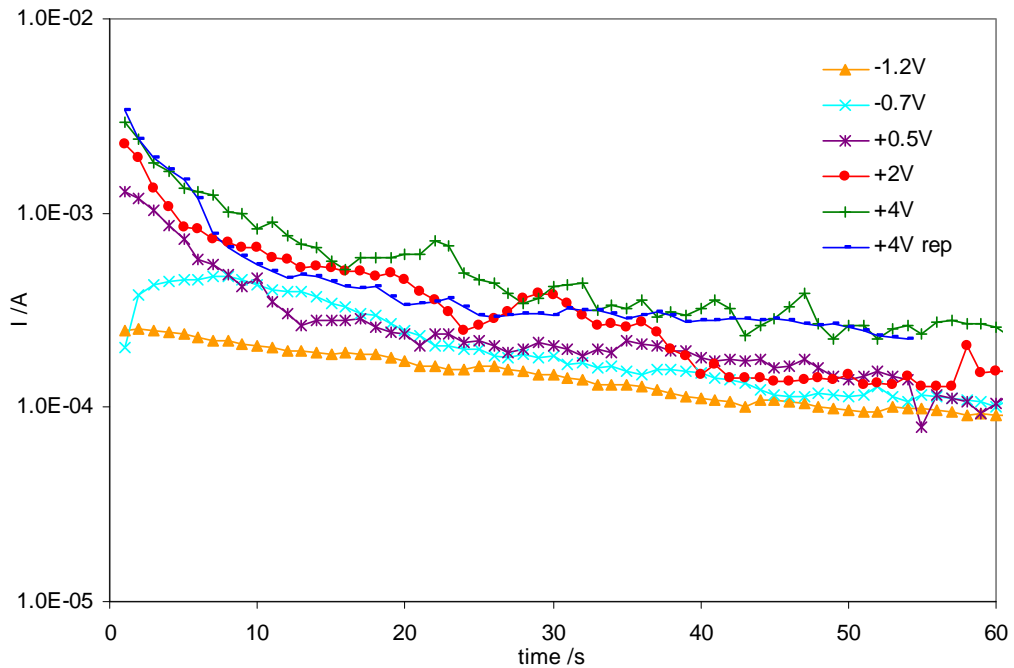
6.2.2   Results of substrate dissolution measurements

The integrated charges show clear potential dependence which is a strong indication that the electrode surface did not have a full salt film coverage. This can also be confirmed from examination of the electrode images which show that although the entirety of the original surface of the electrode is dissolved in all tests, the dissolution is not uniform. In many cases it is very apparent that certain areas are dissolving rapidly whilst others are remaining unaffected for a period of time. It was notable that whilst the extent of undercutting was minimal (no grain dropout was apparent) and corrosion product precipitation in the cavity was not discernable, it was clear that the cavity was full of hydrogen which produced channels in the electrolyte layer and these could be seen to change in distribution according to areas of electrode activity. Although the image of the exterior of the electrode was poor quality, it was apparent that hydrogen was generated voluminously.

Comparison of the electrochemical and optical corrosion rate results show a good correlation, although it is apparent that there is a sensitivity in synchronisation of the time bases, as the maximum rate of the digital image capture was 1 Hz, which corresponds to a substantial loss of metal. However, these discrepancies would only significantly affect the initial seconds of each test.

164

The calculated current efficiencies show a overall rise from around 60-70% in the first 5 seconds to around 80%, with the exception of the -1.2V test which drops from near 90% to around 80%. These initial fluctuations are treated with caution due to the impact of time-base synchronisation as discussed above. The overall trend from 10 seconds is one of gradual increase and there is a relatively low scatter taking the dataset as a whole. The results for -0.7 and +0.5 V appear more consistent with an initial increase followed by a levelling off, however the -1.2 V test shows an initial decrease and then increases similarly to the high overpotential tests.

6.2.3   Summary of transoptic microelectrode tests

These tests provide not only quantitative information on the current density for polarised electrodes undergoing pitting corrosion, but also provide an insight into the mechanism of pitting for a surface which is not fully covered by a salt film (i.e., is in the ohmic region), which will normally be the case in corrosion tests, or for plant material corroding under galvanic or internal polarisation.

These electrodes were observed to corrode in a manner consistent with salt film dissolution, but were under ohmic control, as typical of a surface with incomplete salt film coverage (Section 6.1). It was also evident that areas of the surface dissolved and stabilised alternately.

The calculated current density showed some variability, probably due to electrode crevicing at the relatively poorly retained transoptic mount edge, but was insensitive to potential and was in the range 60-90%, which agrees well with previous work on magnesium corrosion under electrochemically polarised, and freely corroding conditions.

These results therefore strongly indicate that the mechanism of magnesium corrosion involves dissolution across a salt film even in the absence of a high overpotential.

Figure 6-22: Integrated charge (top), correlated total corrosion measurements from electrochemical current and optical measurement (middle) and calculated current efficiency (lower) for transoptically mounted magnesium electrodes
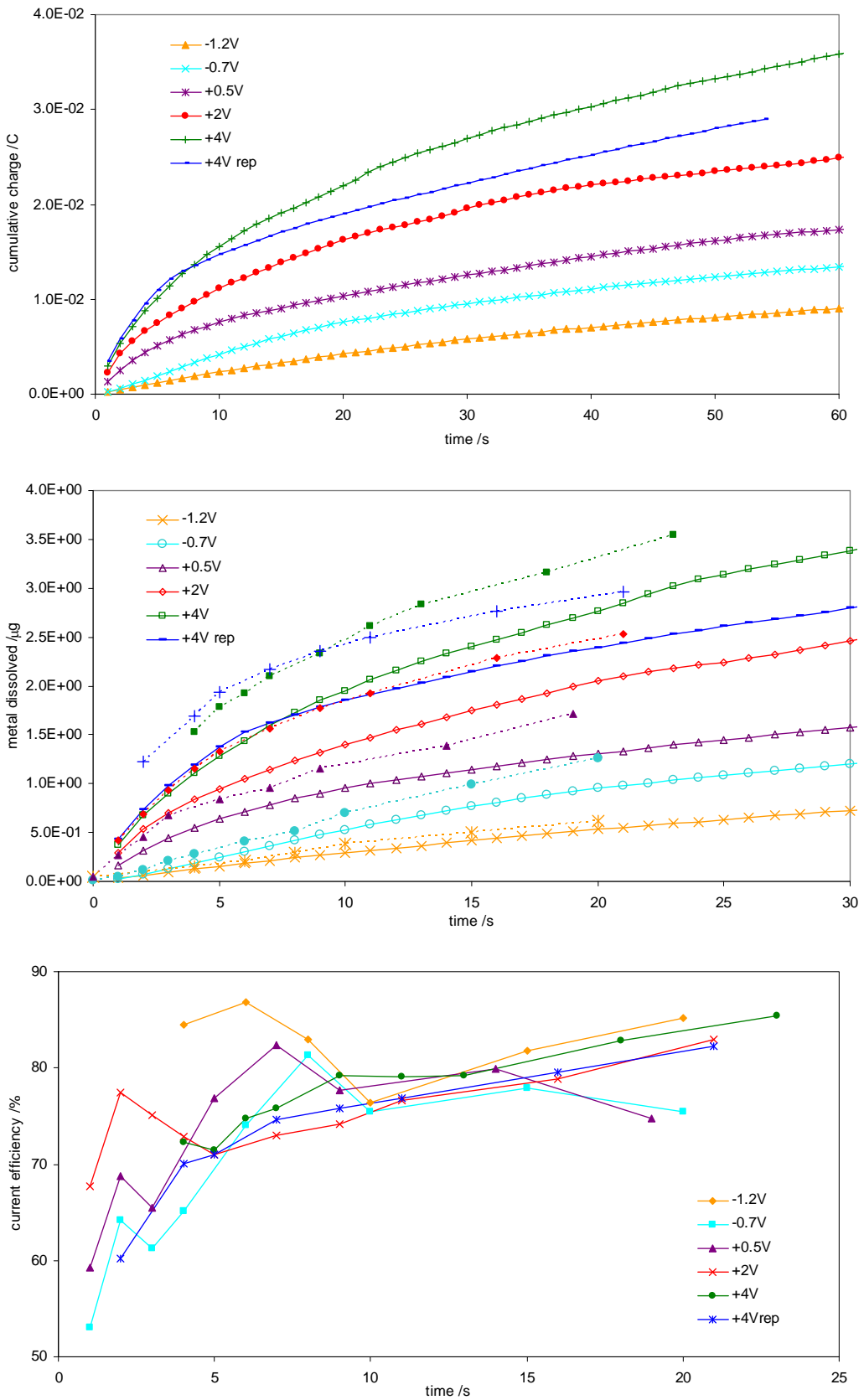
6.3 Magnesium Corrosion under a Salt Film

The involvement of a salt film in the pitting mechanism of magnesium has been shown in the work described in the preceding sub-sections. In this section, detailed investigations of the processes occurring on a microelecrode dissolving under a salt film are reported. The mechanistic implications of changes in predominance of the reactions corresponding to metal dissolution and hydrogen evolution under differing conditions are outlined.

6.3.1 Quantitative videomicroscopy methodology

In this investigation, the mechanism of magnesium corrosion has been examined with respect to the salt film corrosion mechanism. This involved correlated kinetic studies in which the rate of hydrogen evolution was determined using videomicroscopy of magnesium microelectrodes (Type D) under potential control with simultaneous collection of current response data. This is a powerful combination of techniques as it allows highly time resolved quantitative correlation of hydrogen evolution and electrochemical behaviours for material undergoing salt film dissolution, which would not be possible with conventional techniques for a variety of reasons. A number of techniques exist for measuring hydrogen evolution rate, however, the use of quantitative image analysis has allowed a high resolution of rate measurement with relatively little impact on the electrochemical cell.

Although a series of tests was undertaken, the bulk of the analysis has been performed on three particular experiments, which were all at 200 mg kg^{-1} sodium hydroxide (pH 11.7), with differing potentials; two tests were potentiostatic, at potentials of 2V and 4V, and the third was potentiodynamic, with potential decreasing from 3V to -1V (all potentials vs. Ag/AgCl). All these tests were initiated by potentiodynamic anodic polarisation in the same manner as described in Section 6.1. The potentiostatic tests were undertaken at 2000 mg kg^{-1} (6×10^{-2} M) chloride (as sodium chloride) whilst the potentiodynamic test was at 200 mg kg^{-1} (6×10^{-3} M).

High purity magnesium wire microelectrodes (1.23×10^{-4} cm^2 cross sectional area) were utilised, which were produced as described in Section 3.2.

Electrochemical parameters were measured using the standard apparatus as described in Section 3.1. Current information was used to determine the charge passed in a particular time period and consequently the amount of magnesium reacted. This initially

employed an assumption of 100% current efficiency although this is shown to be supported.

Image correlation was performed manually using standard software (GNU Image Manipulation Program, Fraps and Microsoft media suite) to time index hydrogen bubble emission and measure size relative to the known diameter of the microelectrode surface.

The size of bubbles was determined through measurement of the pixel size in 2 dimensions from screen grabs from the video file. The pixel size was derived by measurement of the electrode surface which is a known dimension. For the test at 2V, where a smaller number of bubbles with a greater variation were produced, the dimension of each bubble was derived. For this test only, a third measurement was taken of each bubble and the individual bubble diameter was taken as the mean of the three measurements. For the other two tests, where the bubble dimension was very consistent, a selection of the evolved bubbles were measured in duplicate and a mean of all the measurements was used as an average bubble diameter for each test. For the test at 4V, measurements were made for every second bubble. For the variable potential test, the bubble measurement frequency was decreased as the rate of bubble evolution increased, so that measurements were initially based on every other bubble and were then decreased to every fourth bubble. Towards the end of this test, the rate of bubble evolution was very high and so screen shots contained several bubbles with insufficient separation to allow measurements in two dimensions. In these cases, a single measurement was taken from two bubbles in each shot and these included in the mean as per the other measurements. The approach of averaging bubble sizes rather than using individual bubble dimensions is seen as reasonable for these two tests as the variation in bubble size was not large and there are a large number of bubbles evolved so variations are less likely to be significant. Also, in the later stages of the variable potential test, the rate of evolution and the lack of separation would preclude individual measurement, as noted above. This approach is further supported by visual inspection of the video files which do not show any clear trend in terms of bubble size through the tests. In both these tests (although most notably in the latter part of the variable potential test), there were periods when bubbles could not be counted either due to temporary obscuration of the cavity by larger bubble, or due to presence of a continuous stream of bubbles in which movement was indistinguishable between video frames. In the early part of the potentiodynamic test, the bubbles produced are substantially smaller and are almost all obscured by adherent bubbles. A separate average size has been used for bubbles in this period, and it is noted that the mean size is based on only a small number of measurements

From a mean bubble size (whether for individual bubbles or for a test), the volume and hence the amount of hydrogen comprised were calculated from standard relations. This calculation assumes that the bubbles are exclusively hydrogen and are under standard conditions of temperature and pressure. This is proposed to be reasonable as the rate of carbon dioxide evolution from possible acidic off-gassing of carbonate in the cavity and electrochemical oxygen evolution are expected to be low. Also the bubble size appears to be very stable whereas if bubbles were expelled from the cavity under non-standard conditions then a rapid fluctuation in size would be expected. This size stability also suggests that the frame rate of the video capture is sufficient to gain a good measurement while the bubble at a very similar distance from the lens as the electrode surface (as would be expected for the short focal length microscope optics) which supports use of this as a reference.

The timing of individual hydrogen bubble evolution was measured through frame-by-frame inspection of the video files. At certain points the cavity opening was obscured or other factors prevented clear identification of the timing of emission and no data was derived for these time intervals. For periods in which more than one bubble was present near the cavity entrance, the number of bubbles produced in a particular time period was measured rather than the timing of each individual release. The presence of a continuous stream of hydrogen bubbles was problematic in certain cases where the movement of bubbles was sufficiently regular as to obscure individual motion and no data was generated in these cases. These periods were usually temporary as it was found that small periodic distinguishing characteristics (disruptions in the stream, or occasional agglomeration of bubbles) were frequent and sufficient to enable clear counting of individual bubble evolution.

Corrosion rates were thereby calculated by standard derivations from electrochemical current and evolved hydrogen volume. The current efficiency presented is the apparent corrosion rate (from electrochemical current) as a fraction of the total corrosion rate (corrected for current leakage on the basis of hydrogen evolution rate).

6.2.3   Microelectrode salt film dissolution results

The general behaviour of magnesium microelectrodes has been discussed in Section 6.1. The electrochemical and optical characteristics of the potential independent phases of both potentiodynamic and potentiostatic polarisation tests (at 6×10^{-3} and 6×10^{-2} M chloride respectively) and have been analysed in detail and further observations made below.

169

Figure 6-23: Potential independent region of potentiostatic test on magnesium microelectrode at +4 V showing hydrogen bubble emission transients
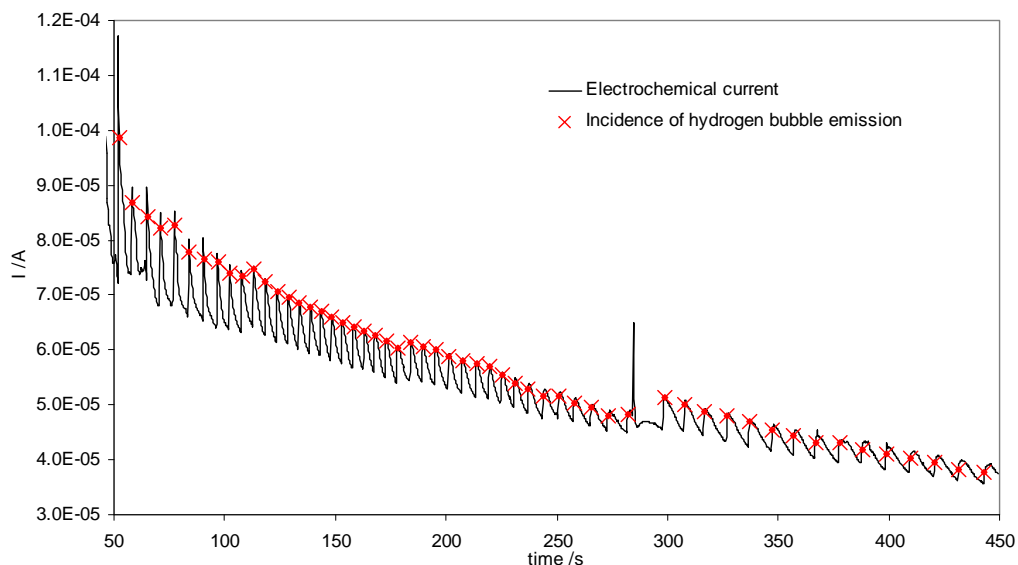
At a static polarisation of +4V (Figure 6-23), the hydrogen evolution transients had a consistent form, which evolved over the duration of the test, and were of relatively high frequency (~0.14 Hz). The size of hydrogen bubbles observed was also very consistent with little variation through the test. The potentiostatic test at +2V (Figure 6-24) exhibited much lower frequency transients (~0.02 Hz) with less consistent forms and a much greater variation in bubble size, with small bubbles corresponding to sharper transients and occasional larger bubbles coinciding with less well defined current responses. The potentiodynamic test (+2.5 to -1V) showed an evolving hydrogen evolution behaviour (Figure 6-25), with the initial stable transients having a high frequency (~0.50 Hz) and low amplitude (corresponding to small hydrogen bubbles), followed by a change to larger transients (~0.16 Hz) similar to those in the +4V potentiostatic test. As the potential fell to close to the transition to ohmic control, the rate of bubble emission increased, until a continuous stream of bubbles was present (~10 Hz).

Figure 6-24: Potential independent region of potentiostatic test on magnesium microelectrode at +2 V showing hydrogen bubble emission transients
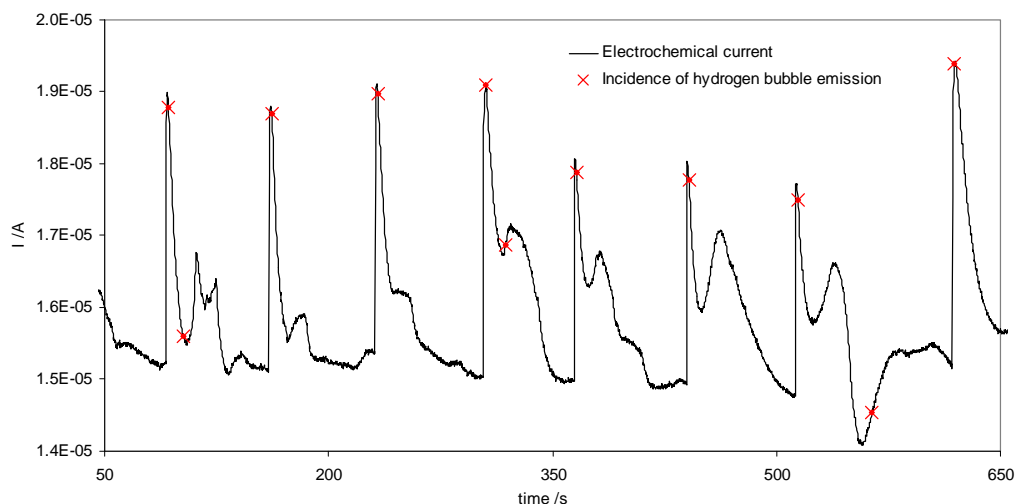
In all instances it was possible to unambiguously correlate hydrogen bubble emission with current transients through the majority of the tests and hence robustly synchronise the time bases. In addition, the form of current transients in these tests can be qualitatively related to hydrogen evolution behaviour, with changes in current transient shape and size generally corresponding to a change in bubble size or presence/geometry of adherent bubbles at the cavity entrance. In Figure 6-23, a gradual change in the form of the transients is apparent, which corresponds to a notional expectation for convective transport in a channel of increasing depth.

The integrated current from a single typical transient (Figure 6-26) corresponds to around 1.4×10^{-10} moles of H_2 which is well over an order of magnitude greater than the equivalent volume of hydrogen observed in a bubble (around 2.9×10^{-12} moles), showing that these transients represent convective transport due to bubble movement in the pit cavity, rather than a change in electrode reaction. In other words, the transients are caused indirectly by hydrogen evolution rather than a direct indication of a competing mechanism. This has been considered further in Burrows *et al.* (2012) and the direct correlation proposed of convective transport due to laminar flow around hydrogen bubbles moving from the saturated solution at the pit base, to the bulk electrolyte.

Figure 6-25: Potential independent region and transition to ohmic behaviour for potentiodynamic test on magnesium microelectrode at showing hydrogen bubble emission transients
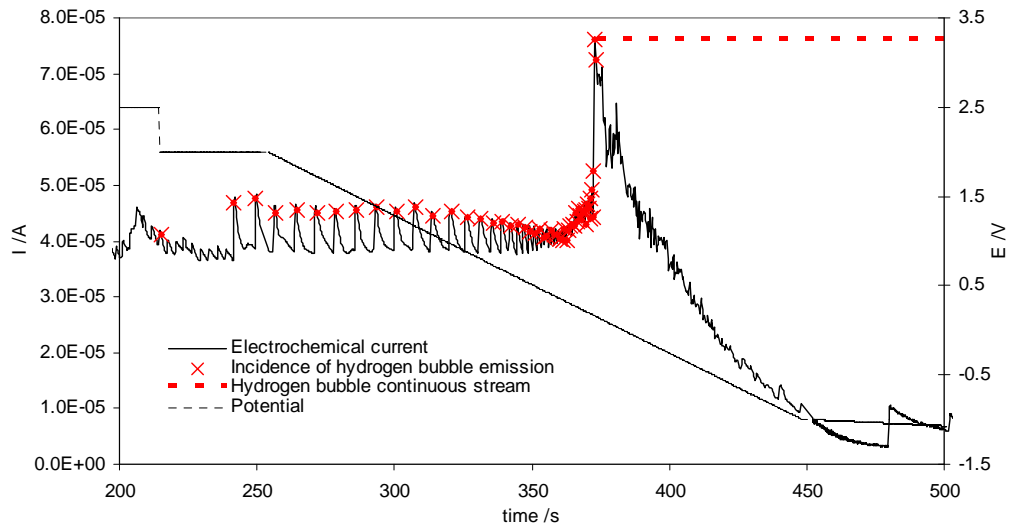
Figure 6-26: Current response and integrated charge covering time period of a single hydrogen bubble emission transient
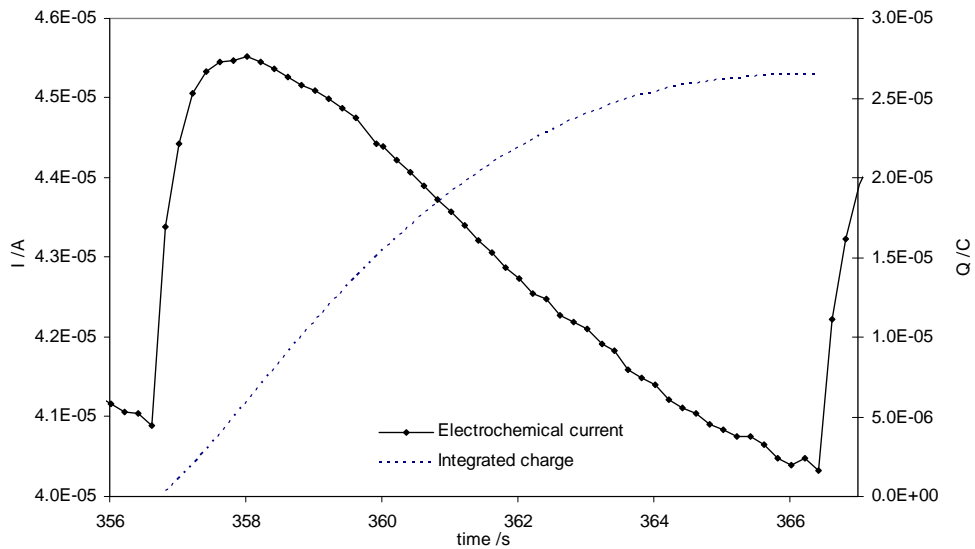
The current efficiency in the test at +4V (Figure 6-27) has a low variance whilst in the test at +2V, the lower bubble emission frequency and greater size range means this parameter is more variable (again implying that the transients are indirect products of hydrogen evolution). These two tests represent potential independent salt film corrosion throughout and comparing the mean current efficiencies (99.85 and 99.61 % for 4V and 2V respectively) with that in the corresponding phase of salt film corrosion in the

potentiodynamic test (99.85%) shows that the electrodes are behaving very similarly and that the hydrogen evolution rate is minimal compared to the metal dissolution rate. In other words, for an electrode in the salt film regime, the electrochemical measurement of magnesium dissolution is almost indistinguishable from the actual dissolution rate.

This is corresponds very closely with Beck & Chan (1983) and on the basis of their detailed observations in conjunction with those reported here, it can be proposed that the hydrogen evolution during the salt film regime is due to direct reduction of water on the electrode surface following diffusion across the film.

The reactions occurring can therefore be summarised as:

at the substrate-salt film interface

$$Mg + 2Cl^- \rightarrow MgCl_2 + 2e^- \qquad \{6\text{-}1\}$$

$$H_2O + 2e^- \rightarrow O^{2-} + H_2 \qquad \{6\text{-}2\}$$

at the salt film-electrolyte interface

$$MgCl_2 \rightarrow Mg^{2+} + 2Cl^- \qquad \{6\text{-}3\}$$
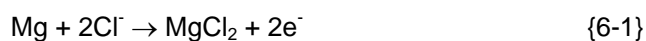
It is also interesting to note that Beck & Chan (1983) determined that the salt film thickness corresponded to applied potential according to the high field model. Therefore the mechanism of magnesium pitting can be directly compared to the passive behaviour, which has also been shown to be governed by a steady state film thickness described by the high field model. As the high field model is based on the movement of ions within a film lattice (Section 3.5), it appears that magnesium reacts by a similar mechanism under an oxide film as it does under a salt film, in both cases this relating to solid state ionic transport. Beck & Chan (1983) also showed that the magnesium chloride film was mechanically unstable (in addition to undergoing dissolution) with increasing film thickness, which is analogous to the oxide film behaviour presented in Section 4.2.

Figure 6-27: Rates of Hydrogen generation rate (blue), magnesium dissolution rate (red) and calculated current efficiency (green) for potentiostatic +4V (upper) and +2V (middle) and potentiodynamic (lower) tests
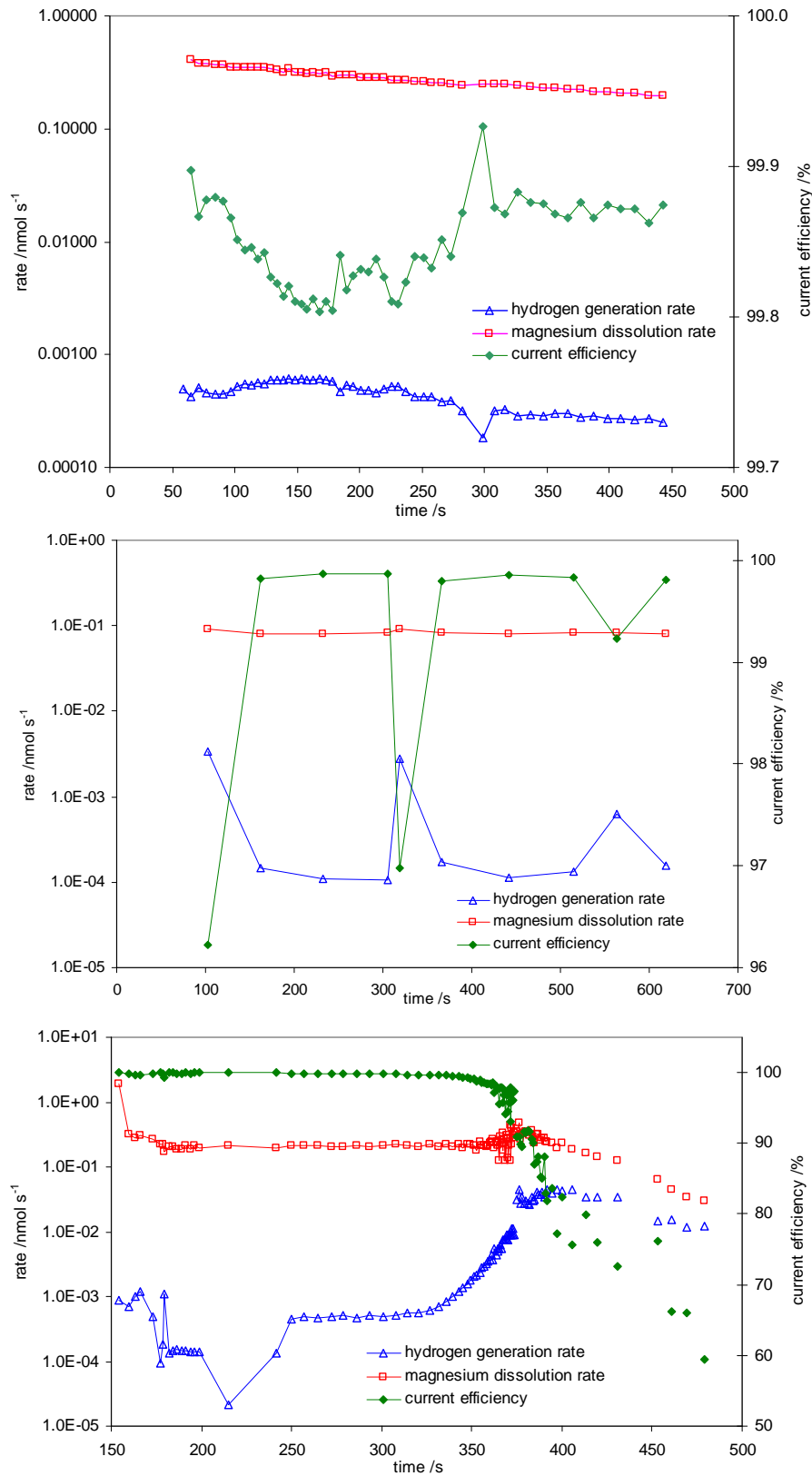
From the current efficiency of the potentiodynamic test, it can be seen that the situation changes substantially in the ohmic region, which represents much more closely the conventional behaviour of a corroding surface, in which only a small fraction of the surface will be covered by salt film. The current efficiency (Figure 6-28) drops from a consistent value of >99% initially to around 90% at the transition from potential independence and then to around 60-70%, which notably is consistent with the values measured in Section 6.2 as well as data from other workers (Beck & Chan, 1983, and Song & Atrens, 2007, Bender *et al.,* 2011). It is notable that the drop in current efficiency is at first mainly due to an increase in hydrogen generation rate at the transition, but subsequently, as both rates fall from peak values, represents a more rapid decrease in the dissolution rate than hydrogen generation.

Figure 6-28: Variation of calculated current efficiency (apparent magnesium dissolution rate as a fraction of actual magnesium dissolution rate) with potential for magnesium microelectrodes under potentiostatic (diamond and circle) and potentiodynamic (triangle) control
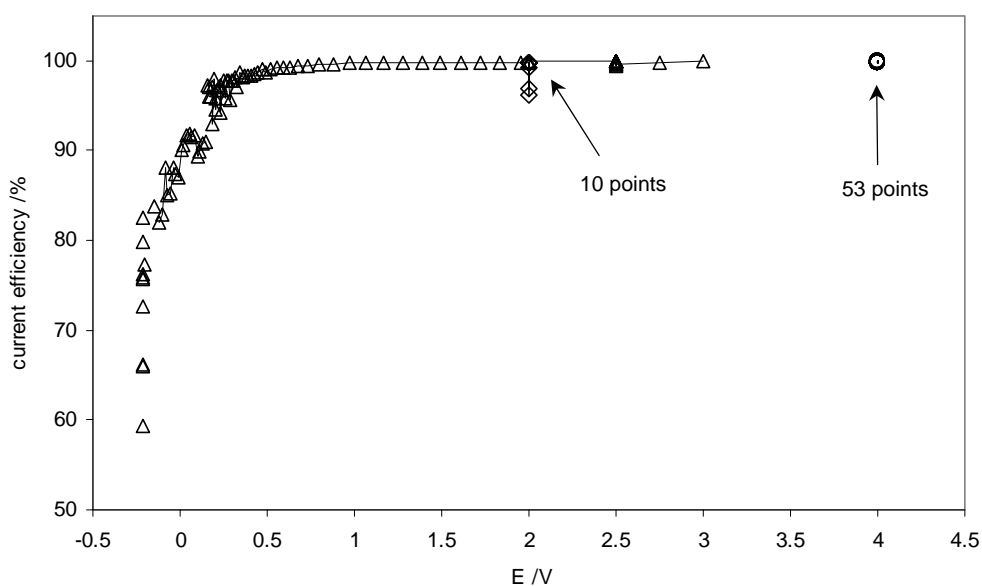
The basis for the transition between potential independent and ohmic behaviour requires consideration. The former represents a condition where a continuous salt film exists across the surface, whereas in the latter, the film is discontinuous and moving. Beck & Chan (1983) proposed that the permittivity of the salt film matrix to hydrogen would be high enough to allow diffusion of hydrogen created very close to the metal surface back to the film-solution interface before nucleation. An extension of this mechanism may be proposed which could provide an explanation for the transition between the two regimes. As the potential drops, the steady state thickness of the film will also reduce, according to the high field model (Beck & Chan, 1983). Assuming that

the rate of hydrogen production is dependent upon the flux of water molecules at the metal interface, this will increase with reducing film thickness. At some point, the rate of hydrogen production would exceed the permittivity of the matrix and nucleation of micro-bubbles within the film would occur, mechanically disrupting the lattice. As this would itself increase availability of water at the metal interface, once initiated, the disruption of the continuous salt film would be rapid, as observed. It would also be characteristic of the permittivity of hydrogen and steady state film thickness which would correspond to the consistent value observed for the transition potential. Once the surface was disrupted by hydrogen nucleation (or due to production of oxide ions above the concentration which could be incorporated into the salt film lattice), localised repassivation of the surface would occur where sufficient water was available to form an oxide layer. This freshly formed and rapidly passivating surface would then be spontaneously disrupted by the high local chloride concentration as described in Section 5, implying rapid movement and alternation of the phases on the surface. This would be consistent with the very noisy and rapidly fluctuating character of the current density observed in the ohmic region, and particularly at potentials close to the transition from salt film corrosion. This also broadly corresponds to the alternating passivation and dissolution of electrode surface on a two dimensional artificial pit described in Section 6.2.

A further extension of this hypothesis could suggest a mechanistic basis for the characteristic current efficiencies observed for localised corrosion occurring on an electrode under ohmic control. This would consider the point at which the salt film is first disrupted by hydrogen bubble nucleation as a microscopic steady state boundary between a freshly formed passivating oxide film and a salt film, where the rate of reaction would be highest due to the high transport rates. The size of the salt film phase (where potential independent dissolution would be occurring) would be constrained by the disruptive nature of the hydrogen evolution. On the basis that the area of the phase (proportional to dissolution rate) would probably be geometrically related to the oxide-salt film boundary length (proportional to hydrogen evolution), the relation between the dissolution and hydrogen evolution rates also becomes characteristic and potential independent, consistent with observation. It is noted that this mechanism would satisfactorily explain the phenomenon of anodic hydrogen evolution on magnesium as the rate of hydrogen evolution would be related only to the area of salt film. Although this latter would be expected to be potential dependent due to film breakdown and migrative effects (see Section 5), the ratio between the two rates would remain constant.

Such a mechanism would involve very violent alternation in the processes occurring on the surface, with rapid changes in reaction rate of as much as 8 orders of magnitude.

This would lead to immense stress at the substrate surface and could be readily related to disruption of the metal surface. This would be consistent with the observations made by Straumanis & Bhatia (1963) of fine grained but stable metal particulates in the corrosion product from localised attack, and also correlate closely with the observation of Section 4.1, and so explain the colour of the surface corrosion filaments and underlying pit corrosion products. Features similar to etch pits have also been observed and this may represent the salt film corrosion morphology under freely corroding conditions.

Salt film corrosion has previously been proposed as the basis for the filiform-like corrosion on magnesium (Lunder et al., 1994) and this is supported by the observation that macroelectrodes exposed to high levels of chloride experienced current densities during surface filiform-like corrosion almost immediately after initiation approaching those measured for microelectrodes under salt film regime (see Figure 4.1-30). This also corresponds to the localised current densities measured with surface techniques for magnesium surfaces undergoing surface corrosion (Williams & McMurray, 2008). The cathodic activation observed in the latter work shows an aspect of the mechanism by which bulk pitting propagates on freely corroding samples.

For a salt film which is not within an occluded cavity, transport of corrosion products would be rapid, but complicated by the alkaline electrolyte. This would tend to suggest a situation in which the salt film surface is directly hydrated to magnesium hydroxide which would then form a transport barrier, so favouring surface propagation of the salt film at the passive oxide boundary. When the conditions are conducive to a substantial fraction of the surface undergoing this type of corrosion, the corrosion density for the heterogeneously reacting surface would tend towards the value for a salt film.

6.3.3   Summary of salt film corrosion behaviour

The results presented above provide a clear insight into the mechanism of pitting in magnesium and a number of important observations have been made which elucidate aspects of surface behaviour.

A magnesium surface corroding under a salt film exhibits a near-zero rate of hydrogen evolution. This shows that the predominant process occurring on the electrode surface is dissolution of metal according to the standard half-cell reaction involving electrochemical production of divalent magnesium.

As the salt film on the electrode surface dissolves (in this case due to the potential dropping below that required to maintain a stable coverage on the whole surface), the hydrogen evolution rate increases substantially. Although the metal dissolution rate also increases initially due to increased convective transport, the relative increase in hydrogen evolution rate is sufficiently large that this soon accounts for a little under half the total magnesium dissolution rate which agrees closely with the findings of Section 6.2 and previous work.

Overall, these results correlate closely with the detailed observations of Beck & Chan (1983) and strongly support the postulated reactions of water and magnesium at the metal surface.

A number of further interpretations have been made on the basis of the microelectrode results presented here along with those reported in previous mechanistic work. In certain cases, these are further supported by results discussed in previous sections.

The transport and reduction of water at the metal interface provides a possible explanation for the consistently observed transition between potential independent and ohmic behaviour. This considers disruption of the film due to the effect of hydrogen gas nucleating within the salt film matrix when the concentration exceeds the permittivity of the lattice as production rate exceeds removal by diffusion.

The film kinetics appear to have a similar basis for the magnesium reaction whether covered with either an oxide or a salt film. This would be consistent with the mechanism involving ion transport through the surface film. A implication of this would be that corrosion behaviour is dictated by phases comprising very small amounts of material which could be consistent with the problematical nature of firmly identifying mechanisms which is apparent in the literature,

The results show that the changes observed in hydrogen evolution behaviour are consistent with standard electrochemical processes occurring on the electrode surface but represent a change in the predominance of corrosion mechanisms according to coverage of the surface with either an oxide or a salt film. One particular significance of the salt film is that it appears to allow direct access of water to the metal surface.

Relating these findings to macroscopic behaviour, it is apparent that on an electrode undergoing localised corrosion by chloride attack, the number of individual active sites (i.e., the total area of salt film, whether filiform sites or pits), increases with potential, so that the overall response is ohmic. This is likely to be due to a higher availability of

chloride at surface sites due to migration and the initiation of sites according to the local pitting potential.

For a pitting macroelectrode, or a microelectrode at low potential, a mixture of passive layer corrosion, active localised (salt film) corrosion sites and cathodic hydrogen evolution areas exists on the anode, with a proportion of the hydrogen evolution occurring on the cathode, whilst on a salt-film covered microelectrode the entire metal surface is experiencing dissolution and hydrogen evolution is limited almost exclusively to the cathode.

These results therefore reconcile a number of the characteristic behaviours observed for Magnox and magnesium on the basis of a limited set of underlying standard chemical reactions at work which relate to very different macroscopic corrosion processes due to a strong dependence on the mass transport mechanisms specific to different interfaces in the system.

7   Conclusions

From the contextual review described in Section 1 of this document, three areas of priority for study of Magnox corrosion behaviour have been highlighted. These relate to the requirement to maintain spent fuel clad passivity over long timescales whilst avoiding corrosive failure of clad integrity.

These were expressed as three questions with corresponding hypotheses:

1. What happens during Magnox passivation?

The short term passivation behaviour of Magnox is dominated by the presence of a thin oxide layer, however, the long term behaviour is also influenced by the thick outer hydroxide layer.

2. Why does localised corrosion initiate?

Initiation of localised corrosion occurs as a result of the interaction of aggressive anions with the passive film interface at the atomic scale.

3. How does surface attack develop into destructive pitting?

Pitting of magnesium occurs due to the presence of a salt film on the metal surface which allows dissolution at very high rates in localised areas even for relatively low bulk levels of aggressive ions.

The extent to which each of these has been resolved is discussed in the following sections.

7.1   Passive Behaviour

The film growth model for Magnox oxide kinetics has been extended to describe the behaviour of the passive film as it evolves from a thin, dense, largely non-hydrated oxide layer into a thick porous hydroxide film with an underlying oxide barrier layer. This has been fitted to data for passivating electrodes undergoing different types of electrochemical experiments and shows semi-quantitative agreement (Section 4.2).

The model which has been developed here considers that the dense inner oxide film at the metal interface controls the film growth reaction according to high field kinetics

according to the findings of other workers, but that the film is rapidly hydrated at the solution interface into a non-protective hydroxide, at a rate which increases with inner film thickness, probably due to stresses within the film. This outer film does not appear to contribute directly to reducing ionic flux, but does stabilise the inner oxide film. This complements the findings of workers investigating other metals who have identified impacts of porous outer hydroxide films on passivity in addition to the dominant inner oxide, although the specific behaviour noted was different to that proposed here.

This work reconciles the previous observations of a thin, freshly formed oxide film and a thick hydroxide layer. It also explains certain key aspects of the electrochemical behaviour which were not understandable on the basis of the previous model (see Section 4.2).

The results provide a basis for understanding and interpreting the behaviour of Magnox surfaces which bear thick passive corrosion films, as would be typical of real clad material stored over long timescales in a pond environment.

7.2   Localised Corrosion Initiation

The transition from a stable passive layer experiencing a very low rate of corrosion to a highly heterogeneous surface with small areas undergoing corrosion rates up to 10^8 times higher clearly involves a very dramatic change in conditions. For magnesium and Magnox, this is typically a near-instantaneous breakdown in passivity (Section 4.1).

Quantum mechanical atomistic studies of the interaction of hydroxide, chloride and fluoride groups with the solution interface of the magnesium oxide passive layer have shown that the breakdown behaviour can be related to the effect of these surface groups on surface energy. Differences in preferential substitution between aggressive and passivating species are apparent which are consistent with the effect of these anions on surfaces (Section 5).

Chloride does not strongly interact with the passive film until a high coverage is reached but over a small range, becomes favourably substituted into the lattice. Fluoride is substituted from significantly lower coverages which is consistent with the observed inhibiting effect.

The extent of surface chloride coverage identified in the calculations as the boundary to lattice substitution has been related to the ratio of chloride to hydroxide in bulk electrolytes. This shows a close agreement with electrochemical tests at high pH and

some simple considerations of migrative effects have suggested that movement of chloride in an ionic flux close to a surface could explain the trend in localised corrosion boundary at lower alkalinities.

The observations on chloride are consistent with film breakdown being a cascade failure mechanism involving destabilisation of the oxide surface at highly defected sites by adsorption of chloride ions leading to self-propagating fissuring of the initially stable film as chloride adsorbs onto the newly created surface within the oxide. An important implication of this is that it would ultimately result in disruption of the film until impingement on the metal-oxide interface. At this point, an occluded phase of chloride is in contact with the bare unfilmed magnesium surface. This would be an initiating condition for micro-scale salt film corrosion which is consistent with the filiform-like features which typify the initial localised corrosion morphology of the material.

7.3   Pitting Mechanism

The production of magnesium microelectrodes and application in corrosion studies have been reported here for what is understood to be the first time. These were found to behave readily as artificial pits with foil electrodes behaving two-dimensionally and showing alternating division of the surface into active and passive areas, while wire electrodes behaved one-dimensionally (Section 6).

Results from the latter tests showed that the material undergoes salt film corrosion in bulk alkaline electrolyte conditions with aggressive ion levels some 4 orders of magnitude lower than observed previously. The levels of chloride were credible in relation to a pond environment fault scenario and the applied potential range covered possible galvanic polarisations within a storage environment, although higher potentials were required for initial breakdown. The hydrogen evolution rate during this regime has been found to be minimal and the valency of dissolution consistent with the conventional magnesium reaction, in common with previous mechanistic studies.

A number of observed consistencies between the mechanisms identified in different corrosion regimes have been discussed. The passive behaviour, filiform-like corrosion and bulk pitting behaviour can be reconciled primarily by consideration of the reaction of the metal under a thin film (oxide or salt) alongside a corrosion product transport mechanism, whether oxide surface hydration or ion migration and re-precipitation, which determines the corrosion evolution and morphology.

Consequently, on the basis of the work described here and in the light of previous investigations, the following reaction scheme can be proposed for the corrosion reactions of magnesium under passive behaviour and chloride induced pitting.

For a passive film (see Section 4.2):

at the metal-oxide film interface
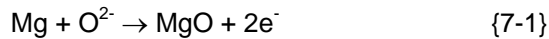
$$Mg + O^{2-} \rightarrow MgO + 2e^- \qquad \{7\text{-}1\}$$

at the oxide-hydroxide interface

$$MgO + 2OH^- \rightarrow Mg(OH)_2 + O^{2-} \qquad \{7\text{-}2\}$$

cathodic reaction

$$2H_2O + 2e^- \rightarrow H_2 + 2OH^- \qquad \{7\text{-}3\}$$
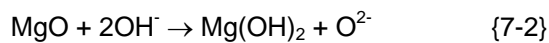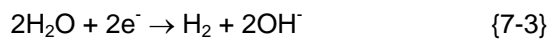
at the hydroxide-solution interface (including spalled products) and precipitated corrosion products (re-precipitated corrosion product)

$$Mg(OH)_2 \longleftrightarrow Mg^{2+} + 2OH^- \qquad \{7\text{-}4\}$$

For an active pit area (see Sections 5 and 6):

at the metal-salt film interface

$$Mg + 2Cl^- \rightarrow MgCl_2 + 2e^- \qquad \{7\text{-}5\}$$

at the salt film-electrolyte interface

$$MgCl_2 \rightarrow Mg^{2+} + 2Cl^- \qquad \{7\text{-}6\}$$
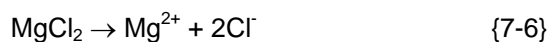
cathodic reaction under the salt film (after Beck & Chan, 1983)

$$H_2O + 2e^- \rightarrow H_2 + O^{2-} \qquad \{7\text{-}7\}$$
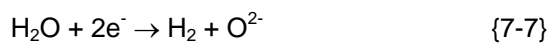
with the oxide ion then being hydrated possibly following incorporation into a film structure

$$O^{2-} + H_2O \rightarrow 2OH^- \qquad \{7\text{-}8\}$$

in addition to the cathodic reaction on the non-salt film surface as in reaction 7-3 above.

the rapid reactions would lead to microfracturing (Straumanis & Bhatia, 1963) and it may be the case that for surface filaments, the underlying salt film areas are directly hydrated to hydroxide

$$MgCl_2 + 2OH^- \rightarrow Mg(OH)_2 + 2Cl^- \qquad \{7\text{-}9\}$$
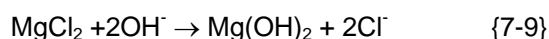
Overall reaction:

In both cases, where the film at the metal interface (whether passive oxide film or salt film) is conserved, then the overall reaction for reaction sequences (see Figure 7-1) representing (i) passive corrosion, (ii) filiform-like corrosion, (iii) bulk pitting, and (iv) the observed electrochemical reaction are as follows:

(i) 1, 2, 3, 4
(ii) 5, 7, 8, 9
(iii) 4, 5, 6, 7, 8
(iv) 1, 2, 3

Notably these are equivalent and ostensibly:

$$Mg + 2H_2O \rightarrow Mg(OH)_2 + H_2 \qquad \{7\text{-}10\}$$
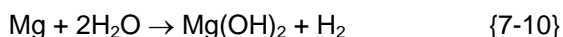
The microelectrode tests also showed that the transport processes away from the salt film within the artificial pit are consistent with diffusion from a saturated solution near the pit base into the bulk electrolyte with some convective transport by the hydrogen bubbles which were periodically produced (Section 6.2). This shows that the flux of magnesium ions was sufficient to suppress the local pH. When under normal ohmic conditions, the relative hydrogen evolution rate was many times higher and so the convective transport could be expected to be dominant (Section 6.3). This relates to the observed morphology of macro-scale pits with channelling of hydrogen through re-precipitated corrosion product in pit voids (Section 4). This points to an important aspect of macroscale pit evolution with the related and competing processes of convective transport and precipitation removing corrosion product from areas of active pitting and concurrently affecting admission of passivating alkaline bulk electrolyte as well as reactive water molecules and chloride ions.

Figure 7-1: Illustration of proposed reaction sequences for (i) a passive film, (ii) filiform-like corrosion and (iii) salt film corrosion (left to right)

$Mg(OH)_2 \rightarrow Mg^{2+} + 2OH^-$

$MgO + 2OH^- \rightarrow Mg(OH)_2 + O^{2-}$

$Mg + O^{2-} \rightarrow MgO + 2e^-$

$2H_2O + 2e^- \rightarrow H_2 + 2OH^-$

$Mg^{2+} + 2OH^- \rightarrow Mg(OH)_2$

$MgCl_2 \rightarrow Mg^{2+} + 2Cl^-$

$O^{2-} + H_2O \rightarrow 2OH^-$

$Mg + 2Cl^- \rightarrow MgCl_2 + 2e^-$

$H_2O + 2e^- \rightarrow H_2 + O^{2-}$

magnesium metal

magnesium hydroxide

electrolyte

oxide film

salt film

hydrogen bubble
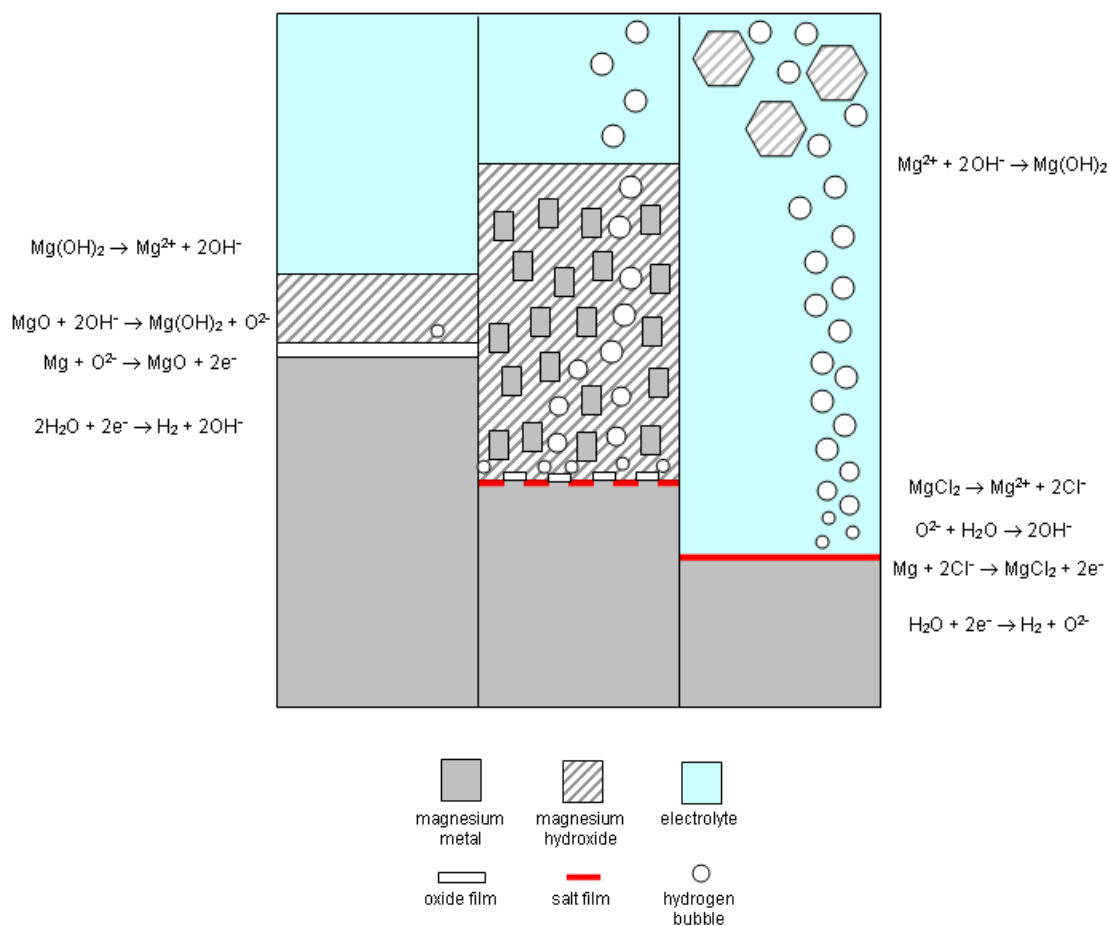
7.4   Opportunities for Forward Investigation

Further kinetic information could be determined from microelectrode studies and these would provide a promising means of studying inhibition reactions, particularly for propagating pits. Further use of *in situ* analysis would also allow additional aspects of the processes at work to be established and examined. Identification of transoptic mount material with enhanced crevice resistance, or novel means of achieving this would facilitate further optical investigations.

The use of *in situ* tomography would also present an excellent means of studying open circuit pitting morphology in comparison to polarised pits and also the impact of hydrogen transport within occluded zones. Additional processing of existing data from tomography experiments should allow measurement of quantitative corrosion rates. Further use of high resolution surface techniques to look at small scale modifications in the pre-initiation period would be very interesting, particularly if this could be reconciled against the microstructure, inclusions and grain orientation. The use of visual examination, SVET, AFM and SEM would each allow different aspects to be investigated. ESEM investigation in tandem with *in situ* hydrogen evolution measurements (such as with use of a sensor within the ESEM cavity) would be an interesting means of studying atmospheric corrosion processes. Modelling of EIS spectra could provide a means of examining the mechanisms proposed here if unique features or behaviours can be convincing reproduced based on a developed equivalent circuit.

Although the aggressive ion concentrations studied have been brought much closer to those in real plant environments, these are still above those known to cause pitting, plus most understanding of initiation relates to relatively high polarisation. Opportunities to reconcile these differences further should be sought. The impact of geometrical features such as crevices on initiation is a very relevant area which could be studied readily. Also the evolution of crevice regions with time alongside a passivating surface would be of direct relevance to clad material storage as well as being mechanistically informative.

The passivation behaviour over very long timescales is clearly of interest, and the ability for this to be accelerated and extent to which this is equivalent to open circuit growth are very relevant.

The hydrogen evolution behaviour of magnesium continues to be an area of international academic interest. Considering the results here along with previous studies suggests that the evolution of hydrogen from direct reduction of water at the metal surface may be a very promising proposition in the quest for conclusion of mechanistic

speculation. It has previously been proposed that hydrogen evolution under a salt film is potential independent and variations are related to film thickness and is consistent with diffusion through the solid magnesium chloride matrix, of water to the metal surface, and molecular hydrogen back to the electrolyte interface where it nucleates. This could be confirmed if parameters which affected the nucleation of hydrogen, but not other aspects of the corrosion mechanism could be affected in kinetic tests. This may lead to opportunities to further develop the hypothesis that geometrical or kinetic characteristics of the mechanism may relate to the consistently observed value of current efficiency.

Considering the context of a corrosion filament suggests the identical considerations in rate ratio would apply despite the two modes of corrosion being morphologically very different, which is again supported by observation. Further investigation of this would also possibly allow the conditions for bulk pitting propagation to be identified as on this basis, macro-scale pitting will ensue once a sufficient modification of surface geometry has occurred to allow a large area of adjacent microscopic salt film areas to persist and be maintained by local precipitation of porous corrosion product, allowing access of water but encouraging enrichment of chloride by migration and egress of hydrogen. The fact that these processes could be cyclical would explain some of the observations of periodic activity in macro-scale pits, with hydrogen convection causing deactivation of an active pit area by admission of alkaline electrolyte and then migration of ions through the tortuous path to the subsequently re-passivating surface and causing increase of chloride concentration to the point where breakdown re-occurs and areas of salt film can reform. Use of numerical models and finite element based calculations represent very powerful means of testing and investigating such mechanistic propositions.

There are evidently very promising and extensive possibilities to use atomistic modelling for investigation of corrosion processes, with the ability to simulate passive film interfaces having been demonstrated extensively. This could clearly be developed further with substantial benefit, as well as application alongside multiscale techniques. The fact that both the oxide and salt film typical thicknesses are consistent with the size of a structure that can be simulated with quantum mechanical methods points to opportunities to study static properties such as formation of sub-phases, interface behaviour and permittivity, as well as use of techniques to simulate kinetic behaviour such as derivation of lattice diffusion

In particular, the opportunity to use quantum mechanical atomistic modelling to examine the reaction pathway in the initial steps of the magnesium ionisation and charge transfer steps would seem an ideal addition to the examination of reaction intermediates and the lifetime of a hypothetical monovalent magnesium ion. Quantum mechanical methods would present a means of convincingly establishing what the credible maximum period

between the first and second electron transfers is and consequently whether the lifetime of an intermediate species is consistent with a chemical reaction taking place.

8   Summary

The work presented here represents a series of substantial advancements in the understanding of Magnox and magnesium behaviour under alkaline systems and specifically the processes affecting transition from passive behaviour to pitting. This directly relates to the performance of Magnox as a spent fuel element clad in aqueous storage. Investigations have covered length ranges from the atomic scale to realistic clad dimensions, with a clear focus on electrochemical behaviour, supported by various observational and characterisation techniques.

The results underline, explain and, in key instances, reconcile the outcomes of previous programmes of work. The possibility for Magnox to remain passive over substantial timescales is evident, as is the potential for destructive pitting and rapid clad failure to occur under adverse conditions. This work has featured an evident focus on chemistry aspects of this corrosion issue which is appropriate due to the status of the material. Manufacture of Magnox fuel has now ceased and only a single reactor of this type now continues electrical generation worldwide. The future production of spent fuel is therefore relatively small and consequently opportunities for affecting behaviour from a front end perspective are constrained even more than previously when corrosion performance was only one of a large number of requirements for fuel elements. Due to the expectation that wet storage of spent Magnox clad fuel and associated waste forms will continue for some years into the future, the completion of this work represents an incremental reduction in the risk associated with management of these materials.

The techniques which have been developed and applied here provide a powerful toolset for ongoing technical support to aqueous storage of spent fuel, and other aspects of Magnox behaviour, whether these involve non-aqueous storage or relate to options for processing and disposition of wastes comprising clad material. This would facilitate focussed plant support on specific quantitative questions, or wider investigation into behaviour outside the currently understood envelopes. Potential for further academically valuable investigation relating to mechanistic corrosion science for magnesium and other materials is also apparent.

9 References

Aghion E & Lulu N, 2010, The corrosion performance of die-cast magnesium alloy MRI230D in 3.5% NaCl solution saturated with Mg(OH)2, Materials Characterisation, 61 p1221.

Albright D, 1994, North Korea's corroding fuel, Science & Global Security, 5 p89.

Allen JP, Parker SC, Price DW, 2009, Atomistic simulation of the surface carbonation of calcium and magnesium oxide surfaces, J. Phys. Chem. C, 113 p8320.

Ashworth TV, Pang CL, Wincott PL, Vaughan DJ, Thornton G, 2003, Imaging in situ cleaved MgO (100) with non-contact atomic force microscopy, Applied Surface Science, 210, p2.

Atkiv Nuclear JV, 2012, Case study: Isolation and Risk Reduction Project Sellafield UK, acktivnuclear.com/index.php/case-studies/108-isolation-and-risk-reduction-project-sellafield-uk, accessed 18/12/12.

Baborovsky G, 1903, Ueber das magnesiumsuboxyd, Berichte der deutschen chemischen gesellschaft, 36 (3) p2719.

Beck TR & Chan SG, 1983, Corrosion of magnesium at high anodic potentials, J. Electrochem. Soc., 130 (6) p1289.

Becke AD, 1988, A multicentre numerical integration scheme for polyatomic molecules, J. Chem. Phys., 88, 4 p2547.

Beetz W, 1866, On the development of hydrogen from the anode, Philosophical Magazine Series 4, 32:216, 269.

Bender S, Goellner J, Heyn A, Schmigalla S, 2011, A new theory for the negative difference effect in magnesium corrosion, Mat. and Corr., 63 (8) p707.

Boese AD & Handy NC, 2001, A new parameterisation of exchange-correlation generalised gradient approximation functionals, J. Chem. Phys., 114 p5497.

Bouzoubaa A, Costa D, Diawara B, Audiffren N, Marcus P, 2010, Insight of DFT and atomistic thermodynamics on the adsorption and insertion of halides onto the hydroxylated NiO(111) surface, Corr. Sci. 52 p2643.

Bouzoubaa A, Diawara B, Maurice V, Minot C, Marcus P, 2009, Ab initio modelling of localised corrosion: study of the role of surface steps in the interaction of chlorides with passivated nickel surfaces, Corr. Sci., 51 p2174.

Bradford PM, Case B, Dearnaley G, Turner JF, Woolsey IS, 1976, Ion beam analysis of corrosion films on a high magnesium alloy (Magnox AL80), Corr. Sci., 16 p747.

Burrows R, Cook A, Stevens N, 2012, Magnesium microelectrode corrosion product transport modelling in relation to chloride induced pitting, Proceedings of International Conference on Chemistry of Nuclear Reactor Systems 2012 (NPC 2012), 24-27th September 2012, Paris.

Burrows R, Harris S, Stevens NPC, 2005, Corrosion electrochemistry of fuel element materials in pond storage conditions, Trans. IChemE, Pt. A, Chemical Engineering Research and Design, 83 (A7), 887-892.

Burrows RW & Harris S, 2007, Electrochemical Corrosion Study of Magnox Al80 and Natural Uranium *article in* EFC Publications No. 49, Electrochemistry in light water reactors – Reference electrodes, measurement, corrosion and tribocorrosion issues, Ed. Bosch RW, Féron D, Celis JP, Woodhead Publishing, Cambridge.

Bussy M, 1832, On magnesium, Philosophical Magazine Series 2, 11:61, 74.

Cabrera N & Mott NF, 1949, Theory of the oxidation of metals, Rep. Progr. Phys., 12 163.

Cabrera-Sierra R, Pech-Canul ME, Gonzalez I, 2006, The role of hydroxide in the electrochemical impedance response of passive films in corrosion environments, J. Electrochem. Soc., 153, 3 pB101.

Carrasco E, Brown MA, Sterrer M, Freund H-J, Kwapien K, Sierka M, Sauer J, 2010, Thickness-dependent hydroxylation of MgO (001) thin films, J. Phys. Chem. C, 114 p18207.

Case B, Bradford PM, Garbett K, 1977, Silicate and the aqueous corrosion of a high-magnesium alloy, Nature 268, p223.

Case B & Hilton DA, 1978, Water chemistry control and corrosion inhibition in Magnox fuel storage ponds, Water Chemistry of Nuclear Reactor Systems, BNES London.

Catlow CRA, Faux ID, Norgett MJ, 1976, Shell and breathing shell model calculations for defect formation energies and volumes in magnesium oxide, J. Phys. C: Solid State Phys., 9 p419.

Catlow CRA, Freeman CM, Royle RL, 1985, Recent studies using static simulation techniques, Physica 131B p1.

Chen J, Wang J, Han E-H, Ke W, 2009, In situ observation of pit initiation of passivated AZ91 magnesium alloy, Corr. Sci., 51 p477.

Christomanos AC, 1903, Zur verbrennung des magnesiums, Berichte der deutschen chemischen gesellschaft, 36 (2) p2076.

Clark SJ, Segall MD, Pickard CJ, Hasnip PJ, Probert MJ, Refson K, Payne MC, 2005, First principles methods using CASTEP, Z. Kristallogr., 220, p567.

Cook AB & Newman RC, 2002, Critical conditions for stability of pits in aluminium: A contribution to the mechanisms of tunneling corrosion, Electrochemical Society Proceedings, 24 p187.

Costa D, Chizallet C, Ealet B, Gonaikowski J, Finocchi F, 2006, Water on extended and point defects at MgO surfaces, J. Chem. Phys., 125 054702.

Cowan KG & Harrison JA, 1979, The dissolution of magnesium in Cl$^-$ and F$^-$ containing aqueous solutions, Electrochimica Acta, 24 p301.

Davenport AJ, Padovani C, Connolly BJ, Stevens NPC, Beale TAW, Groso A, Stampanoni M, 2007, Synchrotron x-ray microtomography study of the role of Y in corrosion of magnesium alloy WE43, Electrochem and Solid-State Lett., 10 (2) pC5.

de Leeuw NH & Parker SC, 1998, Molecular dynamics simulation of MgO surfaces in liquid water using a shell-model potential for water, Phys. Rev. B, 58 (20) p13901.

de Leeuw NH, 2001, Density functional theory calculations of hydrogen-containing defects in forsterite, periclase, and a-quartz, J. Phys. Chem. B, 105 p9747.

de Leeuw NH, Watson GW, Parker SC, 1995, Atomistic simulation of the effect of dissociative adsorption of water on the surface structure and stability of calcium and magnesium oxide, J. Phys. Chem., 99 p17219.

Delley B, 1990, An all-electron numerical method for solving the local density functional for polyatomic molecules, J. Chem. Phys. 92, 1 p508.

Delley B, 2000, From molecules to solids with the DMol^3 approach, J. Chem. Phys. 113, 18 p7756.

Delley B, 2006, The conductor-like screening model for polymers and surfaces, Mol. Sim. 32, 2 p117.

Delley B, 2010, Time dependent density functional theory with DMol^3, J. Phys.: Condens. Matter, 22 384208.

DMol^3 User Guide, 2001, Density Functional Theory Electronic Structure Program, Accelrys Software Inc., San Diego, US.

Do T, Splinter SJ, Chen C, McIntyre NS, 1997, The oxidation kinetics of Mg and Al surfaces studied by AES and XPS, Surface Science, 387, p192.

Duckworth FC, Holm RA, Molloy T, Rhodes D, 1988, Performance of Magnox fuel elements at peak element irradiations up to 9000 MWd/t, Nucl. Energy, 27 (2) 99.

Fairhall GA & Palmer JD, 1992, The encapsulation of Magnox swarf in cement in the United Kingdom, Cement and Concrete Research, 22 p293.

FEMLAB Chemical Engineering Model User's Guide, 2004, Version 3.0, COMSOL AB.

FEMLAB User's Guide, 2004, Version 3.0, COMSOL AB.

Fairhall GA & Palmer JD, 1992, The encapsulation of Magnox swarf in cement in the United Kingdom, Cement and Concrete Research, 22 p293.

Frankel GS, 1998, Pitting corrosion of metals: A review of the critical factors, J. Electrochem. Soc. 145 (6) p2186.

Friskney CA, 1981, The corrosion of etched Magnox Al80 in dry steam at ~10^5 Pa pressure in the temperature range 373-573 K, J. Nuc. Mat., 99 (2-3) p165.

Friskney CA, Pearce RJ, Robins IH, Simpson KH, Cutler ABJ, Grant CJ, Case B, Bradford PM, 1982, The corrosion of Magnox Al80 alloy in aqueous and moist environments, Gas Cooled Reactors Today, BNES, London (UK).

Gale JD & Rohl AL, 2003, The general utility lattice program (GULP), Molecular Simulation, 29, 5.

Ghali E, Dietzel W, Kainer K-U, 2004, General and localised corrosion of magnesium alloys: A critical review, J. Mater. Eng. and Perf., 13, 1 7.

Goldberg S, 2005, Equations and models describing adsorption processes in soils, *chapter in* Chemical Processes in Soils, SSSA Series No. 8, Madison, US.

Gonzalez Torreira M, 2004, Corrosion of Magnox AL80 fuel cans in storage environments, University of Birmingham Thesis for the degree of Doctor of Philosophy.

Gonzalez Torreira M, Fones A, Davenport AJ, 2003, Passivation and dissolution of magnesium, J. Corr. Sci. & Eng., 6 C034.

Gray J, Jones SR, Smith AD, 1995, Discharges to the environment from the Sellafield site, 1951-1992, J. Radiol. Prot., 15, 2 p99.

Greef R, Harvey PR, Tyfield SP, 1986, The corrosion of Magnox alloy Al80 in alkaline media, Materials Science Forum, 8 p395.

Hansard, 2003, House of Commons Written Answers for 17 July 2003, www.publications.parliament.uk/pa/cm200203/cmhansrd/vo030717/text/30717w21.htm, accessed 11/07/12.

Hara N, Kobayashi Y, Kagaya D, Akao N, 2007, Formation and breakdown of surface films in magnesium and its alloys in aqueous solutions, Corr. Sci., 49 p166.

Harris JE, 1985, The development and use of magnesium alloys in UK Magnox reactors, Key Eng. Mat., A8 p225.

Hoar TP, 1967, The production and breakdown of the passivity of metals, Corr. Sci., 7 p341.

Huggins ML & Sakamoto Y, 1957, Lattice energies and other properties of crystals of alkaline earth chalcogenides, J. Phys. Soc. Japan, 12, 3 p241.

IAEA, 1998, Durability of spent nuclear fuels and facility components in wet storage, IAEA-TECDOC-1012, IAEA, Vienna (Austria).

Jia JX, Song G, Atrens A, 2007, Experimental measurement and computer simulation of galvanic corrosion of magnesium coupled to steel, Adv. Eng. Mater., 9 (1-2) 65.

Jones D de G & Masterson HG, 1961, Effect of chloride concentration on the aqueous corrosion of a magnesium alloy, Letters to Nature, 191 p165.

Kantorovich LN & Gillan MJ, 1997, Adsorption of atomic and molecular oxygen on the MgO (001) surface, Surface Science, 374 p373.

Kirby C, 1987, Galvanic and crevice corrosion effects in Magnox Al80 alloy, Corrosion Science, 27, 6 p567.

Kinnunen P, 2002, Electrochemical characterisation and modelling of passive films on Ni- and Fe-based alloys, PhD thesis from the Helsinki University of Technology, Finland.

Kohn W & Sham LJ, 1965, Self-consistent equations including exchange and correlation effects, Physical Review, 140, 4A pA1133.

Kolotyrkin JM, 1961, Effects of anions on the dissolution kinetics of metals, J. Electrochem. Soc., 108 (3) p209.

Kumagai N, Kawamura K, Yokokawa T, 1994, An interatomic potential model for H_2O: applications to water and ice polymorphs, Molecular Simulation, 12 (3-6) p177.

Labidi M, Labidi S, Ghemid S, Meradji H, El Haj Hassan F, 2010, Structural, electronic, thermodynamic and optical properties of the alkaline earth oxides MgO, SrO and their alloys, Phys. Scr., 82 045605.

Laycock NJ & Newman RC, 1997, Localised dissolution kinetics, salt films and pitting potentials, Corr. Sci., 39 10 p1771.

Lee C, Yang W, Parr RG, 1988, Phys. Rev. B, 37 p786.

Lewis DW & Catlow CRA, 1994, A computational study of the role of chlorine in the partial oxidation of methane by MgO and Li/MgO, Topics in Catalysis 1 p111.

Lewis GV & Catlow CRA, 1985, Potential models for ionic oxides, J. Phys. C: Solid State Phys., 18 p1149.

Li J, Zhang T, Shao Y, Meng G, Wang F, 2010, A stochastic analysis of the effect of magnetic field on the pitting corrosion susceptibility of pure magnesium, Mat. and Corr., 61 (4) 306.

Li L, 2010, Corrosion mechanism and model of anodised film on AZ91D magnesium alloy, Int. J. of Modern Phys. B, 24 (15&16) 3077.

Lide DR (Ed.-in-Chief), 2001, CRC Handbook of Chemistry and Physics 82nd Ed, CRC Press.

Lunder O, Lein JE, Hesjevik SM, Aune T Kr, Nisanciogiu K, 1994, Corrosion morphologies on magnesium alloy AZ91, Werkstoffe und Korrosion, 45 p331.

Macdonald DD & Sikora E, 2002, Nature of the passive film on nickel, Electrochimica Acta, 48 p69.

Magnox Ltd, 2012, "Damaged fuel leaves site", Wylfa news article, 18/07/11 www.magnoxsites.com/news/site-news/wylfa-news/2011-07-18/damaged-fuel-leaves-site, accessed 11/07/12.

Manning P, 2003, Sellafield Fuel Handling Plant pondwater update, Nuclear Safety Committee paper NuSAC(03)P10, www.hse.gov.uk.

Masterson HG & Harrison JT, 1961, Fuel element storage at the nuclear power stations of the Central Electricity Generating Board, First Intern. Congr. Metallic Corrosion, London.

Materials Studio User Guide, 2010, Accelrys Software Inc., San Diego, US.

Moayed MH & Newman RC, 2005, Using pit solution chemistry for evaluation of metastable pitting stability of austenitic stainless steel, Materials and Corrosion, 56, 3 p166.

Morris J, Wickham S, Richardson P, Rhodes C, Newland M, 2009, Contingency options for the dry storage of Magnox spent fuel in the UK, Proceedings of the 12th International Conference on Environmental Remediation and Radioactive Waste Management (ICEM2009), October 11-15 2009, Liverpool (UK).

NDA, 2010, Magnox Operating Plan (MOP8) including Addendum 2 of August 2010, www.nda.gov.uk, accessed July 2012.

NDA, 2011, NDA Strategy: Post Consultation Responses – Spent Magnox Fuel, April 2011, www.nda.gov.uk, accessed July 2012.

NDA, 2012, Insight magazine, Issue 2, http://www.nda.gov.uk/stakeholders/newsletter/fgmsp.cfm, accessed 11/07/12.

Nordlien JH, Ono S, Masuko N, 1995, Morphology and structure of oxide films formed on magnesium by exposure to air and water, J. Electrochem. Soc., 142, 10 p3320.

Newman RC & Ajjawi MAA, 1986, A micro-electrode study of the nitrate effect on pitting of stainless steels, Corr. Sci., 26, 12 p1057.

Perdew JP & Wang Y, 1992, Accurate and simple analytic representation of the electron-gas correlation energy, Phys. Rev. B, 45, p13244.

Perdew JP, Burke K, Wang Y, 1996, Generalised gradient approximation for the exchange-correlation hole of a many-electron system, Phys. Rev. B, 54, 23 p16533.

Petty RL, Davidson AW, Kleinberg J, 1954, The anodic oxidation of magnesium metal: evidence for the existence of unipositive magnesium, J. Am. Chem. Soc., 76 (2) p363.

Pineau N, Minot C, Maurice V, Marcus P, 2003, Density functional theory study of the interaction of Cl^- with passivated nickel surfaces, Electrochem. and Solid-State Letts., 6 (11) pB47.

Pistorius PC & Burstein GT, 1992, Growth of corrosion pits on stainless steel in chloride solution containing dilute sulphate, Corr. Sci. 33, 12 p1885.

Richardson & Maher, 2004, Sellafield Fuel Handling Plant pondwater update, Nuclear Safety Committee paper NuSAC(04)P17, www.hse.gov.uk.

Robinson JL, 1963, Investigation of the magnesium anode, DOW metal products company report reference AD401553.

Russo S & Noguera C, 1992, Acido-basic properties of simple oxide surfaces: I – magnesium oxide, Surface Science, 262 p245.

Ruggeri RT & Beck TR, 1983, An analysis of mass transfer in filiform corrosion, Corrosion, 39, 11 p452.

Sakuma H, Tsuchiya T, Kawamura K, Otsuki K, 2004, Local behaviour of water molecules on brucite, talc, and halite surfaces: a molecular dynamics study, Molecular Simulation, 30 (13-15) p861.

Sangster MJL, 1973, Interionic potentials and force constant models for rocksalt structure crystals, J. Phys. Chem. Solids, 34 p355.

Sangster MJL, Peckham G, Saunderson DH, 1970, Lattice dynamics of magnesium oxide, J. Phys. C: Solid State Phys., 3 p1026.

Seyeux A, Maurice V, Klein LH, Marcus P, 2008, Initiation of localised corrosion at the nanoscale by competitive dissolution and passivation of nickel surfaces, Electrochimica Acta, 54 p540.

Shi Z, Liu M, Atrens A, 2010, Measurement of the corrosion rate of magnesium alloys using Tafel extrapolation, Corr. Sci., 52 579.

Shi ZM & Atrens A, 2011, An innovative specimen configuration for the study of Mg corrosion, Corr. Sci. 53 (1) 226.

Shreir's Corrosion, 2010, Volume 3: Corrosion and Degradation of Engineering Materials, Section 3.09 - Corrosion of Magnesium and its Alloys, 4th Edition, Ed.-in-Chief Richardson TJA, Elsevier BV.

Sikora E & MacDonald DD, 2002, Nature of the passive film on nickel, Electrochimica Acta, 48 p69.

Simpson DJ, Bredow T, Smart RSC, Gerson AR, 2002, Mechanisms of acidic dissolution at the MgO (100) surface, Surface Science 516 p134.

Soltis J, Laycock N, Cook A, Krouse D, White S, Artificial pit studies of anodic dissolution kinetics in localised corrosion of aluminium, ECS Trans., 11, 15 75, 2007.

Song G & Atrens A, 2007, Recent Insights into the mechanisms of magnesium corrosion and research suggestions, Adv. Eng. Mater., 9 (3) 177.

Song G, Atrens A, St John D, Wu X, Nairn J, 1997, The anodic dissolution of magnesium in chloride and sulphate solutions, Corr. Sci., 39 (10-11) p1981.

Speckert L & Burstein GT, 2011, Combined anodic/cathodic transient currents within nucleating pits on Al-Fe alloy surfaces, Corrosion Science, 53 p534.

Straumanis ME & Bhatia BK, 1963, Disintegration of magnesium while dissolving anodically in neutral and acidic solutions, J. Electrochem. Soc., 110 (5) p357.

Tang YC & Davenport AJ, 2007, Magnetic field effects on the corrosion of artificial pit electrodes and pits in thin films, J. Electrochem Soc., 154, 7 pC362.

Thomas & Weber, 1968, Pitting and contact corrosion in magnesium canned fuel rods, Werkstoffe und Korrosion, 19 (10) p895.

Thyveetil M-A, Coveney PV, Suter JL, Greenwell HC, 2007, Emergence of undulations and determinations of materials properties in large-scale molecular dynamics simulation of layered double hydroxides, Chem. Mater., 19 p5510.

Tunold R, Holtan H, Berge M-B H, Lasson A, Steen-Hansen R, 1977, The corrosion of magnesium in aqueous solution containing chloride ions, Corr. Sci., 17 p353.

Turrentine JW, 1908, Reversed electrolysis, J. Phys. Chem., 12 (6) p448.

Uhlig's Corrosion Handbook, 2011, Section 58 - Magnesium and magnesium alloys, 3rd Edition, Ed. Winston Revie R, John Wiley and Sons Inc, Hokoken, New Jersey (US).

Wang Y, Nguyen HN, Truong TN, 2006, Mechanisms of and effect of coadsorption on water dissociation on an oxygen vacancy of the MgO (100) surface, Chem. Eur. J.,12 p5859.

Weinhert M & Davenport JW, 1992, Fractional occupations and density-functional energies and forces, Phys. Rev. B, 45, 23 p13709.

White A, 2010, Nuvia Presentation on sharing good practice in decommissioning and waste management: Sludge processing extraction head, from www.safegrounds.com/ pdfs/E10402_presentation_Andrew_White.pdf, accessed 11/07/12.

Williams G & McMurray HN, 2008, Localised corrosion of magnesium in chloride-containing electrolyte studied by a scanning vibrating electrode technique, J. Electrochem. Soc., 155 (7) pC340.

Williams G, McMurray HN, Grace R, 2010, Inhibition of magnesium localised corrosion in chloride containing electrolyte, Electrochimica Acta 55 p7824.

Windsor BW, 1982, Twenty years of pond-water treatment on gas-cooled reactors, Gas Cooled Reactors Today, BNES London.

Winzer N, Atrens A, Dietzel W, Song G, Kainer KU, 2007, Magnesium stress corrosion cracking, Trans. Nonferrous Met. Soc. China, 17 150.

Xu RZ, Song G, Wang Z, 2009, Corrosion characteristics of AZ91 magnesium alloy weldments, Mat. Res. Innov. 13 (4) 441.